Development of Electronic Materials for Infra-Red Detector Systems

John-James Stuart Duncan McChesney BSc (Hons)

A thesis submitted in partial fulfilment of the requirements of Sheffield Hallam University for the degree of Doctor of Philosophy

Autumn 1999

Division of Applied Physics, Sheffield Hallam University

Abstract

Indium antimonide (InSb) and gallium antimonide (GaSb) are technologically important III-V semiconductor materials used in infrared detector systems. Yet, the application of these materials is to a certain extent limited, in that the techniques currently used for their growth are both expensive and problematic. Semiconductor electrochemical deposition, which has been successfully applied to the generation of II-VI semiconductor materials, may offer the prospect of overcoming such limitations. This work presents results that represent a significant contribution to the development of electrochemical methods for both InSb and GaSb thin film growth.

The direct electrochemical co-deposition of InSb was achieved via the potentiostatic electrolysis of aqueous halide/citric acid electrolyte solutions, and for the first time, non-aqueous (ethylene glycol) electrolyte solutions containing the halides and tetraethylammonium chloride. This choice of solvents allowed the compound's deposition to be studied over a wide range of temperatures (RT to 185 ^{o}C). A first report was also made of the direct potentiostatic co-deposition of GaSb from an aqueous solution containing $Ga_2(SO_4)_3$ and $SbCl_3$.

An extensive study was carried out on the relationship between the technique's fundamental growth parameters (temperature, deposition potential, solution composition etc.) and the film's compositional, crystallographic and morphological properties. The material's characterisation showed that there was tendency for the films to be non-stoichiometric. X-Ray diffraction patterns obtained from InSb films deposited from aqueous electrolyte solutions showed them to generally consist of two phases, the compound and, depending mostly on deposition potential, one of the elements. Films containing three phases, the compound and both elements, were deposited on Ti substrates from aqueous solutions and on to ITO substrates from non-aqueous solutions. These results were interpreted from both thermodynamic and kinetic viewpoints. This led to the conclusion that kinetic barriers to the formation of InSb still existed, even at the highest temperature used (~185 ^{o}C). In respect of GaSb, the compound's formation was complicated by a side reaction involving the evolution of H_2.

New studies involving Scanning Electron Microscopy of the electrodeposited materials showed that they exhibited a nodular morphology, which can be explained in terms of the film's limiting current growth conditions. Energy Dispersive X-Ray Analysis (EDX) and Glow Discharge Optical Emission Spectroscopy (GDOES) identified indium chloride as a major impurity in the InSb films, especially those deposited from non-aqueous solutions. A mechanism for the incorporation of indium chloride was proposed, based on the physical entrapment of a precipitate of the compound.

Acknowledgements

It is with great warmth that I thank the following people for their many contributions to my life and work throughout the course of this study. Firstly, I would like to acknowledge the help, support and patience of my supervisors, Dr IM Dharmadasa, Dr J Haigh and Dr D Mowthorpe.

My gratitude also extends to the technical staff of the Applied Physics Division, the Applied Chemistry Division and the Materials Research Institute. Particularly, I would like to thank Mr K Blake for his invaluable assistance with all matters regarding XRD, Mr P Slingsby for my SEM training and Dr M Ives for my GDOES training. I am also in gratitude to Dr S Clark and Mr D Cammack for letting me join in with their work at the Daresbury Synchrotron Research facility.

I was fortunate to gain experience additional to my PhD studies through the university's participation in Sheffield's Regional Technopole. I thank both Dr J Crawley and Mr J Metcalf for the opportunity of representing the university as a project advisor with this initiative. I would also like to thank Ms J Orchard for her wise counsel.

To my friends, a pint (or two!) of the usual goes to: Dr S Boyes, Dr W Cairns, Dr J Davidson, Mr J Haynes, Dr A Jansen, Miss M Jansen, Miss J Kelley, Mr M Rawson, Mr A Silvestri. Double whiskeys go to the lads in the lab. Particular thanks go to Miss L Cecchinato and Miss S German (if fishes were wishes...). Melbourne – the jury's still out, it being so close.

Mr V Singh deserves a paragraph to himself, cheers mate; I'll try to give you back the PC in one piece! I wish your new company, TGB Ltd, every success.

Finally, thanks to all my family for their love and support throughout the years.

'One does not discover new lands, without consenting to lose sight of the shore for a very long time.'

André Gide (1869-1951)

Contents

Chapter 1

Introduction

'One day, Sir, you may tax it.'

Michael Faraday (1791-1867) [To Mr Gladstone, the Chancellor of the Exchequer, who had asked about the practical worth of electricity.]

1.1 Preface

The electrochemical growth methods used by Faraday were, in some ways, simpler than those described in this thesis, and the optoelectronic properties of the materials under investigation unknown. However, it is testament to his work that the fundamental relationship he elucidated still remains central to electrochemistry, namely, that the amount of a substance discharged during electrolysis is proportional to the electric charge passed. Ultimately, the work presented herein can be described as concerning an examination of the use of electricity in the production of materials, whose applications depend in many ways upon their electrical (and optical) properties.

This chapter briefly describes the properties and applications of the materials under investigation, and introduces electrochemical deposition as a semiconductor preparative route.

1.2 The Materials Under Investigation

The study of the growth and application of systems[1] based upon indium antimonide (InSb) and gallium antimonide (GaSb) still represents only a small part of the effort directed to the

---

1 For an in-depth survey of these areas, the reader is directed to the following works and the references therein: (Willardson & Beer (1975), Milnes & Polyakov (1993)). In addition, a very up to date source of information, certainly in terms of what 'off the shelf' materials are commercially available, as well as their industrial applications, is the World Wide Web (WWW).

III-V materials as a whole, especially as compared to GaAs. However, interest in these systems has intensified over the last ten years, reflecting their increasing importance in diverse areas including power generation, high-speed electronics and optoelectronics.

III-V binary antimonides, and their alloys, have been grown as both single crystals and epitaxial layers using a variety of techniques. Currently, bulk single crystals of the antimonides are typically grown from melts via Liquid Encapsulated Czochralski (LEC) and Horizontal Bridgman techniques. Epitaxial materials are usually grown by methods that include Molecular Beam Epitaxy (MBE) and Metal Organic Chemical Vapour Deposition (MOCVD). These techniques have been used in the fabrication of complex multi-layered device structures that are based on antimony's binaries and alloys. Indeed, it is reasonable to suggest that, right from the start, epitaxial techniques have led the way in the development of the alloys, because early efforts in growing, say In(As,Sb) from the melt were hampered by the large difference in the constituent elements' melting points. This absence of congruence was initially seen to result in difficulties controlling the materials' stoichiometry and crystal quality (Rogalski (1989)). Table 1.1 lists some of the basic properties that characterise InSb and GaSb.

Crystal structure	Zinc Blende	Zinc Blende
Lattice constant (Å)	6.09593	6.479
Melting point (^{O}C)	712	527
Density (g cm^{-3})	5.61	5.77
Standard molar Gibb's energy of formation at 298.15 K (kJ mol)	–25.5	-38.9
Energy gap (eV)	0.726	0.17
Intrinsic carrier concentration (cm^{-3})	1.5 x 10^{12}	2 x 10^{16}
Electron mobility (cm^2 V^{-1} s^{-1})	<3000	7.7 x10^4

Table 1.1 Basic characteristics of the materials at 300 K, from Willardson & Beer (1975) and Milnes & Polyakov (1993).

Common to III-V materials, InSb and GaSb crystallise to form a zinc blende structure. The lattice constants of both materials are appreciably larger than GaAs (5.654 Å) and InAs

(6.058 Å). However, a variety of heterostructures have been grown successfully, for example GaSb/GaAs, section 1.2.2. The melting points of both the antimonides are quite low, certainly when compared to GaAs (1240 ^{O}C). Consequently, temperatures for processing the materials have to be selected carefully, especially as there is a tendency towards them losing their stoichiometry by way of Sb loss, even at moderate temperatures. This tendency for non-stoichiometric growth, and the fact that the growth temperatures for the materials are still quite high, can also cause problems relating to high lattice-defect densities, section 1.3.

GaSb and InSb are both direct band gap materials that emit and absorb light within the infrared (700 nm to 100 μm) portion of the electromagnetic spectrum. Specifically, the band gap of GaSb (1.75 μm) is in the near infrared (NIR) of the spectrum, whilst that of InSb (7.29 μm) falls within the mid-wavelength IR[2] (MWIR). Investigations into the growth of the materials' alloys, for example In(As,Sb), has extended the range of wavelengths in which antimonide based devices can operate. Finally, InSb exhibits the highest electron mobilities of any semiconductor, and those of GaSb are compatible to GaAs. This, with their bandgaps, offers the opportunity of high-speed IR optoelectronic devices.

The following sections further discuss the materials of interest in more specific terms.

1.2.1 Indium Antimonide (InSb)

Commercially available InSb single crystals are typically grown by the liquid encapsulated Czochralski (LEC) method from multiple zone refined polycrystalline ingots, table 1.2. This zone refining stage is necessary to remove donor impurities such as S, Se & Te, in

---

[2] InSb & GaSb belong to a class of materials that allow the fabrication of devices that operate right across the entire IR portion of the spectrum. Since their early development in the 1940's and 1950's, detectors based on PbS, PbTe and InSb have been used for the mid-IR portion of the spectrum (up to 8 μm). Cu, Zn, and Au doped Ge (and extrinsic Si) materials have been used to make devices that operate in the long wavelength IR (LWIR, 8-14 μm) and very long wavelength regions (VLWIR, 14-30 μm). Finally, the II-VI alloy HgCdTe, with its tuneable bandgap, has been extensively used across a broad range of wavelengths. For example, if the Cd/Hg half of the material is divided to be 30% Cd & 70% Hg, the material's cutoff wavelength is around 5 μm, i.e. within the MWIR. If however, these concentrations are made 20 % Cd & Hg 80%, then the cutoff wavelength is approximately 10 μm, i.e. in the LWIR.

addition to acceptor impurities that include Cd and the difficult to avoid Zn[3]. Usually, the single crystal ingots produced are processed into 3" polished wafers that are approximately 500 μm thick. InSb is also grown using the Horizontal Bridgman method, though LEC generally produces materials with lower impurity levels, contamination from the growth crucible being lower. Work continues apace to refine such growth techniques, with particular emphasis being placed upon further understanding the liquid-solid interface dynamics (Campbell & Koster (1999)).

Dopant	Type	Carrier Concentration (cm^{-3})	Mobility ($cm^2V^{-1}s^{-1}$)
Undoped	n	$5 \times 10^{13} - 3 \times 10^{14}$	$(4\text{-}6) \times 10^5$
Te	n	$7 \times 10^{14} - 2 \times 10^{15}$	$\geq 2.5 \times 10^4$
Ge	p	1×10^{14} - 1×10^{15}	8000 - 4000

Table 1.2 Some properties of commercially available 'epi ready' InSb single crystal materials (Wafer Technology Ltd).

Epitaxial methods for the generation of InSb thin films are obviously dominated by MOCVD and MBE. In the case of MOCVD, trimethylindium and triethylindium may be used as precursors for the group III element. However, the chemical reactivity[4] and poor stability of the former means that it is little used. For antimony, the precursors used mostly are trimethylantimony or triethylantimony as opposed to its hydride, whose decomposition temperature is below that of typical deposition temperatures. Complex alloy systems incorporating As, from AsH_3, have also been deposited for the construction of long-wave detectors. Biefield (1986) has reviewed the early MOCVD work, however, as with all the growth methods discussed in this chapter, the interested reader is referred to the ever-increasing volume of literature that is being published.

Turning to MBE, this technique uses the elements as sources. These are evaporated from crucibles and directed to heated substrates, the entire system, with analytical

[3] Zinc ore refineries are the most significant source of indium metal.

[4] The use of methyl sources for group III elements is limited by thermal decomposition of the precursor to form methyl radicals that lead to carbon incorporation in the films.

instrumentation, being held within ultrahigh vacuum chambers. Most often, III-V compounds are grown in a regime where the flux of the group III (In, Ga or Al) determines the growth rate of the film. Each III group atom is assumed to stick on the surface during growth, and only those group V atoms sufficient to ensure stoichiometry are incorporated, with any excess re-evaporating. Therefore, the growth rate of the film can be determined by measuring the flux of the incoming group III atoms. A disadvantage of MBE (and MOCVD) is that the technique involves complex apparatus, and relies on the use of ultrapure precursor materials. Nevertheless, this is to an extent balanced by their ability to enable the manufacture of complex device structures such as superlattices, which require the formation of abrupt junctions between dissimilar materials.

Vacuum evaporation on to mica substrates, followed by a recrystallisation stage, has been used to prepare InSb of high electron mobility. Okimura et al (1995) demonstrated that the stoichiometry of the materials grown can be maintained, and the amount of In segregation lowered, if the films were evaporated with excess Sb (4 %). These authors were able to produce p-type samples whose electron mobilities were comparable to those of melt grown undoped materials.

InSb based photon detectors are typically based on photoconductive or photovoltaic device structures. Photoconductive detectors function by way of detecting small variations in device current caused by the photo-generation of charge carriers. Photovoltaic detectors require an internal potential barrier with a built in electric field in order to separate photo-generated electron-hole pairs, which results in a measurable current. The impetus for these systems initially derived from the military, however InSb imaging systems are also extensively used by astronomers[5] and by meteorologists. Most of the effort in InSb (and In(As,Sb)) device research[6] is directed towards the development of arrays of photodiodes

---

[5] Startling images of the recent collisions between fragments of the Shoemaker-Levy comet and Jupiter were taken with a 256 x 256 InSb focal plane array (FPA) camera mounted on the Keck telescope in Hawaii. These images can be obtained from the observatory's 'home page' on the WWW.

[6] Detectors based on InAsSb offer several advantages over InSb detectors. Firstly, the addition of arsenic to the compound material, e.g. InAs(0.80)Sb(0.20), increases the bandgap slightly and consequently reduces the maximum detectable wavelength to 5 μm--compared to almost 6 μm for InSb. At the same time, the detector maintains the high performance typical for III-V-type IR detectors, with thermoelectric cooling being sufficient, which has advantages such as compactness and reduced cost.

for infrared imaging systems that are based on p-n junctions or metal-insulator-semiconductor (MIS) structures. Figure 1.1 shows an image from such a system. The detectors are formed in arrays, and are often hybridised with Si readout electronics to construct high resolution imaging systems. Because of the small bandgap of InSb, the detectors are operated at low temperatures (77 K) to improve their sensitivity.

Figure 1.1 Image taken using an infrared device (256 x 256) InSb focal plane array (FPA) camera (SBRC Ltd).

The high electron mobility of InSb, together with its large saturation electron velocity (the greatest speed electrons can reach in a lattice), has allowed the fabrication of fast transistors (Semiconductor International (April 1998)). Another application of InSb is in the fabrication of magnetoresistors (MR's) used in magnetic position sensing. These devices are based on the Hall effect. Essentially these devices operate by modulating the controlling electronics output in response to variations in current, caused by the motion of a permanent magnet in relation to an array of InSb MR devices.

1.2.2 Gallium Antimonide (GaSb)

GaSb single crystals are commercially grown by the liquid encapsulated Czochralski (LEC) method from directionally frozen polycrystalline ingots, table 1.3. In contrast to InSb, the undoped material is p-type, rather than n-type, the native defect responsible being Ga on a Sb site. A more 'exotic' route to the bulk material has used a Liquid Encapsulated Melt Zone (LEMZ) technique in space (Gatos (1982)). In this technique, the material is grown under microgravity conditions from a melt generated by the optical heating of a LEC

grown GaSb single crystal that is encapsulated in KCl-NaCl. The structural and compositional perfection of the materials grown by these authors was seen to be greater than those produced by the equivalent technique on earth. This was thought to be due to several factors, such as the suppression of convectional currents in the melt, and lower melt-crucible interaction.

Dopant	Type	Carrier Concentration (cm^{-3})	Mobility ($cm^2V^{-1}s^{-1}$)
Undoped	p	1×10^{17}	650
Te	n	$(1\text{-}9) \times 10^{17}$	3500-2500

Table 1.3 Some properties of commercially available 'epi ready' InSb single crystal materials (Wafer Technology Ltd).

Following processing that includes suitable etching in, for example, a bromide/methanol solution (Milnes & Polyakov (1993)), bulk materials have been used as substrates for a variety of structures, based on the binaries and alloys. Generally, epitaxial growth of semiconducting materials as a whole is complicated by several factors, and the generation of systems based upon GaSb (and its alloys) is no different in this respect. One of the most technologically important aspects of both MBE and MOCVD techniques is the ability to form complex layered structures using materials whose lattice constants are quite dissimilar, for example GaAs and GaSb. Such structures, however, can be prone to high dislocation densities, which can impede their device operation. For instance, consider the development of tandem p–GaSb/n-GaAs thermophotovoltaic devices. The efficiency of these devices can be limited significantly by premature electron-hole recombination at lattice-mismatched induced dislocation sites. Even so, Haywood et al (1998) has shown that such devices can be grown via MOCVD from trimethylgallium and trimethylantimony. The authors showed that device performance could be improved by growing the materials under conditions where large numbers of small nucleation sites are generated.

1.3 Electrochemical Deposition of Semiconductors

It is reasonable to suggest that the impetus behind the recent interest in the electrodeposition of semiconductors originated from the desire to produce thin films inexpensively for use in terrestrial based solar cells. Consequently, most of the interest in

the technique's utilisation has concentrated on II-VI, rather than III-V, compound deposition. Indeed, a plethora of research has been conducted into the electrodeposition of II-VI semiconductor heterojunction solar cells, formed from cadmium chalcogenide thin films such as CdTe and CdS, section 3.3. Even so, it remains true that the amount of literature published regarding other semiconductor growth methods, for example MBE, is vast in comparison to electrodeposition.

Overall, methods used in electrochemical deposition can be divided into three general categories. Such a division is based upon the solvent used, and the temperature at which electrolysis is performed. The first category encompasses the electrolysis of aqueous solutions at low temperatures (<100 ^{o}C). Historically, these systems have been utilised by the electroplating industry the most extensively, and this is due to their simplicity in construction, ease of operation, and because their solution chemistry is well understood. Yet, though preferable, the ability to deposit from aqueous solutions is not universally suitable for all the materials. For example, such systems can not be used to deposit Si, as its salts easily hydrolyse and because its very negative reduction (deposition) potential favours H_2 evolution, section 3.2.1. Hence, high temperature techniques have been developed that employ molten salt solutions, (typically at 500 ^{o}C to 900 ^{o}C), the most commercially successful example being the Hall Process that is used during the extraction of aluminium from bauxite ore. The final, and least studied electroplating category, includes those systems based upon 'high' temperature non-aqueous (organic) electrolyte solutions at 100^{o} to 300 ^{o}C. With regard to the work described herein, the electrolysis of both low temperature aqueous solutions and high temperature non-aqueous solutions was investigated.

There are several advantages associated with electrochemical methodologies that are worth mentioning at this junction. In comparison to other, more expensive and time-consuming, techniques such as MBE, electrogrowth offers the ability to deposit material over large, and non-planar, surfaces. Further, the typical growth temperatures used in electroplating are well below that of the material's melting point, which therefore may confer the materials with low lattice defect densities. As discussed in section 1.2, this is of particular relevance to the materials under investigation. Moreover, difficulties with the preparation of the materials can also be caused by their elements' low vapour pressures, which can make

stoichiometric control difficult[7]. Finally, electrolysis is convenient for epitaxial deposition, since growth occurs uniformly over the sample area. This is especially important, in that one of the limiting factors for using antimony bearing III-V compounds is that, in comparison to GaAs & InP, there is a relative lack of InSb and GaSb substrates. Such limitations could obviously be overcome, if a technique was made available that inexpensively produces epitaxial substrate materials.

That is not to say that semiconductor electrodeposition is without its challenges. As with any thin film deposition method, the early developmental stages involve a large amount of work in understanding and optimising the growth processes, so that the end properties of the materials produced match those demanded by their applications. Perhaps this explains the immaturity of the semiconductor electrodeposition field. Namely, whilst the development of other growth techniques has been extensive, for example LEC, semiconductor electrodeposition has had to await an interest in applications for which the materials grown to date are particularly suited, i.e. solar cells. On a more practical level, it is often stated that an advantage of the technique is that purification occurs during growth, because of differences in the deposition potentials between major and minor components in solution, although doping of the materials can still be achieved by carefully controlling the deposition parameters. This is in comparison to other methods such as MOCVD, which demand extremely pure, and thus expensive, starting materials. However, as shown in this thesis, the undesired physical incorporation of the growth medium (i.e. the solvent) or elements from the precursor compounds can cause problems.

1.4 Aims & Approach

As stated above, whilst there exists a wealth of information regarding the growth of II-VI semiconductor materials, III-V electrodeposition as a whole has not been studied greatly. Moreover, this is especially true when considering InSb and GaSb electrodeposition. Sb-In alloy deposition has been studied to a limited extent, although these studies were aimed at developing protocols for the electroplating of anti-corrosion coatings on, for example, ball bearings. Therefore, it can be said that the area affords many opportunities for the

[7] An additional challenge for the melt techniques is that many of the antimony bearing III-V compounds have a miscibility gap.

interested researcher to explore. However, before any semiconducting material can be applied technologically, it must have certain properties, in terms of composition, crystal structure, morphology and level of impurities, etc. Hence, the overall course of this investigation was directed with these criteria in mind.

The aims of this study were to investigate the electrochemical deposition of InSb and, to a lesser extent, GaSb thin films. To achieve this, a detailed examination was performed on the effects of the electrochemical growth parameters on the deposited films' properties. The fundamental growth parameters studied included: deposition potential, current density, solute concentration, and electrolysis temperature. In addition, the role of the substrate was also scrutinised.

In light of the above, the electrodeposited films were examined using a variety of analytical techniques, so that several of their material properties could be studied in depth. Specifically:

- X-Ray diffraction (XRD) was used to examine the materials' crystal structure, and to gain basic information regarding their composition. In addition, new work was carried out in determining grain size averages for electrochemically co-deposited InSb.

- For the first time, the morphology of electrodeposited InSb & GaSb was probed using a Scanning Electron Microscope (SEM).

- In the absence of precedent work in the literature, the InSb films particularly were examined using Energy Dispersive X-ray Analysis (EDX) and Glow Discharge Optical Emission Spectroscopy, to establish what major impurities were present. Also, the results of such analysis naturally gave further information regarding the overall material composition.

Finally, when considering the semiconductor electrodeposition field as a whole, it can be seen that great significance has been placed upon describing electroplating systems in essentially thermodynamic terms. Most likely, this is a reflection of the majority of research being concerned with II-VI deposition. Nevertheless, for III-V electrodeposition it is reasonable to suggest that growth kinetics should play a critical role in dictating a growth method's success. Indeed, this is especially evident when recalling the fact that III-V compounds have less favourable heats of formation than II-VI semiconductors. Consequently, it was decided early on to consider both the kinetics and thermodynamics of

the electrochemical systems under investigation. This involved, studying electrodeposition of the films with both aqueous and non-aqueous electrolyte solutions. Namely, in employing such systems, it was possible to examine the deposition process over a wide range of temperatures. Indeed, the deposition of InSb from non-aqueous electrolyte solutions was studied at the highest temperatures to date, approximately 190 ^{o}C.

1.5 The Structure of this Thesis

Obviously, electrochemical deposition ('electroplating') is a vast field. Despite this, chapter two of this thesis presents a brief outline of the relevant theory. Following this, the literature specifically concerning semiconductor electrodeposition is reviewed in chapter three, particular emphasis being placed upon III-V electrodeposition as a whole, and the materials of interest to this study. The succeeding chapter then describes the experimental techniques used during this investigation. The subsequent three chapters detail the results from the study of the electrochemical deposition of InSb from aqueous and non-aqueous electrolyte solutions, as well as those from the study of GaSb electrodeposition. These results are then discussed at length in chapter eight. Finally, the conclusions from the work, along with suggestions for future research, are offered in chapter nine.

Chapter 2

Electrodeposition Theory

2.1 Introduction

Electroplating of at least two alloys (bronze and brass) is as old as the plating of single metals. These alloys were electrodeposited by De Ruolz in 1842, fairly soon after the discovery of the Daniel element. During the subsequent 156 years, over 180 alloys have been electroplated involving 40 elements, and an extensive review of their deposition is given in Brenner (1963).

To assume its modern form, the theory of electrodeposition, and more generally electrochemistry, had to await developments in other areas such as thermodynamics and kinetics. Such knowledge has been applied to alloy deposition in such treatises[1] as those written by Gorbunova & Ploukarov (1967), Fedot'ev et al (1962), Faust (1963), and Despić & Jović (1995). However, the subject remains at an elementary level, orientated to assist practical electroplaters. Nevertheless, a more fundamental, and in the most part mathematical, understanding of the alloy plating process has recently begun to be developed.

The following treatment of the theory of electrodeposition introduces the subject's fundamental concepts in terms of the deposition of a single metallic element. Having discussed these, the conditions and factors influencing the deposition of an alloy (or compound) are outlined. Finally, a general discussion of the electrocrystallisation process is given.

[1] Modern treatises tend to consider more specific subjects, for example the, treatise on laminar film growth and inert particle inclusion by Despić & Jović (1995).

2.2 Single Metal Deposition

2.2.1 The Electrode Double Layer

The expression 'double layer' is something of a misnomer, which arose from Helmholtz's (1879) simple condenser model of an electrode-solution interface that forms when a metal is at equilibrium with a solution of its own ions, figure 2.1(a). However, this representation was not complete, as it neglected interactions occurring further away from the electrode's first layer of absorbed species, and also the effect of the electrolyte solution's concentration.

Subsequently, Gouy (1910) and Chapman (1913) independently developed a model that considered how the capacitance of the interface was affected by the electrolyte solution's concentration, and the potential applied across the cell. These authors found that the double layer was not as compact as in Helmholtz's description, but of variable thickness, with ions free to move within a diffuse region near the electrode.

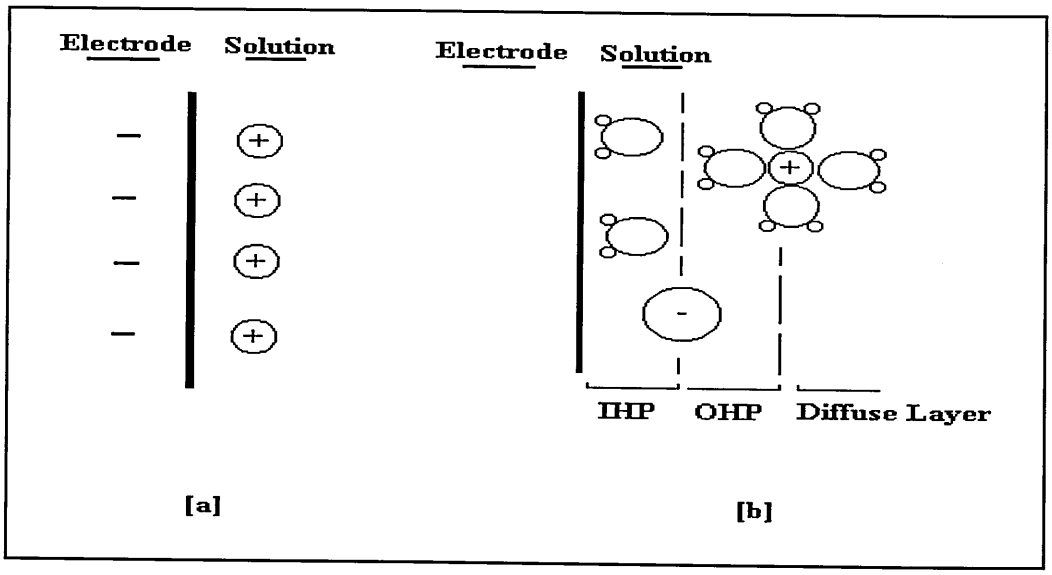

Figure 2.1 Two models of electrode-electrolyte solution interface: (a) Helmholtz simple condenser model and (b) the modern view, incorporating an Inner Helmholtz Plane (IHP), Outer Helmholtz Plane (OHP) and a diffuse layer.

Stern (1924) combined both the aforementioned models, and introduced the concept of the Outer Helmholtz Plane (OHP), figure 2.1(b). This OHP demarcates ions at the electrode from those in the diffuse layer, and marks the closest distance to the electrode that solvated ions can reach. Hence, the diffuse layer is a consequence of the 'bulky' size of solvated species forming at the OHP, which prevents a sufficient number of them fitting into the OHP for electroneutrality to be achieved. This means that the additionally required charges are held, with increasing disorder, progressively further away from the electrode, where electrostatic forces become weaker, and dispersion by thermal motion becomes more efficient.

Grahame (1947) furthered the above model after considering specific adsorption effects. This resulted in another area of the double layer being identified, namely, the Inner Helmholtz Plane (IHP), figure 2.1(b). In the IHP, processes in which van der Waals and chemical forces participate allow the ions to approach the electrode very closely. Most anions are specifically adsorbed, losing most, if not all, of their inner hydration shell, whilst cations tend to retain theirs.

Finally, O'M Bockris (1963) updated the description of the interfacial region through taking into account solvent dipoles and their orientations, though the actual profile of electrostatic variation with distance remains qualitatively the same as previous models.

2.2.2 Electrode Potential

Helmholtz's (1879) model limits the interfacial region to a simple condenser model whose potential gradient is linear, figure 2.2(a). Gouy (1910) & Chapman (1913), by contrast, appreciated that a large charged plane would, rather like a giant ion, induce a one-dimensional distribution similar to that in three dimensions proposed for the Debye-Hückel model of electrolyte behaviour. In this approach, the potential variation is non-linear, figure 2.2(b); and the interface region extends to a region where the ions behave as though the electrode was not present (diffuse layer). Modern interpretations apply Stern's (1924) 'compromise' model, taking into account both diffuse and Helmholtz regions. Subsequently, a linear and non-linear variation of potential is ascribed across the whole interface, figure 2.2(c).

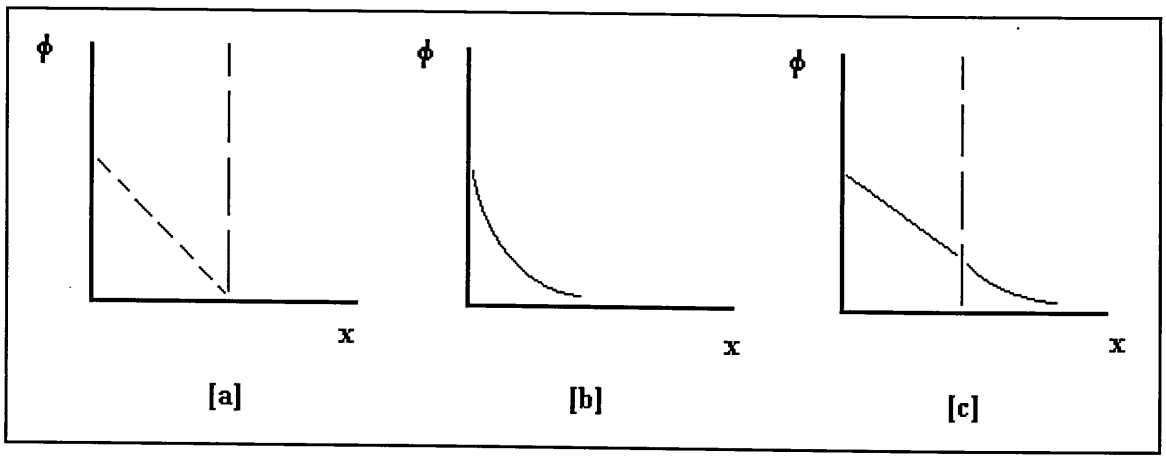

Figure 2.2 Variation of potential (ϕ) with distance (x) at an electrode-electrolyte solution interface according to: (a) Helmholtz (1879), (b) Gouy (1910) & Chapman (1913) and (c) Stern (1924). The vertical broken lines mark the boundary between the OHP and diffuse part of the double layer.

The variation of potential across the interface can be further described by considering the changes in potential experienced when a charge passes from a solution phase (S) to metal phase (M). In a solution phase, a charge will assume an inner Galvani[2] potential, ϕ_S. As it approaches within 100 nm of the electrode its potential rises with the Volta[3] potential, ψ, and then experiences a sharp rise with a surface potential[4], χ. Finally, after penetration of the surface, the charge will then experience the inner region of the electrode, whose constant Galvani potential is denoted ϕ_M. Accordingly, the overall change in potential ($\Delta\phi$) a charge experiences as it passes across the two phases is

---

[2] Formally, the Galvani potential at a point is the work needed to bring a charge from infinity to that point.

[3] The Volta (contact) potential is that due to the charge on the phase, for a metal this is the work required to bring a charge from infinity to ~100 nm from the surface.

[4] This is the surface potential associated with the work done in crossing a surface dipole layer, e.g. orientated water molecules.

Equation 2.1 $$\Delta\phi = \phi_M - \phi_S$$

Species of charge z in a phase will have electrical energy ($z\phi$) and chemical free energy (G), the algebraic sum of equalling its electrochemical free energy, G^E. Therefore, in the case of reactions involving the production or elimination of ions and electrons, the driving force for the reaction of a particular chemical entity will be to lower its *electrochemical free energy*, equation 2.2.

Equation 2.2 $$G^E = G + z\phi_i$$

2.2.3 Electrochemical Potential and the Nernst Equation

Following Crow's (1994) argument, chemical potential (μ_i) is the change in free energy of a system when 1 mole of an un-charged species i is added to it. In an ideal solution, where particles do not interact with one another, μ_i can be given in the form of equation 2.3. With x_i the mole fraction;

Equation 2.3 $$\mu_i = \mu_i^O + RT \ln x_i$$

For non-ideal solutions, the rational activity coefficient (γ_i) is introduced into equation 2.3, to take into account the interactions between the particles in solution.

Equation 2.4 $$\mu_i = \mu_i^O + RT \ln x_i + RT \ln \gamma_i$$

If the solute species are ions, particulary strong interactions occur as a result of electrostatic forces between charges, namely, equation 2.4 requires modification. Charges on ions already present in solution will generate an electrical potential ϕ. Addition of 1 mole of further charges of magnitude z_i will induce an extra change in free energy $z_i\phi$. Thus, the free energy of a system is increased by the transfer of matter and by the transfer of charge. The sum of these contributions is known as the electochemical potential μ_i^E.

Equation 2.5

$$\mu_i^E = \mu_i^O + RT\ln x_i + RT\ln\gamma_i + z_i F\phi_i$$

Equation 2.5 can now be used to derive the Nernst equation thermodynamically. Consider an example redox reaction at equilibrium.

Reaction 2.1

$$Cu^{2+} + 2e^- \leftrightarrows Cu$$

For reaction 2.1 at equilibrium, the electrochemical potentials for the left and right hand sides must be equal, i.e.

Equation 2.6

$$\mu_{Cu^{2+}}^E + 2\mu_e^E = \mu_{Cu}^E$$

Substituting, for each phase, equation 2.5 into equation 2.6, and expressing concentration in terms of activities ($a_i = x_i\gamma_i$)

Equation 2.7

$$[\mu_{Cu^{2+}}^O + RT\ln a_{Cu^{2+}} + 2F\phi_{Cu^{2+}}] + [2\mu_e^O + 2RT\ln a_e - 2F\phi_e] = [\mu_{Cu}^O + RT\ln a_{Cu} + 0F\phi_{Cu}]$$

A negative sign is associated with the $2F\phi_e$ term since electrons have a negative charge, and the term involving ϕ_{Cu} becomes zero due to the neutrality of copper atoms. Further, recalling the potential difference between the solution and metal is: $\Delta\phi = \phi_M - \phi_S$,

Equation 2.8

$$[0F\phi_{Cu} - 2F\phi_{Cu^{2+}} + 2F\phi_e] = [\phi_e - \phi_{Cu^{2+}}]2F = [\mu_{Cu^{2+}}^O + 2\mu_e^O - \mu_{Cu}^O + RT\ln a_{Cu^{2+}} - RT\ln a_{Cu}]$$

Equation 2.9

$$\Delta\phi = \frac{\mu^{O}_{Cu^{2+}} + 2\mu^{O}_{e} - \mu^{O}_{Cu}}{2F} + \frac{RT}{2F}\ln\frac{a_{Cu^{2+}}}{a_{Cu}}$$

Reaction 2.1 and equation 2.9 can now be written in the more familiar and general terms of the Nernst equation

Reaction 2.2

$$aM^{n+} + ne^{-} \leftrightarrows bM$$

Equation 2.10

$$E = E^{O} + \frac{RT}{nF}\ln\frac{(a_{ox})^{a}}{(a_{red})^{b}}$$

The standard equilibrium potential, E^{O}, of a metal is an indication of its 'basicity' (in electrochemical terms, not pH) or 'nobility'. 'Base' metals have high negative values of E^{O}, and thus large positive values of $\Delta\mu^{E,O}$ for ion reduction, indicating non-spontaneity. The converse is true for 'noble' metals.

Thus far, the treatment of electrode reactions presented has considered electrochemical thermodynamics. For *net* deposition to occur, an external electromotive force must be applied to disturb the system's equilibrium. To determine if deposition will occur at a 'useful' rate, the system's kinetics must be considered

2.2.4 The Kinetics of Electrode Processes: the Butler-Volmer Equation

Section 2.2.3 demonstrated that an equilibrium potential E is adopted by a metal electrode when placed in an aqueous solution of its own ions, equation 2.10. This steady state potential results from the rapid establishment of the equilibrium, reaction 2.3. The potential attained gives an indication of the position of the equilibrium, for example the more positive the equilibrium potential, the more to the right the reaction lies.

Reaction 2.3

$$M^{n+}_{(aq)} + ne^{-} \leftrightarrows M_{(s)}$$

A net current is only achieved when the system is under non-equilibrium conditions, i.e. no net current is observed at equilibrium, because the rates of the forward and reverse reactions are equal and opposite. If an external potential, progressively more negative than E, is applied to the system, and the subsequent current recorded, a curve (linear sweep voltammogram or 'voltammogram') such as illustrated in figure 2.3 is observed. The extra potential, or overpotential η, to bring about a net (reduction) current at the new potential E_{RED} (a potential more negative than E) is defined

Equation 2.11

$$\eta = E_{RED} - E$$

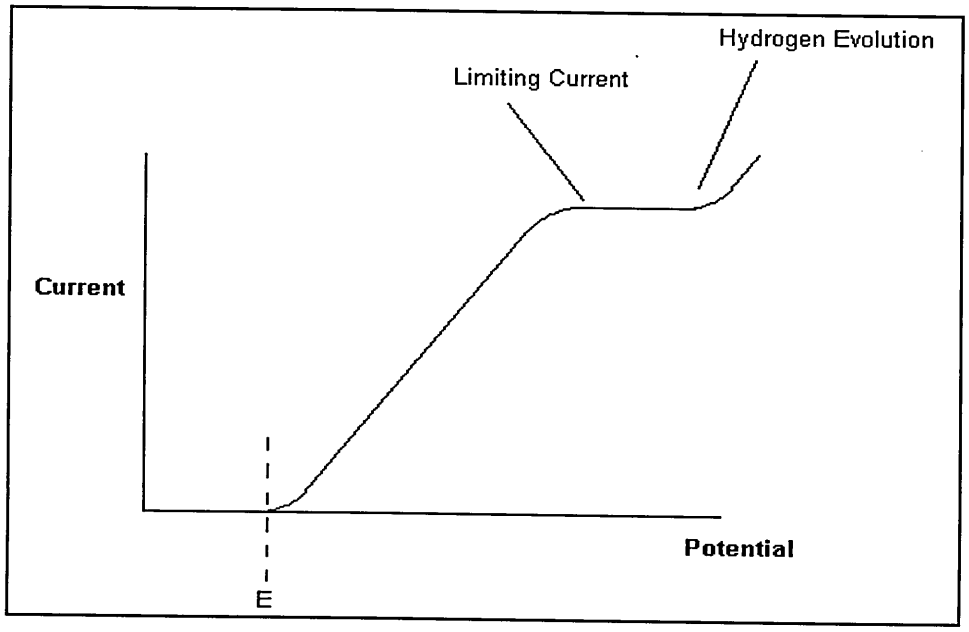

Figure 2.3 Cathodic portion of a simple linear sweep voltammogram.

Common features of voltammograms are plateau regions, where further polarisation of the electrode fails to produce increases in the observed current. At these 'limiting currents', the mass transport of ions to the electrode (through migration, convection, and diffusion) has reached its maximum rate, and is unable to keep pace with the charge transfer processes occurring at the electrode. Thereafter, if the cathode's potential is made even more negative, the reduction of other species, e.g. the solvent, becomes possible and the current begins to rise once more.

Following the argument of Barrow (1988), the existence of η implies that there are kinetic barriers to the cathodic and anodic processes. In other words, when charged species transfer from the solution to the electrode, they must overcome an energy maximum within the double layer, indicated by FE^*_c. Conversely, for the anodic process an energy maximum FE^*_a will exist, figure 2.4(a).

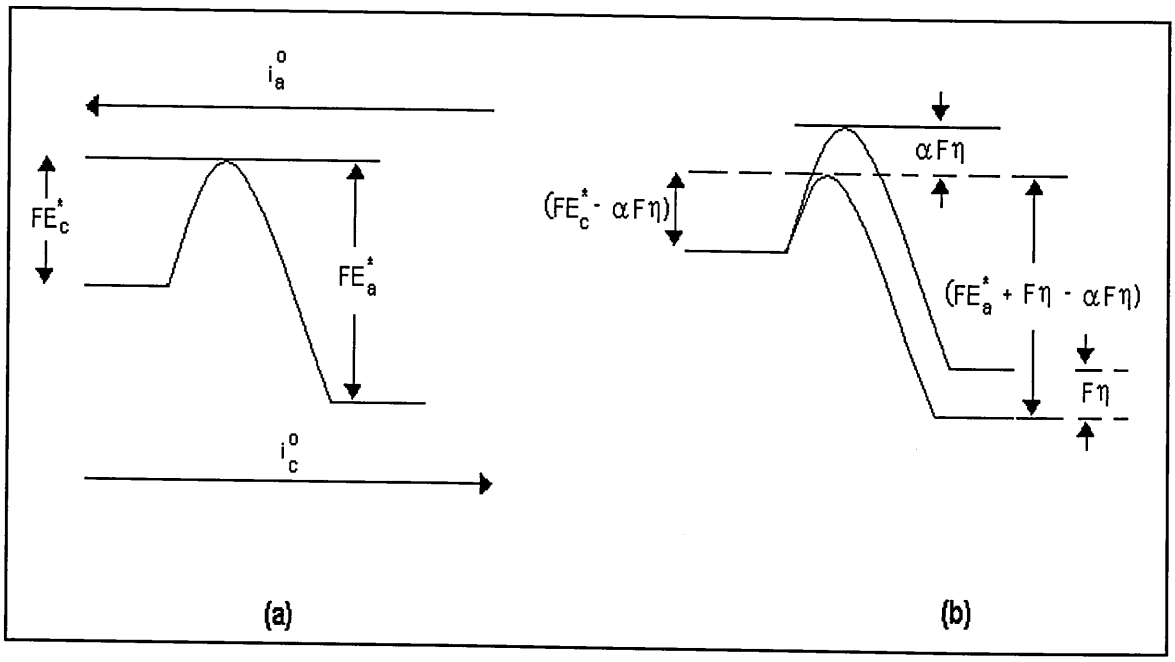

Figure 2.4 The barrier to the cathodic and anodic currents (a) under equilibrium conditions and (b) following the imposition of an overpotential η.

Only a fraction of the species in the system will have sufficient energy to overcome these kinetic barriers. This fraction is suggested by the Boltzmann distribution to be proportional to an exponential term, $\exp.^{-[(\text{energy barrier})/RT]}$. Consequently, the dependence of the electrode's respective reversible cathodic and anodic currents (i^o_c & i^o_a) on FE^*_c & FE^*_a under equilibrium conditions may be expressed, with proportionality constants k_a and k_c, as:

Equation 2.12

$$i_c^o = k_c \exp\left(-\frac{FE_c^*}{RT}\right)$$

and,

Equation 2.13

$$i_a^o = k_a \exp\left(-\frac{FE_a^*}{RT}\right)$$

When a cathodic overpotential is applied to the system, the energy barriers are affected in some intermidiate way that is not easy to deduce. A symmetry factor α (the transfer coefficient, section 2.2.5) is introduced to express the fraction of the overpotential that is effective in altering the energy barriers to the cathodic and anodic processes. The effect on the cathodic process is to lower the barrier from FE^*_c to FE^*_c-$\alpha F\eta$, figure 2.4(b). Conversely, the anodic process is retarded, as the barrier is increased from FE^*_a to FE^*_a + $F\eta$-$\alpha F\eta$ (i.e. FE^*_a + (1-α) $F\eta$). Hence, after the imposition of an overpotential, η, the new cathodic and anodic currents are:

Equation 2.14

$$i_c = k_c \exp\left(-\frac{FE_c^* - \alpha F\eta}{RT}\right)$$

Equation 2.15

$$i_a = k_a \exp\left(-\frac{FE_a^* + (1-\alpha)F\eta}{RT}\right)$$

Expressions for the cathodic and anodic currents in terms of the reversible currents $i_c^o = i_a^o = i_o$ can be obtained thus:

Equation 2.16

$$i_c = i_o \exp\left[-\frac{\alpha F\eta}{RT}\right]$$

Equation 2.17

$$i_a = i_o \exp\left[\frac{(1-\alpha)F\eta}{RT}\right]$$

Combining equations 2.16 and 2.17, the net current $i = i_c - i_a$ is fully written:

Equation 2.18

$$i = i_c - i_a = i_o\left(\exp\left[-\frac{\alpha_c nF\eta}{RT}\right] - \exp\left[\frac{\alpha_a nF\eta}{RT}\right]\right)$$

Equation 2.18 is known as the Butler-Volmer equation. The above version has been modified to take into account processes where the number of electrons (n), is greater than one. In addition, the $(1-\alpha)$ has been replaced by α_a, (and α_c introduced), to reflect that the transfer coefficients for the anodic and cathodic processes are not necessarily equal, section 2.2.5.

2.2.5 The Transfer Coefficient, α

The value of α is a measure of the slope of the energy profiles in the transition state zone, where the free energy profiles for the reactants and products intersect, and therefore of the barrier symmetry. Values of α can vary between zero and one for the anodic (α_a) and cathodic (α_c) processes, and usually for metals $\alpha_a = \alpha_c = 0.5$. This value indicates that the activated complex is halfway between the reagents and products on the reaction co-ordinate, its structure reflecting them both equally. If the value of α is close (or equal) to unity, this implies that almost all the overpotential is being used to form the reaction's transition state. In addition, because the overpotential reaches a maximum at the electrode's surface, the transition state will have a structure closer to the product's rather than the reactant's.

Electrode processes for which $n>1$ take place in a series of single electron steps, one of which is the rate-determining step. In such cases, the interpretation of experimentally determined α_n values is not clear. For example, in a two electron process with experimentally determined $\alpha_n = 1.4$, α may not be equal to 0.7. The first step may be fast

with $\alpha_1=1$, resulting in $\alpha_2=0.4$ for the second step. Values for α should thus be quoted in terms of α_n until the reaction's mechanism has been elucidated.

2.2.6 Classes of Overpotential

As discussed in section (2.2.4), for reduction to occur at a significant rate a potential negative to the reaction's equilibrium potential must be applied. This particular excess potential is more correctly described as the activation overpotential (η_A), which emphasises that it is associated with the surmounting of an activation barrier. The exponential growth and decay of η_A, after a polarising current is applied and then shut off, is in accordance with the concept of η_A being a function of the activation energy of the electrode process. In addition, the magnitude of η_A is strongly affected by the physical and chemical nature of the electrode material. This can be seen from the hydrogen evolution overpotentials measured from various metal electrodes. For example, the overpotential for the discharge of hydrogen at copper electrodes is more than twice that for 'bright' platinum electrodes (-0.23 V and -0.10 V respectively), Crow (1994). There are three other sources (or classes) of overpotential that exist in addition to η_A. These are the resistance, concentration and crystallisation overpotentials.

The resistance overpotential (η_R) is due to the inherent resistance of the solution to the passage of current, which results in an ohmic (IR) drop in potential between the working electrodes. A less common form of η_R is caused by the formation on the surface of the electrode of an adherent layer of reaction products, for example surface-oxide films that conduct electricity relatively poorly.

The origins of concentration overpotential (η_C), begin at the moment electrolysis initiates, when ions from the immediate vicinity of the electrode's surface become depleted. Even if the solution is stirred, or a rotating electrode employed, the rate of mass transport (via migration, diffusion and convection) remains slower than the electron transfer processes. Hence, the electrode becomes 'concentration polarised', and it is necessary to apply an extra overpotential (η_C) to overcome such effects. η_C is unique in that it is affected by stirring, and is unaffected by the nature of the surface of the electrode. Finally, an

overpotential exists (η_{XSTAL}) as a result of the generation of a crystal via electrodeposition (section 2.5). The total overpotential of an individual electrode may be expressed as a summation of all contributing overpotentials described above

Equation 2.19 $$\eta = \eta_A + \eta_C + \eta_R + \eta_{XSTAl}$$

2.2.7 The Relationship Between Current Density and Overpotential (The Tafel Equation)

For a large cathodic reaction overpotential the terms for the anodic process in equation (2.18) become negligible, and the dependence of the cathodic current on applied overpotential is:

Equation 2.20 $$\ln i = \ln i_o - \frac{\alpha F n \eta}{RT}$$

Thus, η is then given by,

Equation 2.21 $$\eta = \frac{2.3RT}{\alpha Fn}\log i_o - \frac{2.3RT}{\alpha Fn}\log i$$

Conversely, for a large overpotential for the anodic reaction, only the second term in equation (2.18) is of significance, and:

Equation 2.22 $$\eta = -\frac{2.3RT}{(1-\alpha)nF}\log i_o + \frac{2.3RT}{(1-\alpha)nF}\log i$$

Equation (2.21) & equation (2.22) are identical in form to that of proposed by Tafel, viz.

Equation 2.23 $$\eta = a + b \log i$$

Graphs of η versus $\log i$ are called Tafel plots, which under certain current-potential conditions show a linear portion in conformity to the Tafel equation. Values for the equilibrium exchange current density[5], obtained from the graphs' intercepts where the overpotential is zero, have been found to vary widely. For example, exchange current densities obtained from the evolution of hydrogen at the mercury electrode are small, allowing many ions to be discharged that have a larger electrode potential than hydrogen. Conversely, reduction of hydrogen ions at a Pt electrode yields high exchange-current densities. Therefore, the discharge of species whose reduction potentials are negative to that of the hydrogen ions is inhibited.

2.2.8 Pourbaix Diagrams

To decide upon which electrolytic solution should be investigated, data regarding the solute species may be readily obtained from Pourbaix diagrams. These isothermal diagrams represent metal-ion-oxide equilibria plotted with potential and pH as co-ordinates (Pourbaix (1961)). Originally developed from studies of corrosion processes, the diagrams are constructed under specific conditions. These conditions do not necessarily reflect those found during electrodeposition conditions (i.e. temperature & concentration). However, the form of the diagrams is still valid, though the actual co-ordinates will be shifted. Their use derives from how they illustrate in a graphical form a large body of thermodynamic data, though their interpretation should be supplemented by information regarding the system's kinetics. The value of these diagrams is that they show the thermodynamic stability of the various species in the electrochemical system. Hence, it may be seen, Appendix I, that gallium metal in contact with a solution of its salt is thermodynamically stable over a wide range of pH.

On the complete phase diagram there are two important lines representing the equilibria

---

[5] It should be noted that current is usually expressed as current density, e.g. mA cm^{-2}.

Reaction 2.4 $O_2 + 2H_2O + 4e^- \leftrightarrows 4OH^-$

Equation 2.24 $E^O = 1.23 - 0.059 \times pH$

Reaction 2.5 $H^+ + e^- \leftrightarrows \frac{1}{2}H_2$

Equation 2.25 $E^O = 0.00 - 0.059 \times pH$

'Above' the line representing the 'oxygen line', oxygen will evolve. Below the 'hydrogen line', hydrogen will be evolved. The production of these gases may significantly affect the current efficiency of the reaction and damage the deposit.

2.2.9 Single Metal Deposition Concluding Remarks

Some practical conclusions may now be drawn from the above discussion of electroplating theory:

1. The Nernst equation explicitly relates thermodynamic concentration and temperature to the equilibrium potential of an electrode.

2. Reduction is accompanied by a change in electrochemical potential. This energy change is balanced by the electrical energy liberated as ions traverse the double layer.

3. For a net cathodic (deposition) current to flow, a potential more negative with respect to a species's equilibrium potential must be applied. Principally, this extra 'overpotential' redefines the kinetic energy barriers to the reduction process. The magnitude of the reaction rate, i.e. current flow, is proportional to the applied overpotential (Butler-Volmer equation).

4. The rate of the cathodic (or anodic) reaction may be expressed in terms of the Arrhenius equation. Accordingly, the rate of deposition will increase exponentially with temperature.

2.3 Alloy deposition

The co-deposition of an alloy or compound is difficult because the conditions favouring the deposition of one constituent may differ considerably from those required by the others. Further, the problem assumes greater complexity given the rigorous demands of compound semiconductors for specific stoichiometric (this section) and crystallographic (section 2.4) properties. In essence, to generate the required thin film, equality in the various components' growth conditions must be found.

2.3.1 Conditions for Co-deposition

For the co-deposition of the components (A & B) of an alloy, or compound, ($A_xB_{(1-x)}$) to occur, their discharge potentials should be equivalent. Hence, if $E_{(A)}$ and $E_{(B)}$ are the components' equilibrium potentials and η_A, η_B their respective overpotentials,

Equation 2.26

$$E_{(A)} + \eta_A = E_{(B)} + \eta_B$$

Generally, components whose equilibrium potentials differ by less than 200 mV can be deposited from simple salt solutions because their respective overpotentials may bring their deposition potentials together. In extreme cases, the nobler element is deposited under 'limiting current' conditions (section 2.2.4).

To assist the conditions of equation 2.26 being met, the deposition potentials of the components may be manipulated by changing the precursors' ionic concentrations, (Nernst equation). A reduction in metal ion activity results in a shift in deposition potential towards the negative (base) direction, and conversely an increase in ion activity moves the potential to more positive (noble) values. For example, in the case of a monovalent ion, the shift is 0.059 V per order of magnitude change in activity at room temperature. However, merely altering the concentration of a simple salt is only practical within a few

orders of magnitude, and is limited by analytical control techniques to >0.001 mol dm^{-3}, and by solubility to <10 mol dm^{-3}. This corresponds to a potential range of 0.22 Volts for a monovalent ion. To circumvent these constraints, very low concentrations of free metal ions are obtained by forming complexes of a stable nature, whose dissociation is limited. Of these, the most commonly complexants used include; cyanide, halide, and amphoteric oxides like stannate, but amines, citrates and tartrates etc., also find application.

Given that deposition potential is an undefined quantity unless current density is specified, equation 2.26 may only serve as a rough assessment of whether or not co-deposition will occur. Despić & Jović (1995) suggest that the terms for the conditions for co-deposition should include that the partial current densities be in the ratio required to form a deposit of the desired stoichiometry. Conceptually, this is akin to controlling the molecular flux rates of an MBE machine. Nevertheless, even in the absence of competing reactions, it is difficult to ascribe quantitatively the different components' partial currents during a practical deposition experiment. Indeed, Gorbunova & Ploukarov (1967) discussed this problem in terms of resolving "partial polarisation" (current density–potential) curves for the individual constituents of the alloy.

A cursory study of the literature, e.g. Lockhande & Pawar (1989), provides three general rules for alloy deposition at current densities below the 'limiting' current density.

(a) The discharge of the most noble metal is favoured, causing deposits to be richer in this metal than would be expected from their concentration.

(b) All variations in electrolysis conditions that increase "polarisation" shift the composition to the side of the less noble metal in the alloy.

(c) All variations in electrolysis conditions that decrease "polarisation" increase the concentration of the nobler element in the alloy.

2.3.2 The Reversible Potential of an Alloy

As in the case of single element deposition, an alloy (or compound) will establish a potential when immersed in a solution of ions of its constituent elements. Alloys though, often consist of different phases each having different thermodynamic properties, which assume different reversible potentials. However, each phase may be treated as though it was the only one present in a given situation. Consequently, phase stability is determined by whether the imposed potential is more positive than the phase's own reversible potential (causing dissolution), or whether it is more negative (causing deposition).

The reversible potential of an alloy, or compound, is not only determined by the activities of the constituent ions in the solution and deposit. The free energy associated with the formation of the material will shift the deposition potential by E_{form} ($= -\Delta G_{form}/nF$). Hence, for an alloy $A_xB_{(1-x)}$, where B is the less noble species (i.e. $E_{(A)}>E_{(B)}$) the reversible potential $E_{(AxB(1-x))}>E_{(B)}$. Further, where ΔG_{form} is large, the material's reversible potential may take up a value more positive than all the individual constituents, $E_{(AxB(1-x))}>E_{(A)}>E_{(B)}$. The shift in potential is constant for the formation of a compound, but varies depending on composition in the case of alloy formation. This makes stoichiometric control in the latter case more difficult.

Kröger (1978) treated the question of alloy reversible potentials in terms of the Nernst equation applied to the "less noble" metal, the "more noble" component of the alloy being considered an inert matrix. However, such an approach yields unrealistic results. For example, consider an alloy containing a less noble metal that is divalent, and which exhibits a reversible potential more positive than its standard potential by 0.6 Volts. The activity of the metal in the alloy, as calculated from the Nernst equation, is 10^{-20} moles, which has no physical meaning. Despić & Jović (1995). proposed that a more correct approach does not assign thermodynamic properties to the individual components in an alloy. Instead, "a phase should be treated as composed of a chemical entity of stoichiometric composition corresponding to the composition of the alloy". This is consistent with ascertaining factors such as which reversible potential the alloy will assume and its thermodynamic stability. However, when practically determining the effects of the various experiment conditions

(pH, temperature, etc.) it is still valid to consider the constituents individually. Hence, the conclusions drawn in section 2.2.9 remain valid.

2.3.3 Classification of Alloy Deposition Systems

Brenner (1963), after surveying the results of many electrochemical deposition studies, proposed the following terminology, which is useful for distinguishing different types of 'plating system' utilised:

(a) 'Regular solutions' under diffusion control. Uncomplexed metal ions of two metals of widely differing nobility. This encompasses alloys where the noble metal is deposited under limiting current conditions.

(b) 'Irregular solutions' under cathode potential control, the deposition potential affected by complexing alone; e.g. cyanide bath for copper-zinc alloys. Here, the diffusion is sufficient that the reaction rate is determined by the system's kinetics, such as the discharge's activation energy.

(c) 'Equilibrium solutions', the "equilibrium" term referring to potential at which, under low current density conditions, the bath's metal concentrations give the deposit's metal ratio directly; e.g. lead-tin alloys from acid baths.

(d) 'Anomalous solutions' in which the less noble metal deposits preferentially, i.e. a "reversal of nobility" is observed; e.g. iron, cobalt or nickel.

(e) 'Induced solutions' in which a metal can be co-deposited as an alloy although it will not deposit alone; e.g. molybdenum or tungsten with iron group metals.

The foundation of such a division is the relation between the deposit composition and the "metal ratio", that is, the ratio of the precursor metal ions in solution. The first three are generally considered as normal systems, in that the proportions of the metal deposited may

be estimated on the basis of the polarisation curves of the individual metals. Thus, regular co-deposition is that where the composition of the deposit corresponds to the metal ratio. Irregular co-deposition represents the situation in which the more noble metal is obtained in a higher percentage, and the less noble metal in a lower percentage, than would be expected by the metal ratio. Anomalous co-deposition corresponds to the reverse of irregular co-deposition.

2.4 Electrocrystallisation

Electrocrystallisation consists of two fundamental stages. Firstly, growth units are generated via *electrodeposition*, and secondly, these units aggregate to form a crystal lattice, i.e. *electrogrowth*.

Overall, many commonalties exist between mechanistic descriptions of electrocrystallisation and other crystal growing techniques, such as those from a vapour phase. Consequently, electrochemists have been able to draw upon a large body of established theory and observation, to assist in the understanding of the electrocrystallisation phenomenon[6].

This above does not imply that these fields are fully matured, and surprisingly little is known about the processes occurring during crystallisation. Recent advances have been facilitated by mathematical simulations using modern high-powered computing (Dukovic (1990) & Li & Szpunar (1993)), and studies employing relatively new surface science instrumentation, such as the Scanning Tunnelling Microscope (Lagally (1993)).

---

[6] General introductions to the theory of crystal growth processes include, *Crystal Growth, Theory and Techniques,* Edited by CHL Goodman, Plenum Press, London, (1974), K Sangwal & R Rodriguez-Clemente, *Surface Morphology of Crystalline Solids*, Trans Tech Publications, USA, (1991). For electrocrystallisation specifically, a mathematical introduction is given in M Fleishman and HR Thirsk, *Advances in Electrochemistry and Electrochemical Engineering*, (eds. P. Delahay & C. Tobias), **3**, 145, (1962).

A large motivation for such work has been the investigation of the relationship between the electrical characteristics of semiconductor devices, and the crystallographic properties of the materials used in their construction. In the case of electrochemically generated semiconductor materials, this is illustrated by work done in the development of solar cell devices (Chu & Chu (1995)). Here, several studies have related device end performance (solar cell efficiency) to the properties of the materials deposited, and hence to the conditions employed in electrochemically generating their component materials (Chapter 3 of this thesis).

2.5 Electrodeposition

Overall, the growth of crystals from an isotropic (vapour, melt, solution) phase is a typical example of a phase transition, and takes place only when the system is supersaturated. The formation of growth nuclei, and their subsequent growth into crystal faces, will be related to surface energy, and the degree to which the system is supersaturated.

This is exemplified when considering the nucleation activation energy ($\Delta G_{(n)}$) for the formation of 2-dimensional nuclei (thickness h, molecular volume Ω) on an atomically flat surface (Pletcher (1991)).

Equation 2.27

$$\Delta G_{(n)} = \frac{\pi h \Omega \omega^2}{\Delta \mu}$$

Here it is seen that the activation energy is related to the surface free energy, ω, which depends on the nature of the crystal, and to the degree of supersaturation, by way of the change in chemical potential, $\Delta\mu$. With k, T having their usual meanings, supersaturation and $\Delta\mu$ are related,

Eqaution 2.28

$$c = c_0 \exp\left[-\frac{\Delta \mu}{kT}\right]$$

For electrodeposition, the actual and equilibrium solute concentrations at the interface (c & co) will be determined by the potential applied. Consequently, for an electrochemical system, the degree of supersaturation is related to overpotential.

The electrocrystallisation mechanism chosen by a system will reflect its tendency to grow in a manner that most readily overcomes the kinetic barriers to crystallisation. Accordingly, to aid in the description of the electrocrystallisation process in general, two classifications of electrodeposition may be distinguished, which are based on the system's degree of supersaturation (i.e. overpotential), and the predominating growth mechanism. These are deposition at low overpotentials, and deposition at high overpotentials.

2.5.1 Deposition at Low Overpotentials

Electrodeposition is preceded by the generation of ad-ions. These partially charged absorbed ions are formed following charge transfer (CT) between the substrate and solvated ion in the double layer. CT is facilitated by electron tunnelling that is itself enabled by distortions in the ion's solvation sheath. Furthermore, sites on the substrate surface that allow CT to occur with a minimum change in solvation have the lowest activation energies. Thus, ad-ion formation occurs on the more numerous crystal plane sites, figure 2.4, as opposed to kink sites.

At low overpotentials (less than 10 mV (West (1971)), ions discharging through the double layer possess only a small amount of kinetic energy and this negates 2-d nucleation on plane sites. The ad-ions diffuse along concentration gradients to sites of high lattice energy such as kinks and dislocations, the electric field being normal to the substrate negating electromigration. Each type of site is distinguished by an effective co-ordination number. For example, for a simple cubic lattice, an ad-ion will form 1 bond to a surface site, 2 with a step, and 3 with a kink etc. As the effective co-ordination number increases, so the energy of lattice formation becomes more negative. Hence, atoms diffuse across the crystal plane, undergoing stepwise de-solvation, to find sites where they can co-ordinate with the most atoms in the metal lattice, kinetic barriers at these sites being the lowest. Growth at low overpotentials subsequently predominates at kink sites, these being more numerous than edge vacancies and holes.

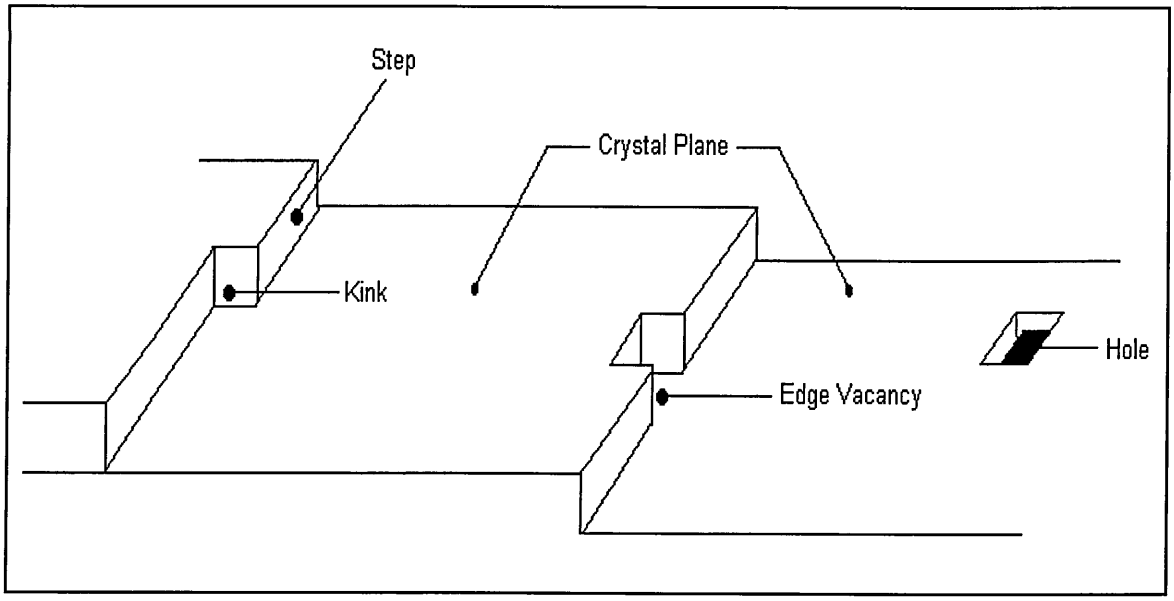

Figure 2.5 Typical surface features of a crystalline substrate.

This process is akin to that described by the "terrace-ledge-kink" (plane-step-kink) model developed by Kossel, Stranski and Volmer for an ideal crystal (Sangwal & Rodriguez-Clemente (1991)), which has been applied to several non-electrolytic growth techniques.

2.5.2 Transient Techniques

The above process has been investigated using "transient techniques", O'M Bockris (1967). Essentially, this experiment monitors the rate of the increase in overpotential as a function of time when an electrochemical cell, operating under low constant current conditions, is electrodepositing[7]. The measurement of this rate, discussed in terms of "rise time", allows the identification of the rate-determining step (rds) of the deposition process. High rates suggest that the CT process is the rds. Under these conditions, the metal interface is

[7] A caveat should be associated with the use of transient techniques. Erroneous results may be given if side reactions such as H_2 evolution are taking place, or if the nucleation sites are inhomogeneously distributed over the surface, Allonge & Souteyrand (1993).

charging because the electrons of the metal can not transfer to the incoming solvated ions quickly enough. Conversely, longer rise times indicate that slow diffusion is the rds.

The steady state overpotential (η_∞) of the deposition process, involving a two-step charge transfer that includes surface diffusion is given (O'M Bockris & Reddy (1970)):

Equation 2.29

$$\eta_\infty = \left[\frac{RT}{F}\frac{i}{i_o}\right] + \left[\frac{RT}{F^2}\frac{i}{kc_o}\right]$$

R, T, F have their usual meanings, i and i_o are the deposition and equilibrium current densities respectively. k is a proportionality constant determining the surface diffusion flux, and c_o the equilibrium concentration of surface ad-ions. The first term on the R.H.S. is that component of η_∞ due to the CT process, with the second term being due to surface diffusion.

It can be shown that at high overpotential, k becomes large and the second term becomes negligible, making CT the rds. Under these conditions, deposition rates are high, and nucleation at sites of intrinsically lower lattice energy is feasible.

2.5.3 Growth at High Overpotentials

When the cathode is polarised to more cathodic overpotentials, the ad-ions acquire large amounts of kinetic energy. Eventually, a point is reached where the kinetic barriers to nucleation on planar sites are overcome, section 2.5.1. This leads to 2-dimensional nucleation on the planar sites predominating, as these sites are statistically more numerous. Such nucleus formation follows first order kinetics (Pletcher (1991)), and their number density N(t) is:

Equation 2.30

$$N(t) = N_o(1-\exp(-At))$$

N_o is the total number of sites where nuclei may form, and A is the rate constant for nucleation.

From equation 2.30, it follows that when $At>>1$, $N(t) = N_o$, instantaneous nucleation is observed, yielding nuclei of similar dimensions widely dispersed across the substrate. If $A<<1$, $N(t) = N_oAt$, progressive nucleation occurs, yielding nuclei with a broad size distribution. These nuclei formed can then go on to successively grow and overlap, to form a continuum. If the cathode is polarised still further, concentration polarisation sets in. Under these conditions, the concentration overpotential can become comparable to the activation overpotential. This leads to nodular growth predominating, as activation control is lost. The variation of crystal form with growth parameters is shown in in figure 2.6.

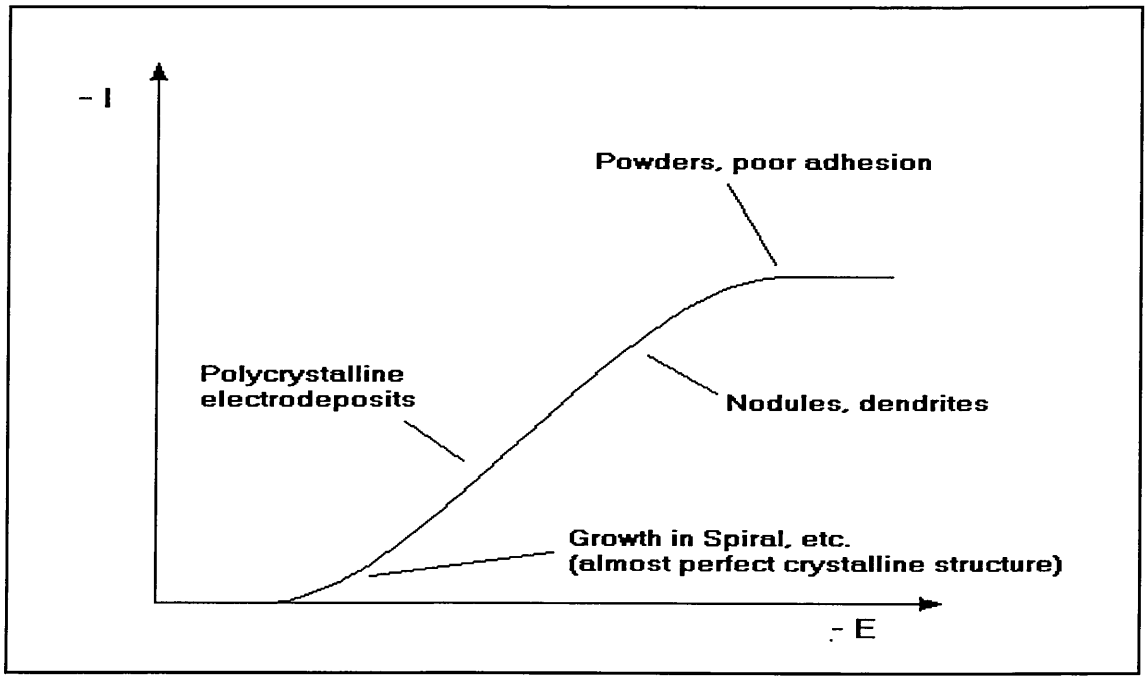

Figure 2.6 Variation of growth morphology with deposition conditions.

Rastogi & Balakrishnan (1989) observed the relationship between deposition current density and film morphology during a study of the deposition of CdTe from an aprotic solvent. Specifically, the morphology of the films deposited by the authors were: monocrystalline hexagonal CdTe (~0.1 mA cm^{-2}), polycrystalline hexagonal CdTe (~0.3 mA cm^{-2}), polycrystalline hexagonal & cubic CdTe (0.8 mA cm^{-2}), and polycrystalline hexagonal & cubic CdTe + Cd (1.0 mA cm^{-2}). Finally, powdery films were produced at current densities above >1.0 mA cm^{-2}.

2.6 Electrogrowth

At low overpotentials, ad-ions are eventually incorporated into lattice sites at kink sites. The kink sites build up the steps, which advance along the surface of the substrate until they reach its edge. Against common experience, this implies a limit to electrogrowth, because the disappearance of steps leaves no more nucleation sites. This phenomenon has been explained in the spiral growth models proposed by Frank (1947). According to this model, the point of emergence of a screw dislocation is a persistent source of repeatable steps, one atomic layer in height, that ensure growth even at low overpotentials. Since the angular velocity of the step is greater nearer the point of dislocation than that away from it, a spiral hill (microspiral) is formed, figure 2.7.

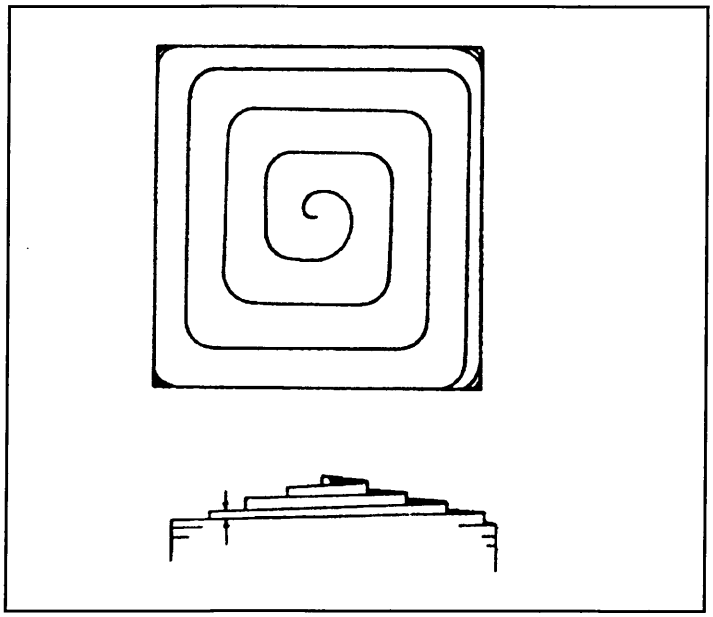

Figure 2.7 Plan and elevation view of a microspiral growth, the arrows indicate the thickness of one atomic layer.

These microspirals, and microsteps, are smaller than the wavelength of light, and thus can not be viewed through a microscope. However, large macrospirals and macrosteps are often observed. Frank (1947) and Cabrera & Vermilyea (1958) have described numerous explanations for the formation of macrosteps that are based on the relative velocities of the advancing microsteps. These authors suggest that faster surface microsteps bunch together with underlying steps, whose velocity has been reduced by the proximity of the other

microsteps or by the adsorption of impurities, figure 2.8. Further, macrospirals are generated in the same way as microspirals, but with the additional bunching of microsteps.

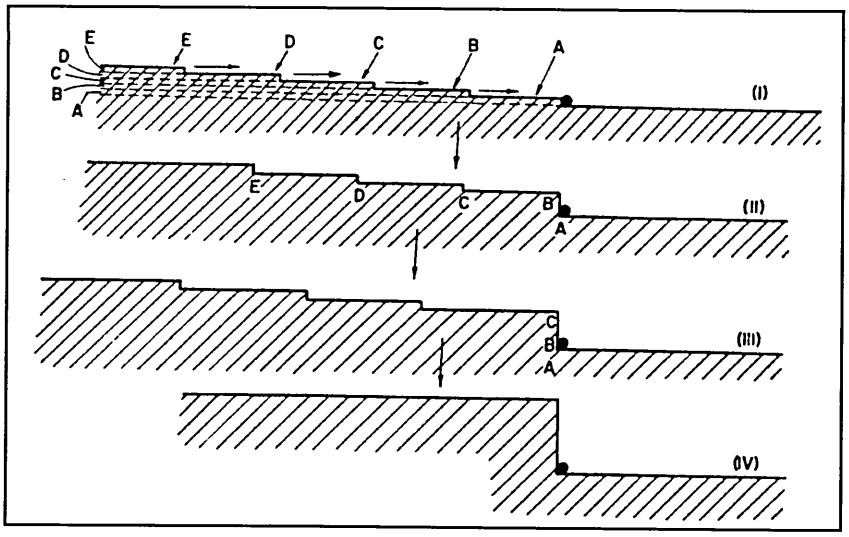

Figure 2.8 Representation of the formation of the formation of a macrostep by microstep bunching, with the letters indicating the position of the microstep's advancing faces, O'M Bockris (1967).

Both micro- and macro- spirals can interact via collisions that, for example, may lead to their annihilation. The tip of a macrospiral can serve as a point source, high in density of steps and kinks, with a concentrated hemispherical diffusional profile. Under these conditions, concentration and activation overpotentials can be lower at the tip, which will then grow faster than the material at the base of the microspiral. This results in the formation of dendrites.

Surface roughness is another feature that can be observed at both the micro and macro level. Here, deposition rates are higher at those sites that protrude from the substrate surface, as ions can more readily diffuse to those points. Organic additives, or inhibitors, will not be considered here. However, their action may be understood as selectively retarding growth of the various features discussed above.

The growth mechanism described above will generally take place on all the crystal planes presented to the solution. However, as can be shown by x-ray diffraction studies, the

different planes will be developed at the expense of others. Damjanovic (1964) proposed that this is a result of different growth rates for the different crystal faces. This was illustrated by measuring the exchange current densities for deposition of copper on single crystal copper substrates of various crystallographic orientations. Here, it was found that at constant overpotential the relative rates of deposition increase (110) > (100) > (111).

There are several explanations for the disparity of growth rates. The simplest relates the different growth rates to the density of steps and kinks on the crystal plane. Hence, singular faces, e.g. (100) of a simple cubic lattice, have low density of steps, and grow slowly. Faces with a high density of steps, grow at higher rates, and are called non-singular faces. The number of steps increases as the angle between the non-singular and singular faces increase, figure (2.9).

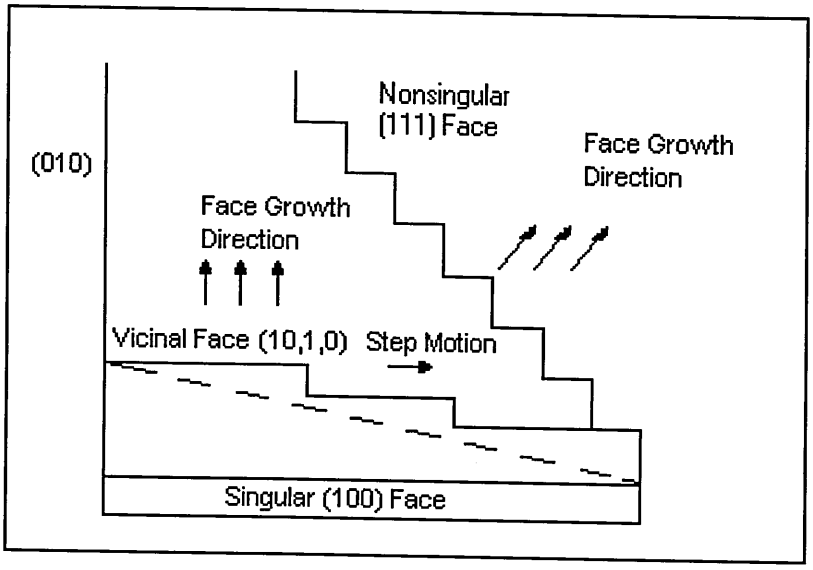

Figure 2.9 Cross-sectional view of simple cubic lattice faces which have different orientations (Sangwal & Rodriguez-Clemente (1991)).

For growth at high overpotentials, Pangarov (1962) suggested that the different growth rates might be explained in terms of different 2-d nucleation energetics. Another explanation that is applicable to growth at both high and low overpotentials concerns the number of underlying metal ions that are in contact with the ad-ion. This depends on the substrate's crystallographic orientation. An ad-ion sitting on the (111), (100), and (110) planes will have 3,4, and 5 close lattice-atoms neighbours, respectively, to which it will be

bonded. As the number of bonds increases, so does the rate of the charge transfer step, and hence the growth rate.

Fast growing crystal faces will tend to grow out of existence, whilst slow growing faces tend to survive. This seemingly contradictory assertion follows from geometric arguments, as illustrated in figure (2.10). Finally, electrogrowth has been discussed so far in terms of single crystals. However, the models outlined are equally valid for growth on polycrystalline substrates, because each grain may be treated as a micro-substrate. Growth will be abnormal at grain boundaries, though as the actual area they occupy on the substrate is so small, this is negligible.

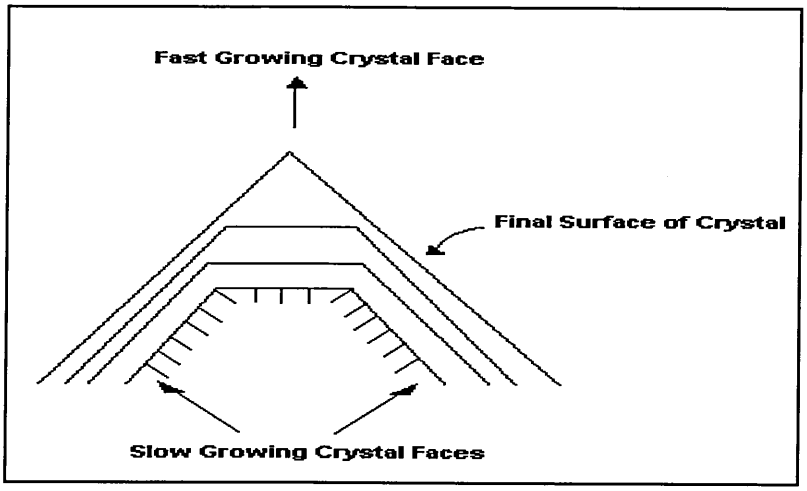

Figure 2.10 The growth of a crystal, illustrating how a face forming quickly grows out of existence, whilst a slow growing crystal face continues to grow.

Chapter 3

The Literature of Semiconductor Deposition

3.1 Introduction

Due to the field's infancy, the reviewer is at some disadvantage when considering the electrochemical deposition (ED) of III-V semiconductor materials. In contrast, a large body of work has been published over the last 30 years concerning the ED of solar cell materials such as: Si, the II-VI cadmium chalcogenides CdX (X= S, Te, Se), HgCdTe (MCT) and $CuInSe_2$. Such materials have been successfully used in the fabrication of devices that have achieved efficiencies comparable to those generated by other techniques, for example close space sublimation (CSS). Indeed, ITO/n-CdS/p-CdTe/metal solar cells based on electrodeposited chalcogenides routinely achieve efficiencies of 13.1% (Morris et al (1991)), approaching the 15.8% efficiency of cells fabricated from CSS materials (Moutinho et al (1998)).

The disparity in research effort has led previous reviewers to concentrate on II-VI ED at the expense of III-V materials[1]. Therefore, this review reassesses the subject whilst addressing two specific aims. Firstly, to demonstrate the development of devices fabricated from electrodeposited semiconductor materials. Secondly, to provide the reader with an overview of semiconductor electrodeposition, particularly III-V materials. Such aims have been achieved by reviewing II-VI ED, with an emphasis on CdTe and CdS, and by providing, to the author's knowledge, the most comprehensive review of III-V ED to date. For completeness, the ED of elemental and ternary semiconductor materials has also

---

[1] Fulop & Taylor (1985), Lockhande & Pawar (1989), Ortega (1991), DeMattei & Feigelson (1992) and, amongst other 'novel' materials, Searson (1992). Specific ED topics have been reviewed, including: the mechanistic aspects of II-VI ED, Rajeshwar (1992), and the ED of CdTe and $CuInSe_2$ for solar cells, Basol (1992).

been included. Finally, for brevity the less successful anodic deposition studies have been omitted.

3.2 Elemental Semiconductors

3.2.1 Silicon (Si)

Of historical interest are the attempts of various workers to deposit elemental Si during the second half of the 19th century. The first report was by St. Claire De Ville (1854), following the electrolysis of impure molten $NaAlCl_4$. However, this claim is doubted, as the material did not oxidise in white heat. Nevertheless, Monnier (1983) reports that De Ville later electrolysed a melt containing SiO_2-KF-NaF, and deposited Si on to a Pt cathode, where it reacted to form a Pt silicide.

The ED of Si from an aqueous solution is not possible because its salts easily hydrolyse. In addition, its very negative reduction potential favours H_2 evolution. Hence, the current efficiency of the process is low, and 'pitting' of the films common. Therefore, work has concentrated on the electrolysis of molten salts, mainly from silicates and fluorosilicates, and deposition from aprotic electrolyte solutions. For a detailed review, the reader is directed to Elwell & Rao (1988).

Methods employing silicate based melts are developed from the electrowinning[2] of Al, and are thus characterised by extremely vigorous growth conditions. For example, De Mattei et al (1981) deposited 99.98 % pure Si on to graphite cathodes from BaO-SiO_2-BaF melts at 1450 ^{o}C. The deposition potential was between 1 V to 8 V, and with current densities in the order of 0.5-1.0 Acm^{-2}. Subsequently, the authors were able to fabricate 10% efficient solar cells[3] from this material, following a single purification step. Nevertheless, the

---

[2] Electrowinning is a process used to recover many metals from their ores.

[3] Pearsall (1993) discusses Si, amongst other materials, in an introductory review of solar cell technology.

current efficiency (20-40%) of this ED method was judged too low for commercial application. The highest purity Si grown using a molten salt bath was reported by Elwell et al (1983), who employed a fluorosilicate based electrolyte (K_2SiF_6-LiF-KF) to grow 5N (99.999%) Si onto graphite substrates at 745 ^{O}C. Undoped samples were n-type, with carrier concentrations of 10^{17} cm^{-3}, a resistivity of 3.0 Ωcm and recorded mobilities of 100 cm^2/V-sec. No further characterisation, or fabrication of solar cell devices, was reported.

A major draw back of molten salt electrolysis is the energy required, via Joule or external heating, to maintain the system's molten state. Hence, in an effort to reduce the final product cost, low temperature (20-200 ^{O}C) non-aqueous electrolyte solutions have been investigated, with simple silicon halides or silane (Si_nH_{2n+2}) as the solute. However, the Si deposited to date has been amorphous, presumably due to the near room temperatures used. For example, Lee & Kröger (1982) grew phosphorus doped Si (changing its type from p to n), from SiF_4 in ethyl alcohol, though its resistivity was 10^{11} Ωcm.

3.2.2 Germanium (Ge)

The ED of germanium is of interest by its analogy to Si, and Elwell (1981) has reviewed its growth. Generally, with GeO_2 as the solute, three methods have been used for its deposition: (a) deposition from molten salts such as Na_3AlF_6 and Na_2CO_3-K_2CO_3, (b) deposition from aqueous alkaline solutions, and (c) deposition from organic solutions.

Szekely (1951) carried out Ge deposition from $GeCl_4$ in propylene glycol at 59 ^{O}C. The microstructure was found dependent upon the concentration of Ge in the solution, higher concentrations yielding needle-like structures.

3.3 II-VI Semiconductors

In respect of II-VI ED, a brief description of device technology is sufficient. A comprehensive account of photovoltaic technology using these materials may be found in Chu & Chu (1995) and the references therein.

II-VI compounds, such as CdS and CdTe, are ideal candidates for solar cell applications. This is because they are direct bandgap semiconductors, with a sharp optical absorption edge, and large absorption coefficients above their band gap wavelengths. This makes them particularly suited to thin film device technology as, for example, a II-VI semiconductor only 1 μm thick will absorb 99 % of impinging energy that is higher than its band gap. All efficient polycrystalline solar cells are based on a heterojunction configuration because of (1) the difficulty of forming a very shallow (0.1μm) junction with a high conductivity surface layer, and (2) surface recombination effects (Chu & Chu (1995)). Figure 3.1 illustrates a typical device, which comprises a transparent substrate layer, an n-type "window" layer and a p-type "absorber" layer.

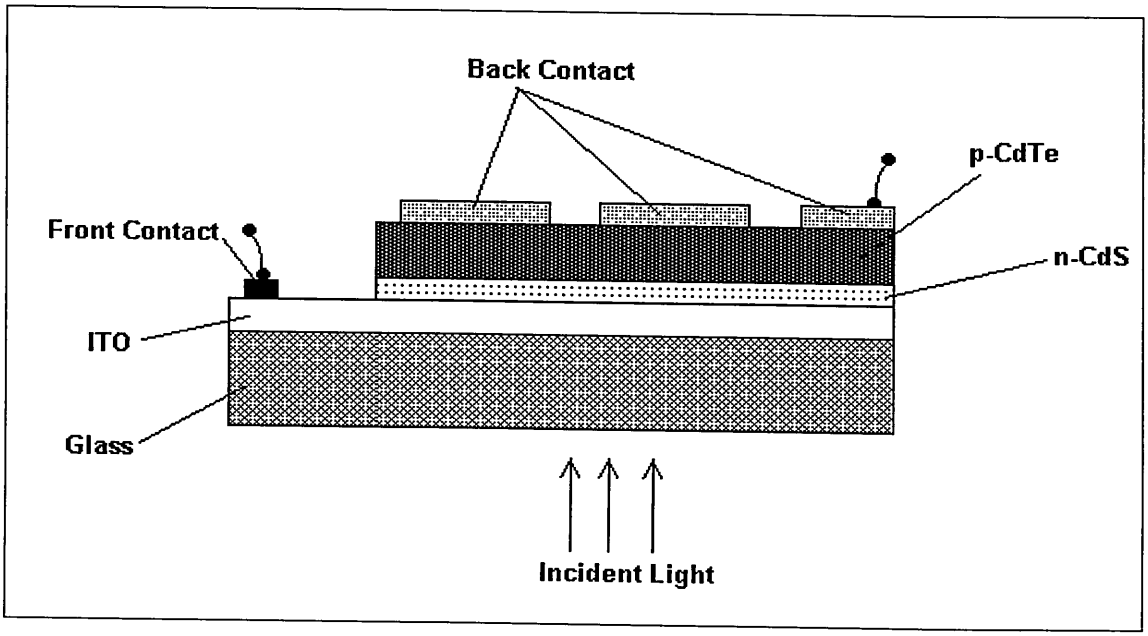

Figure 3.1 Schematic illustrating a typical solar cell structure.

The substrate most commonly used for electrodeposited solar cells is soda lime glass, coated with a thin layer (110 nm) of transparent conducting oxide (TCO). Typically, the TCO is tin doped indium oxide (ITO), whose sheet resistance is $<10\ \Omega\square^{-1}$, transmissivity >82%, and whose bandgap, depending on deposition conditions and doping levels, is between 2.8-3.7 eV. The substrate is scrupulously cleaned in a multistage process involving ultrasonic cleaning in organic solvents and Milli-Q water, followed by vapour degreasing in dichloromethane.

Onto the TCO layer, a 500-1000 Å thick CdS window layer (band gap 2.42 eV) is deposited, allowing for the removal of the high-energy photons without too detrimental a loss of lower energy photons[4]. This is followed by the ED of the thicker CdTe absorber layer (band gap CdTe 1.45 eV). Following surface preparation via a suitable wet etching process (Dharmadasa et al (1995(a)), a top metal contact (e.g. Sb, Au, or Au-Cu) is then evaporated under vacuum onto the CdTe.

Under optimised conditions, polycrystalline thin film solar cells consist of micrometer sized columnar grains characterised by a high degree of crystalline perfection, i.e. with a low level of dislocations and stacking faults. In contrast, the grain boundaries are highly disordered, and potential barriers exist due to the interruption of the crystal's periodicity. In addition, atoms at the grain boundaries may be bonded to impurity atoms, which give rise to a high density of surface states, and thus act as recombination centres. Consequently, conditions are employed where the material's average grain size is maximised, especially in the absorber layer whose depletion region serves as the main area for the photogeneration of the charge carriers.

Despite the success of using ED to generate such structures as above, the field affords future study. For example, surface preparation of the CdTe has been demonstrated to be important to device operation (Blomfield (1995)), and a comprehensive study of the properties of electrodeposited surfaces, and their effect on end device performance, is yet to be completed. The following sections (3.3.1 & 3.3.2) discuss specifically the ED of CdS and CdTe.

---

[4] Also, CdTe adheres better to the CdS than directly to ITO, and is less prone to pinhole formation.

3.3.1 Cadmium Sulfide

Thiosulfate has been used exclusively as a precursor for the CdS deposition from aqueous electrolyte solutions. McCann & Skyllas-Kazacos (1981), and Power et al (1981) described the formation of CdS from $Na_2S_2O_3$ containing baths. The former used alkaline solutions in which the Cd^{2+} was complexed with ammonia-EDTA, and CdS was formed only within a limited range of potentials and ammonia concentrations. High ammonia concentrations were seen to retard growth, whilst low concentrations produced Cd rich films.

Power et al (1981) used non-complexed Cd^{2+}, though actually Cd^{2+} forms a very weak complex with thiosulfate. The CdS only deposited at a significant rate after the solution's pH had been lowered from pH 6.7 to 2.8, where the thiosulfate decomposed, (reaction 3.1). Deposition was carried out whilst continuously cycling the applied potential, i.e. excess Cd was dissolved anodically. X-ray analysis of the films was inconclusive, due to the films' thickness (<1μm), or poor crystallinity, and scanning electron microscopy revealed a surface consisting of closely packed crystallites.

Reaction 3.1 $S_2O_3^{2-} \rightarrow S$ (colloidal) + SO_3^{2-}

Using the same plating bath as Power et al (1981), Jayachandran et al (1989) grew Cd rich polycrystalline CdS on to Ti, Al, and tin oxide coated glass substrates. The maximum deposition rates for the different substrates were found to be different, namely, 14, 7.5 and 3.5 nm min^{-1} respectively. (2.0 x 10^{-3} M $CdSO_4$, 0.1 M Na_2SO_4, pH 2.5, 25 ^{O}C, -1.0 V vs. SCE, with average current densities of 0.03 to 0.3 mA cm^{-2}).

The CdS films deposited had a hexagonal (Wurtzite) structure, with a resistivity of 2.5 Ωcm, direct band gap of 2.48 eV, and an average grain size between 0.02 to 0.05 μm. Layers grown on Ti had the largest, and most defined, grains, and this was attributed to accelerated nucleation due to the polished, highly conductive nature of the substrate surface. Those films grown on SnO_2 conducting glass exhibited a preferential orientation, with the c-axis perpendicular to the substrate, as demonstrated by the presence of a very intense X-ray diffraction peak corresponding to the (002) plane of hexagonal CdS.

However, preferred crystallographic orientation usually has no profound effect on the photovoltaic characteristics of a solar cell, Chu & Chu (1995).

The CdS growth conditions were further optimised by Dennison (1993), who concluded that higher (90 ^{O}C) growth temperatures were required to produce films with the desired crystallographic properties. However, this shortened the electrolysis bath's lifetime to 2 days, due to the spontaneous formation of CdS in the electrolyte. A detailed study of the reaction mechanism suggested the compound formation could be a result of one of two processes.

Reaction 3.2 $$Cd^{2+} + S_2O_3^{2-} + 2e^- \rightarrow CdS + SO_3^{2-}$$

Reaction 3.3 $$2Cd^{2+} + S_2O_3^{2-} + 6H^+ + 8e^- \rightarrow 2CdS + 3H_2O$$

The above reaction 3.2 would involve the generation of "Cd^0" followed by reaction with the thiosulfate ion, whilst reaction 3.3 would explain why CdS growth is more favourable at lower pH's.

To prepare an n-type CdS solar cell "window" layer, the method used by Morris et al (1991) could be forwarded as a representative 'recipe'. Specifically, the author deposited CdS on to an ITO/glass cathode at –320 mV vs. normal hydrogen electrode (NHE), from a bath of Cd^{2+} (0.2 M) and $S_2O_3^{2-}$ (0.01 M). The pH of the bath was ~2.0, and its temperature 90 ^{O}C. This ED is carried out in a single compartment cell, with three electrodes: substrate, graphite anode, and standard calomel reference electrode (SCE).

Typically, CdS electrodeposits require post-growth annealing, usually under nitrogen, to improve their crystallinity. Goto et al (1998) deduced, by monitoring photoluminescence peaks attributed to defects, that annealing under oxygen could reduce the defect density. This was attributed to oxygen atoms refilling vacancies generated by sulphur evaporation. In other words, as oxygen in CdS is an isoelectronic impurity, and thus electronically inactive, oxygen doping via annealing can be used as a defect reduction strategy.

Common to many of the films grown (Jayachandran et al (1989) and Morris et al (1991)), is a measured optical bandgap higher than that of standard CdS (2.53, 2.63, and 2.42 eV respectively). This would appear at first to indicate quantum size effects (QSE), where the dimension of the semiconductor is comparable to (or smaller than) the bulk exciton diameter. Nevertheless, this must be discounted, as the recorded grain sizes are too large. Therefore, this, and the decrease of the band gap after annealing, requires further investigation.

ED of CdS from non-aqueous solutions has also been investigated. Baranski et al (1981) investigated CdS deposition from dimethylsulfoxide (DMSO) and diethylene glycol (DEG) (Baranski & Fawcett (1984)) solvents, at temperatures above 100 ^{O}C. The former study used $CdCl_2$ and elemental sulphur as solutes. The films were characterised by cracking, which was attributed to a piezoelectric effect. Generally, annealing the films under nitrogen at 200 ^{O}C for 2 hrs lowered their electrical resistance.

Copper doping of CdS *in situ* has also been achieved (Edamura & Muto (1993)) by galvanostatic deposition from DMSO solutions at elevated temperatures. It was found that if the concentration of the $CuCl_2$ solvent exceeded 5.0×10^{-4} M, the films exhibited poor adhesion.

A recent development of the use of non-aqueous electrolysis, is the generation of nanowires. Routkevitch et al (1996) have developed a technique for fabricating arrays of n-type CdS nanowires, probably doped with excess Cd, from an electrolyte containing Cd^{2+} and elemental S in DMSO[5]. These nanowires were formed within the pores of an anodically prepared aluminium oxide film template, and had lengths up to 1 μm and diameters as small as 9 nm. X-ray analysis revealed that the CdS crystallites were textured, with the crystalline c-axis (hexagonal CdS) aligned preferentially along the length of the pores.

---

[5] Non-aqueous solvents were preferable, as the electrolysis of aqueous electrolytes led to the anodic attack of the aluminium oxide template.

Finally, molten salt electrolysis has received a small amount of attention. Markov et al (1983) deposited CdS onto Cu and Ag in a fused LiCl-KCl eutectic. Smooth films were deposited at 450-500 ^{O}C, 0.2-0.5 mA cm^{-2}.

3.3.2 Cadmium Telluride (CdTe)

CdTe is electrochemically generated using a method that has changed little since the original work by Panicker et al (1978). The electrolyte bath consists of 2.0-2.5 M $CdSO_4$, 30-40 ppm $HTeO_2^+$, adjusted to pH 1.6 using H_2SO_4. The bath temperature is carefully maintained at 90 ^{O}C, to ensure crystalline layers are formed.

The large ratio of cadmium to tellurium ions in solution is necessary because: (1) the great difference in standard electrode potentials for cadmium and tellurium (respectively -0.403 V and + 0.551 V vs. SHE), and (2) the low solubility of the TeO_2 precursor. Consequently, the concentration of $HTeO_2^+$ is quickly depleted, and growth is limited by tellurium diffusion. An appropriate level of $HTeO_2^+$ is maintained in solution by either deploying a second sacrificial Te anode, or by just 'manually' topping up the plating bath with TeO_2 solution as required.

Several groups have investigated the mechanism of CdTe growth, these include Sharma & Chang (1989), Mishra & Rajeshwar (1989), Saraby-Reintjes et al (1993), and more recently, Meulenkamp & Peter (1996). Principally, the deposition of CdTe can be considered as a two step reaction, Panicker et al (1978). That is, a reduction of Te^{IV} to Te^0, reaction 3.4, followed by the 'under potential deposition' (UPD) of Cd^{2+} at a Te surface site, reaction 3.5.

Reaction 3.4 $$HTeO_2^+ + 3H^+ + 4e^- \rightarrow Te^0 + 2H_2O$$

Reaction 3.5 $$Cd^{2+} + Te^0 + 2e^- \rightarrow CdTe$$

Essentially, UPD means that CdTe electrodeposits at potentials slightly more positive than that of the $Cd^{2+}/Cd_{(S)}$ equilibrium potential. This is a result of the large value for the free energy of formation of CdTe (-25.5 kcal/mole), and the high cadmium concentration in the bath. These factors also led to a preference for compound, rather than alloy,

formation. Moreover, since the Te 'substrate' is being continuously formed anew, the UPD occurs wherever the Te has been deposited, facilitating CdTe epitaxial growth.

Obviously, excess Te or Cd co-phases can be deposited with CdTe, if the relative rates of reactions 3.4 and 3.5 are unequal. Therefore, so that no free Cd is deposited, growth is carried out at only a slightly positive potential to the $Cd^{2+}/Cd_{(S)}$ equilibrium potential. This description is a simplification of some very complex electrochemistry, and a six-electron reduction product, H_2Te, may well play a part, reaction 3.6.

Reaction 3.6 $$2H^+ + 2e^- + CdTe \rightarrow Cd + H_2Te$$

More recently, Colletti et al (1998) extended the use of UPD to the electrochemical equivalent of atomic layer epitaxy (ECALE), whereby thin films of CdTe, CdS and CdSe were formed an atomic layer at a time using surface-limited reactions. UPD can be classed as a surface-limited reaction as, by definition, it only occurs when it is energetically more favourable to deposit on another element than it is to deposit on itself, due the free energy of compound formation. Hence, once the surface is coated with the first element, no more of the substrate is available to react, and deposition will stop. Obviously, in practice, ECALE involves depositing each of the film's components from separate electrolyte solutions a monolayer at a time. Consequently, the cells employed are complex, involving computer-controlled potentiostats, automated pump and valve systems etc. However, the aforementioned authors have reported the development of such a system, as well as encouraging results for the deposited film's material properties.

A benefit of the CdTe ED method is that it presents several strategies for conferring n- or p- character on the semiconductor layers formed. These are: post-growth treatment, co-deposition of allowed impurities, and deposition potential. Of these, the most common method for converting as grown n-CdTe to p-CdTe is the Type Conversion Junction Formation (TCJF) process, Basol (1988). In this process the deposited ITO/CdS/CdTe 'sandwich' is annealed at 350-450 ^{O}C in air for ~ 15 minutes. Basol (1988) suggests a possible model for this post-growth treatment, involving the out diffusion of Cd from the bulk of the grains to the grain boundaries, with the chemisorption of oxygen at these surfaces. In this way, Cd vacancy acceptors are created in the bulk of the grains, and band

bending is partially controlled by the oxygen at the boundaries. This process would also reduce the number of recombination centres, by increasing the materials' grain size and driving off free tellurium, Takahashi et al (1985).

Zanio (1978) reviewed how the presence of impurities in ED[6] CdTe affects end device performance, and it was suggested that Ag, Cu, As, and P may act as p-type dopants. Indeed, Bhattacharya & Rajeshwar (1985) deposited p-CdTe from aqueous baths containing deliberately added Cu and As.

Subsequently, Dennison (1994) investigated the relationship between solar cell efficiency and the level of Ag^+ or Cu^{2+} in the electrolyte solution. It was found that device efficiency decreased if the concentrations of Ag^+ and Cu^{2+}in the bath were above 5 ppb and 30 ppb respectively. The change of the behaviour from dopant to impurity was probably due to a change from substitutional to interstitial incorporation into the CdTe lattice. Cu is already found in the bath (7 ppb) as an impurity deriving from the Te anode used (Te is produced from the electrowinning of Cu).

In addition, Dennison (1994) demonstrated the benefits of including *in situ* Cl^- (0.2 M $CdCl_2$) in both the CdTe and, more importantly, CdS ED procedures. This is despite chlorine atoms being shallow donors, which should assist in conferring n-type conductivity to the semiconductor. Further work is needed to explore the origins of this effect, though two mechanisms were suggested. Firstly, Cl^- inclusion improves current transport in the device, by lowering CdTe's bulk resistance and countering the activity of traps in the polycrystalline semiconductor. Secondly, through an unknown mechanism, Cl^- assists in the formation of the junction[7].

---

[6] Lyons et al (1989) published a detailed study of the origins of advantageous impurities in CdTe electrodeposition systems, which is relevant to all ED semiconductor systems.

[7] Via an unknown mechanism, the inducement of the formation of CdS_XTe_{1-x} at the junction interface may well occur. Further, Qi et al (1996) used XRD/SEM to investigate the mechanism of annealing CdTe, and

Following the work of Kröger (1978), Panicker et al (1978) found that the conduction type of ED CdTe is influenced by the deposition potential. They reported a critical value for the quasi-rest potential[8] (QRP) of +240 mV vs. the Cd/Cd^{2+} electrode. Below this QRP n-type CdTe is deposited, whilst more positive deposition potentials yield p-type CdTe. The formation of p-type (Te rich) CdTe can be explained by considering the relative rate of reactions (3.4) and (3.5). If the potential is made more positive, the reaction generating Cd is too slow to keep up with the generation of Te. This leads to Te interstitial atoms or cadmium vacancies in the CdTe, which act as acceptors (Kampmann et al (1995)), and hence p-type material. The n-type material that forms at potentials only slightly more positive than the CdTe QRP, may be explained in terms of UPD of Cd into interstitial sites in the semiconductor. These interstitial atoms act as doubly ionised donors in CdTe. The driving force of this UPD is presumably the Gibbs energy of dissolution of elemental cadmium in CdTe. A disadvantage of this method is that it is difficult to avoid the co-deposition of a second phase of free tellurium.

The use of QRP's to control the physical and photovoltaic properties of ED CdTe has recently been questioned. Dennison (1995) conducted an extensive study of this subject. The author concluded that the value of QRP did not exert any influence, because the substrate's electrical resistance swamps the QRP's. These conclusions do not refute Kröger's (1978) assertion that an instantaneous, and measurable, equilibrium potential

---

proposed that layers annealed after being sprayed with a $CdCl_2$ solution recrystallised at a faster rate. In addition, it should be noted that experience from growth techniques, such as MOCVD, showed that great improvements in CdTe photovoltaic activities can be accomplished by treating the material with a $CdCl_2$/methanol solution, followed by annealing in oxygen.

[8] QRP's are defined as the potential of the deposit relative to the electrolyte with activities of potential determining species as they are at the solid electrode interface during deposition. They are measured following (10^{-3} sec) interruption of the deposition current when the electrode has unpolarised. QRP's are treated as equilibrium potentials, though this is not strictly true as no complete equilibrium exists immediately after the current is interrupted.

exists between the depositing phase and electrolyte solution. Neither do they compromise the above-described deposition process kinetics. Instead, they demonstrate that further work be undertaken, to define an experimentally reproducible thermodynamic and kinetic model of the CdTe growth process. Though, by observing a 'potential of perfect stoichiometry', the work does go some way to support Engelken & Van Doren's (1985) Butler-Volmer equation based kinetic model. However, as Dennison (1994) states, this model has not gained much support to date, due to its unwieldy nature, and failure to calculate current-voltage behaviour consistent with that observed experimentally.

Examples of CdTe deposition systems that use non-aqueous solvents include those employing DMSO (Rastogi & Balakrishnan (1989)), Ethylene Glycol (EG) (Gore et al (1989)), and Propylene Carbonate (PC) (Darkowski & Cocivera (1987)). Some advantages in ED from a non-aqueous solvent are: (a) the absence of hydrogen evolution, which causes pinhole formation, (b) no hydrolysis of tellurium salts, and (c) higher temperatures can be used, conferring the product with better crystallinity.

Atypically, Darkowski & Cocivera (1987) used an organometallic source of tellurium, tri (n-butyl) phosphine telluride [$(C_3H_8)_3PTe$]. Photoelectrochemical (PEC) activity data recorded in the growth solution produced a cathodic current, indicating that the films were p-type. The best films (photocurrent density 4.2 mA cm^{-2}) were produced from a solution of 3 mM Cd^{2+}, 12 mM phosphine telluride, and 100 mM lithium perchlorate electrolysed at -1200 mV (vs. Ag/AgCl reference electrode), and approximately 100 ^{O}C.

3.3.3 Cadmium Selenide (CdSe)

Electrodeposited polycrystalline n-CdSe films, in for example $Fe(CN)_6^{4-/\ 3-}$ solutions, have been employed as photoanodes for PEC's that have yielded in excess of 7.5 % conversion efficiencies (Lockhande (1987)). Gruszecki & Holmström (1993) have reviewed the material's ED.

Mishra & Rajeshwar (1989) have studied the reaction mechanism in detail, and concluded that it is different to that of CdTe. Indeed, such is indicated by the morphology of CdSe, which tends to be porous and cauliflower-like, as opposed to the epitaxial growth

characteristic of CdTe. The authors propose, in contrast to other models, a direct six-electron reduction to CdSe. However, they go on further to highlight that Se^{4+} reduction occurs at potentials much more negative than Te^{4+}. Hence, *a priori*, highly reduced species such as H_2Se would be expected to play more of a dominant role, as illustrated by the following reactions 3.7 and 3.8.

Reaction 3.7 $$H_2SeO_3 + 6H^+ + 6e^- \leftrightarrows H_2Se + 3H_2O$$

And, in the presence of Cd^{2+} ions

Reaction 3.8 $$Cd^{2+} + H_2Se \leftrightarrows CdSe + 2H^+$$

ED CdSe films tend to suffer from the presence of a second free Se phase, reaction 3.9, which is detrimental to device efficiency. Hence, together with the deposit's poor crystallinity, this means that the films are nearly always annealed to drive off the excess Se.

Reaction 3.9 $$2H_2Se + H_2SeO_3 \leftrightarrows 3Se + 3H_2O$$

In contrast, Löizos & Spyrellis (1991) proposed that CdSe does form via a mechanism analogous to CdTe. The authors offer in support of their argument the improvement in PEC efficiency and material morphology for CdSe deposited with Se precursor concentrations comparable to those of the Te precursors in CdTe growth. To muddy the waters further, Tomkeiwicz et al (1982) suggested that two different mechanisms might occur, as the formation of an initial compact CdSe layer usually precedes the deposition of a bulk layer of poorer morphology. In conclusion, it is fair to propose that further investigation is needed to clarify the ED growth mechanism of CdSe.

An interesting aside, is the report by Golan et al (1996) of the epitaxial growth of quantum sized CdSe dots (5 nm) on gold. The authors used a non-aqueous (DMSO) electrodeposition protocol using elemental Se and $Cd(ClO_4)_2.6H_2O$.

3.3.4 Zinc Telluride and Zinc Selenide (ZnTe & ZnSe)

Mondal et al (1992) deposited 30-300 nm thick layers of Cu doped ZnTe onto ITO/CdS/CdTe substrates. The electrolyte solution consisted of $ZnCl_2$, TeO_2 and $CuCl_2$ (or $CuSO_4$), with the concentration of Cu^{2+} being controlled through complexing with triethanolamine to prevent the formation of free Cu co-phases. The low solubility of the TeO_2 was overcome by first dissolving it in NaOH to form Na_2TeO_3, with the Te remaining being in the +4 state. Efficiencies of 8.6 % were achieved for solar cells fabricated using this method.

Königstein & Neumann-Spallart (1998) investigated the growth mechanism of ZnTe, and found it generally analogous to CdTe, reactions 3.10 and 3.11. An important difference in growth mechanism proposed was that Zn^{2+} ion absorption onto Te is weaker than Cd^{2+}. Hence, growth 'autoregulation', where the deposited Te atoms trigger the reduction of a metal ion, is not as prevalent as in the case of CdTe deposition

Reaction 3.10 $$H_2SeO_3 + 4H^+ + 4e^- \Leftrightarrow Se^O + 3H_2O$$

reaction 3.11 $$Zn^{2+} + Se^O + 2e^- \leftrightarrows ZnSe$$

Electrochemically grown ZnSe is p-type, and has been found to exhibit reasonable photoelectric stability when used in PEC cells with zinc sulphate solutions containing the I^-/I_2 redox system Rai (1993). However, PEC cell efficiencies are low, probably due to the resistive nature of the films. PEC studies were also used by Samantilleke et al (1998) to determine the conductivity type of doped ZnSe. The authors demonstrated that they were able to electrochemically produce n-ZnSe through *in situ* doping with Ga from its sulphate.

Analogous to CdSe, Natarajan et al (1994) concluded that the deposition of stoichiometric ZnSe was complicated by dominant Se chemistry. Despite having conducted a comprehensive study of the compound's aqueous deposition, the authors concluded that more work was needed to limit the formation of Se co-phases. As with CdSe, post-growth annealing is typically employed to rid the layers of excess Se.

Wei & Rajeshwar (1992) reported a novel way of forming superstructures based on CdSe/ZnSe via ED. The authors used a 'flow synthesis' technique, wherein the respective electrolyte solutions were pumped successively through a cell containing the substrate. Other than recording closely matching band gaps for both materials, no other characterisation was reported.

3.4 III-V Binary Semiconductors

A variety of electrochemical techniques has been used to deposit GaP, InP, GaAs, InAs, InSb, and GaSb, table 3.1. However, it is worth re-iterating here that the development of III-V semiconductor ED protocols is far behind those for II-VI compounds. Part of the explanation for this has been discussed elsewhere in this thesis.

There are precedents in the literature that can be drawn on to provide useful information regarding InSb ED, viz. deposition conditions and electrolyte bath composition. In general, however, the aims of such studies were to deposit Sb-In *alloys* for anti-friction and/or anti-corrosion coatings. Therefore, the remit of the electroplaters was different, and the quality of the materials formed was judged primarily in terms of visual appearance, hardness, resistance to corrosion, and mechanical properties.

In other words, the direct formation of the compound InSb, certainly for semiconductor device applications, has not been studied in detail, and only three papers concerning this subject have been published. The first two (Okubo (1988) and Ortega & Herrero (1989)) report the use of a citrate based plating bath developed previously by Sadana & Singh (1985), who had investigated the galvanostatic deposition of Sb-In metal finishes. The third paper (Carpenter & Verbrugge (1994)) reported the co-deposition of In and Sb from a chloroindate molten salt.

Unlike Sb-In alloys, Sb-Ga alloys have not been extensively used for metal finishing, and even less background literature exists. Liquid Phase Electro-Epitaxy (LPEE) (Zytkiewicz and Dobosz (1995)) and sequential layer deposition (Paolucci et al (1990)) have been utilised to form GaSb films.

Compound	Principal Author & (Year)	ED Technique
GaP	Cuomo (1968)	Electrolysis of a Ga_2O_3 /$NaPO_3$/NaF fused salt mixture.
GaP	DeMattei (1978)	Electrolysis of a Ga_2O_3 /$NaPO_3$/NaF fused salt mixture.
InP	Elwell (1981)	Electrolysis of a In_2O_3 /$NaPO_3$/NaF/KF fused salt mixture.
InP	Sahu (1989)	Galvanostatic growth from an aqueous solution of $InCl_3$/NH_4PF_6.
InP	Ortega (1989)	PH_3 treatment of an electrodeposited indium layer
InP	Sahu (1992)	Galvanostatic growth from a non-aqueous solution of $InCl_3$/NH_4PF_6.
InP	Cattarin (1995)	PH_3 treatment of an electrodeposited Indium layer.
InAs	Mengoli (1992)	Sequential deposition of In & As, followed by annealing.
GaAs	DeMattei (1978)	Electrolysis of a $NaAsO_2$ /Ga_2O_3 /B_2O_3/NaF fused salt mixture
GaAs	Dioum (1982)	Electrolysis of a $KGaCl_4$/AsI_3 fused salt mixture
GaAs	Chandra (1987)	Galvanostatic growth from an aqueous solution of $GaCl_3$/As_2O_3.
GaAs	Wicelinski (1987)	Deposition from a chloroaluminate melt at 40°C
GaAs	Murali (1987)	Successive potentiostatic deposition of elemental layers, followed by annealing.
GaAs	Perrault (1989)	Galvanostatic growth from an aqueous solution of Ga_2O_3/ As_2O_3.
GaAs	Carpenter (1990)	Potentiostatic deposition from a chlorogallate melt at room temperature
GaAs	Yang (1992)	Potentiostatic growth from an aqueous solution of Ga_2O_3/ As_2O_3.
GaAs	Villegas (1992)	ECALE
GaAs	Gao (1994)	Galvanostatic growth from an aqueous solution of Ga_2O_3/ As_2O_3.
InSb	Okubo (1988)	Potentiostatic from an aqueous solution of $InCl_3$ and $SbCl_3$.
InSb	Ortega (1989)	Potentiostatic from an aqueous solution of $InCl_3$ and $SbCl_3$.
InSb	Mengoli (1991)	Successive potentiostatic Deposition of elemental layers, followed by annealing.
InSb	Carpenter (1994)	Electrodeposition from a chlorinate molten salt.
InSb	Kozlov (1997)	Deposition of In on Sb electrodes, followed by annealing.
GaSb	Paolucci (1990)	Successive potentiostatic Deposition of elemental layers, followed by annealing.
GaSb	Zytkiewicz (1995)	LPEE

Table (3.1) III-V Semiconductor ED Studies

3.4.1 Gallium Phosphide (GaP)

Cuomo & Gambino (1968) were the first to electrodeposit a III-V semiconductor compound. These workers epitaxially deposited single crystals of GaP on to silicon substrates (<111>, <100>, and <110>), by the constant voltage electrolysis of a fused salt. 100 μm thick layers, with polycrystalline dendrites on their surfaces, were produced using a bath containing (in molar ratio): 2.0 $NaPO_3$, 0.5 NaF, and 0.1225-0.25 Ga_2O_3 at 800 °C. The liquidus temperature of the melt composition (750 °C) and extensive volatization of the precursors above 1000 °C limited the temperature range available for growth. Samples had to be carefully cooled to prevent them cracking. A growth rate of 10-20 mm hr^{-1} was achieved at voltages around 0.9 Volts, but decreased with film thickness because of the

relatively high resistivity of the GaP formed. Thicker layers could be deposited by *in situ* n- and p- type doping, using Na_2SeO_4 and ZnO respectively, because the resistivity of the films was lowered.

Deposits were found to contain the following impurities (in atomic percent): Si (0.0001), Al (0.05), Te (0.01), and Cu (0.001). Those from mixtures of alkali halides (LiCl-KCl and NaCl-KCl) were of poorer quality, as were those formed in their attempts to synthesize AlP and ZnSe. Electroluminescent p-n homojunctions were fabricated by electrochemically growing a p-type GaP layer on an n-type layer grown by the Bridgeman technique. The light emitted from the diodes was red at both room temperature and 77 K, and device efficiency was approximately 10^{-4}.

Using the same temperature and bath compositions as above, De Mattei et al (1978) conducted a limited study of GaP deposition on graphite, Si, and GaP substrates. The electrochemical reactions for GaP at the cathode probably were:

Reaction 3.12 $$8e^- + Ga^{3+} + 4PO_3^- \rightarrow GaP + 3PO_4^{3-}, \text{or}$$

Reaction 3.13 $$8e^- + Ga^{3+} + PO_3^- \rightarrow GaP + 3O^{2-}$$

And at the anode:

Reaction 3.14 $$2O^{2-} \rightarrow O_2 + 4e^-$$

Or,

Reaction 3.15 $$2PO_4^{3-} \rightarrow 2PO_3^- + O_2 + 4e^-$$

Layers grown at 40 $mAcm^{-2}$ had surface craters due to excess P forming gas bubbles on the substrate surface. More uniform crystalline deposits that were epitaxial formed at lower current densities (20 $mAcm^{-2}$). The minimum deposition potentials for growth were dependent on the substrate used: graphite (0.68 V), Si (100) (0.55 V), and GaP (100) (0.86 V).

The above studies illustrated that GaP electrodeposition from fused salts was possible, and that morphologies comparable to those produced by early MOCVD techniques (Andre et al (1975)) could be achieved. Yet, much more systematic experiments are needed to improve the quality of the deposits to modern standards. However, in light of the advancement of vapour deposition techniques, no further work has been conducted.

3.4.2 Indium Phosphide (InP)

Sahu (1989) reported the galvanostatic deposition at 22 ^{O}C of non-stoichiometric InP on Ti substrates, from an aqueous solution of $InCl_3$ (1.25 mM) and NH_4PF_6 (58.6 mM). 0.45 μm thick InP films were obtained within 7 minutes, using a constant current density of 20 $mAcm^{-2}$.

Energy Dispersive X-ray Analysis (EDX) of the as grown films revealed their composition to be 49 % In and 51 % P. However, in a subsequent paper (Sahu (1992)) the author states that the error in determining film stoichiometry by EDX is +/- 5%. The composition of the plating bath was seen to affect that of the film. The P content of the films slightly rose with increasing NH_4PF_6 concentration. Moreover, a slight increase in $InCl_3$ concentration in the plating bath resulted in a dramatic increase of indium in the deposit. Hydrogen evolution predominated at higher current densities and lower pH's. Unpublished scanning electron micrograms revealed the films to have poor surface morphology, and grain sizes <10 nm. Optical absorption spectra showed the material's band gap to be 1.22 eV, versus the standard 1.35 eV.

To circumvent the concurrent evolution of hydrogen, Sahu (1992) continued the study of InP electrodeposition, using a non-aqueous solvent, dimethyl formamide (DMF), at 23 ^{O}C. Fluorine doped SnO_2 glass was used as a substrate to allow the band gap of the thin films to be easily recorded. The films were annealed in vacuum at 300-400 ^{O}C, and SEM micrograms revealed a dramatic change in surface morphology, from a carpet of thread like features, to a bed of globules. Analysis using x-ray diffraction (XRD) showed that as grown films comprised a non-stoichiometric mixture of InP, P and In. After annealing, those XRD peaks attributed to reflections from InP planes were not observed. This was explained in terms of the loss of P from InP when the samples were annealed without

encapsulation, apparently an effect observed in other growth techniques. The band gap of the as-grown films was 1.30 eV.

Another route to the generation of InP thin films was initially developed by Ortega & Herrero (1989), and furthered by Cattarin et al (1995). This method involved the electrodeposition of an indium layer from an aqueous $InCl_3$ solution, followed by treatment in a PH_3 gas to form InP. Following annealing at 450 ^{O}C, Cattarin et al (1995) observed, using XRD and SEM, the formation of InP and a secondary indium 'globular' phase. Samples prepared at higher temperatures showed limited improvements in crystallinity, but had a poorer surface morphology, due to the formation of larger In globules. Whereas a minimum annealing time was necessary for the quantitative conversion of In/P to InP, the P uptake tended to be self-limiting. Indeed, samples submitted to a prolonged annealing in PH_3 show In/P ratios in the range 0.97 to 1. This was tentatively attributed to a loss of catalytic activity of the sample surface toward PH_3 decomposition once the whole In surface had reacted. The layers were investigated using a photoelectrochemical cell in an acidic polyiodide medium, and were seen to exhibit n-type photoactivity. P-type doping was achieved by depositing a small amount of Zn on to the In layers prior to phosphorization.

The deposition of InP from fused salts has also been investigated, Elwell et al (1981). The authors explored, with various bath systems, the conditions required to deposit InP on a variety of substrates, notably CdS and InP. Deposits were formed at 1-3 $mAcm^{-2}$, from a eutectic mixture of $NaPO_3/KPO_3/NaF/KF$ as a solvent. The use of the technique is complicated by the high volatility of the most common sources of In ions (In_2O_3 and InF_3) above 650 ^{O}C, and by the decomposition of InP at elevated temperatures in an inert atmosphere. These factors limited the temperature range to 600-650^{o}C. Nevertheless, uniform films, 2-5 μm thick, were deposited at rates of 1-2 μm per hour at potentials 0.9-1.0 V. No device structures were fabricated.

3.4.3 Gallium Arsenide (GaAs)

To produce GaAs, De Mattei et al (1978) utilised a molten salt solution containing $NaAsO_2$ and Ga_2O_3, in a B_2O_3-NaF solvent at 720-760 ^{O}C. The composition of the solution was

carefully selected to minimise the volatility of the $NaAsO_2$ and Ga_2O_3. More than a stoichiometric amount of arsenic was needed to prepare single phase GaAs deposits. The minimum deposition potentials, at the temperatures used, were 1.7 V and 2.0 V for GaAs and nickel cathodes respectively. Epitaxial GaAs layers 10 μm thick were deposited on (100) n-type (0.05 Ωcm) GaAs substrates. Dioum et al (1982) attempted unsuccessfully to electrodeposit stoichiometric GaAs at a relatively low temperature (300°C) from $KGaCl_4$ and AsI_3.

Electrolysis of melts at room temperature has recently received attention, as in themselves they offer prospects for investigating novel electrochemistry. Accordingly, Wicelinski & Gale (1987) deposited GaAs from a chloroaluminate melt at 40 °C (with the Ga and As precursors dissolved in an $AlCl_3$: 1-butylpyridinium chloride, or $AlCl_3$: 1-methyl-3-ethylimidazolium (ImCl)).

As described by Carpenter & Verbrugge (1990), and the references therein, the solvents have a large potential "window" of stability against electrolytic breakdown. In addition, the systems are capable of affording a large range of acidity. This is achieved by varying the relative proportions of the aluminium chloride and organic chloride. Melts with molar ratios less than unity of $AlCl_3$ to organic chloride are basic, and the melt is formed according to the following reaction

Reaction 3.16 $$RCl + AlCl_3 \leftrightarrows R^+ + AlCl_4^-$$

where the R^+ is the pyridinium or imidazolium ion. For ratios greater than one, the corresponding melts are acidic, and an aluminium chloride dimer ion is formed.

Reaction 3.17 $$AlCl_4^- + AlCl_3 \leftrightarrows Al_2Cl_7^-$$

The potential windows of the melts are determined on the positive side by the oxidation of Cl^-, and on the negative side by the reduction of the organic cation in the basic melts, or the Al (III) species in the acidic melts. (Al can not be deposited from basic melts.) This window is large for the ImCl melt, which itself is also able to maintain a low melting point over a wide range of compositions.

To avoid Al contamination of the GaAs, Carpenter & Verbrugge (1990) used a $GaCl_3$: ImCl melt, as used by Wicelinski et al (1987). Contrary to the $AlCl_3$: ImCl melt, it was found that Ga(III) species could be reduced to Ga metal from melts at basic pH values. Formation of the melt was, by analogy to the chloroaluminate melt, presumed to follow

Reaction 3.18 $$ImCl + GaCl_3 \leftrightarrows Im^+ + GaCl_4^-$$

The deposition of gallium metal results from the reduction of the gallium chloride species

Reaction 3.19 $$GaCl_4^- + 3e^- \leftrightarrows Ga + 4Cl^-$$

Presumably, addition of $AsCl_3$ to the basic $GaCl_3$: ImCl melt yields $AsCl_4^-$. The plating system could be described as 'anomalous'. This was because, that although cyclic voltammetry showed arsenic to be the noble species, its mole fraction in the GaAs (as measured by EDAX) decreased with respect to gallium at the more negative potentials applied. The authors were able to deposit mixtures containing Ga, As and a small amount of GaAs (as determined by XPS) onto glassy carbon electrodes at potentials between –0.4 to –1.0 Volts (vs. an aluminium reference electrode placed in an 40:60 $GaCl_3$: ImCl melt). The morphology was found to comprise a carpet of spherical nodules of ~3 μm.

The first report of the deposition of GaAs by the electrolysis of an aqueous solution was discussed in two papers by Chandra & Khare (1987). The experimental conditions employed were; Ti substrate, Ga (10gl^{-1}) metal dissolved in HCl, As_2O_3 (10 gl^{-1}), pH 0.7, 2.5 $mAcm^{-2}$ for 7 minutes, and the temperature at 22 ^{O}C. To select an appropriate solution pH, the Pourbaix diagrams for Ga and As were overlaid, to estimate their common immunity region[9]. The best stoichiometry achieved was $Ga_{1.04}As_{0.96}$, as determined by

[9] The term immunity stems from the fact that Pourbaix diagrams were originally developed to assist in the study of the corrosion properties of certain elements. Hence, 'immunity' means that a species is thermodynamically stable in the electrolytic system under the specified conditions laid out by the Pourbaix diagram.

EDAX. The author noted the limitations of EDAX for accurately determining the stoichiometry of inhomogeneous films. Photoelectrochemical cells using the electrodeposited material exhibited poor efficiency (~0.3 %), due to the low quality of the GaAs. The films' bandgaps were found to be ~1.5 eV (vs. 1.43 eV for standard samples).

Perrault (1989) used the latest thermodynamic data available to recalculate the Pourbaix diagrams for gallium and arsenic. In addition, the author calculated the Pourbaix diagram for GaAs itself. It was concluded there was a large (pH 1.3-13.3) stability region where GaAs would be stable when in contact with an aqueous solution of arsenious and gallium species. A series of deposition experiments were conducted using Ga_2O_3 and As_2O_3 under acidic, neutral, and alkaline conditions. (No mention was made of the insolubility of gallium oxides, and hydroxides, at pH values between 3-12.) The results of the study may be summarised as follows. From alkaline (~ pH 14) solutions, at temperatures above the melting point of Ga, small drops of fused Ga metal containing small traces of arsenic formed. Deposition from neutral (pH 6-8) solutions yielded mirror like films of arsenic. Finally, films containing segregated Ga and As were deposited from acidic (pH 0-4) solutions. Hence, the author was unable to deposit GaAs under any of the conditions used. Thus, Perrault concluded that the direct co-deposition of GaAs was not possible using arsenious compounds, and that non-oxygen bearing compounds should be used in the future. Minimal details of the experimental procedures employed were given.

Yang et al (1992), following unsuccessful attempts to reproduce the results of Chandra and Khare (1987), conducted an extensive study of the deposition of GaAs from $GaCl_3$ (or Ga_2O_3) and As_2O_3, in alkaline and acid solutions. Non-stoichiometric 'microcrystalline' GaAs was deposited potentiostatically under alkaline conditions, and galvanostatically under acidic conditions. The best composition of the films (as measured by EDAX) from an alkaline bath was by atomic percent Ga (49.5 %), As (50.5 %), deposited onto tin substrates. Gallium levels close to 50 %, was also recorded for films deposited at pH <0.7, using high current densities (350 $mAcm^{-2}$), and the adhesion of layers grown under acidic conditions were superior. The concentrations of the components in the deposit were seen to vary with the applied deposition potential; the higher the potential the more Ga deposited. Secondary ion mass spectrometry (SIMS) suggested that a small quantity of

GaAs was formed in the as grown samples. Significantly, prolonged (up to 21 hrs) post growth annealing in N_2 was used in the production of all the best films.

Gao et al (1994) galvanostatically deposited (current densities of <6 $mAcm^{-2}$) at 22 ^{O}C polycrystalline $Ga_{0.91}As_{1.09}$ on to ITO and $Ga_{0.93}As_{1.07}$ on to Ti substrates, from a Ga metal/As_2O_3 bath. The pH of the baths was below pH 1.0. XRD diffraction patterns showed good agreement with standard samples. The J-V characteristics of a $Ga_{0.91}As_{1.09}/S^{2-}/S_2^{2-}$ electrolyte junction was measured and its efficiency found to be 0.51 %.

Finally, Murali et al (1987) deposited gallium on copper foil from sodium gallate solution, then arsenic from arsenite solution. The samples were then annealed in a high vacuum at temperatures in the range 520-800 ^{O}C. No characterisation of the films was reported.

In summary of the aqueous GaAs deposition systems, the best 'quality' deposits have been obtained from acidic solutions (pH < 0.7) by the galvanostatic electrolysis of solutions of Ga and Arsenic trioxides. The thin films formed tend to be composed of a segregated mixture of Ga and As, which require post growth annealing to form GaAs. The highest growth temperatures used were well below 100 ^{O}C.

3.4.4 Indium Antimonide (InSb)

The electrochemical preparation of Sb-In *alloys* for use as soft solders and anti-corrosion coatings has been the subject of several publications. The first mention of Sb-In alloy deposition was by Smart (1956), who claimed to have plated from aqueous solutions, hard, bright, and smooth corrosion-resistant coatings. In subsequent years, the alloy was plated using a variety of baths; sulphate (Ostroumov et al (1963)), chloride (Busch et al (1957)), fluoride/sulphate (Zaburdaeva & Kochegarov (1965)), tartrate/chloride (Bespalko & Vdovenko (1972)), and fluoroborate (Mogilov & Falicheva (1974)). Details of the composition of these baths can be found in the general review of Sb alloy plating by Sadana et al (1985).

In a succeeding publication (Sadana & Singh (1985)), the authors investigated the galvanostatic deposition of Sb-In alloys from baths comprising antimony trioxide and indium metal in a potassium citrate solution. Various temperatures, pHs, current densities, and bath compositions were explored. Although the effect of these various deposition conditions on the deposit composition was studied, the main criterion for assessing the quality of the films produced was their visual appearance, i.e. dull, bright, etc. Generally, applying the same terminology as Brenner (1963), the plating system could be described as 'regular', i.e. the nobler element Sb deposited preferentially. XRD confirmed the presence of the InSb compound, though the stoichiometry of the films indicated that In or Sb co-phases were also deposited.

Okubo (1988) obtained, using a similar citrate based bath at room temperature, amorphous deposits of Sb-In (1:1 atomic ratio). Subsequently, Ortega & Herrero (1989) attempted the potentiostatic direct co-deposition of compound InSb onto titanium substrates, from aqueous solutions at room temperature. The bath composition was 0.3 M citric acid, 0.033 M $InCl_3$, and 0.047 M $SbCl_3$. According to the XRD diffraction patterns of the as-grown deposits recorded, film stoichiometry varied with applied potential, under the range studied (-0.4 to -1.2 V vs. SCE). It was claimed that stoichiometric as-grown deposits of InSb were deposited between -0.9 and -1.0 V (vs. SCE). Unusually, no further characterisation of the material, such as determination of the material's band gap, was performed.

Another route that has been investigated for the deposition of InSb from aqueous electrolyte solutions (Mengoli et al (1991)) was the sequential deposition of Sb and In on Pt, followed by annealing. Sb layers were deposited from 0.6 M $SbCl_3$ / 1.6 M H_2SO_4 / 1.7 M HCl, whilst the In layers were formed from a bath of 0.3 M $InCl_3$, and 1 M KCl. XRD patterns indicated that the deposited In and Sb layers could be completely converted to InSb by annealing for 5-10 hrs at 185 ^{O}C in a nitrogen atmosphere.

The above authors used stripping voltammetry to characterise both annealed and as-grown films. A single anodic peak at -0.050 V was observed for the films that had been annealed, and this was attributed to the oxidation of InSb. The asgrown films exhibited two anodic

peaks at ~ –0.021 V and ~ -0.630 V (vs. SCE), due to the dissolution of the Sb and In layers respectively.

Kozlov et al (1997) continued the study of In deposition on Sb electrodes, with particular emphasis of determining the mechanism, and coefficient, of the diffusion of In into Sb. The formation of InSb at the indium/antimony interface was seen, not surprisingly, to increase with temperature and annealing time. Moreover, the diffusion coefficient of In (D ~10^{-20} m^2s^{-1}) is on average considerably higher than common semiconductors such as Si (D ~10^{-50} m^2s^{-1}).

Non-aqueous electrolyte solutions have been used to deposit Sb-In alloys. Styrkas et al (1964) studied the galvanostatic preparation of InSb on Pt and Sb coated quartz cathodes, from a bath of indium sulphate hydrate and antimony sulphate. Compositional data was obtained using amperometric titration. The quantity of Sb in the deposits formed was seen to increase with increasing temperature and current density. The composition of the deposits was 50 % In and 50 % Sb when the ratio of In : Sb in the electrolyte solution was 1 : 1. Poorly adherent layers were deposited, even at the highest temperature employed (160°C). Analysis of the XRD data obtained is difficult, due to the lack of data presented by the authors. Examination of the patterns given indicates that at 20 °C a mostly amorphous film is deposited, which crystallises on annealing (1 hr at 450 °C in hydrogen). These authors arrived at a very important conclusion, that even at 160 °C there are kinetic barriers to the formation of stoichiometric InSb. This is in contrast to Ortega & Herrero (1989), who claims to have deposited such material at room temperature. This difference in opinion is deliberated further in the discussion chapter of this thesis.

Kochegarov & Belitskaya (1971) obtained high quality (in terms of adhesion) Sb-In alloy deposits onto Cu substrates from a glycerol electrolyte solution containing $InCl_3$ 0.35 M, $K(SbO)C_4H_4O_6.1/2H_2O$ 0.05 M, and alkali 70 gl^{-1}, with cathodic current densities of 0.25-0.5 Acm^{-2}, at 85 °C. An increase in the current density, Sb precursor concentration, and solution stirring lead to an increase in the concentration of Sb in the deposits. XRD data was not reported.

Low temperature (50-60 ^{O}C) chloroindate melts have been used to generate InSb. Carpenter & Verbrugge (1994) primarily analysed the chemistry of indium in such systems, using $InCl_3$ and 1-methyl-3-ethylimidazolium chloride (ImCl), with $SbCl_3$ being employed thereafter for the co-deposition studies. The formation of the chloroindate melt is analogous to that of the chloroaluminates mentioned previously (section 3.4.3), i.e:

Reaction 3.20 $$ImCl + InCl_3 \leftrightarrows InCl_4^- + Im^+$$

In addition, the melt can also be either basic and acidic depending on the relative ratio of $InCl_3$ to ImCl. The authors used a slightly basic medium (45/55) in which the indium precursor was more soluble. Moreover, the viscosity of the more basic solutions, e.g. $InCl_3$: ImCl 2:3, was higher. The $SbCl_3$ precursor was readily soluble in the melt, probably due to its reaction with the basic melt's excess chloride to form $SbCl_4^-$.

By the author's admission, further investigation is needed to be able to fully describe the complex chemistry of this system, though reactions 3.21 to 3.24 are thought to play a significant role in the system's chemistry:

Reaction 3.21 $$In \leftrightarrows In(I) + e^-$$

Reaction 3.22 $$In \leftrightarrows In(III) + 3e^-$$

Reaction 3.23 $$2In + In(III) \leftrightarrows 3In(I)$$

Reaction 3.24 $$In(I) \leftrightarrows In(III) + 2e^-$$

Cyclic voltamograms suggested that, in the absence of the Sb precursor, when small negative overpotentials were applied to the system, a small amount of In was deposited via reduction to In (I), i.e. reaction 3.24 followed by reaction 3.21. At more negative overpotentials, In was able to deposit directly from In (III), reaction 3.22.

The stoichiometry of the deposited films was investigated using x-ray photoelectron spectroscopy (XPS). Approximately 67% of the antimony was in the form of InSb, whilst the rest was in the form of the metal or oxides. Voltammetry demonstrated that the

dominant chemistry depended on the applied potential, with Sb reduction dominating at more positive applied potentials, In at more negative potentials.

3.4.5 Gallium Antimonide (GaSb)

Sb-Ga alloys have been galvanostatically grown by Khamudkhanova et al (1973) from a glycerol solution onto various substrates. The nature of the substrate was seen to influence the potential at which the alloys deposited, and the quality (adhesion, visual appearance) of the coatings formed. A rise in temperature and agitation shifted the deposition potential, at the current density specified, to values that were more positive. 'Best' quality deposits were grown on Cu substrates at current densities of 2-2.5 $mAcm^{-2}$.

Paolucci et al (1990) studied the formation of GaSb by sequential potentiostatic deposition of Sb and Ga followed by annealing. The Sb layer was deposited on to Cu plated Ni substrates at –0.25 V (vs. SCE) using a solution comprising $SbCl_3$ 0.3 M, 1.6 M H_2SO_4, and 1.7 M HCl. To avoid the concurrent evolution of hydrogen, Ga was then deposited from an alkaline solution of 0.3 M $GaCl_3$ in 5 M KOH, at –1.85 V (vs. SCE). The order of deposition was chosen to avoid anodic dissolution of Ga. However, the sequence employed resulted in the loss of Sb by the evolution of $SbCl_3$. Stripping voltammetry of the annealed (100 ^{O}C for 4 hours under nitrogen) samples showed a single peak at –0.78 V, with an emerging shoulder peak that was not discussed. XRD characterisation confirmed the formation of GaSb. Reflections were also observed for excess Sb, though the absence of those for Ga indicated that it had all been converted to GaSb.

As a part of a study of the LPEE growth of AlGaSb, Zytkiewicz & Dobosz (1995) grew GaSb doped with Te and S onto GaSb (100) substrates. The deposition system utilises a high temperature melt of Ga and Sb, from which the material is galvanostatically deposited using current densities over a 5-10 Acm^{-2} range. The free carrier concentrations and mobilities of the materials were measured using a Hall probe. For example, those of n-type GaSb: Te were found to be 3×10^{17} cm^{-3} and 500 $cm^2V^{-1}s^{-1}$ respectively.

3.5 Ternary & Alloy Semiconductors

Particularly in the solar cell field, II-VI ternary (and above) semiconductors have received much attention due to an ability to modulate the material's band gap and lattice constant through compositional control. ED has been shown to enable such stoichiometric manipulation, and several systems have been in studied, especially those to replace CdTe as an absorber layer in the aforementioned devices. Amongst others, the list of materials so far deposited includes: $Hg_{(1-X)}Cd_XTe$ (Sahu (1989)), $CuInSe_2$ (Guillemoles et al (1996)), $Zn_{(1-X)}Cd_XTe$ (Natarajan et al (1994)), $CdSe_{(1-X)}Te_X$ (Bhattacharya et al (1985)), $Zn_{(1-X)}Fe_XS$ (Kashyout et al (1995)), and $CuIn_{(1-X)}Ga_XSe_2$ (Bhattacharya et al (1997)).

As the most extensively studied materials are $Hg_{(1-X)}Cd_XTe$ and $CuInSe_2$, these have been selected as examples for the following sections, and the reader is referred to the above references for further details of this ED application.

3.5.1 Mercury Cadmium Telluride ($Hg_{(1-X)}Cd_XTe$)

The composition of mercury cadmium telluride (MCT) is tuneable over a wide range. Consequently, the materials' electrical properties range from the semimetallic (X=0), to semiconducting (X > 0.15). Electrochemical methods have produced MCT compositions generating bandgaps ranging from HgTe (0.3 eV) to CdTe (1.45 eV), with applications ranging from IR devices to solar cells. However, in general, most research effort has been directed to Cd rich MCT for use in solar cells. Moreover, the use of Cd rich MCT as an absorber layer in solar cells, replacing CdTe, has been shown to be beneficial, and solar cells with efficiencies in excess of 9 % were achieved early on, Basol (1988). Primarily, this is considered due to the former material's bulk resistivity being lower, making the formation of ohmic contacts easier.

Standard protocols for MCT electrogeneration may be found in Basol (1992) and Morris et al (1991). As with Sahu (1989), these authors used a deposition method very similar to that for CdTe, but with the controlled addition of $HgCl_2$ into the electrolyte solution. Typically, annealing and chemical wet etching was then performed prior to contact evaporation. The latter procedure usually comprised a dip in acid solution ($H_2SO_4/K_2Cr_2O_7$) to produce a

Te (and Te oxide) rich surface, followed by a prolonged soak in hydrazine to remove surface oxides.

The composition of the ED films has been seen to be non-homogeneous. Further, depending on the composition of the plating solution, surface clusters rich in Hg have been mentioned in all of the above references. Indeed, Sahu (1992) reported the presence of HgTe, CdTe and MCT in the ED films.

Mori et al (1990) investigated the growth mechanism of MCT, and found it to be similar to CdTe, though with Hg offering nucleation sites to Te. The authors also demonstrated that HgTe growth is kinetically more sluggish than CdTe.

As with aqueous deposition regimes, non-aqueous methods (e.g. Colyer & Cocivera (1992)) are seen to suffer from a gradual decrease in the content of Hg in the films as the concentration of its solution precursor exhausts. Colyer & Cocivera (1992) deposited films with band gaps ranging from 1.03 to 1.32 eV from a propylene carbonate solution of Cd(II), HgI_2, and tri-n-butyl phosphine telluride. The film's Hg content decreased, and hence band gap increased, with prolonged use of the plating solution.

3.5.2 Copper Indium Diselenide ($CuInSe_2$)

In terms of its electrochemical preparation, the ternary compound $CuInSe_2$ has been most extensively studied. Indeed, PEC's with efficiencies >12 % have been routinely constructed with the ED material in solutions of I/I^-. Such devices have been seen to maintain their efficiencies over an extended time period (800 operational hrs), which is thought due to the formation of a surface layer of $CuInSe_3.Se^0$ that protects against photocorrosion.

The first attempt to electrodeposit the material was by Bhattacharya et al (1985), who used a SeO_2 based bath containing $InCl_3$ and CuCl complexed with triethanolamine and ammonia. However, the materials were characterised by poor crystallinity. Pottier & Maurin (1989) employed a citrate based bath, and found that the ratio of Cu/In in the deposits decreased as the applied potential was more negative, thereby conferring n or

p-type character to the films. They also found that the morphology of the deposits grown using this complexant were superior to those mentioned above. It was proposed that this effect was a consequence of a diffusion limited growth regime, coupled with a slow surface reaction. Molin et al (1994) studied the variation in composition with applied potential in more detail, and were able to obtain films with compositions corresponding to CuSe, Cu_3Se_2, $CuInSe_2$, and In doped $CuInSe_2$, at successively higher negative potentials. Annealing in air at 350 ^{O}C was seen to significantly improve the films' crystallinity, without adversely changing their composition.

In a subsequent paper, Molin & Dikusar (1994) used a rotating disk electrode (RDE) method to investigate the macrokinetics of the system's growth mechanisms in citrate baths. It was concluded that, independent of which compound was generated, the electrodeposition rate was determined by mixed kinetics (i.e. ion mass transfer complicated by a chemical reaction). Moreover, it was shown that the chemical reaction determining the common rate of electrodeposition was SeO_3^{2-} reduction by metallic copper, and that the diffusion stage of CuSe and Cu_3Se_2 formation was determined by the speed of the ion mass transfer of Cu(II).

Guillen & Herrero (1995) and Guillemoles et al (1996) et al investigated the effect of post-growth annealing procedures. Highly crystalline materials were obtained by annealing directly or sequentially deposited precursors at 400 ^{O}C. Annealing under a Se vapour was seen to increase the rate of recrystallisation. It was proposed that the improvement in device efficiency was a result of an increased grain size, and improved interface with the window layers employed.

Chapter 4

Experimental Techniques

4.1 Introduction

The experimental techniques described herein fall into two categories. The first, electrochemical techniques (section 4.2) refer to those methods employed in the generation of the semiconductor films, namely, potentiostatic and controlled voltage electrochemical deposition.

Into the second category fall those characterisation techniques (section 4.3) used in the investigation of the film's morphological, compositional and crystallographic attributes, i.e. Scanning Electron Microscopy (SEM), Energy Dispersive X-Ray analysis (EDX) and X-Ray Diffraction (XRD). The applicability of Glow Discharge Optical Emission Spectroscopy (GDOES) for compositional depth profiling of electrodeposited samples was also investigated.

4.2 Electrochemical Techniques

The same basic electrochemical cell configuration, figure 4.1, was used for both potentiostatic and controlled voltage electrochemical deposition, though controlled voltage electrolysis did not require the potentiostat.

For convenience, the following terminology is used in the thesis: V_{cell} represents the potential difference between the anode and cathode, and V_{ref} corresponds to that between the cathode and reference electrode. Thus in these terms, the difference between the controlled voltage and potentiostatic deposition was that the former required V_{cell} to be kept constant, whilst the latter V_{ref}.

A dual function EG & E Princeton Applied Research Model 362 scanning potentiostat was used for potentiostatic growth. Controlled potential depositions employed a Farnell Instruments Ltd 4T30-2 stabilised power supply. V_{cell}, V_{ref} and the cell current were

measured with either Keithley 179 TRMS or Fluke 8010A digital multi-meters. The details behind the fundamental operation of the control instrumentation electronics are outside the concern of this investigation, and the reader is directed to Sawyer et al (1995).

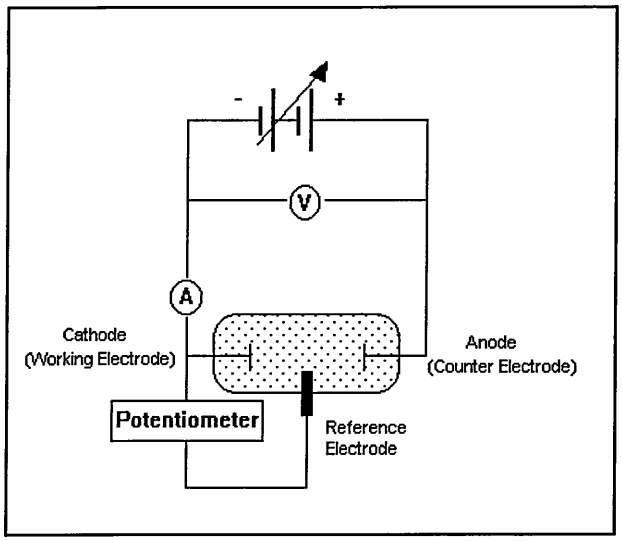

Figure 4.1 Schematic of electrodeposition experimental set up, after Harris (1987).

Polarisation (current vs. voltage) curves were obtained either by manually scanning V_{cell} (or V_{ref}) whilst recording the current produced, or by using the potentiostat's own scanning features together with an X-Y plotter.

Samples were grown on titanium plate (Johnson Matthey), copper (PCB RS catalogue), or glass coated with a 110 nm layer of 10 Ωcm^{-2} tin doped In_2O_3 (Indium Tin Oxide (ITO)). Each type of substrate had a particular cleaning procedure. Titanium substrates were polished with emery paper, degreased with acetone, etched in HCl/H_2SO_4 (Ortega and Herrero (1989)), and rinsed in Millipore water. One side of the Ti substrates was given a thin clear polymeric coating to prevent deposition. The copper substrates were prepared in a similar fashion, with the exception of the polishing and polymer coating steps. Finally, the ITO/glass substrates were prepared by ultrasonic cleansing in acetone, degreasing in a dichloromethane vapour, followed by rinsing in Millipore water. All substrates, before and after use, were gently dried under a nitrogen stream.

The reagents used were a minimum of 4 'nines' purity, as supplied by the Aldrich Chemical Co. Inc. or Johnson Matthey Fine Chemicals. Deposition studies were conducted at temperatures above and below 100 ^{O}C, and different cells were constructed for each temperature range.

4.2.1 'Low Temperature' (<100 ^{O}C) Deposition Studies

A single compartment three-electrode cell (cathode, anode, and reference electrode) was used for the low temperature studies, figure 4.2. The electrolyte solution was held in a 100 ml Pyrex glass beaker, placed upon a standard laboratory heating mantle that also provided stirring.

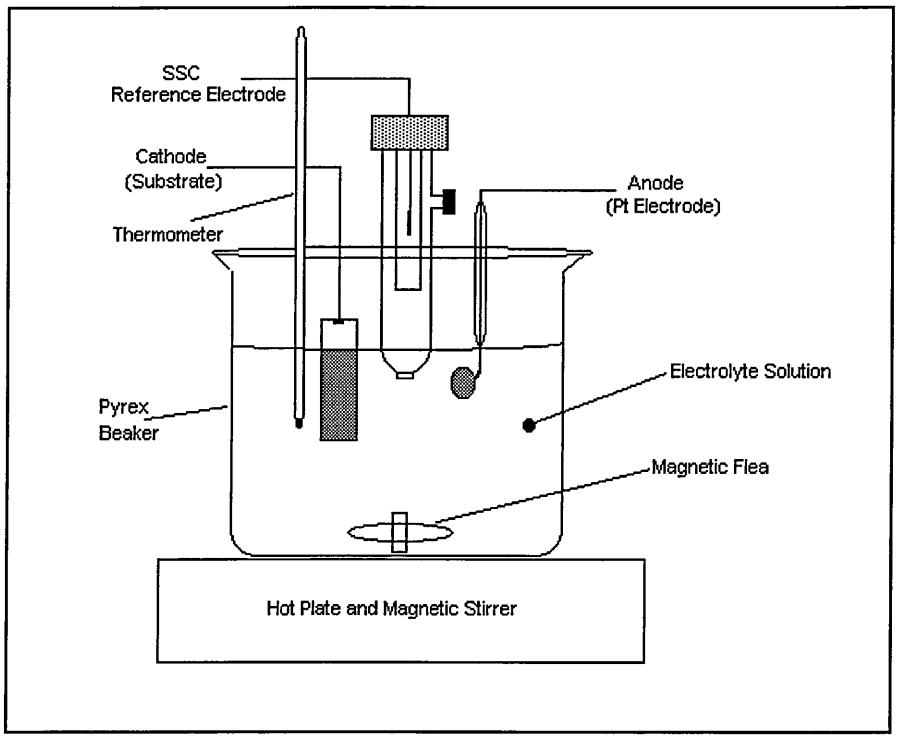

Figure 4.2 Diagram of electrolysis cell used for 'low' temperature (<100 ^{O}C) studies.

The anode was a large platinum gauze or disc, which had been cleaned by a quick dip in HCl, acetone, followed by a rinse with Millipore water. A silver-silver chloride (SSC) reference electrode (Russell Electrodes) was used, because of its well-known stability up to 100 ^{O}C (Russell catalogue, 1998).

4.2.2 'High temperature' (>100 ^{O}C) Deposition Studies

To prevent evaporation of the electrolyte solution, and to minimise water absorption, the high temperature experiments were performed in an enclosed vessel, figure 4.3. The anode was a glassy carbon rod (Russell pH), and a platinum grid was used as a 'quasi' reference electrode. Samples were electrodeposited on ITO/glass substrates. After carefully removing the plated substrates from the vessel, they were allowed to cool slightly before gently rinsing in clean water and drying under nitrogen. The organic solvents were bought pre-dried and suitable dry handling/storage techniques were used to maintain their dryness. Organic electrolyte solutions, unlike the aqueous ones, were discarded at the end of each day. A standard laboratory mantle supplied heating and stirring. The reaction vessel was placed upon a metal tray containing powdered graphite so as to ensure good thermal contact with the heating mantle. The temperature was closely monitored, and found stable within ± 2^{O}C.

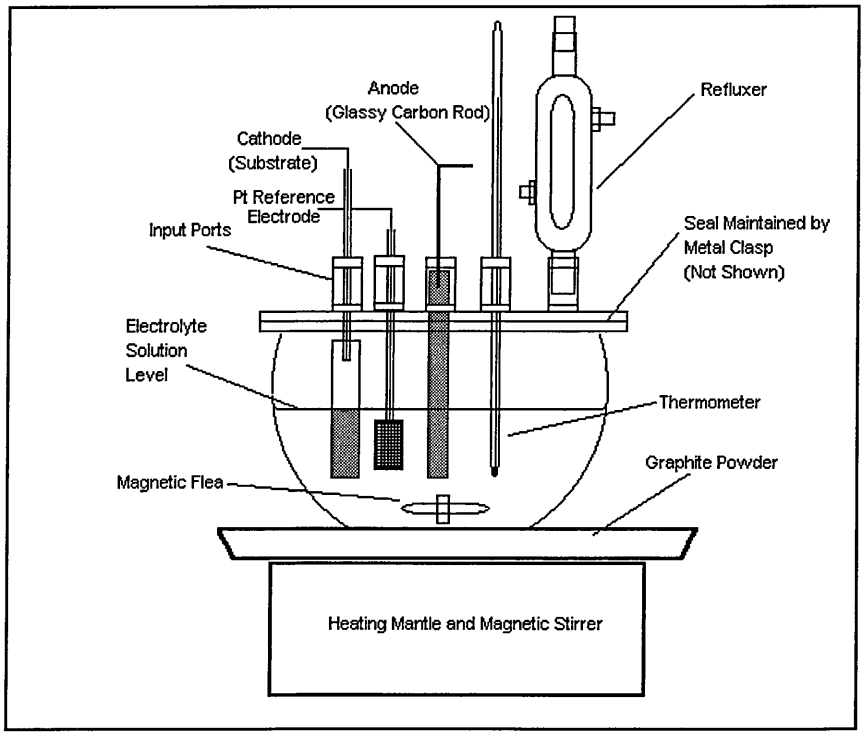

Figure 4.3 Diagram of electrolysis cell used for 'high' temperature (>100 ^{O}C) studies.

4.3 Characterisation Techniques

The nature of the techniques employed in the analysis of the electrodeposited films was such that minimal sample preparation was required. A selection of samples was annealed under nitrogen with a Biorad programmable contact furnace. Otherwise, after cutting into a suitable size, the samples at most required simply mounting onto aluminium stubs with silver dag paste for SEM/EDX analysis.

Fundamentally, both EDX and XRD techniques depend upon the production and detection of x-rays. A definition of x-rays is that they are short wavelength electromagnetic radiation of a wavelength between approximately 10^{-5} Å and 25 Å. They are created by the interaction of either charged particles (e.g. electrons) or photons (e.g. other x-rays) with matter. When electrons of sufficient energy are rapidly decelerated a portion of their kinetic energy is radiated away in all directions from the point of impact as x-rays. As not all the electrons are decelerated to the same extent, a polychromatic (continuous) spectrum of x-rays (Bremsstrahlung or 'braking radiation') is formed. X-ray spectra are characterised in the lower energy region by a short-wavelength limit (λ_{SWL}), which represents the maximum kinetic energy lost by the electrons to the production of x-rays. At progressively longer wavelengths, the intensity of the x-rays produced at first rapidly rises to a maximum and then decreases, with no sharp limit on the long wavelength side. Increasing the kinetic energy of the electrons, for example by adjusting the beam acceleration voltage of a SEM, raises the intensity of the x-rays at all wavelengths. Moreover, both the positions of the λ_{SWL} and intensity maximum are shifted to shorter wavelengths. The total x-ray energy emitted per second, proportional to the area underneath the spectra, is also dependent on the atomic number (Z) of the 'target', in addition to the rate at which the electrons strike the material under investigation (i.e. for SEM, the beam current). However, whilst the material of the target affects the intensity of the x-rays produced, the wavelength distribution of the heterochromatic spectra is not changed.

The analytical use of x-rays in EDX and XRD derives from the fact that above a critical electron beam energy, characteristic lines with sharp intensity maxima appear at certain wavelengths, superimposed on the continuous spectrum. These characteristic lines are a result of the ionisation of an atom by a high-energy electron (or x-ray) wherein an inner

shell electron is removed. Following the inner electron's removal, the atom returns to its ground state through a series of inter atomic shell electron transfers in which electrons from higher energy shells refill the vacancies that have arisen in lower energy shells. Consequently, energy is emitted from the atom in the form of a x-ray, or an Auger electron. For example, a $K\alpha_1$ x-ray is generated when an atom's K shell is ionised and the ejected K shell electron replaced by one from the L_3 shell. Further x-rays may be emitted when the L_3 shell itself is refilled by another electron from a higher energy shell such as the M shell. If an electron from the M refills the K shell, then a $K\beta$ x-ray is emitted, though this line tends to have a lower intensity because the probability of this transition is lower. The energy (i.e. x-ray wavelength) released from each transition is dependent upon the difference in potential energy of the different atomic shells, which are characteristic of each element. Hence, elements can be identified from the x-rays they emit.

4.3.1 Scanning Electron Microscopy (SEM)

The operation of a SEM derives from the interaction of a focused electron beam with the specimen, figure 4.4. Such interactions result in the emission of electrons and/or photons from (or through) the specimen's surface. Subsequently, a large fraction of the electrons emitted are collected by appropriate detectors, whose output is used to modulate the brightness of a cathode ray tube (CRT). The CRT's raster rate is synchronised with that of the electron beam. Hence, if the raster rate of the incident electron beam is low with respect to that of the CRT, a magnified image is generated, Bindell (1992).

The incident beam is formed from electrons that have been thermionically emitted from a tungsten filament heated to incandescence (~ 2850 K) by the passing of a so-called 'filament current'. These electrons are accelerated by a potential (10-30 keV) along an evacuated (10^{-6} mbar) microscope column containing a series of apertures and magnetic lenses that focus and demagnify an image of the beam ('gun-crossover') onto a spot as small as 1-2 nm on the sample's surface. Another series of magnetic coils (deflectors) rasters this spot across the sample.

Upon arrival, the electron beam interacts with the specimen via electrostatic forces, in a pear-shaped region extending approximately 1 μm into the sample. Secondary electrons

(SE), with energies <50 eV, are ejected when primary electrons from the incident beam inelastically collide with atoms within the specimen. This requires that the energy transferred from the primary electrons be in excess of the material's work function. Consequently, those SE's generated deep inside the material do not escape the surface as, following further inelastic collisions, they do not possess sufficient energy.

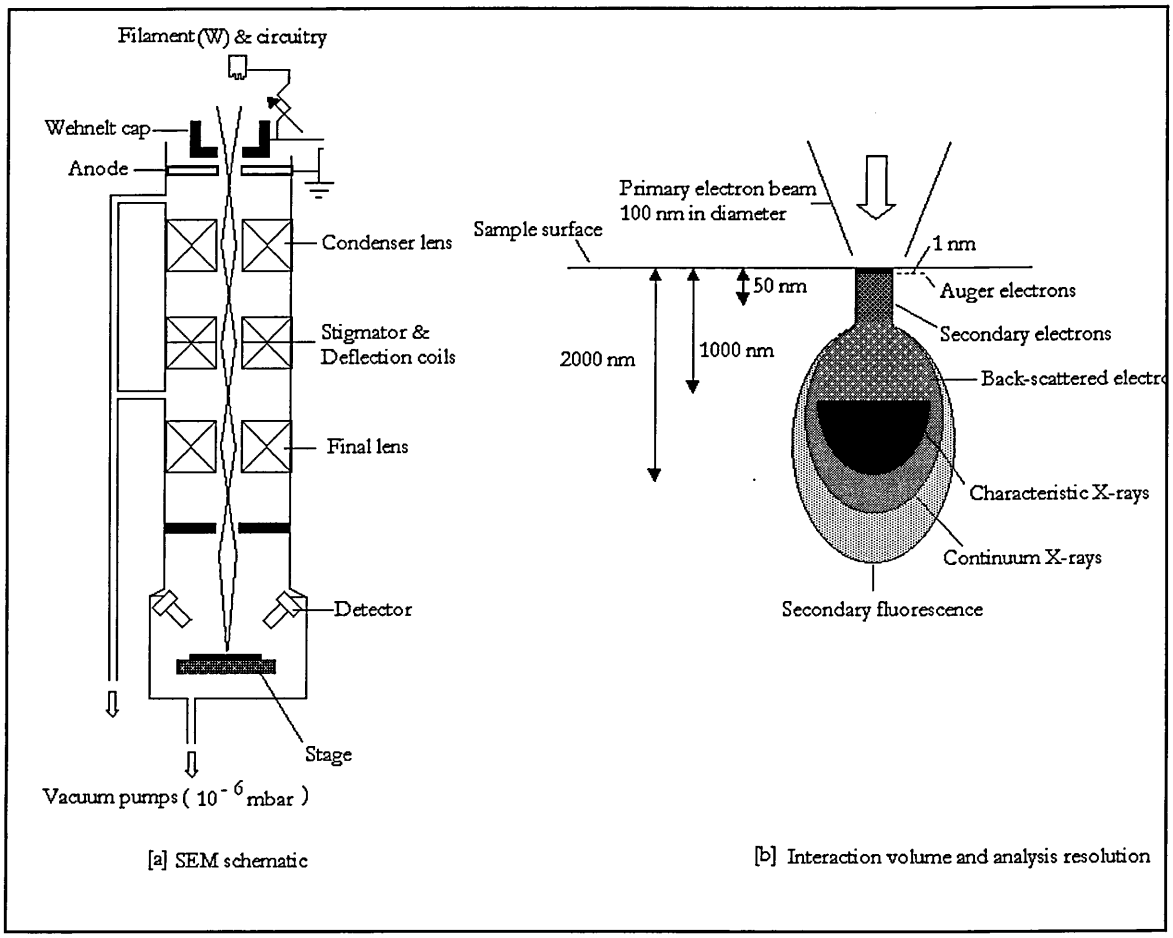

Figure 4.4 [a] Schematic of SEM instrument, and [b] diagram of the interaction volume Ives (1995).

Escaping SE's are attracted to a positively biased grid attached to a scintillator/photomultiplier that is positioned at an acute angle to the specimen surface. Surface topography is observed because those SE's 'shadowed' from the detector grid are not attracted to the detector. Hence, the lack of signal from such areas produces a dark area on the CRT.

Primary beam electrons that undergo elastic collisions are scattered. Such 'back scattered electrons' (BSE) escape the sample surface with energies comparable to those of the primary electrons (> 50 eV to keV's). A proportion of these BSE's however will not escape, but rather go on to generate SE's. As the probability of producing BSE's is related to the material's atomic number (Z), elemental contrast may be achieved. Specifically, when the beam is scanned over an area of high Z, the resultant image is brighter than that produced by a low Z area. Obviously, the greater the difference in Z between the regions, the greater the contrast.

A consequence of the different emissions from the illuminated sample surface, is the existence of three fundamental imaging modes for the SEM. These modes are based upon which detected signal, SE or BSE, is forming the image presented on the instrument's display. In addition, the operator may also form images by combining the SE and BSE output signals with the aid of the instrument's software. X-rays emitted from the sample, section 4.3.2, are also used in a third fundamental imaging mode.

Operationally, the resolution, magnification and depth of field of the SEM are controlled by a number of inter-related factors. When the electron beam leaves the condenser lenses, it diverges. The amount of beam divergence is dependent upon the aperture size, and the condenser lens current. If the condenser lens current is increased, the focal length of the beam is decreased, and the beam's divergence increased. This results in a smaller spot size, and greater image resolution. In addition, increasing the beam's acceleration voltage can also reduce the spot-size, as the beam's wavelength is shortened. However, the SE emission process is weak. Thus, if the spot size is very small, the SE signal generated becomes comparable to that of the controlling electronics' noise, yielding a poor image. Consequently, high magnification images are inherently noisy. Such limitations can be overcome by increasing the beam's current intensity, though only to a small extent if charging of the sample's surface is to be avoided. Ultimately, the final lens, whose distance to the sample is referred to as the 'working distance', focuses the beam. The working distance, together with the final aperture's size, determines the SEM's depth of field by controlling the angle of beam convergence.

The equipment used for analytical scanning electron microscopy was a Philips XL40 series ASEM with a Link eXL EDX and back-scatter facility.

4.3.2 Energy Dispersive X-ray Analysis (EDX)

As discussed in section 4.1, characteristic x-rays are produced following inelastic collisions of electrons (accelerated above a certain critical ionisation energy E_C) with sample atoms. This routinely facilitates the identification of elements to a minimum detection limit (MDL) of 0.1 % wt.

Qualitative, and quantitative (generally 4-5 % wt.), EDX analysis is however limited by; (a) poor energy resolution of EDX peaks, and (b) low peak to background ratios, a consequence of high background noise derived from Bremsstrahlung radiation. Moreover, unlike X-ray photoelectron spectroscopy, EDX provides elemental not chemical information. These disadvantages are balanced by the speed of the technique's data collection and analysis, Russ (1984) and Geiss (1992).

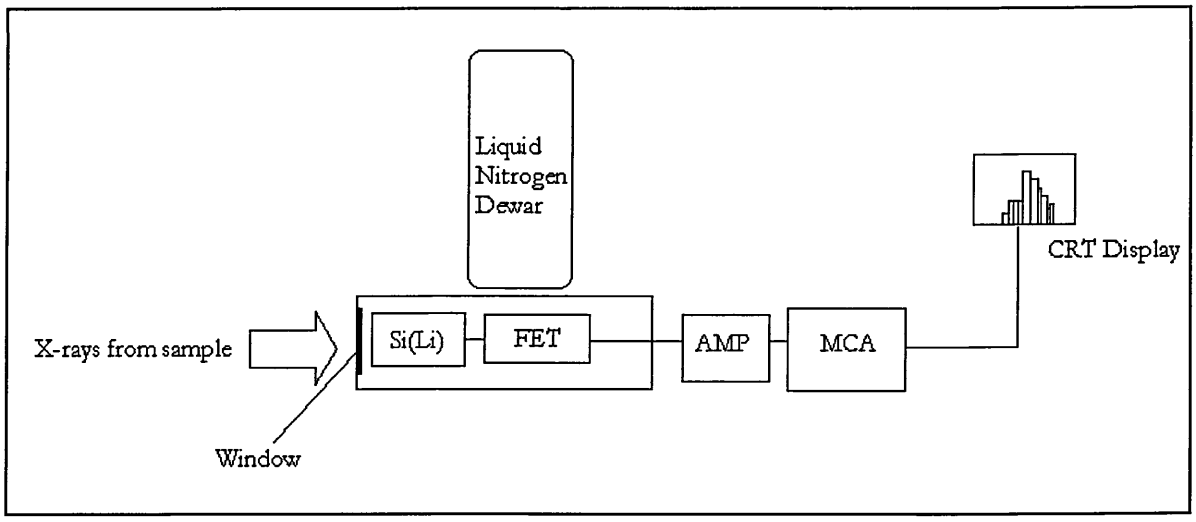

Figure 4.5 Schematic of EDX instrumental system.

The EDX instrumental system is essentially built around a p-i-n Si(Li) field effect transistor (FET) whose active area is between 10 mm^2 to 20 mm^2, figure 4.5. X-rays enter the system

through a Be window, whose function is to shield the detector against the vacuum of the SEM optic column. Having passed through the p-type end of the FET, the x-rays enter its intrinsic region where Si atoms are ionised through the photoelectric effect. Eventually this process leads to the production of electron-hole pairs, for example a 6.4 keV x-ray absorbed by the Si will produce 1684 electron-hole pairs. The resultant signal is amplified and put through an analogue to digital converter, to then form the input for a multichannel analyser (MCA). The resultant signal pulses entering the MCA are then used to charge a capacitor, whose discharge time is measured against an address clock operating at 50 MHz. The time to discharge the capacitor is proportional to pulse amplitude, and hence x-ray energy. By timing the capacitor's discharge, the 50 MHz clock is able to allocate a binary number to one of the 1024 channels typically used by MCA's, incrementing the number previously collected by one. Finally, the results from the MCA are then displayed on a CRT as an energy histogram[1].

At high-count rates, pulse pile up can occur, should the capacitor not have enough time to fully discharge. The resultant 'sun peaks' can be minimised through electronic pulse rejection ('dead time') and by setting the count rate at a suitable level (5000 cps).

Another operational consideration concerns the choice of the incident electron beam's accelerating voltage (E_O). Since the electron range in the material determines the x-ray generation volume, it is desirable for thin films to use accelerating voltages only slightly above that of the critical ionisation energy of the x-rays of interest. For example, to analyse a nm thick film of Cu on Si with reference to the Cu Kα line (E_C=8.98 keV) an E_O near 10 keV would be suitable. However, with thicker films it becomes more important to employ a greater level of E_O (in the previous example 20-25 keV for an μm thick sample) to maximise x-ray production and thereby overcome x-ray absorption effects.

---

[1] EDX area image mapping is achieved using the detector array output set to monitor a pre-selected x-ray energy to modulate the brightness of a CRT.

4.3.3 X-Ray Diffraction

The basis of XRD (Cullity (1978) & Skoog (1979)) relies on the principle that the regular arrangement of atoms in a crystal forms a three-dimensional diffraction grating for electromagnetic waves (x-rays) whose wavelength are of the same order as the length of the inter-atomic plane spacing ('d-spacing'), figure 4.6.

Diffraction itself is a consequence of the phase relationships of waves that have been scattered, whereby waves constructively or destructively interfere depending on whether they are in phase or out of phase respectively. By definition two or more waves may be said to be in phase when their respective electric-field vectors have the same magnitude and direction at the same instant at any point measured along the direction of propagation of the wave.

Bragg's law of diffraction provides a simple geometrical basis (figure 4.6) for determining the conditions under which diffraction occurs, by considering the relative differences in path lengths travelled by the x-rays' wavefronts[2]. If an x-ray beam is incident on an atomic array of d-spacing (d), and is diffracted by a Bragg angle θ by atoms **K** and **L** lying in parallel planes, then the difference in their wavefronts' path lengths is given by,

Equation 4.1 $$ML + LN = d\sin\theta + d\sin\theta$$

Two waves will be in phase when path lengths travelled by their wavefronts are equal, or only differ by a whole number n of wavelengths λ. This, 'Bragg condition', can be now written,

Equation 4.2 $$n\lambda = 2d\sin\theta$$

---

[2] Wavefronts are imaginary surfaces perpendicular to the direction of the wave's propagation.

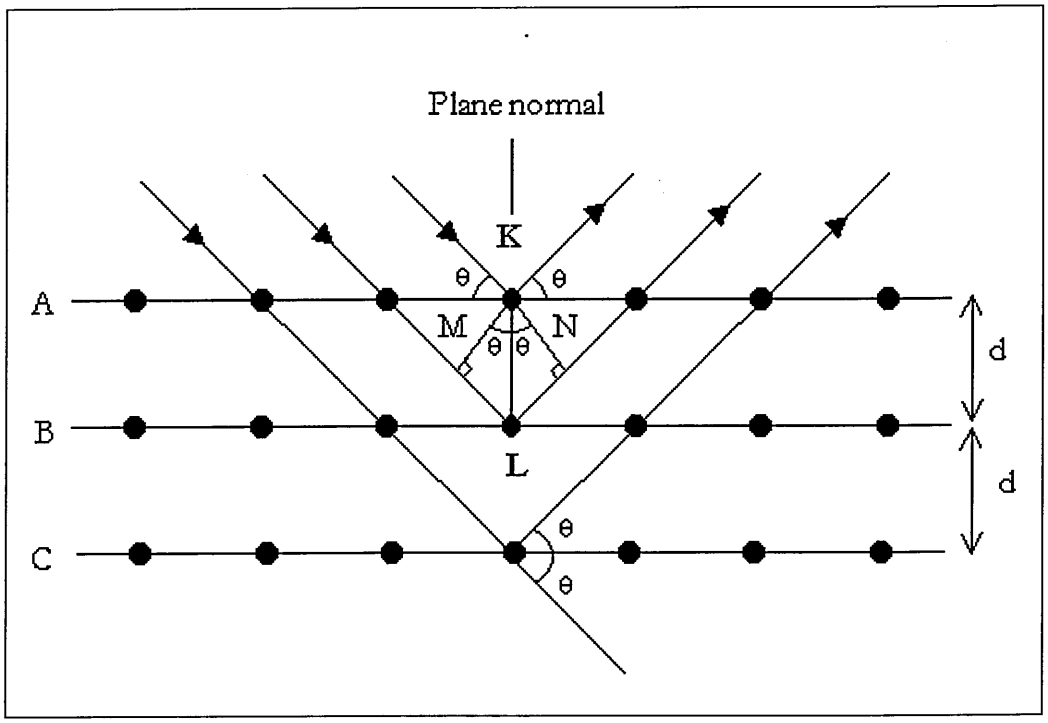

Figure 4.6 Graphical representation of x-ray diffraction by a crystal, with respect to the geometrical basis for Bragg's law.

Hence, by varying the angle θ, the Bragg conditions can be satisfied for the different d-spacings of the various crystal planes in polycrystalline materials. Plotting the angular positions and intensities of the resultant diffraction peaks produce a pattern characteristic of the sample.

Several instrumental systems have been designed to take advantage of the above principles[3], which are distinguished by their x-ray detection method (photographic or electronic counter) and 'geometry', the latter term relating to how the detector and sample are orientated to each other. For the purpose of this investigation an instrument based on Bragg-Brentano geometry was employed, figure 4.7; Philips PW1710 horizontal axis diffractometer (counter movement arranged in the vertical plane) utilising Cu Kα radiation (λ = 1.542 Å). In this system, the x-rays are produced from the impact of electrons on a

[3] Laue, Debye-Scherer, Seeman-Bohlin and Guinier

water-cooled copper target in an evacuated X-ray 'tube'. These x-rays are filtered through a Ni filter to remove the Cu Kβ emission line, thereby providing basically monochromatic radiation. After passing through a collimator, the x-rays diverge from the source to irradiate a planar sample supported in the centre of the apparatus on a table that can rotate about its axis through an angle θ. Diffracted x-rays then pass through another collimator to fall upon a motor driven, constant angular velocity counter that is mechanically coupled to the sample stage in order to ensure rotation about the same axis through an angle of 2θ (to maintain the Bragg condition). The output from the electronic counter is plotted in the form of 2θ vs. intensity. The resultant diffraction patterns (diffractograms for the instrument used) are then identified using reference data from the Joint Committee on Powder Diffraction Standards.

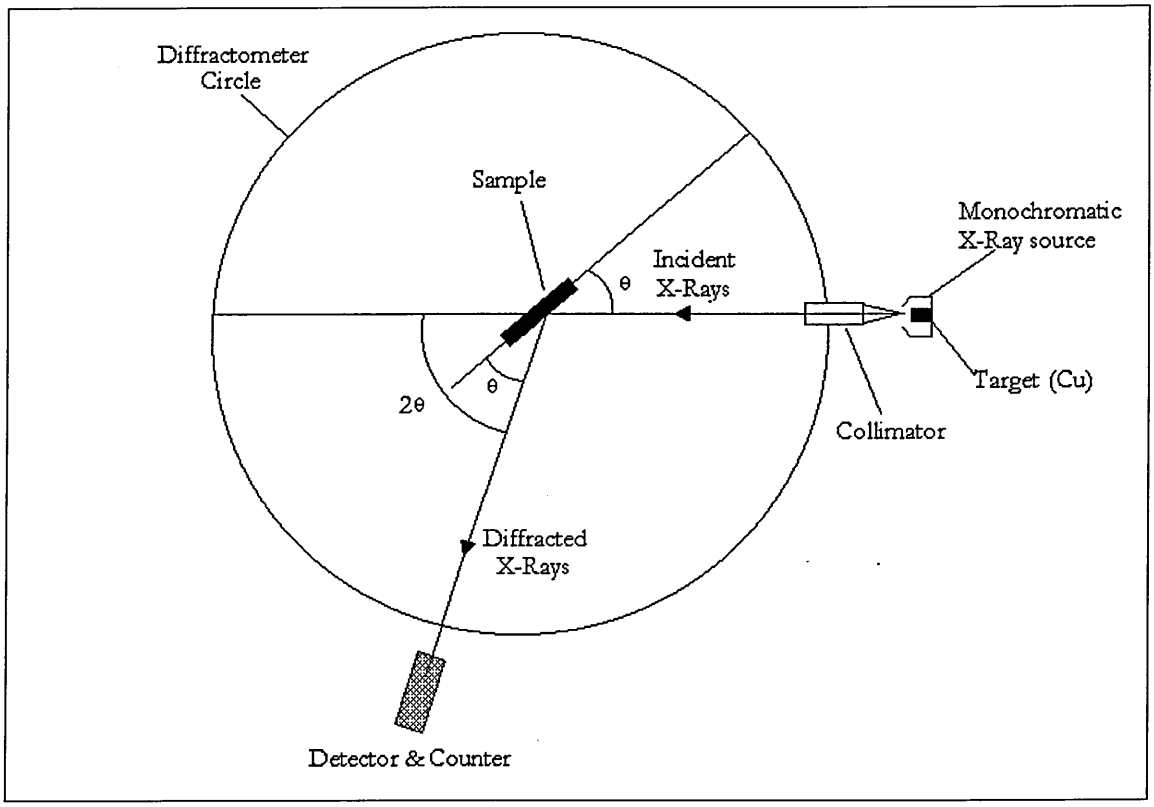

Figure 4.7 X-ray diffractometer instrument schematic.

Analysis of the full width at half maximum (FWHM) of the individual x-ray peaks can also yield information regarding film grain size. This is best understood by recalling that destructive interference is also a consequence of the periodicity of the atom's

arrangements. Recalling figure 4.6, if the path difference between the x-rays scattered by the top two planes are only slightly different from an integral number of wavelengths, then the plane scattering a ray out of phase with the x-ray from the first plane will lie deep within the crystal. If the crystal is so small that this plane does not exist, complete cancellation does not occur, resulting in a diffracted x–ray of smaller amplitude. This coupled to the fact that some of the incident rays will make angles slightly different from the Bragg angle, leads to line broadening[4].

It can be shown (Cullity (1978)) that particle (grains < 1000 Å) size may be estimated by using the FWHM in the Scherrer equation;

Equation 4.3

$$B = \frac{0.9\lambda}{t\cos\theta}$$

Where B is the particle size broadening, t the diameter of the particle, with the rest of the terms having their usual meaning. Above grain sizes of 1000 Å, the line broadening due to particle size falls to zero.

The presence of strain in the material under investigation is reflected in the diffractograms as changes in peak position (uniform strain) and peak width (non-uniform strain). This can be investigated by the following method. A diffraction pattern over a wide range of 2θ is run so as to select a suitable single peak for investigation. Then, the motion of the sample stage and detector is de-coupled. A series of analysis runs are performed over the range of 2θ covering the peak chosen, with the sample orientation slightly varied. If strain is present, the position of the diffraction peak maxima slightly shifts, figure 4.8 reflecting the subtle range of d-spacing values available because of the material's strain. The intensity of the peaks also decreases, as the orientations of the sample and detector move away from those that satisfy the Bragg condition for the plane under investigation.

---

[4] In addition, the x-ray source is not truly monochromatic as it contains some elements of the Kβ and continuous spectrum.

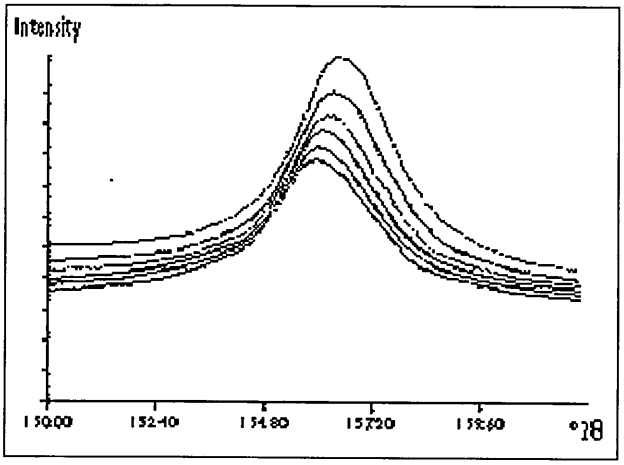

Figure 4.1 Example of the results of an XRD experiment to determine sample strain (Philips Instruments Web Site). Note, values for the $\Delta\theta$ displacement between traces were not supplied with the illustration presented above.

The existence of preferred orientation, where the grains in a polycrystalline material are to a certain extent lined up, can be seen in the diffractograms. This is because these 'texture' effects cause radical disagreement between those relative intensity[5] values given in the reference data and those recorded from the sample.

4.3.4 Glow Discharge Optical Emission Spectroscopy (GDOES)

The GDOES analytical technique may be readily explained through describing the instrument's operation, ((Dharmadasa et al (1995 (b)) & Ives (1995)). The instrument used in this study was a LECO GDS-750 QDP glow discharge spectrophotometer.

The analysis chamber of the GDOES instrument is a Grimm type glow discharge lamp, figure 4.9. This consists of a cylindrical anode (4 mm or 8 mm in diameter) onto which the sample (cathode) is presented. The outside of the anode cylinder is then vacuum pumped to ~1 Pa, and then back filled to ~100 Pa with high-purity argon ('working') gas. A voltage (500 V to 1500 V) is then applied across the electrodes producing a current between

[5] Intensities are reported in reference data as percentages, with the strongest peak representing 100 %.

20 mA to 200 mA. Consequently, argon atoms in the working gas are ionised, and accelerated to an area on the cathode where 90 % of the applied potential is dropped ('dark space'). The impact of these atoms leads to transference of kinetic energy to the atoms in the sample, according to the conservation of momentum principle. As a result, neutral atoms are ejected (sputtered) from the sample surface, together with secondary electrons (SE). Typically, this sputtering rate is between 10 to 100 nm per second, at an operating temperature of 30 ^{O}C and of power 10 W to 25 W for semiconductor samples, Dharmadasa et al (1995(b)).

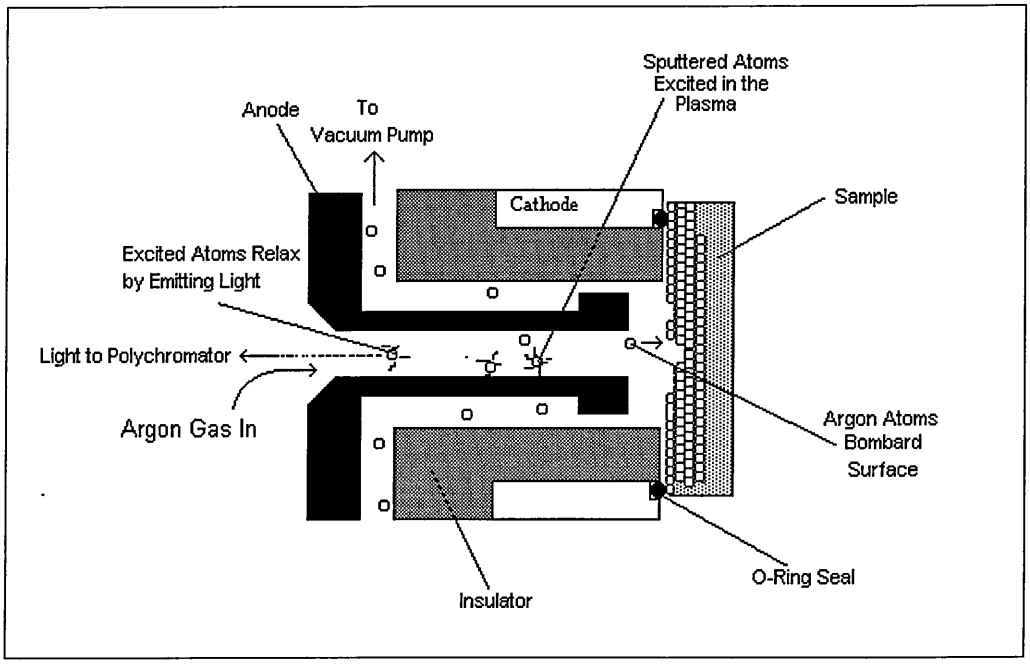

Figure 4.8 Schematic of Grimm type glow discharge plasma source.

After accelerating rapidly away from the cathode, the SE help maintain the plasma through ionising argon atoms in the working gas. Photons are also emitted following the collision of the neutral sputtered atoms with SE and ionised argon atoms. This light subsequently leaves the discharge tube through a transparent window to pass through a lens and collimator. The beam of light (optical image) then narrows after passing through a thin entrance slit, to then enter a Rowland circle polychromator. This polychromator divides up the beam of light into its constituent wavelengths with a concave diffraction grating. After exiting the polychromator through narrow slits, the component wavelengths are then analysed by a series of up to 22 simultaneous operating photomultiplier tubes.

GDOES has several attractive features for determining compositions down to ppm levels, (Ives (1995)). It requires little or no sample preparation. Compositional depth processing is readily achieved because the nature of the technique involves the removal of successive layers of the sample's surface. In addition, as only removed atoms are analysed, matrix effects are minimised. Finally, the excitation and emission layer is thin, minimising self-absorption and giving a linear relationship between intensity and concentration, with sharp emission lines.

Chapter 5

Electrodeposition of InSb from Aqueous Electrolyte Solutions

5.1 Introduction

In plating terminology, this part of the study investigated the electrodeposition of InSb from an aqueous halide/citric acid bath. That is, the electrolyte solution comprised $InCl_3$, $SbCl_3$ and citric acid. As reviewed in section 3.4.4, it was from such a bath that, after conducting a limited study, Ortega & Herrero (1989) claimed the direct potentiostatic deposition of InSb on to Ti substrates. To shed light on some of the general considerations in employing such a bath, it is useful at this point to review some of the system's pertinent solution chemistry. Likewise, it is also appropriate to refer to those empirical rules available to the electroplater.

$InCl_3$ dissolves in acidic solution to form $[In(H_2O)_6]^{3+}$. Under increasingly alkaline conditions (> pH 4) its hydrolysis occurs, as represented by reaction 5.1. This eventually leads to the precipitation of $In(OH)_3$, unless the formation of soluble complexes with other ligands predominates.

Reaction 5.1 $$[In(H_2O)_6]^{3+}(aq) + H_2O \rightarrow [In(H_2O)_5OH]^{2+}(aq) + H_3O^+(aq)$$

In contrast, $SbCl_3$ in acid solutions freely undergoes hydrolysis, which results in the formation of insoluble oxychlorides, reaction 5.2, Mackay & Mackay (1989).

Reaction 5.2 $$SbCl_3 \xrightarrow{H_2O} SbO^+Cl^- \xrightarrow{More\cdot H_2O} Sb_4O_5Cl_2$$

Given that the standard equilibrium potential (E^O) for the Sb/SbO^+ couple is more electropositive than that of the In/In^{3+}, reactions 5.3 & 5.4, the former may be described as the 'noble' species.

Reaction 5.3 $$SbO^+ + 2H^+ + 3e^- \rightarrow Sb + H_2O \qquad E^O = +0.212\ V$$

Reaction 5.4 $In^{3+} + 3e^- \rightarrow In$ $E^O = -0.338$ V

In general, for co-deposition to occur the respective reduction potentials of the components of the alloy, or compound, should be within 0.2 V of each other, section 2.3.1. Therefore, it can be concluded that, under acidic conditions, the electrodeposition of InSb from simple salt solutions is complicated by the low solubility of antimony oxychlorides, and by the large difference (0.550 V) in the precursor's E^O. However, as demonstrated by Sadana & Singh (1985), Sb-In alloys can be electrodeposited if the electrolyte contains a citric acid complexant, which is due to two main factors.

Firstly, soluble citric acid complexes of antimony form in solution. The exact nature of these complexes has yet to be fully resolved[1], and as Cattarin et al (1994) state in their paper regarding As-Sb alloy deposition 'open questions remain on the number of protons released by the citric acid, and on whether the Sb(III) ion involved in the complex contains oxygen'. The second factor is that the reduction of the antimony–complex species occurs at a more 'base' (i.e. negative) potential than SbO^+. Additionally, the reduction potential of the In species is shifted in the negative direction, although to a lesser extent than the Sb species. Consequently, the potentials at which the two species are reduced are brought closer together, Sadana & Singh (1985).

However, to deposit Sb-In alloys it is still necessary to deposit under limiting current conditions, which is implied by Ortega & Herrero (1989) when they state that 'the formation of InSb is diffusion limited'. Hence, a significant amount of indium is only found in films that have been electrodeposited at potentials where the reduction of the antimony-species has reached its maximum rate, because of mass transport limitations. Such limiting current conditions are associated with a well-known disadvantage, in that it commonly results in the formation of nodular films of small grain size. Such deposits may appear 'powdery' to the naked eye, West (1971). Obviously, this is of concern because the operation of a semiconductor device based on electrodeposited InSb ideally should have a well-defined crystallographic structure of large grain size.

---

[1] Indeed, the complicated nature of citrate based electrolyte solutions is demonstrated by Green et al's (1998) modelling of the citrate-Cu-Ni plating bath. They demonstrate that at pH 3 there are up to eight species in solution.

A final point of interest is that the deposition of Sb from its halide has been seen to lead to the incorporation of significant amounts of the halide in the deposit, Mellor (1929). In the case of the deposition of elemental Sb films, this leads to the formation of an 'explosive' amorphous form of the element, that crystallises with the liberation of the entrapped halogen.

In consideration of the above, the morphology of the films was investigated using a Scanning Electron Microscope (SEM), and Energy Dispersive X-ray analysis was employed to determine if Cl was present in the films grown. In addition, the conditions used by the aforementioned authors were further investigated, together with the electrodeposition of InSb on to indium tin oxide coated glass (ITO) and copper substrates.

5.2 Characterisation of the Substrate Materials using X-Ray Diffraction (XRD)

A suitable range of diffraction angles (2θ) for the diffractometer's detector to scan through, was determined by using Bragg's law to analyse the standard[2] Powder Diffraction File (PDF) 'card' for InSb (PDF no. 6-208). Accordingly, it was determined that the planes yielding the most intense diffracted x-ray signals would be observed by scanning the detector through angles corresponding to 15 (or 20) to 80^{O} 2θ. In addition, the PDF cards for InSb, In, Sb and the substrate materials were analysed to identify those planes whose lattice (d-) spacing (dÅ) were similar enough to cause the generation of overlapping diffraction peaks, namely, those values within approximately 0.01 Å of each other, as illustrated in table 5.1.

[2] Those standards set by the Joint Committee on Powder Diffraction Standards (JCPDS).

Sb		PDF	(35-732)	InSb		PDF	(6-208)	In		PDF	(5-642)	Ti		PDF	(5-682)	In_2O_3		PDF	(6-416)
dÅ	Int	hkl	2θ	dÅ	Int	hkl	2θ	dÅ	Int	hkl	2θ	dÅ	Int	hkl	2θ	dÅ	Int	hkl	2θ
3.75	25.00	003	23.69	3.74	100.00	111	23.77												
				2.29	80.00	220	39.31	2.30	36.00	110	39.17								
				1.62	16.00	400	56.78	1.63	12.00	200	56.59								
1.55	15.00	024	59.60													1.53	25.00	025	60.68
1.32	67.00	122	71.53	1.32	25.00	422	71.22					1.33	16.00	103	70.66				
				1.25	12.00	511	76.30					1.25	16.00	112	76.30				
				1.15	10.00	440	84.53	1.15	5.00	220	84.17								

Table 5.1 Summary of XRD PDF card data, showing examples of major peaks whose lattice spacings are approximately equal.

Key:

dÅ, d-spacing

Int, relative intensity

hkl, Miller indices of plane

2θ, angle between incident and diffracted X-rays.

From table 5.1, it can be seen that, in the absence of preferred orientation effects, the aforementioned crystal phases may be readily identified despite the presence of overlapping peaks. For example, although the dÅ values for the (003) Sb and (111) InSb planes are only 0.01 Å apart, their respective relative intensities (100 % & 25 %) are disparate enough to enable identification. Thus, if two phases are present, the relative intensity of a peak at this particular 2θ will be larger than that expected from an individual phase's PDF data.

Before experimental confirmation, with the exception of the (glass)/ITO and Cu substrates, the particular PDF cards selected were those used by Sadana & Singh (1985) and Ortega & Herrero (1989). The XRD patterns of the substrates were collected, figures 5.1 to 5.3, and their structures found to be hexagonal Ti and cubic Cu and cubic In_2O_3.

In the case of the (glass)/ITO substrate[3], the PDF data for cubic In_2O_3 (PDF card 6-416) was found to be the closest matching. Nevertheless, the XRD pattern of the ITO substrate had dÅ values that were in the most part approximately 0.02 to 0.03 Å greater than that of the standard PDF data. However, this may be explained by recalling that the substrate is glass coated with Sn doped In_2O_3, the Sn atoms having substituted into indium sites and bound to interstitial oxygen, Davis (1993). Obviously, this will affect the inter-atomic spacing between the various ITO crystal planes.

Another characteristic feature of the XRD pattern for ITO is the presence of an amorphous background that includes a 'hump' feature covering approximately an area of 15 ^{O} to 39^{O} 2θ. These features are a result of the diffractometer's x-rays being able to penetrate the 110 nm thick ITO layer to the amorphous glass beneath.

[3] For brevity, the '(glass)/ITO substrate' henceforth will be referred to as the 'ITO substrate'.

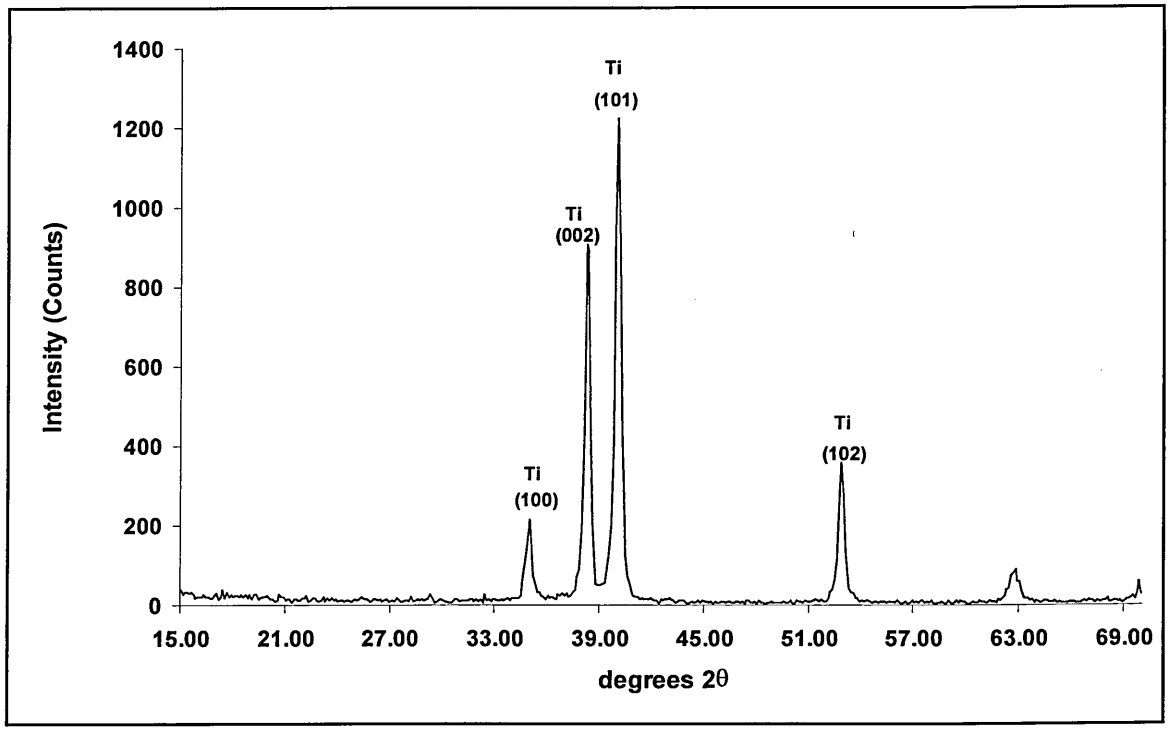

Figure 5.1 XRD pattern of the titanium substrate.

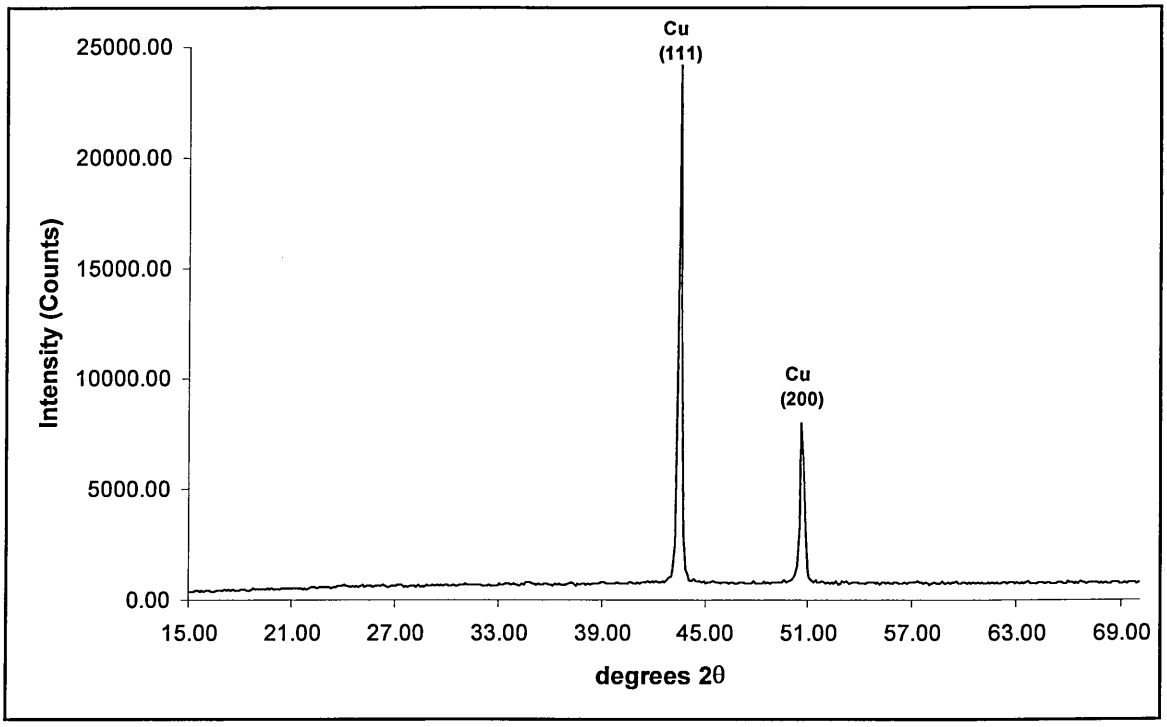

Figure 5.2 XRD pattern of the copper substrate.

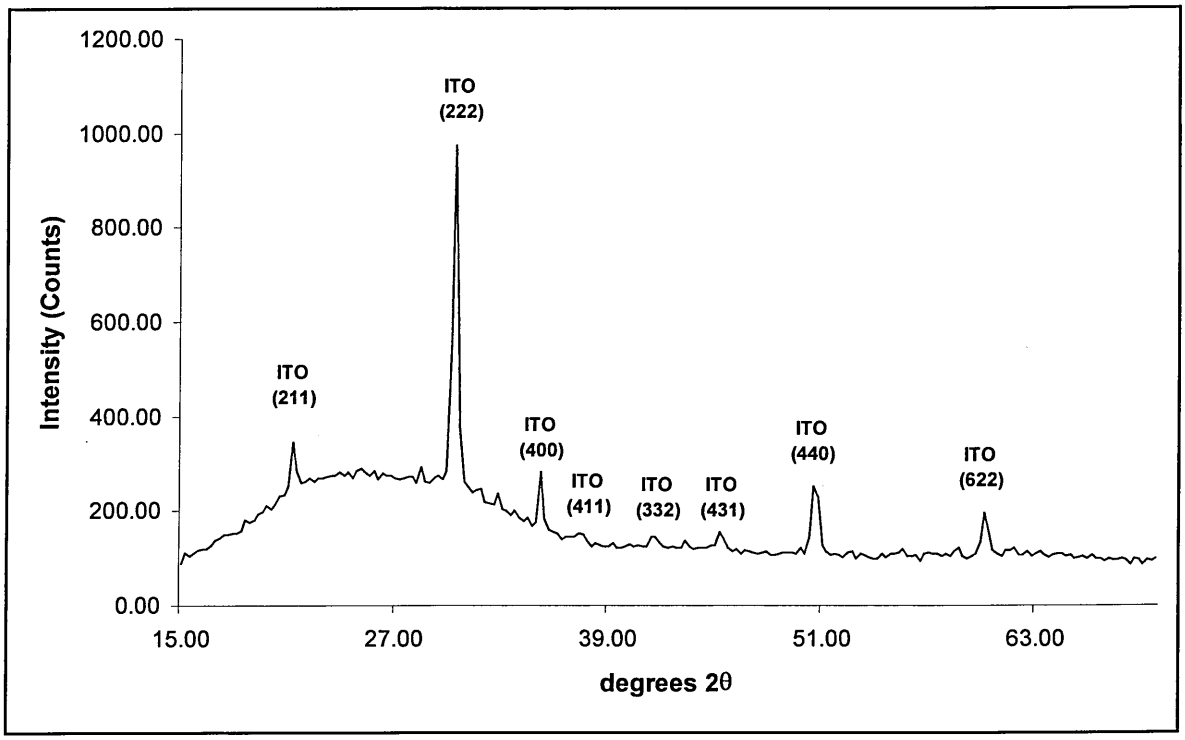

Figure 5.3 XRD pattern of the ITO substrate.

5.3 Study of the Electrochemical Deposition of InSb on to Titanium Substrates

5.3.1 Selection of the Deposition Conditions for Investigation

As mentioned in section 5.1, Ortega & Herrero (1989) reported the direct potentiostatic co-deposition of InSb from an aqueous electrolyte. The conditions (table 5.2) used by these authors were employed as a starting point in this study, which itself began with the collection of voltammograms.

Voltammograms (figure 5.4) were obtained by manually ramping the voltage to the Ti cathode, whilst recording the current produced and the potential (V_{ref}) of the cathode with respect to a silver-silver chloride reference electrode (SSC). In addition, the area of the substrate where electrolysis had taken place was measured, so that current density values could be calculated. The pH of the citric acid solution was measured before and after the addition of $InCl_3$ & $SbCl_3$, and found to be pH 1.6 & pH 1.49 respectively, which indicated the formation of metal-citric acid complexes.

Bath Composition	$InCl_3$ (0.033 mol dm^{-3}), $SbCl_3$(0.047 mol dm^{-3}),Citric acid (0.3 mol dm^{-3})
Temperature	Room Temperature
Bath stirring	None
Substrate	Titanium

Table 5.2 Conditions employed by Ortega & Hererro (1989) for the deposition of InSb.

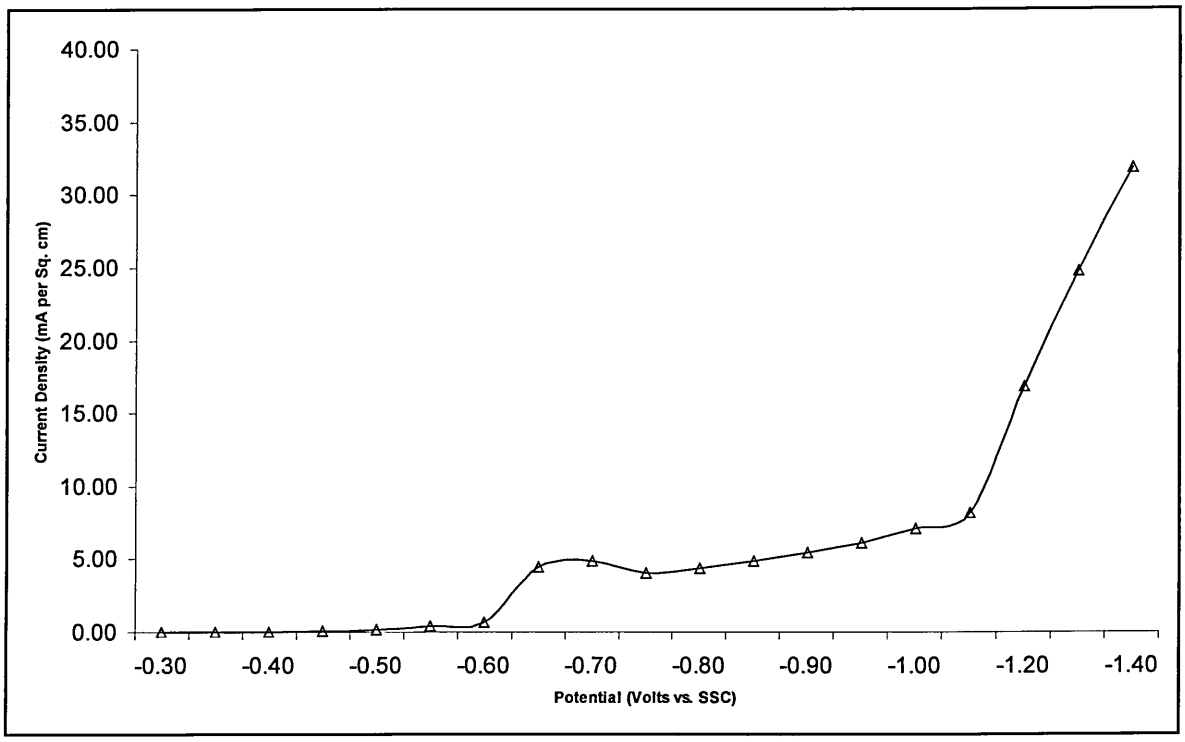

Figure 5.4 Voltammogram obtained at a stationary titanium electrode in an unstirred solution of 0.037 mol dm^{-3} $InCl_3$, 0.047 mol dm^{-3} $SbCl_3$ and 0.3 mol dm^{-3} citric acid.

No significant current density (>0.09 mA cm^{-2}) was seen much below -0.50 V. Further, at potentials more negative than –1.20 V, gas was seen streaming off both the anode and cathode electrodes. Therefore, the 'window' of growth potentials available to this

investigation was -0.50 V & -1.20 V. Consequently, a series of samples were grown within this region[4].

5.3.2 Growth and Characterisation of the Electrodeposited Films

In general, black powdery films formed on the dull grey metallic substrate. Electrodeposits whose XRD patterns indicated a large Sb content presented a characteristic bluish tinge. Adhesion to the substrate was to seen to be a function of growth potential. Films deposited at potentials more electronegative than -0.90 V had a tendency to be only weakly adherent to the basis metal. Indeed, insoluble particles from the films could be dislodged from the deposit with a gentle stream of Millipore water. Nevertheless, a sufficient amount of the electrodeposited films adhered to the substrate for XRD analysis to be performed.

As reported by Ortega & Herrero (1989), the XRD analysis (table 5.3) demonstrated a dependence of film composition on deposition potential, as detailed below. Nevertheless, the formation of crystalline stoichiometric InSb, free of In or Sb co-phases, could not be reproduced. Instead, a mostly amorphous material formed within the potential window where the authors reported the formation of stoichiometric InSb, i.e. in the potential window between that where the formation of Sb 'rich' and In 'rich' InSb occurred. The following paragraphs give in detail the results of these growth experiments.

Electrodeposition at potentials between –0.50 V and –0.70 V produced films whose XRD analysis implied they consisted of hexagonal close packed (hcp) Sb (PDF card 35-732), free of crystalline In or InSb phases, figure 5.5. Intense reflections from the Sb (012), (104), (110) and (202) planes were observed in accordance with the appropriate PDF data. Due to its overlap with the Ti (101) substrate peak, it can be seen that the relative intensity of the Sb (104) peak[5] is greater than expected from the PDF card of hcp Sb. EDX (figure 5.6) revealed the presence of a small amount of In (and a chloride) in the films deposited.

---

[4] Samples were also grown at –1.30 & -1.40 V, but films' XRD analysis was not possible, as they did not adhere to the substrate.

[5] For clarity, only the identity of planes which yield the strongest reflections (cf. their PDF cards) are indicated in the XRD pattern figures. When present, the identities of overlapping peaks are documented in the body of the text.

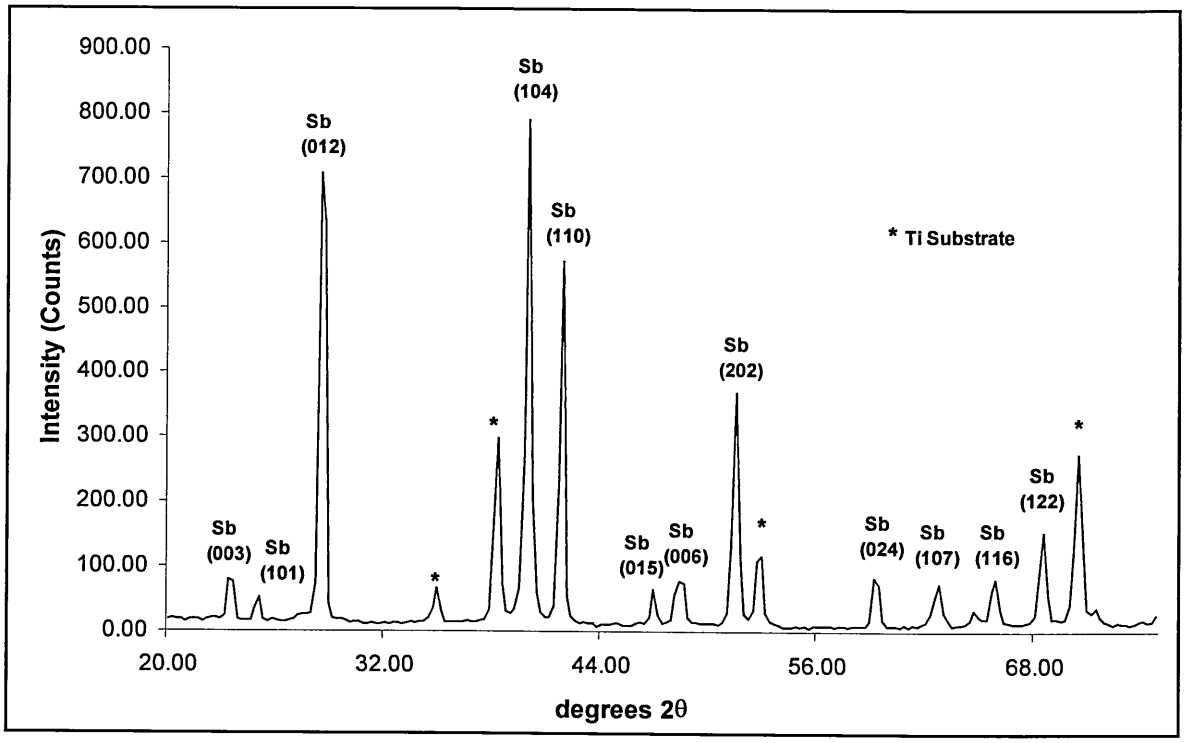

Figure 5.5 XRD pattern of a film deposited at -0.60 V (vs SSC).

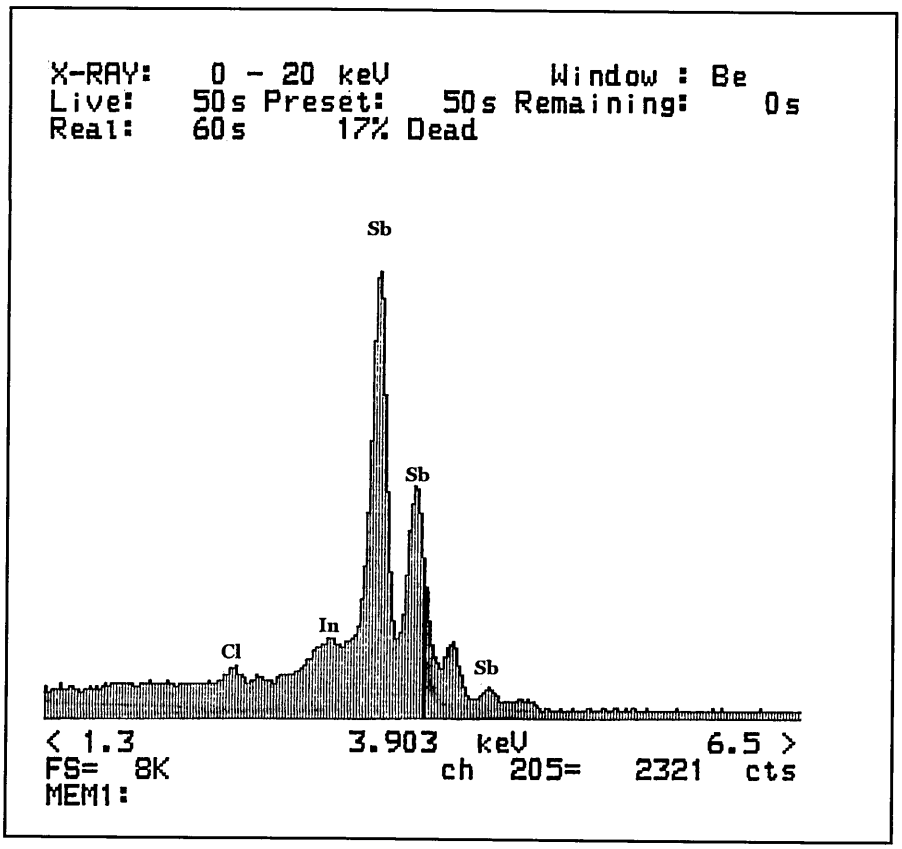

Figure 5.6 EDX spectra of a film deposited at -0.60 V (vs. SSC).

Films deposited at -0.75 V yielded mostly amorphous patterns, though there was still an indication of the formation of a hcp Sb, with smaller amount of face centred cubic (fcc) InSb (PDF card no. 6-208).

XRD patterns of electrodeposits grown at potentials between -0.80 V and -0.90 V comprised mostly of two large amorphous 'humps'. However, some planes of hcp Sb and hexagonal Ti from which the strongest reflections originate could be distinguished, figure 5.7. These films were annealed mildly at 250 ^{O}C for 45 minutes under nitrogen. The annealed samples' XRD patterns were found to show the formation of both fcc InSb and hcp Sb co-phases, figure 5.8, and these patterns included strong reflections from the fcc InSb (111), (220), (311), (331) and (422) planes, together with a weaker reflection from the InSb (400) plane. SEM micrograms of the as-grown and annealed samples indicated that re-crystallisation had occurred. 'As grown' samples presented a uniform collection of multifaceted growth features, 1 to 3 μm in size, figure 5.9. In the case of the annealed samples, the edges of the aforementioned features had rounded to a significant extent, taking on a nodular appearance similar to those grown at potentials that are more negative, figure 5.10. Although descriptions of the morphological properties of annealed III-V films have not been published, Qi et al (1996) have reported a similar phenomenon whilst studying the post-growth annealing of CdTe.

At deposition potentials between –0.95 and –1.20V, the formation of an admixture of three co-phases was observed; fcc InSb, hcp Sb and tetragonal In (PDF card no. 5-642), figures 5.11 and 5.12. This is the first report of the deposition of this admixture from aqueous electrolytes.

In relation to the deposition potential, the relative proportions of the crystalline Sb and In phases changed rapidly in a matter of 0.10 V according to their XRD patterns' In and Sb peak's intensities. This is most clearly illustrated when comparing the intensities of the Sb (012) and In (101) peaks in figures 5.11 & 5.12. Here, it is demonstrated that the relative proportion of crystalline Sb in the films diminished when the films are grown at potentials that are more negative. Conversely, the intensity of the In peak increases, though this increase did not appear as dramatic.

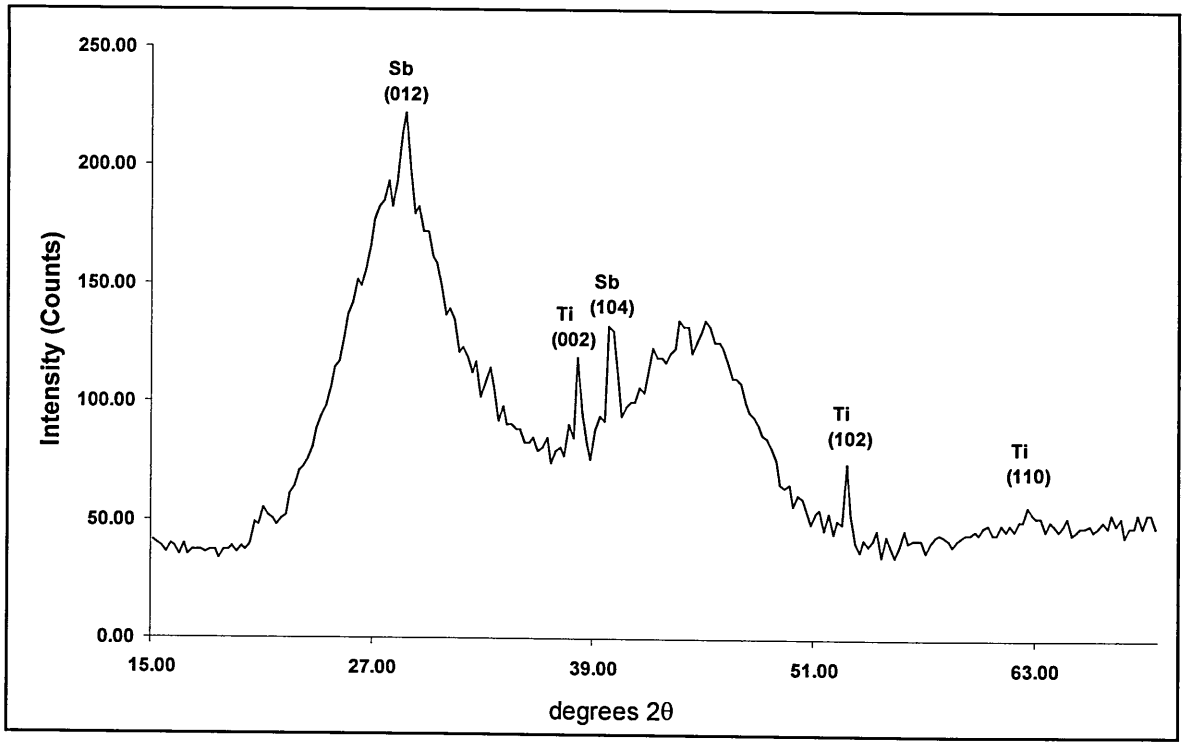

Figure 5.7 XRD pattern of an as-grown film deposited at -0.80 V (vs. SSC).

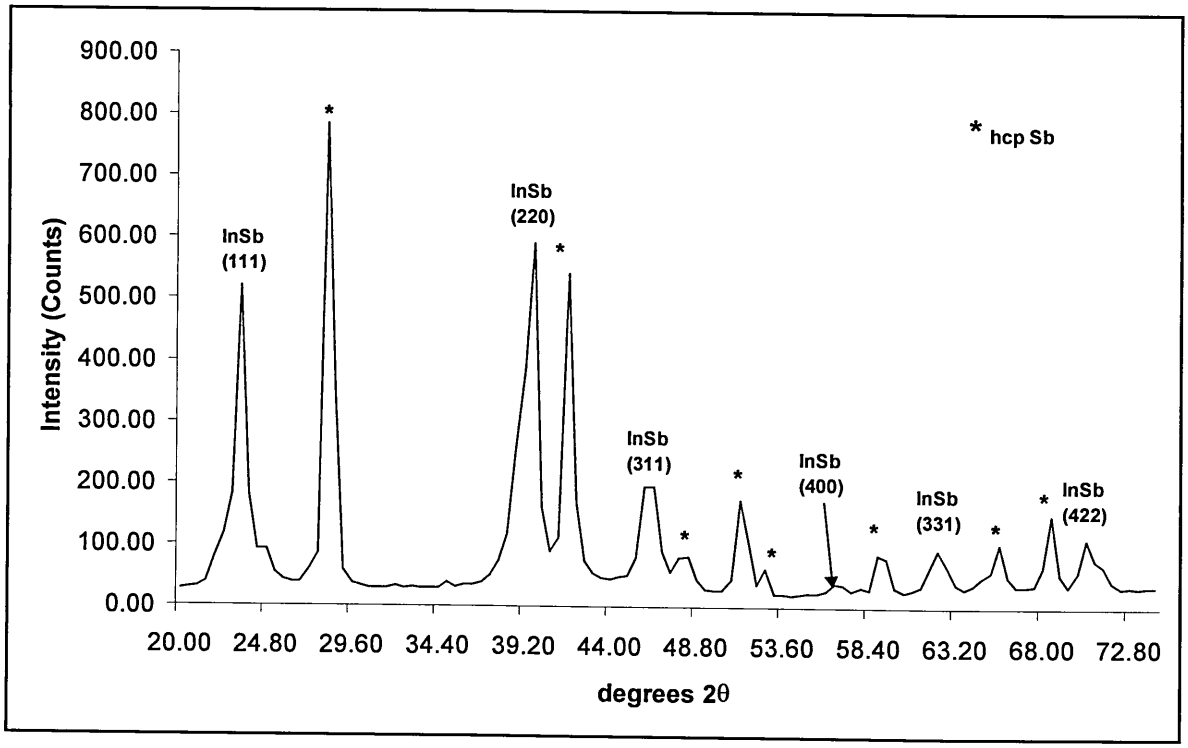

Figure 5.8 XRD pattern of a film deposited at -0.80 V (vs. SSC), annealed under nitrogen at 250 ^{O}C for 45 minutes.

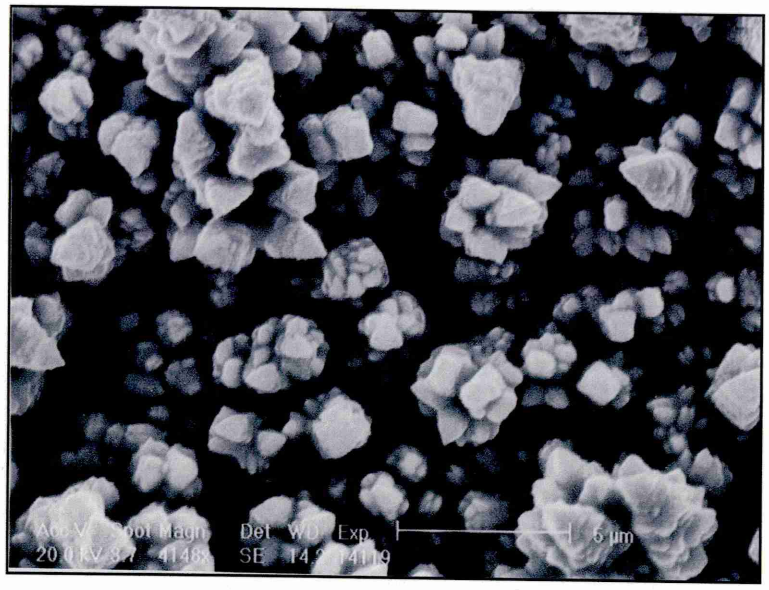

Figure 5.9 SEM microgram (× 4,148) of an as-grown film deposited at -0.75 V (vs. SSC).

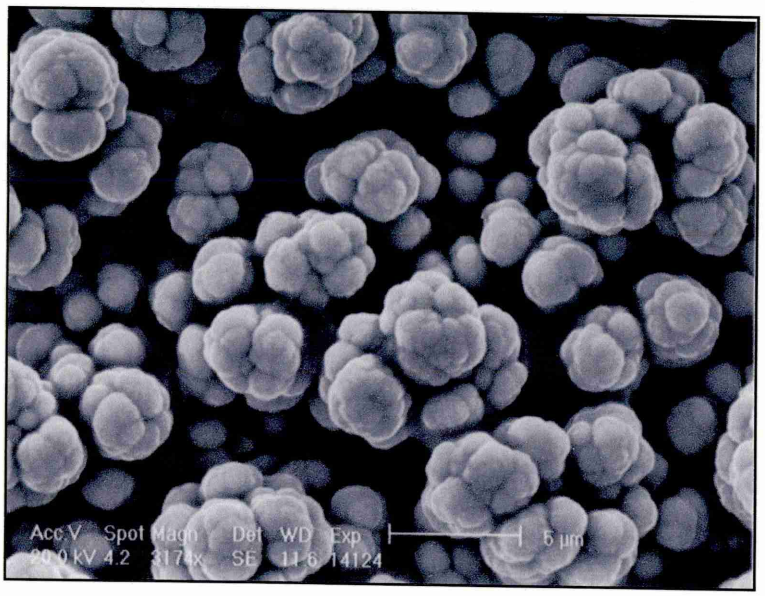

Figure 5.10 SEM microgram (× 4,148) of an annealed film deposited at -0.75 V (vs. SSC).

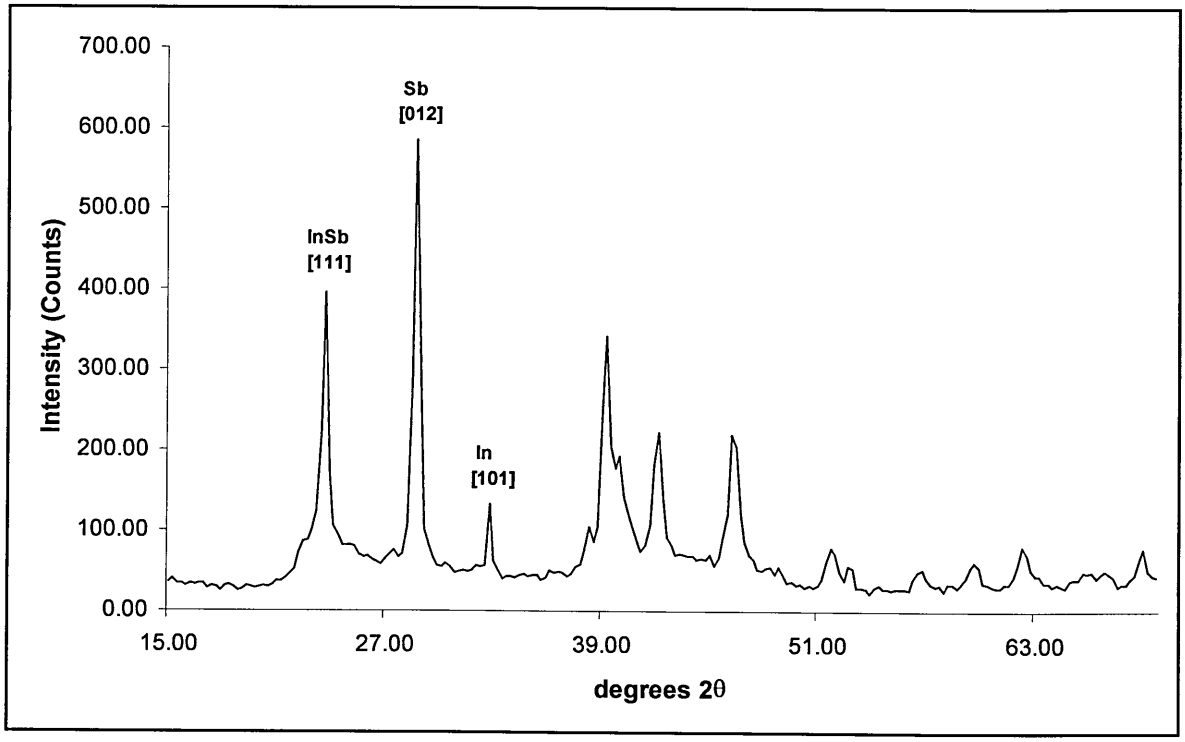

Figure 5.11 XRD pattern of a film deposited at -1.15 V (vs. SSC), illustrating the strongest reflections from planes of the tetragonal In, hcp Sb and fcc InSb phases.

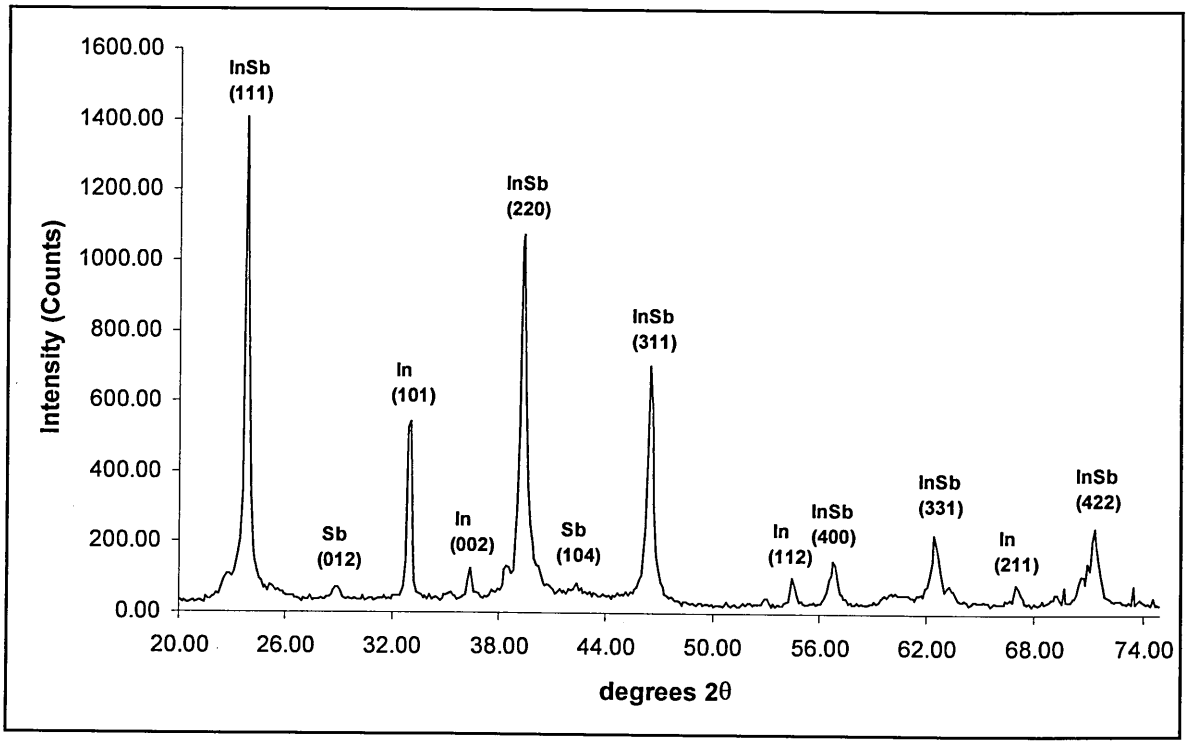

Figure 5.12 XRD pattern of a three-phase film deposited at -1.20 V (vs. SSC).

A general feature of the deposition experiments was that the current density would rapidly rise to a maximum in less than approximately 2 seconds, thereafter remaining stable for up to 30 minutes. This indicates the rapid establishment of a stable double layer. In addition, the maximum current density achieved rose with increasingly negative deposition potentials, table 5.3. All growths were repeated at least once, and EDX determined that the presence of a chloride was common to all the deposits.

Deposition Potential (Volts vs. SSC)	Maximum Current Density mA per sq. cm	Results Of XRD Analysis
-0.50	2.27	Sb
-0.55	2.29	Sb
-0.60	2.72	Sb
-0.65	2.79	Sb
-0.70	2.89	Sb
-0.75	3.10	Sb & (InSb)
-0.80	4.12	Amorphous film
-0.85	4.40	Amorphous film
-0.90	8.22	Amorphous film
-0.95	6.55	In, InSb & Sb
-1.00	15.73	In, InSb & Sb
-1.05	18.50	In, InSb & Sb
-1.10	16.68	In, InSb & Sb
-1.20	23.12	In, InSb & (Sb)

Table 5.3 Summary of the XRD analysis of films electrodeposited onto Ti substrates under the conditions described in the text.

Growth of InSb under the above conditions was first proposed to be diffusion limited by Sadana (Sadana & Singh (1985)). The results of this study provide indirect proof of this proposition. Figure 5.13 illustrates this by overlaying the results of the XRD analysis on to the voltammogram discussed in section 5.4.1. From this it can be seen that a sharp rise in current density at approximately -0.55 V is then followed by an almost flat, more gradual rise starting at approximately -0.75 V. The latter increase is characterised by the generation of progressively more amorphous deposits, which presumably have a small quantity of In incorporated into them. Such behaviour is demonstrative of alloy deposition under limiting current conditions (figure 2.3, section 2.2.4).

The contribution of the antimony-complex species' reduction to the current density can be seen when comparing voltammograms (figure 5.14) obtained from plating baths prepared with different concentrations of $SbCl_3$ (0.002 mol dm^{-3} & 0.047 mol dm^{-3}). Likewise, these also illustrated a rise in current density that occurred at base potentials that may be

associated with the reduction of the In species from the solution. Thereafter, an increase in potential resulted in the current density beginning to rise steeply as a consequence of the evolution of hydrogen and possibly SbH_3.

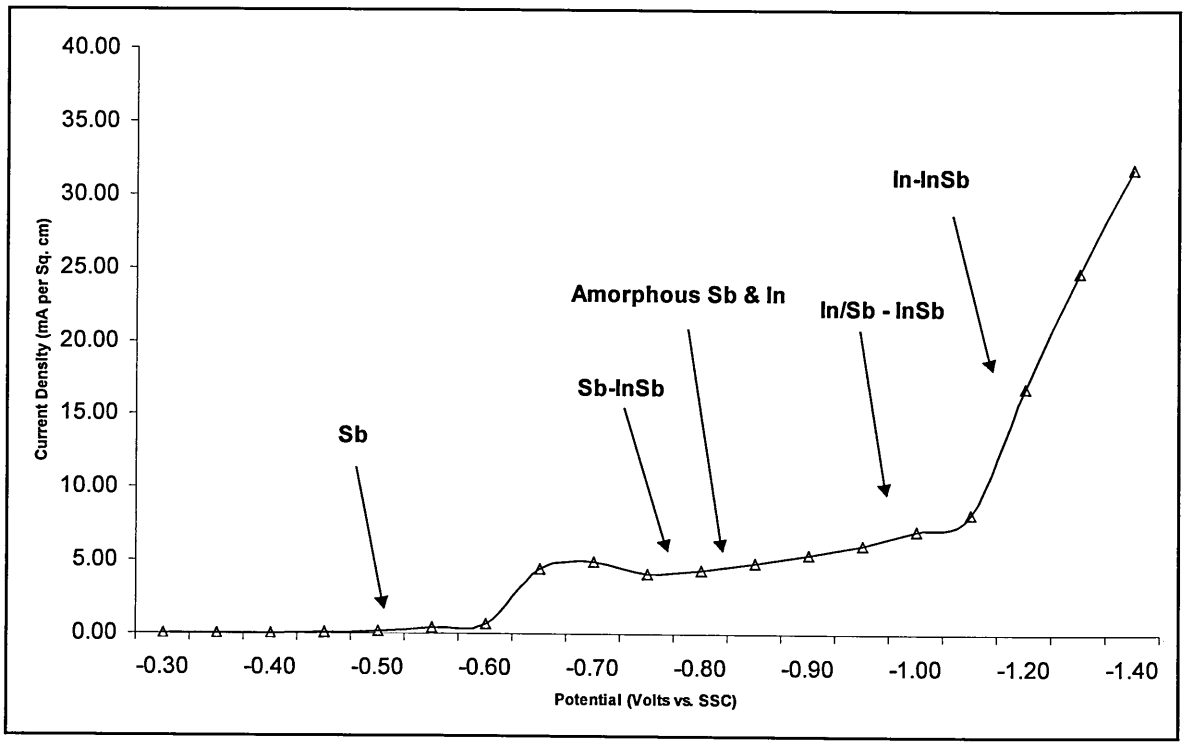

Figure 5.13 Graph illustrating the change in film stoichiometry (as indicated by XRD) with deposition potential.

As the ultimate aim of this study was to investigate the growth of InSb on optically 'transparent' ITO substrates, this investigation now entered its next phase.

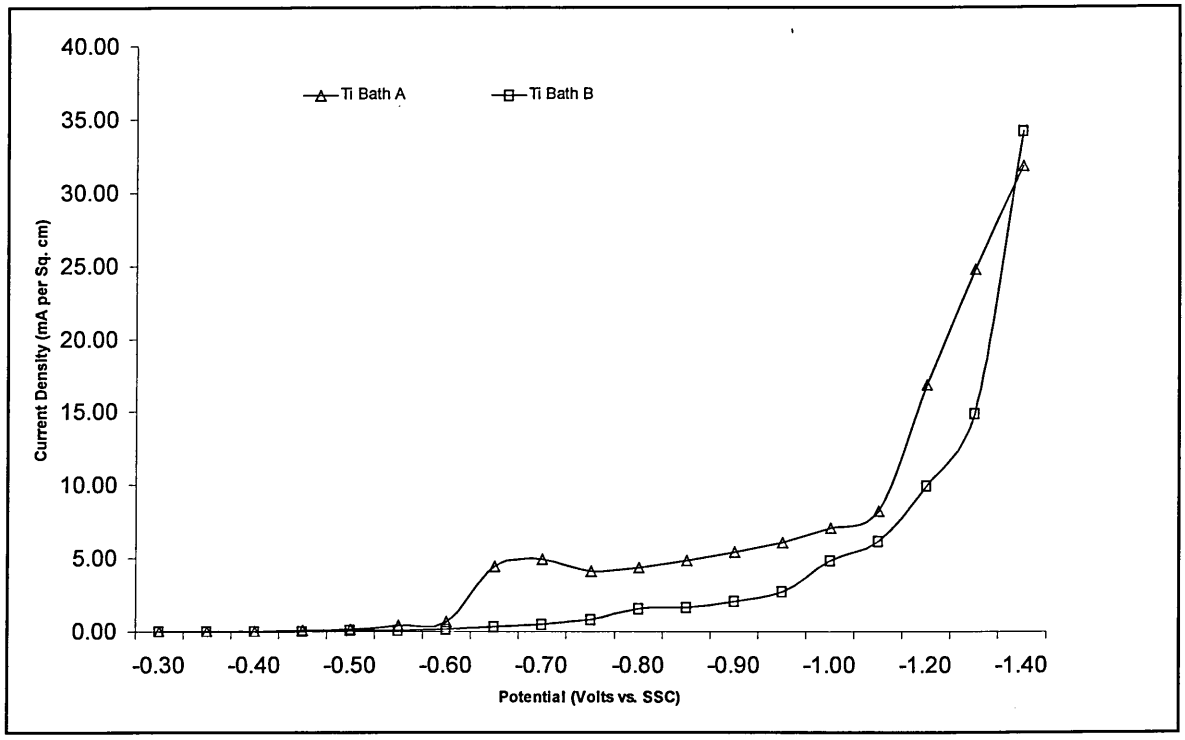

Figure 5.14 Voltammograms obtained at stationary Ti electrodes in unstirred solutions containing 0.033 mol dm^{-3} $InCl_3$ and 0.3 mol dm^{-3} citric acid, but with different concentrations of $SbCl_3$: Bath Ti (A) 0.047 mol dm^{-3} & Ti Bath (B) 0.002 mol dm^{-3}.

5.4 Study of the Electrochemical Deposition of InSb on to ITO Substrates

5.4.1 Selection of the Deposition Conditions for Initial Investigation

With the exception of the ITO substrate, the initial conditions used in this part of the investigation were those used by Ortega & Herrero (1989) (section 5.3.1). A voltammogram, figure 5.15, was collected using the same method also given in section 5.3.1.

Again, the window of potentials available for investigation was found to be bounded by a current density minimum and maximum associated with the evolution of gas at the cathode, specifically –0.35 to –1.20V. Consequently, a series of samples were grown within this region.

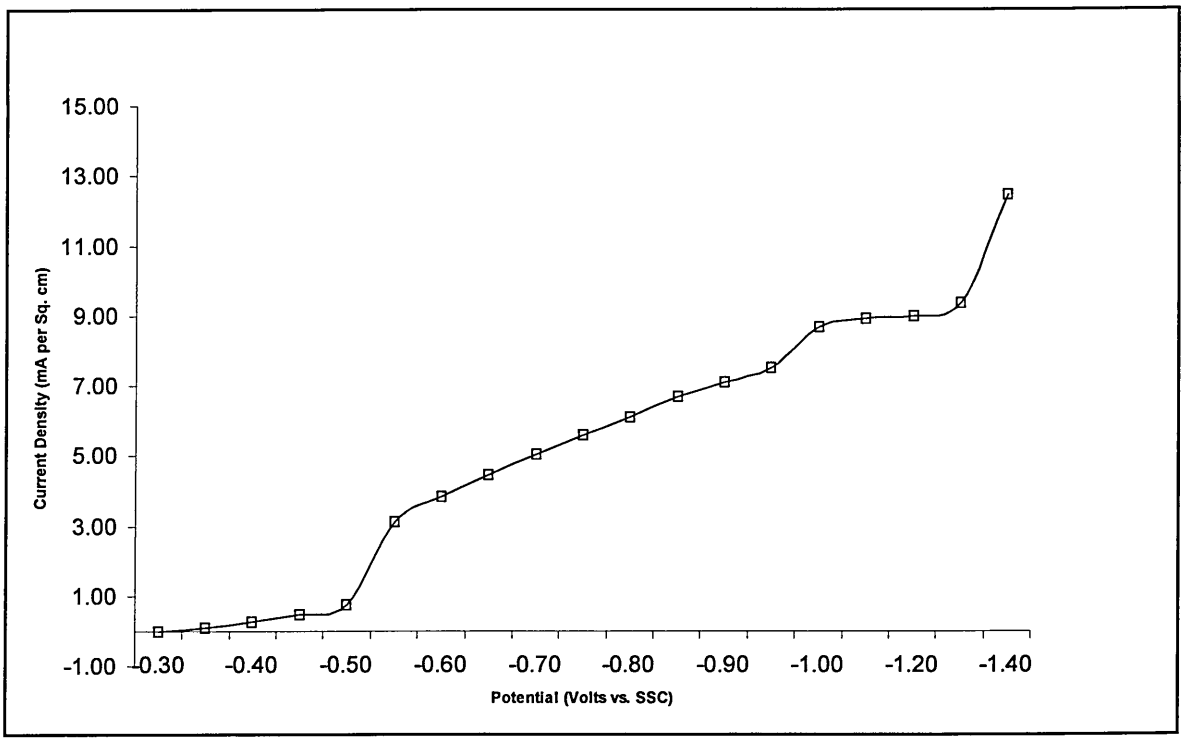

Figure 5.15 Voltammogram obtained at a stationary ITO electrode in an unstirred solution of 0.037 mol dm^{-3} $InCl_3$, 0.047 mol dm^{-3} $SbCl_3$ and 0.3 mol dm^{-3} citric acid.

5.4.2 Growth and Characterisation of Films Deposited under the Initial Conditions Selected

Films grown at more positive potentials than -0.45 V had insufficient material to perform their XRD analysis. However, samples grown at–0.45 V yielded XRD patterns attributable to a thin film of hcp Sb. The film's thinness was indicated by the form of their XRD patterns, which included a significant amorphous 'background' and 'hump' characteristic of the substrate material, figure 5.16.

An interesting feature of these diffraction patterns was the intensity of the peak ascribable to the Sb (003) plane, which was larger than that of the appropriate PDF card, and that of the corresponding Ti samples. Moreover, it was more intense than in the other patterns in this series of growths. Recalling from table 5.1 that the respective d-spacing values for the Sb (003) and InSb (111) planes are 3.75 and 3.74 Å, it could be proposed that this indicates the presence of a separate InSb phase, this especially as (111) yields the most intense peak for that species. However, this proposition is negated by the absence of any other peaks

that would originate from InSb. Therefore, it is reasonable to assume that under these conditions, that growth initially occurs in a preferential orientation along the Sb (003) axis.

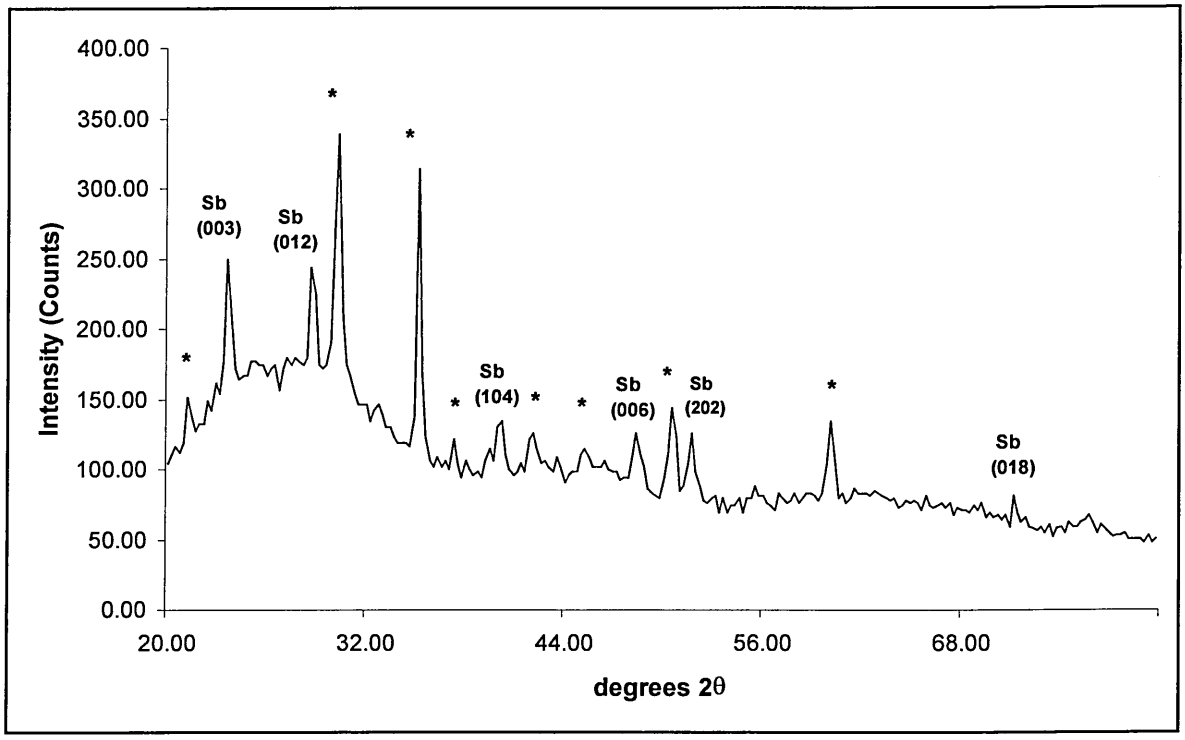

Figure 5.16 XRD pattern of a film deposited at -0.45 V (vs. SSC), with the peaks marked * arising from the substrate.

The applicability of EDX for the analysis was limited for the films grown on to ITO substrates, because the indium of the substrate could not be distinguished from that in the films.

Sb (hcp) films were also deposited at –0.50 V and –0.55 V. The x-ray diffraction patterns of these films indicated that they were thicker than the deposits grown at nobler potentials, figure 5.17. In addition, the Sb (003) peak was no longer the most intense.

Deposits grown at potentials between –0.60 V and –0.75 V consisted of black/grey powders that did not adhere to the substrate. Therefore, it was not possible to carry out their XRD analysis. Poor preparation of the substrate surface and the supply of low quality ITO/glass from the suppliers were eliminated from being causes of this problem. This was because the substrates were taken from non-sequential batches, and they were treated with a scrupulous cleaning regime .

However, the adhesion of films grown at potentials more negative than –0.75 V was better, and their XRD patterns revealed the formation of a mixture of tetragonal indium and fcc InSb. Visually, these films were black to dull grey in appearance. When the samples were mildly annealed (45 minutes, 250 ^{O}C , under N_2) to crystallise any amorphous material that may be present, there were significant improvements to the XRD pattern's peak heights and widths, figure 5.18. Figure 5.19 illustrates a typical XRD pattern for In 'rich' InSb electrodeposited on to ITO with the identity of the peaks given in detail.

SEM examination of the films containing InSb revealed a bed of nodular features up to 2μm in size that had grown on top of a thick coherent underlayer. Figure 5.20 shows a microgram of such a deposit, an area of which has broken away from the substrate to rest reverse side up.

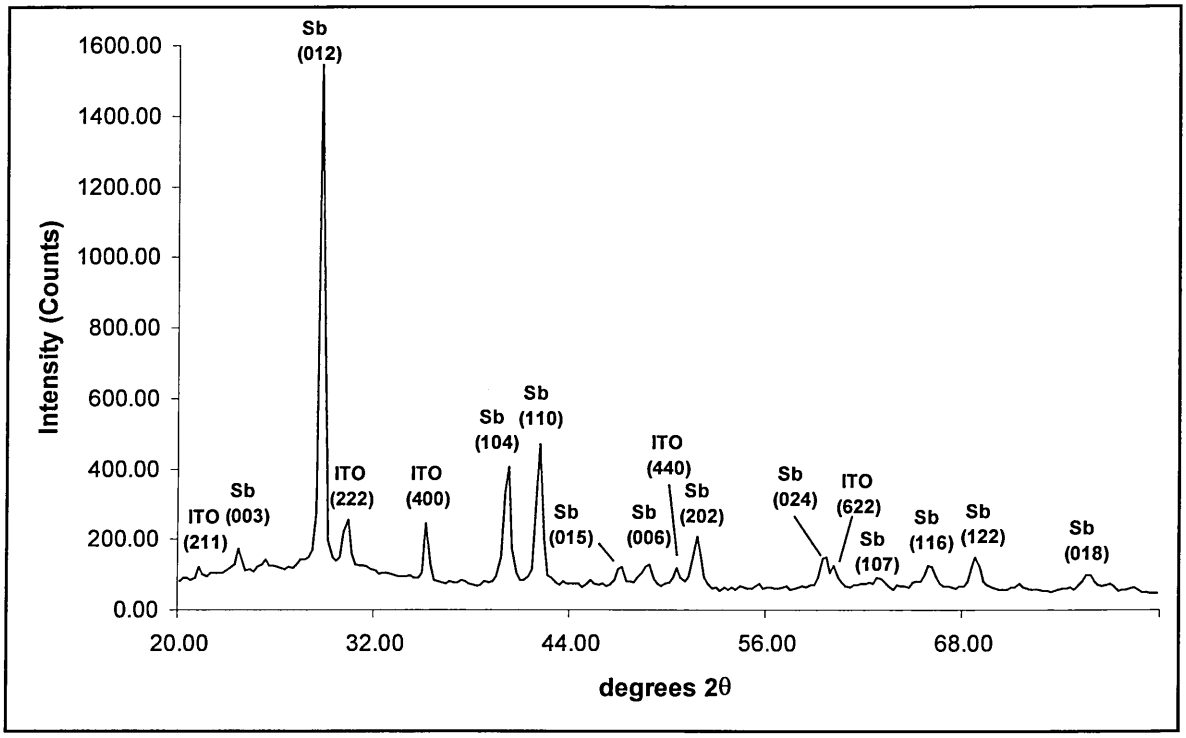

Figure 5.17 XRD pattern of a film deposited at -0.50 V (vs. SSC)

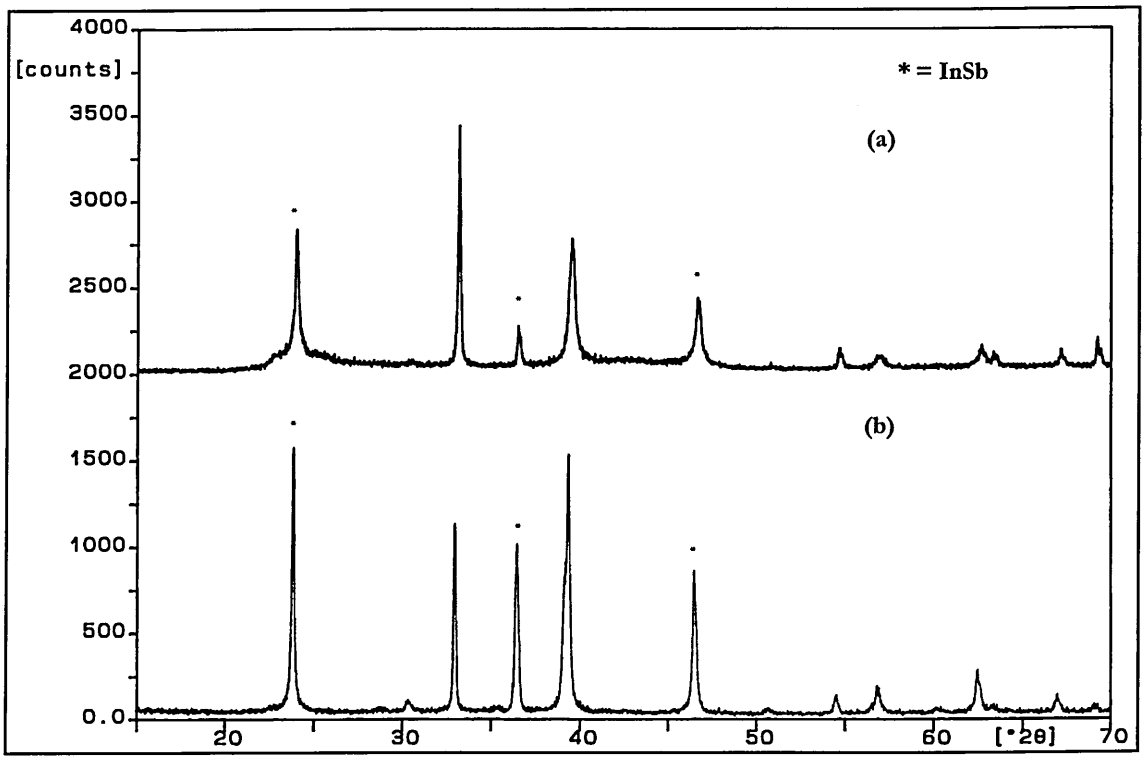

Figure 5.18 XRD patterns of a film (17InSb3S2) deposited at -0.80 V (vs. SSC) (a) before and (b) after annealing at 250 ^{O}C for 45 mins in an N_2 atmosphere.

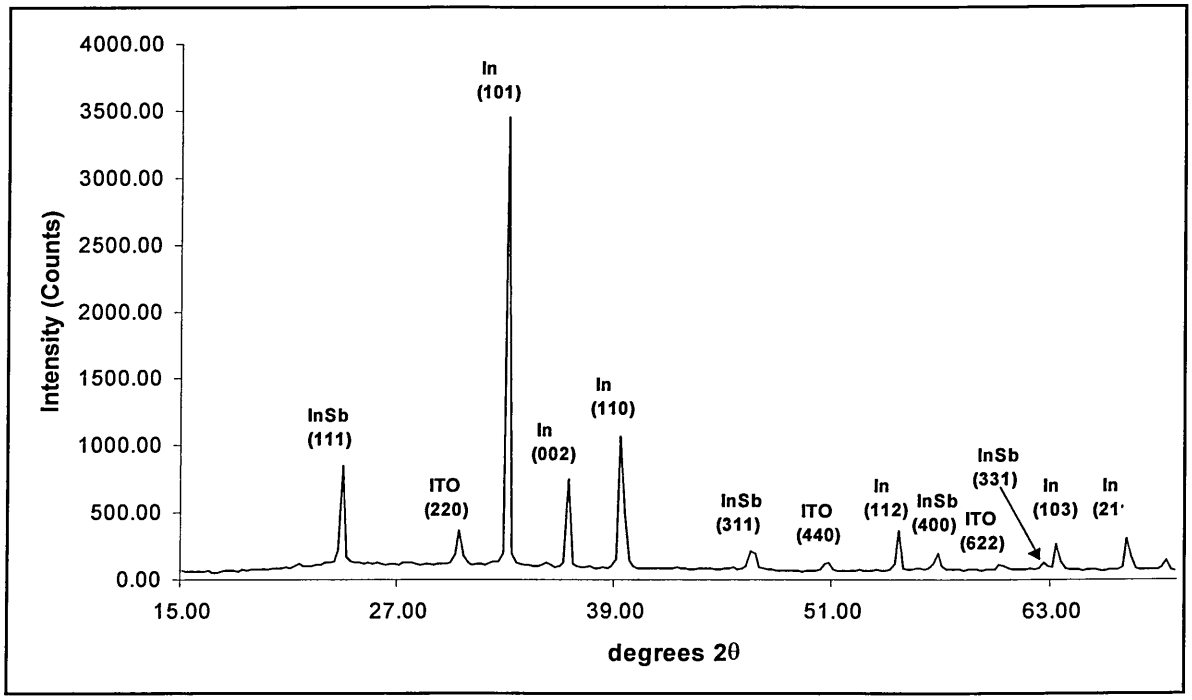

Figure 5.19 XRD pattern of a film deposited at -1.00 V (vs. SSC).

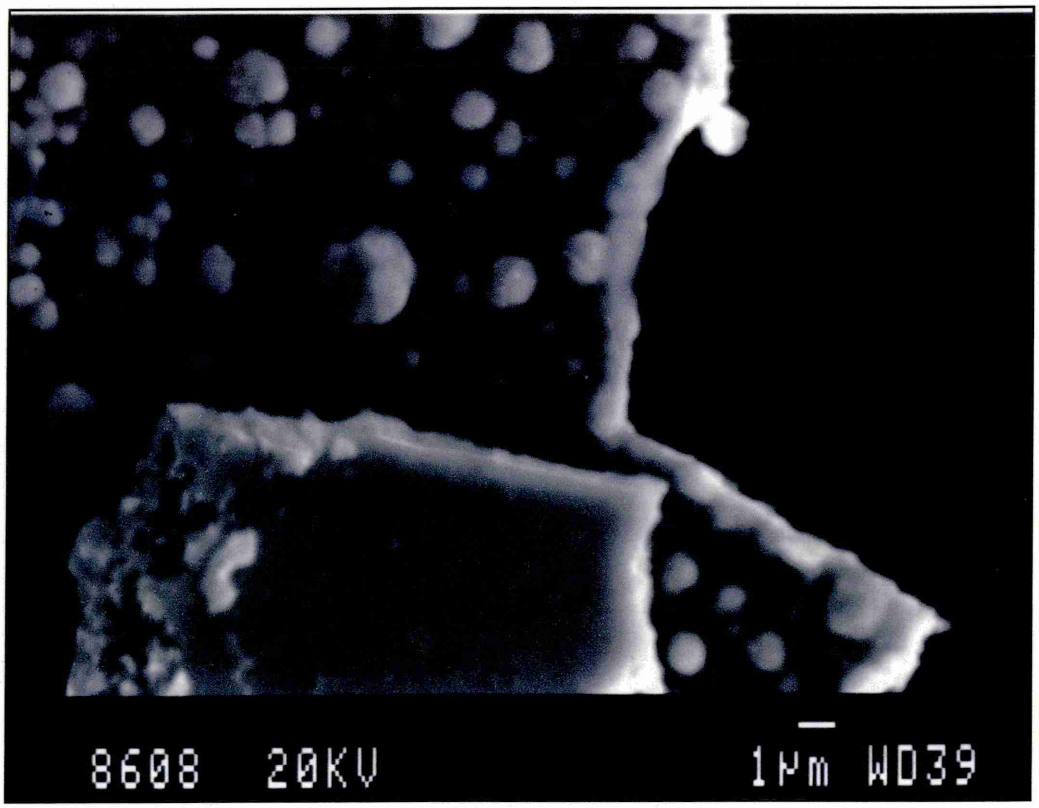

Figure 5.20 SEM micrograph of a film deposited at -1.00 V (vs. SSC).

In summation, a series of depositions were carried out at potentials from -0.30 V to -1.20 V. The composition of the deposit was seen to vary from thin layers of Sb to thicker layers of In rich InSb (denoted In-InSb), table 5.4. Thus, no correlation between deposit composition and growth potential as in the case of growth on Ti substrates was observed. A comparison of the results of the XRD analysis with those of the voltammogram obtained indicated that InSb formed only under limiting current conditions. Given that InSb only formed with the presence of an In co-phase, conditions were applied to make the deposition of the nobler element preferential. These conditions were; temperature 80 ^{O}C, high stirring rate and a low concentration of indium chloride in the electrolyte (0.0052 mol dm^{-3} indium chloride, 0.047 mol dm^{-3} antimony chloride). These conditions yielded powdery black coloured deposits of hcp Sb whose XRD patterns were of the same form as that shown in figure 5.17.

Deposition Potential (Volts vs. SSC)	Maximum Current Density mA per sq. cm	Results of XRD Analysis
-0.30	0.29	No deposit
-0.35	0.31	No deposit
-0.40	0.46	No deposit
-0.45	0.49	Sb
-0.50	0.78	Sb
-0.55	2.89	Sb
-0.60	3.97	Non-Adherent
-0.65	4.21	Non-Adherent
-0.70	4.88	Non-Adherent
-0.75	5.24	Non-Adherent
-0.80	5.39	In-InSb
-0.85	5.81	In-InSb
-0.90	5.99	In-InSb
-0.95	6.15	In-InSb
-1.00	7.24	In-InSb
-1.05	8.69	In-InSb
-1.10	9.00	In-InSb
-1.20	9.03	In-InSb

Table 5.4 Summary of the XRD analysis of films deposited on to ITO substrates under the conditions described above.

5.4.3 Study of the Effect on Film Composition of Lowering the 'Metal Percentage' of $InCl_3$ in the Electrolyte Solutions

Given that the formation of In rich InSb predominated under the conditions described in the preceding section, the effect of reducing the concentration of $InCl_3$ in the electrolyte solutions was investigated.

For convenience, this section refers to the concentration of the In and Sb precursors in the solutions in terms of metal percentage in the electrolyte, table 5.5. Thus, the previous bath used may be described as comprising of 59% $SbCl_3$ (0.047 mol dm^{-3}) and 41% $InCl_3$ (0.033 mol dm^{-3}), with the total (100%) metal concentration equalling 0.08 mol dm^{-3}.

Throughout this series of deposition experiments the concentration of $SbCl_3$ and citric acid was kept constant at 0.047 mol dm^{-3} and 0.3 mol dm^{-3} respectively. The solutions' pH were found to be constant at pH 1.49 (± 0.04).

Plating Bath Reference	$SbCl_3$ (mol dm^{-3})	$InCl_3$ (mol dm^{-3})	$InCl_3$ 'metal percentage' (%)
Bath A1	0.047	0.015	24
Bath A2	0.047	0.012	20
Bath A3	0.047	0.008	15
Bath A4	0.047	0.005	8

Table 5.5 Composition of the plating baths.

With the exception of the bath that contained the lowest percentage of $InCl_3$ (Bath A4), the deposition of In rich InSb predominated at potentials more negative to -0.75 V. Furthermore, for the individual baths, the XRD analysis did not clearly indicate an increase of the film's crystalline indium content at progressively negative deposition potentials.

Sb (hcp) electrodeposited at potentials more positive than –0.60 V. Non-adherent deposits formed between –0.60 V and –0.75V, as in the case of the series of films grown under the conditions described in section 5.4.2. XRD analysis of the films grown from Bath A4 did not show any peaks pertaining to indium containing species.

The relative proportions of In and InSb crystalline phases in the films were seen to be dependent on the relative percentages of $InCl_3$ and $SbCl_3$ in the plating solution. Indeed, visual inspection of the XRD patterns demonstrated that as the percentage of $InCl_3$ in the solutions was decreased, the relative intensity of the InSb peaks increased (Bath A1 and Bath A3). Conversely, the relative intensity of the In peaks diminished, figure 5.21 and 5.22. However, no discernible difference was seen between Bath A1 and Bath A2, in which the percentages of $InCl_3$ were within 5% of each other.

Visually the films consisted of either black powders or dull grey homogeneous layers, with the former predominating at more base potentials. The most adherent films formed at potentials more negative than -0.90 V, though they tended to suffer from peeling if grown at potentials more negative than -1.00 V. SEM of the films showed them to comprise a homogeneous under-layer from which 1-3 μm sized nodules protruded. No distinct change in morphology was observed under all conditions. Further, the presence of a chloride was detected by EDX in the majority of samples, with the exception of those films whose XRD patterns indicated them to be thin. If it is assumed that a chloride was present in all of the samples, then its absence in the thinner films may be explained by its relatively low concentration.

From the above baths, a series of samples were grown at 60 ^{o}C and 80 ^{o}C. The XRD patterns showed no distinct difference in film stoichiometry with respect to those films grown at room temperature in terms of crystalline InSb. A slight change in the width and heights of the XRD peaks, which, especially in the case of the In phase, indicated better crystallinity, was observed for those samples whose patterns indicated a dominance of In, figure 5.23. Further, these films visually appeared more coherent (less powdery and dull grey in appearance). This was especially for those deposited at the more negative potentials, which in the case of Bath A1 and Bath A2 had a bright silvery appearance at the most negative potentials. SEM analysis showed these films to have a more fine structure, figure 5.24.

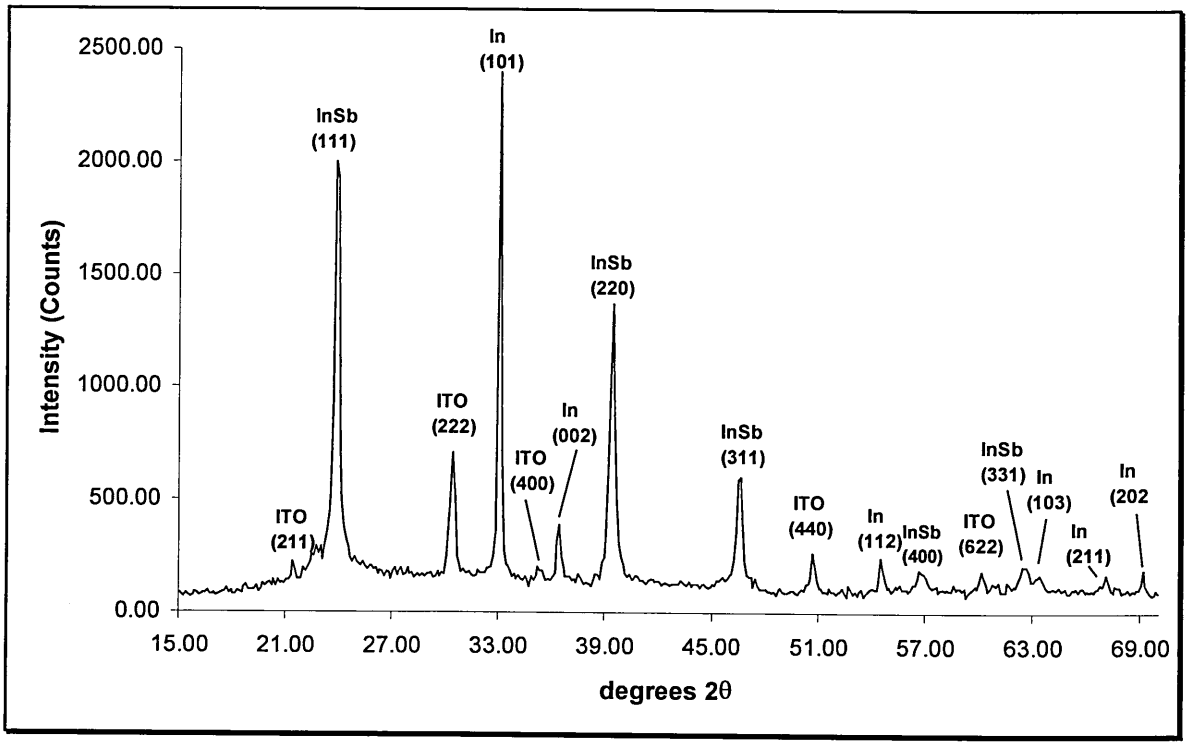

Figure 5.21 XRD pattern of a film deposited at -1.00 V (vs. SSC) using Bath A1.

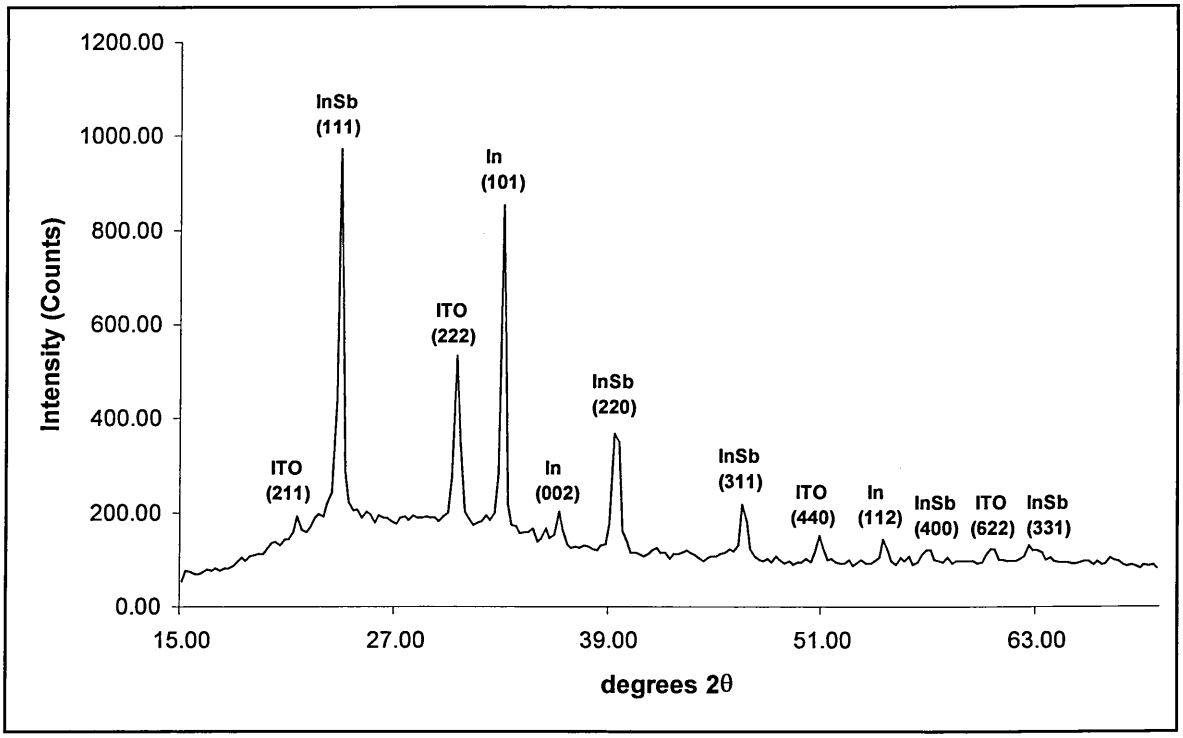

Figure 5.22 XRD pattern of a film deposited at -1.00 V (vs. SSC) using Bath A3.

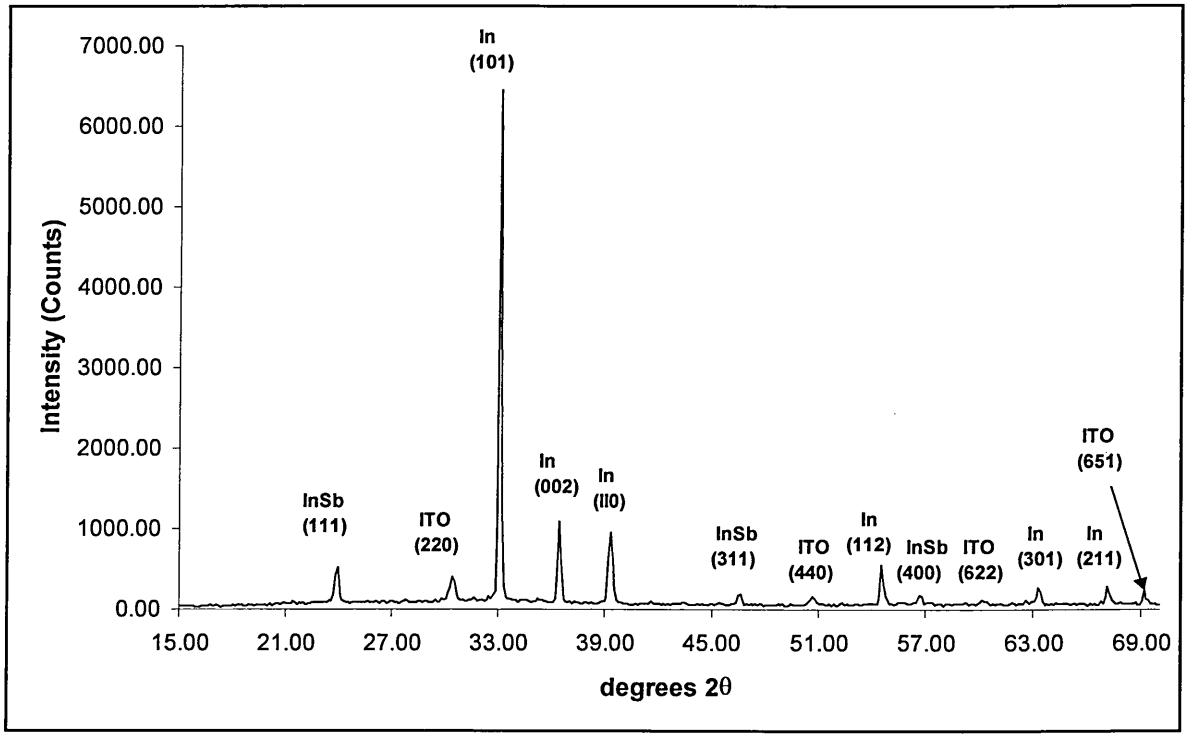

Figure 5.23 XRD pattern of a film deposited from Bath A1 at -1.15 V (vs. SSC) at 80 ^{O}C.

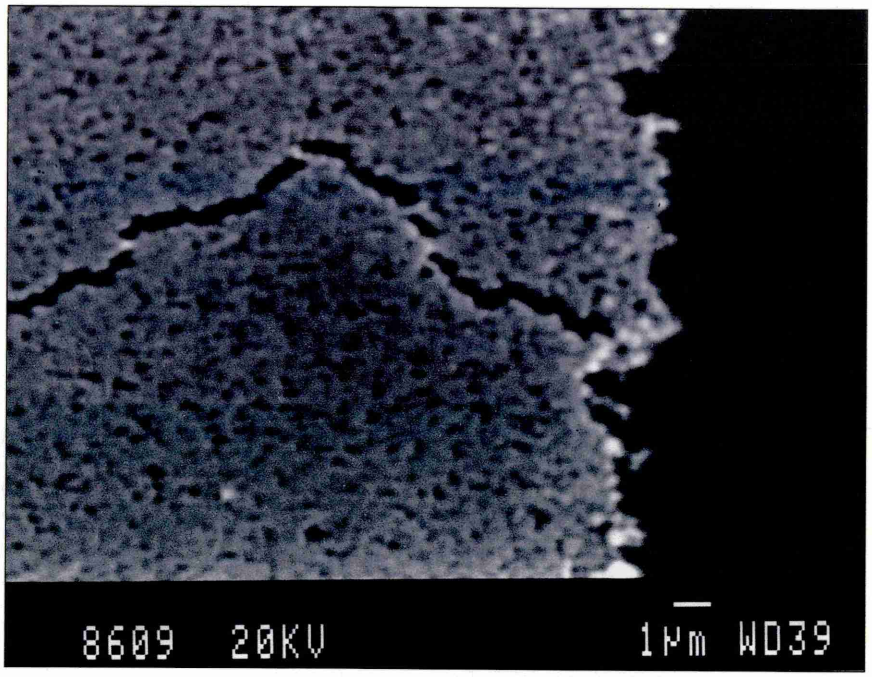

Figure 5.24 SEM micrograph of a film grown from Bath A1 at -1.15 V (vs. SSC) at 80 ^{O}C.

5.5 Study of the Electrodeposition of InSb on Copper Substrates

5.5.1 Selection of the Deposition Conditions

Comparison of the results from the electrodeposits generated under the conditions employed by Ortega & Herrero (1989) tables 5.3 & 5.4, point to subtle differences in the discharge potentials of various crystalline phases for the different substrates. Hence, a third substrate, copper (PCB) board, was selected for further comparison, and a series of depositions were carried out using the aforementioned conditions.

The voltammogram collected indicated that the window of potentials for growth was from -0.40 V to -1.10 V. As previously, a current density minimum and the evolution of gas at the electrodes determined the range of potentials available for investigation. However, because of the deposit's good adhesion to the substrate, films were also grown at potentials from -1.05 V to -1.40 V. Indeed, the films grown on Cu were noticeably more adherent than those grown on ITO and Ti substrates.

Obviously, at the potentials where gas evolution occurs the current efficiency is low. That is to say, the fraction of the current used for gas evolution becomes significant with respect to that used for the deposition of the film.

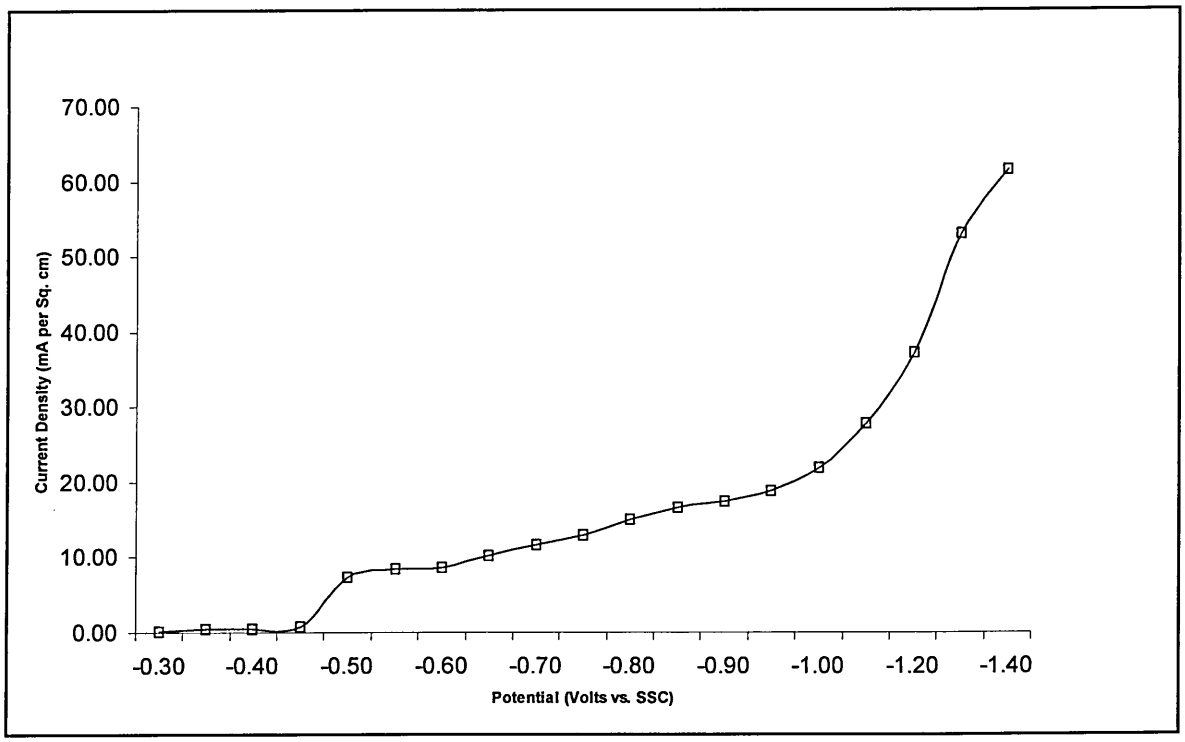

Figure 5.25 Voltammogram obtained at a stationary Cu electrode in an unstirred solution of 0.037 mol dm^{-3} $InCl_3$, 0.047 mol dm^{-3} $SbCl_3$ and 0.3 mol dm^{-3} citric acid.

5.5.2 Growth and Characterisation of the Films

The surface of the Cu substrate material as seen under a SEM was profoundly different to that of the ITO and Ti. Whilst the latters' morphologies were on a macro-scale devoid of any particular noticeable characteristics, the Cu material was distinguished by a surface rich in features. As shown in figure 5.26, the surfaces of the Cu substrates were rough and broken.

At more noble potentials than -0.40 V, the substrate was covered with a thin film of a black powdery material. XRD of the deposits showed them to consist of amorphous material, which is identified by the emergence of hump features in the films XRD patterns, figure 5.27. (This may be more readily distinguished through comparison with the substrate's own XRD pattern, figure 5.2). SEM analysis revealed a surface covered with a fine powdery material, and EDX analysis showed the films to comprise Sb alone.

Figure 5.26 SEM microgram (×1286) of the surface of a Cu substrate.

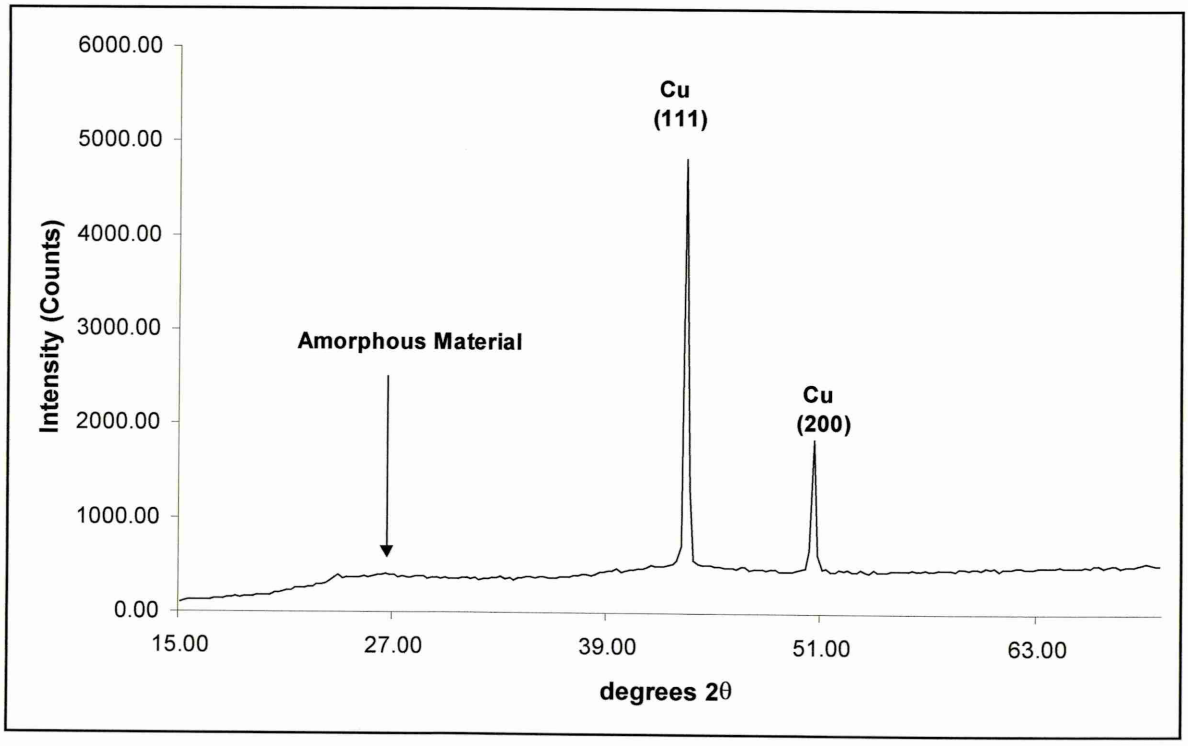

Figure 5.27 XRD pattern of a film deposited at -0.40 V (vs. SSC).

Those films grown at potential more base than -0.50 V yielded XRD patterns demonstrating the formation of a mixture of tetragonal In, fcc InSb and In-Cu[6], figure 5.28.

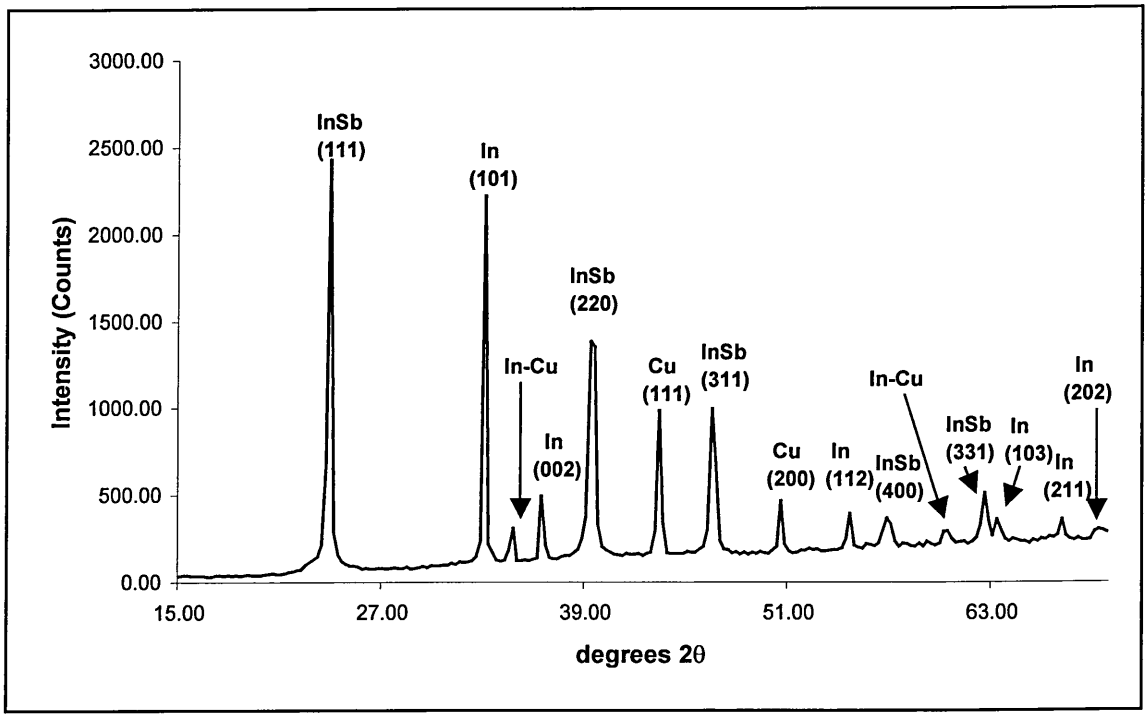

Figure 5.28 XRD pattern of a film deposited at -0.65 V (vs. SSC).

The relative intensity of the InSb XRD peaks with respect to those of the In peaks was seen to diminish as the deposition potential was made more base. This indicated an increase in the proportion of the crystalline film's indium content, figure 5.29. Table 5.6 summarises the depositions onto Cu substrates under the aforementioned conditions. SEM micrograms of the films deposited at potentials more negative than -0.50 V showed the presence of a fine homogeneous under-layer from which large (10-20 μm) nodules protruded, figure 5.30. When the films were deposited at more negative potentials, the size of the nodules decreased and their number density increased, figure 5.31. At potentials more negative than -0.90 V the films appeared to the naked eye homogeneous and 'bright' (silver-grey). EDX analysis showed again the presence of a chloride in the deposits, figure 5.32.

---

[6] The PDF card of Cu-In (no. 35-1150) does not provide the hkl indices for the various dÅ values.

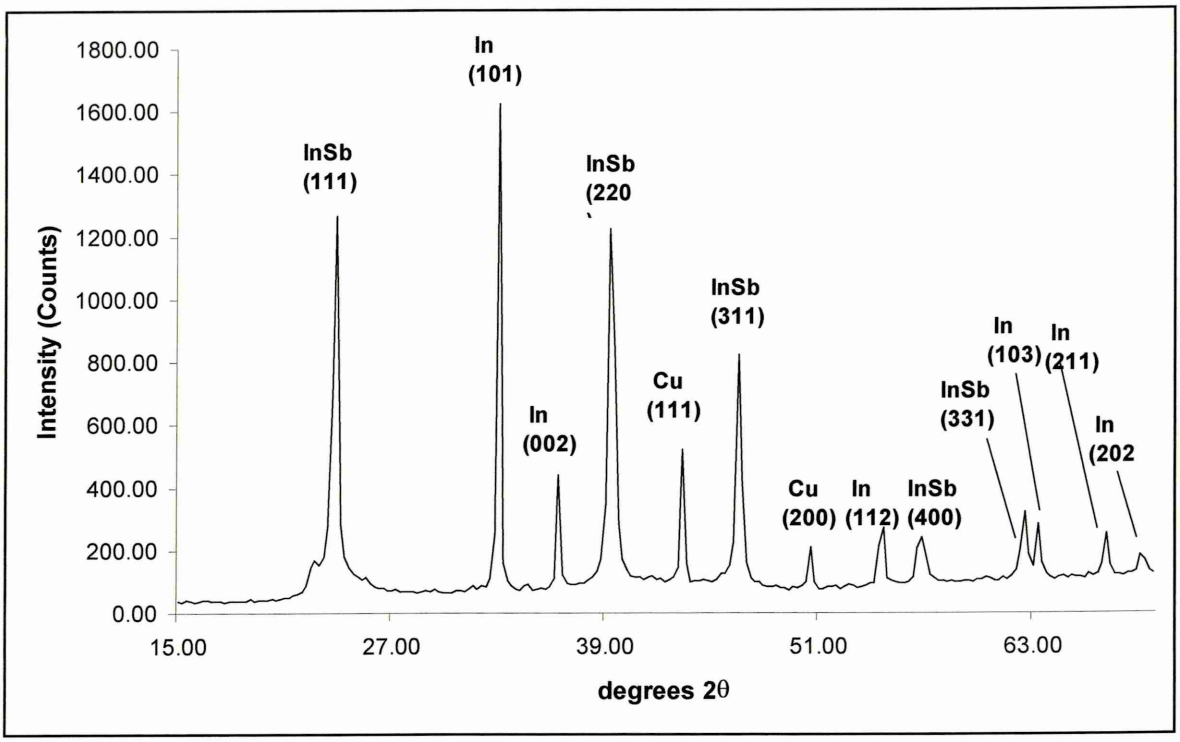

Figure 5.29 XRD pattern of a film deposited at -1.40 V(vs. SSC)

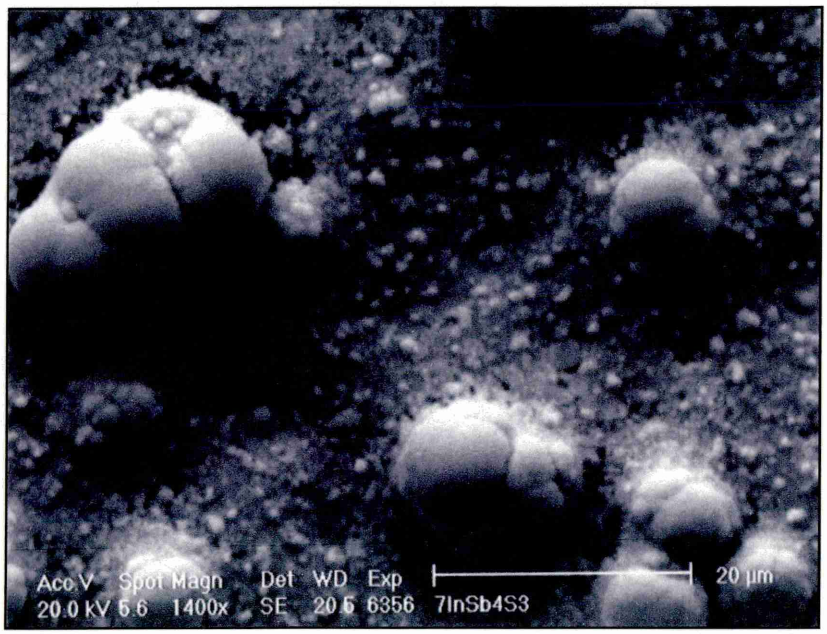

Figure 5.30 SEM micrograph (×1400) of a film deposited at –0.65 V (vs. SSC).

Figure 5.31 SEM microgram (×1654) of a film deposited at –1.10 V (vs. SSC).

Deposition Potential (Volts vs. SSC)	Maximum Current Density mA per sq. cm	Results of XRD Analysis
-0.40	0.542	Amorphous
-0.45	4.468	Amorphous
-0.50	9.062.	In-InSb
-0.55	9.936	In-InSb
-0.60	11.258	In-InSb
-0.65	11.547	In-InSb
-0.70	13.291	In-InSb
-0.75	14.054	In-InSb
-0.80	16.269	In-InSb
-0.85	17.156	In-InSb
-0.90	18.002	In-InSb
-0.95	20.105	In-InSb
-1.00	23.516	In-InSb
-1.05	32.666	In-InSb
-1.10	30.154	In-InSb
-1.15	36.359	In-InSb
-1.20	40.005	In-InSb
-1.25	44.898	In-InSb
-1.30	51.233	In-InSb
-1.35	60.115	In-InSb
-1.40	67.777	In-InSb

Table 5.6 Summary of the XRD analysis of the films deposited onto Cu substrates under the conditions described in the text.

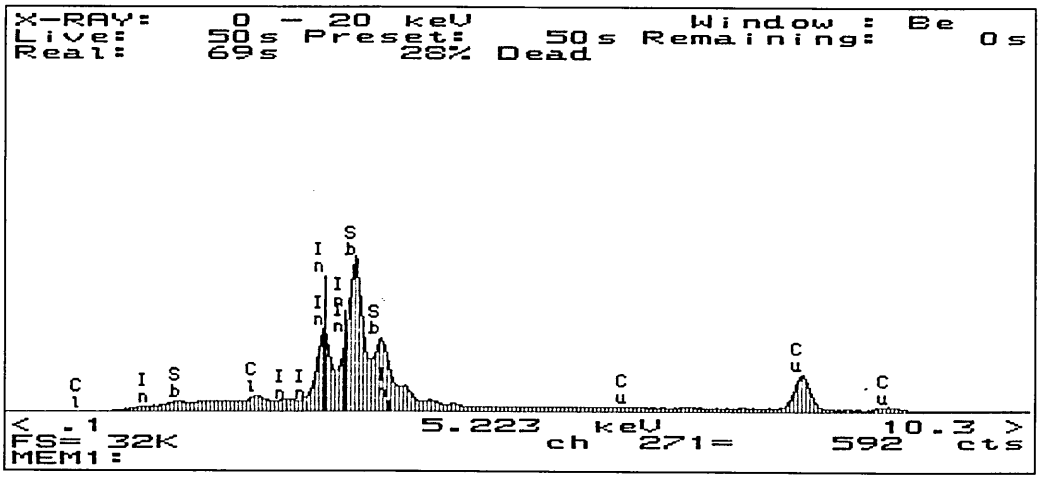

Figure 5.32 EDX spectrum of a film deposited at -0.80 V (vs. SSC).

5.6 Calculation of Crystallite ('Particle') Size

Mengoli et al (1991) reported an average estimated crystallite size of 35 nm for InSb formed after the post growth annealing of electrodeposited In and Sb. However, given the absence of reported data, the authors were unable to make any comparisons with crystalline films grown by other electrochemical methods. Therefore, crystallite sizes were calculated for a representative sample of the films grown during this investigation.

A complicating factor in such calculations was the presence of co-deposited phases with the InSb. For example, the most intense reflections from the InSb phase derive from the InSb (111) plane. Yet, as shown in table 5.1, the dÅ of the Sb (003) plane is such that its peak overlaps with that of InSb (111). Thus, given such considerations, particle sizes were calculated only for those samples that contained an In co-phase.

The sizes of the crystallites were estimated using the Scherrer equation (Cullity (1978)), chapter four section 4.3.3, and found to be on average 47 nm for those grown on Cu and ITO substrates. Films grown on ITO at 80^{o}C were larger (61 nm). Crystallite sizes for samples grown on to Ti substrates were on average 27 nm. These values compare favourably with those determined by Mengoli et al (1991), who reported the crystallite size of In 'rich' InSb grown by their method to be 20-49 nm.

5.7 Summary of the Study of the Electrodeposition of InSb from Aqueous Electrolyte Solutions

- The electrodeposition onto Ti substrates of InSb, free of In and Sb co-phases (Ortega & Herrero (1989) could not be duplicated. Rather a three-phase system comprising fcc InSb, tetragonal In and hcp Sb is reported for the first time.

- The nature of the substrate material affected the discharge potentials of the various phases deposited, as illustrated by figure 5.33.

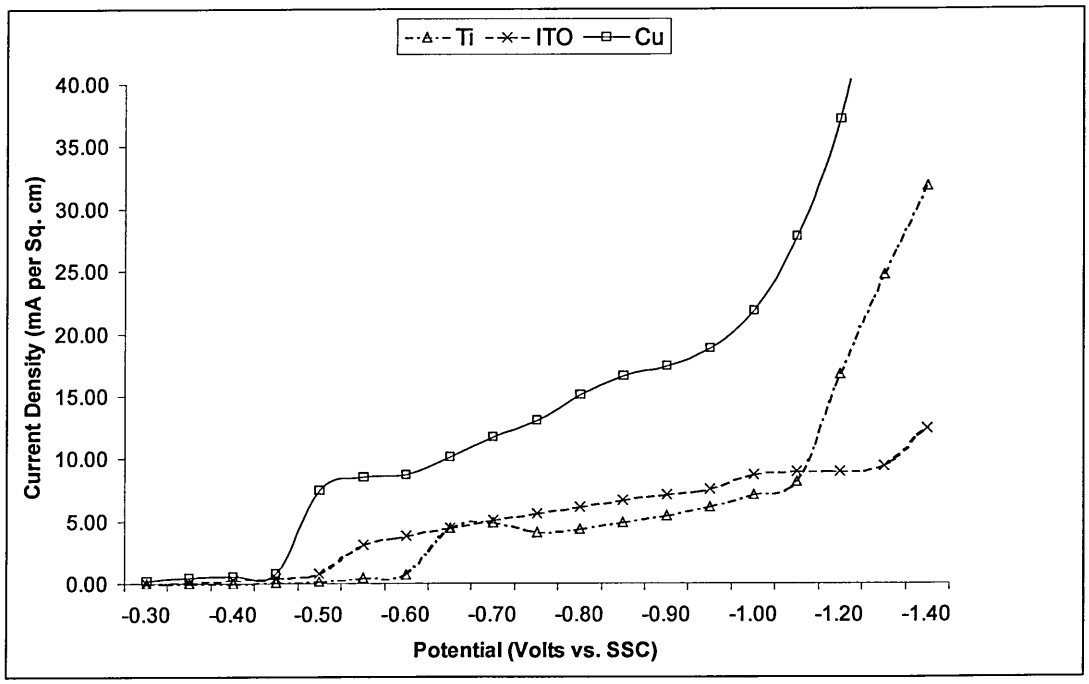

Figure 5.33 Graph overlaying the voltammograms collected on Ti, ITO and Cu stationary electrodes in an unstirred solution of 0.037 mol dm^{-3}, $InCl_3$, 0.047 mol dm^{-3} $SbCl_3$ and 0.3 mol dm^{-3} Citric acid.

- XRD patterns of InSb films grown for the first time on ITO substrates had an associated In co-phase. In addition, this was found to be the case for films deposited on to Cu substrates.

- An estimation of the InSb particle size by XRD analysis for those films containing an In co-phase demonstrated that samples grown at higher (80°C) temperatures crystallites were larger (>60 nm) than those grown at room temperature (<50 nm).

- The first SEM study of electrodeposited films containing InSb showed that nodular growth morphology predominated.

- New EDX analysis of the films deposited showed that a chloride was a major contaminant in the films grown under all conditions.

- The results confirm the proposition made by Sadana & Singh (1985) that InSb electrodeposition is diffusion limited, and as such of a 'regular type' according to Brenner's (1963) empirical classification system (chapter two, section 2.3.3).

Chapter 6

Electrodeposition of InSb from Non-Aqueous Electrolyte Solutions

6.1 Introduction

From the review of the literature given in chapter three, it can be concluded that there are far more reports of semiconductor electrodeposition from aqueous, rather than organic, electrolyte solutions. In part, this reflects the success of II-VI electrodeposition from aqueous solutions, and the relative lack of III-V deposition studies. Indeed, justifiably, there is a tendency in the electroplating field as a whole to only employ non-aqueous plating systems when electrodeposition from aqueous solutions is not possible[1]. Such necessity derives mostly from (a) the hydrolysis of metal salt precursors, and (b) the concurrent evolution of hydrogen at the highly negative potentials required to deposit some metals such as, for example, Al. In itself, hydrogen evolution leads to deposition low current efficiencies, 'hydrogen embrittlement' and poor surface finish.

Other reasons have been proposed on an individual case basis for the employment of organic solvents. For example, Rastogi & Balakrishnan (1989) used dimethyl sulfoxide (DMSO) as the solvent when depositing CdTe because it enabled the use of elemental Te as a precursor, which is insoluble in water, rather than the more commonly used TeO_2. Consequently, the authors state that their method is more efficient, because the mechanism of CdTe deposition from elemental Te involves fewer electrons than that using TeO_2, reaction 6.1.

Reaction 6.1 $$Cd^{2+} + Te + 2e^- \rightarrow CdTe$$

Of direct relevance to this study however, is that deposition temperatures greater than that permissible with water (> 80 ^{o}C) are obviously available using organic solvents. Given that the results of chapter five suggest the presence of kinetic barriers to the formation of InSb from low temperature aqueous electrolyte solutions (<100 ^{o}C), the use of organic solvents at high temperatures becomes therefore especially attractive.

---

[1] Actually, only half of the known metals can be deposited from aqueous electrolyte solutions (Abbot (1993)), though the most commonly electroplated materials fall into the category that can utilise such systems e.g. Au.

Precedents do exist in the literature for Sb-In alloy electroplating from non-aqueous electrolyte solutions (section 3.4.4), and table 6.1 contrasts these electrodeposition protocols with that developed by this investigation.

Principal author	**This thesis**	**Styrkas (1964)**	**Kochegarov (1971)**
'Control mode'	Potentiostatic	Galvanostatic	Galvanostatic
Solvents	Ethylene glycol [I]	Ethylene glycol	Glycerol [II]
Electrolytes	$In_2(SO_4)_3$ or $InCl_3$	$In_2(SO_4)_3$	$InCl_3$
	$Sb_2(SO_4)_3$ or $SbCl_3$	$Sb_2(SO_4)_3$	$K(SbO)C_4H_4O_6.1/2$
	TEAC [III]		H_2O
			KOH
Max temp (°C)	185	165	125
Substrates	ITO [IV]	Pt	Cu
		Sb	
Film analysis	XRD	Amperometric	Amperometric
methods	EDX	titration	titration
	SEM	XRD	
	GDOES		

[I] Ethane-1,2-diol, $(CH_2OH)_2$

[II] Propane-1,2,3-triol, $CH_2OHCHOHCH_2OH$

[III] Tetraethylammonium chloride, $(C_2H_5)_4NCl$

[IV] For brevity, the (glass)/ITO substrate is hereafter referred to as the ITO substrate.

Table 6.1 Comparison of the experimental conditions used in various studies of the deposition of InSb and Sb-In alloys from non-aqueous systems.

One of the most important differences of the above studies is the electrolysis 'control mode'. Recalling section 4.2, electrolysis in a potentiostatic control mode requires a constant potential to be maintained between the cathode and reference electrode. In contrast, for galvanostatic mode (constant-current) electrolysis the cell current is kept constant. A drawback of galvanostatic deposition is the absence of any command over the cathode's potential, making this mode the least selective for electrolysis. This may be understood by considering the effects of concentration polarisation on the cathode's

potential. During electrolysis, the concentration of cations within the cathode's double layer becomes low, because the electron transfer process usually occurs at a much faster rate than the transport of ions to the cathode from the bulk of the solution. This results in a decrease in the current flowing through the cell. Consequently, whilst operating in galvanostatic mode, a constant current is maintained by increasing the potential applied across the cell. This leads to the cathode progressively assuming potentials that are more negative, thereby enabling the reduction of less noble species (or phases).

Common to all of the studies outlined in table 6.1, is the use of polyhydric alcohol solvents that are, by definition, protic. Ethylene glycol (EG) has several physical properties that make it a suitable solvent for this investigation. It has a large liquidus range (-13.0 ^{o}C to 197.3 ^{o}C), with one of the highest B.P.'s of common organic solvents. In addition, EG has properties that facilitate the dissolution of many different electrolytes. For example, the solvent has a large dielectric constant ($\varepsilon = 37.7$) that promotes ionic dissociation. Moreover, it is also a Lewis base (i.e. a 'donor' solvent), and can therefore promote the ionisation of covalent compounds through the solvation of cations, for example reaction 6.2. Anion solvation (via hydrogen bonding) is even stronger than cation solvation, with the solvation of small highly electronegative anions being the easiest. EG has a large voltage range in which it is stable to electrochemical breakdown. Finally, EG undergoes autoprotolysis according to reaction 6.3 (Sawyer et al (1995)). Whilst these properties are also displayed by glycerol, it has a higher viscosity and lower boiling point (56.0 cP & 187.6 ^{o}C respectively).

Reaction 6.2 $2EG + SbCl_3 \leftrightarrows EG_2SbCl_2^+Cl^-$

Reaction 6.3 $2HOCH_2CH_2OH \leftrightarrows HOCH_2CH_2O^- + HOCH_2CH_2OH_2^+$

A common feature of electrochemical studies in organic solvents is the use of an 'inert' supporting electrolyte, whose reduction potential is much larger than the species under investigation, e.g. tetraalkylammonium salts or alkali earth metal salts. As pure organic solvents are essentially non-conductors, the primary role of the supporting electrolyte is to provide a conducting medium. A consequence of using such an electrolyte is that mass transport via ionic migration of the electroactive species is reduced, since most of the cell current is being carried by the supporting electrolyte. Further, as the resistance of the solution is diminished, the potential required to pass a current is reduced.

6.2 Study of InSb Electrodeposition from Sulphate Solutions

Initial deposition experiments from EG employed plating solutions containing indium sulphate hydrate (0.01 mol dm^{-3}) and antimony sulphate (0.01 mol dm^{-3}), Styrkas et al (1964). A series of growths were carried out at deposition potentials between –0.50 V to –1.20 V, with the temperature set at 185 ^{o}C. These conditions yielded low current densities (<< 1 mA cm^{-2}), and no visible films. However, films were generated when the same range of deposition potentials (table 6.2) was used with baths containing higher concentrations of $In_2(SO_4)_3$ and $Sb_2(SO_4)_3$, (0.04 mol dm^{-3} & 0.02 mol dm^{-3} respectively). These dark grey powdery films were identified with XRD as hcp Sb (figure 6.1), and calculation of the average particle size for the Sb (012) diffraction peak gave sizes between 70-80 nm. Increasing the concentration of the indium sulphate hydrate to 0.08 mol dm^{-3} yielded slightly cloudy solutions. No indium bearing crystalline deposits were formed when depositing from these solutions when applying a potential within the aforementioned range. Because of the indium precursor's limited solubility range, and so that comparisons could be made to the aqueous electrolyte solution studies discussed in section 5.4, further deposition experiments used the more soluble $InCl_3$.

Deposition Potential Volts vs. Pt Ref.	Maximum Current Density mA cm-2	Results of XRD Analysis
-0.50	0.91	Sb
-0.55	0.94	Sb
-0.60	1.25	Sb
-0.65	1.41	Sb
-0.70	1.73	Sb
-0.75	1.84	Sb
-0.80	1.98	Sb
-0.85	2.20	Sb
-0.90	2.35	Sb
-0.95	2.77	Sb
-1.00	3.05	Sb
-1.05	3.30	Sb
-1.10	4.38	Sb
-1.20	6.23	Sb

Table 6.2 Summary of the XRD analysis of films deposited under the conditions described in the text.

(In agreement with the above authors, the solubility of the indium sulphate hydrate was found to be limited to ~0.1 mol dm^{-3}.)

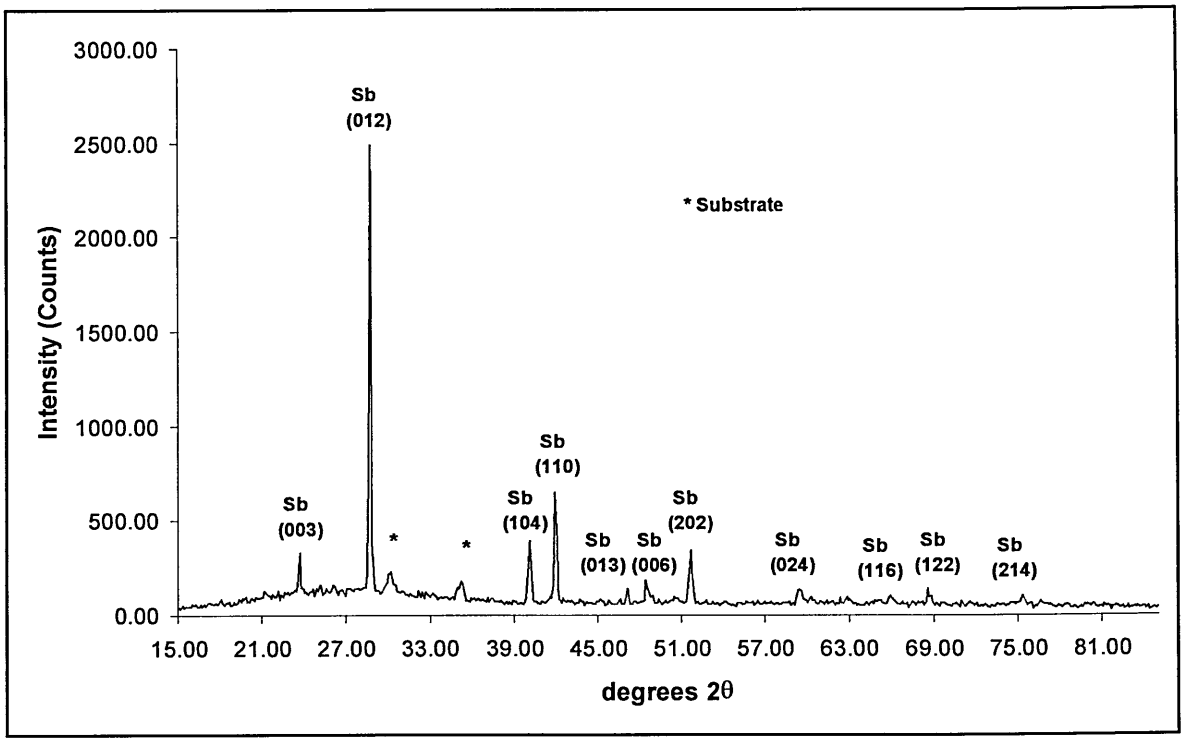

Figure 6.1 XRD pattern of a film deposited at –0.90 V (vs. Pt ref.).

6.3 Study of InSb Electrodeposition from Chloride Solutions

After 2 hours stirring, a clear yellow electrolyte solution was obtained by dissolving $InCl_3$ (0.08 mol dm^{-3}) and $SbCl_3$ (0.03 mol dm^{-3}) in EG at 110 ^{o}C. The solution's temperature was then raised to 185 ^{o}C, and voltammograms obtained using the scanning features of the potentiostat, figure 6.2. These voltammograms were characterised by an increase in current density at approximately –0.30 V. The current density was appreciably smaller (2.90 mA cm^{-2} at –1.50 V) than that achieved with the sulphate EG plating bath (6.20 mA cm^{-2} at –1.20 V), section 6.2. A series of films was then electrodeposited at 185 ^{o}C, within the range of potentials –0.30 V to –1.50 V. The films' XRD patterns contained hcp Sb peaks alone, and the average particle size was estimated to be approximately 70-85 nm. EDX analysis of the films showed that they all contained a chloride, figure 6.3. Film adhesion was poor, resulting in peeling from the substrate. Finally, SEM analysis revealed a homogeneous surface of crystalline 'flakes' 2 to 3 μm in size, figure 6.4, in comparison to the primarily nodular morphology exhibited by the samples grown from the aqueous electrolytes.

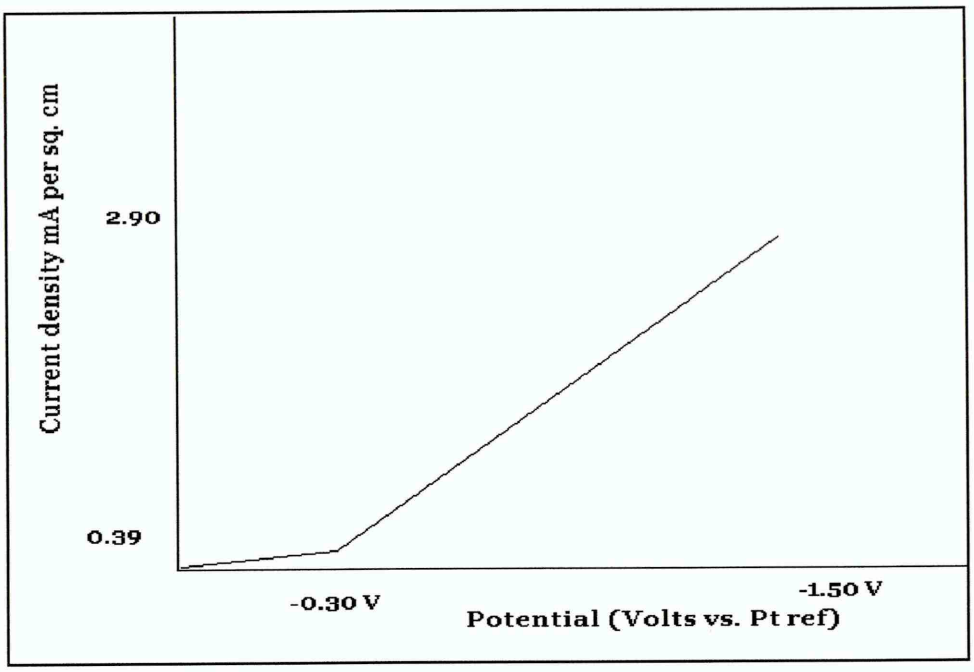

Figure 6.2 Voltammogram obtained at 185 ^{O}C from a stationary ITO electrode in an unstirred EG solution containing 0.08 mol dm^{-3} $InCl_3$ & 0.03 mol dm^{-3} $SbCl_3$.

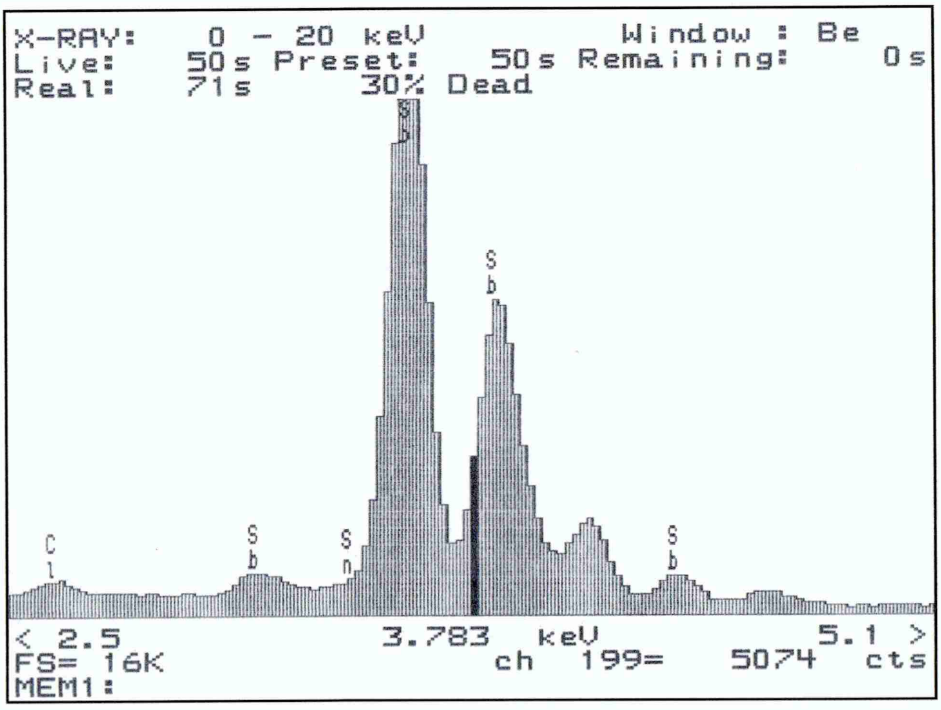

Figure 6.3 EDX spectrum of a film deposited at –1.10 V (vs Pt ref.).

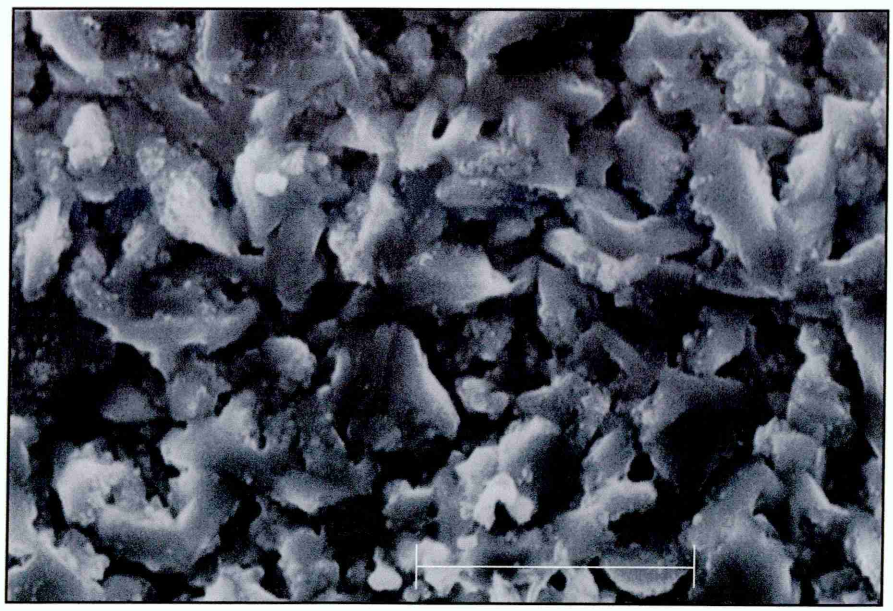

Figure 6.4 SEM micrograph of a film deposited at –1.00 V (vs. Pt ref.), the white bar representing 5 μm.

6.4 Study of InSb Electrodeposition from Chloride Solutions with TEAC- Part I

So that the effect of increasing the electrolyte solution's conductivity (section 6.2) could be investigated, a series of growths was carried out from baths containing TEAC. Again, after dissolving the bath components at 110 ^{o}C, a clear solution was obtained after two hours of stirring. In general, the form of the voltammogram, figure 6.5 was the same as that obtained for the chloride solution containing no TEAC (section 6.3). However, the current densities were higher, and the potential at which the current density rose sharply more positive (-0.24 V).

Electrodeposition was carried out at 185 ^{o}C in the potential range between - 0.50 V and- 1.50 V, table 6.3. All the films generated, excepting those grown at - 1.50 V, were identified with XRD as hcp Sb, as in figure 6.1. The samples grown at - 1.50 V exhibited texture (figure 6.6), resulting in the Sb (110) peak being the most intense, as opposed to the Sb (012) peak. Further, the relative intensities of the major peaks were seen to decrease, Sb (110) > (202) > (012) > (122). This is in contrast to the hcp Sb PDF card (No. 35-732), in which the intensity of the peaks diminishes in the following order; Sb (012) > (104) > (122) > (116). The films were dark grey in appearance, and adhered poorly to the substrate. Finally, particle size, based on the Sb (012) peak was in excess of 100 nm.

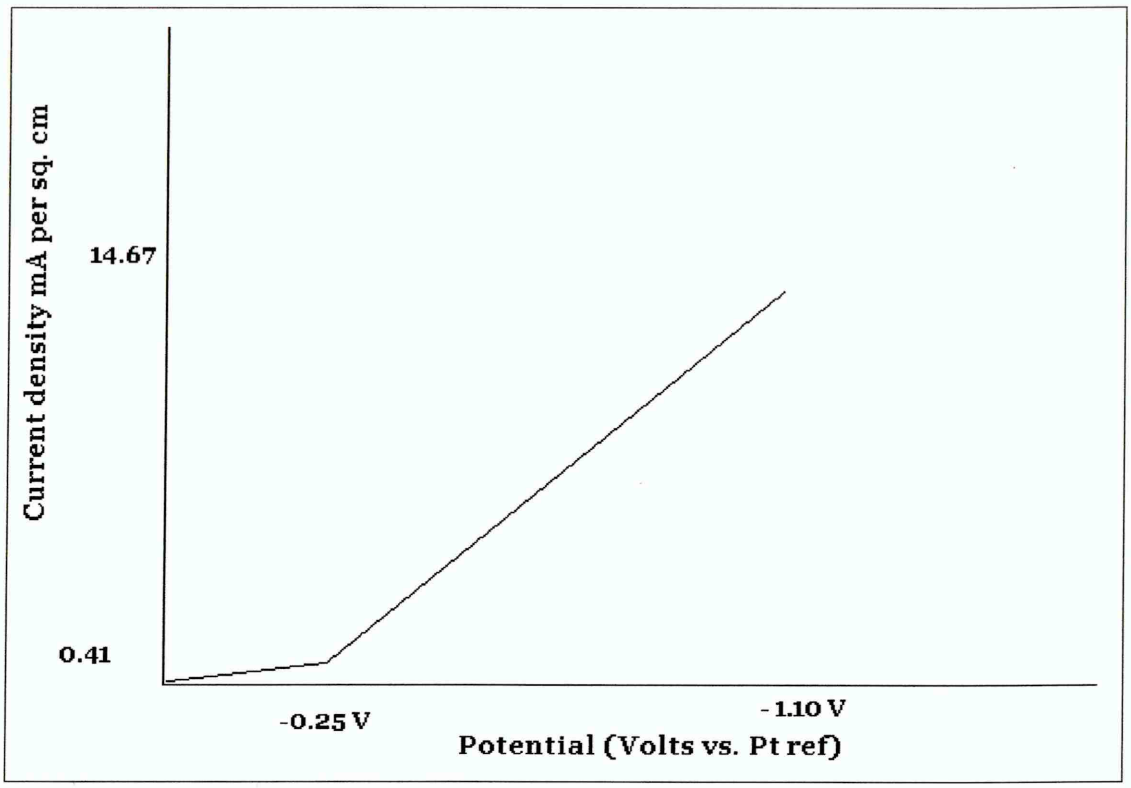

Figure 6.5 Voltammogram obtained at 185 ^{O}C from a stationary ITO electrode in an unstirred EG solution containing 0.08 mol dm^{-3} $InCl_3$, 0.03 mol dm^{-3} $SbCl_3$ and 0.20 mol dm^{-3} TEAC.

Deposition Potential Volts vs. Pt Ref.	Maximum Current Density mA cm^{-2}	Results Of XRD Analysis
-0.50	1.63	Sb
-0.60	2.89	Sb
-0.70	5.64	Sb
-0.80	6.00	Sb
-0.90	7.86	Sb
-1.00	8.78	Sb
-1.10	9.01	Sb
-1.20	9.29	Sb
-1.30	10.67	Sb
-1.40	11.44	Sb
-1.50	13.53	Sb

Table 6.3 Summary of the XRD analysis of films deposited under the conditions described in the text.

Black powdery films consisting of hcp Sb also formed during the electrolysis of baths containing high ratios of $InCl_3$ to $SbCl_3$ (0.3 mol dm^{-3} & 0.01 mol dm^{-3} respectively, with 0.2 mol dm^{-3} TEAC). Electrodeposition was performed at potentials between -0.5 V and -1.50 V at 185 ^{o}C. The identity of the most intense diffraction peak was seen to broadly vary with deposition potential, and texture effects were observed for films deposited at the most positive and negative potentials, figure 6.7. The origins of this variation in texture are unclear, especially given the various competing phenomena occurring during deposition. Possible explanations could be (a) a difference in the activation energies for growth on the various crystallographic planes (chapter two, section 2.6) and (b) dissimilar adsorption 'strengths' of the supporting electrolyte on the growing crystal faces.

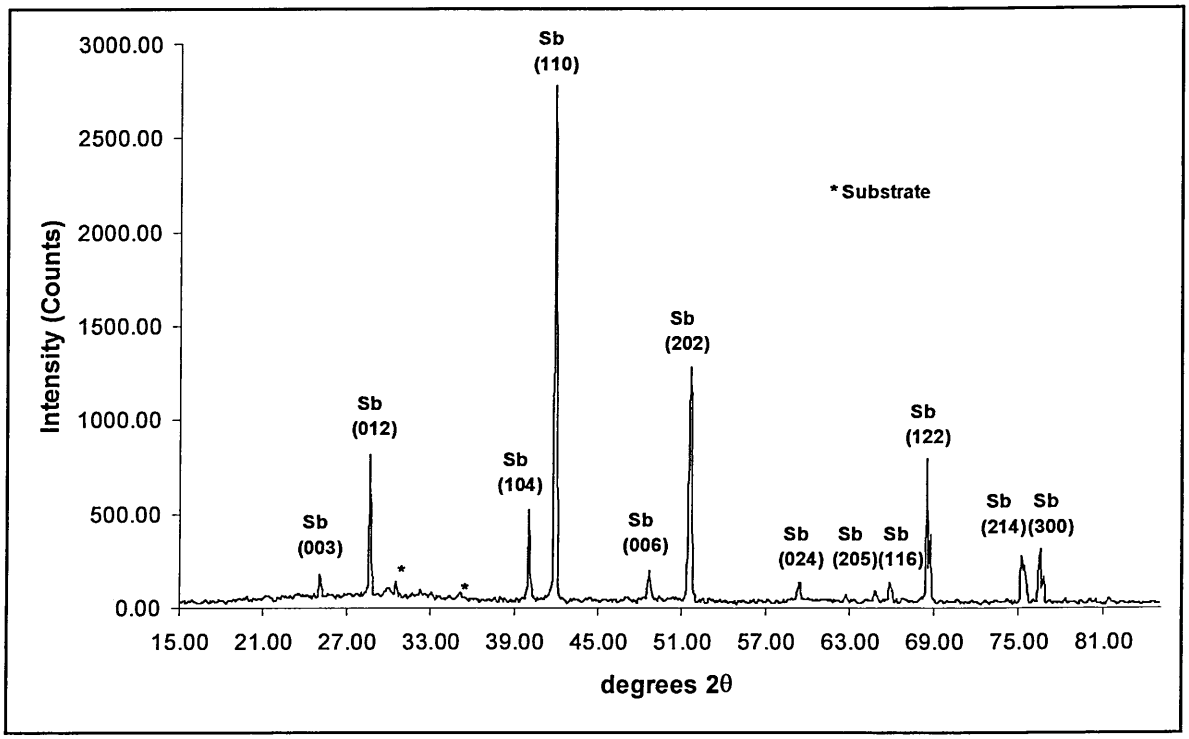

Figure 6.6 XRD pattern of film deposited at –1.50 V (vs. Pt ref.).

The results presented thus far indicate an absence of crystalline indium in the films deposited under the conditions described above. Therefore, it was concluded that a short investigation of the electrodeposition of elemental indium and antimony from EG electrolyte solutions was warranted.

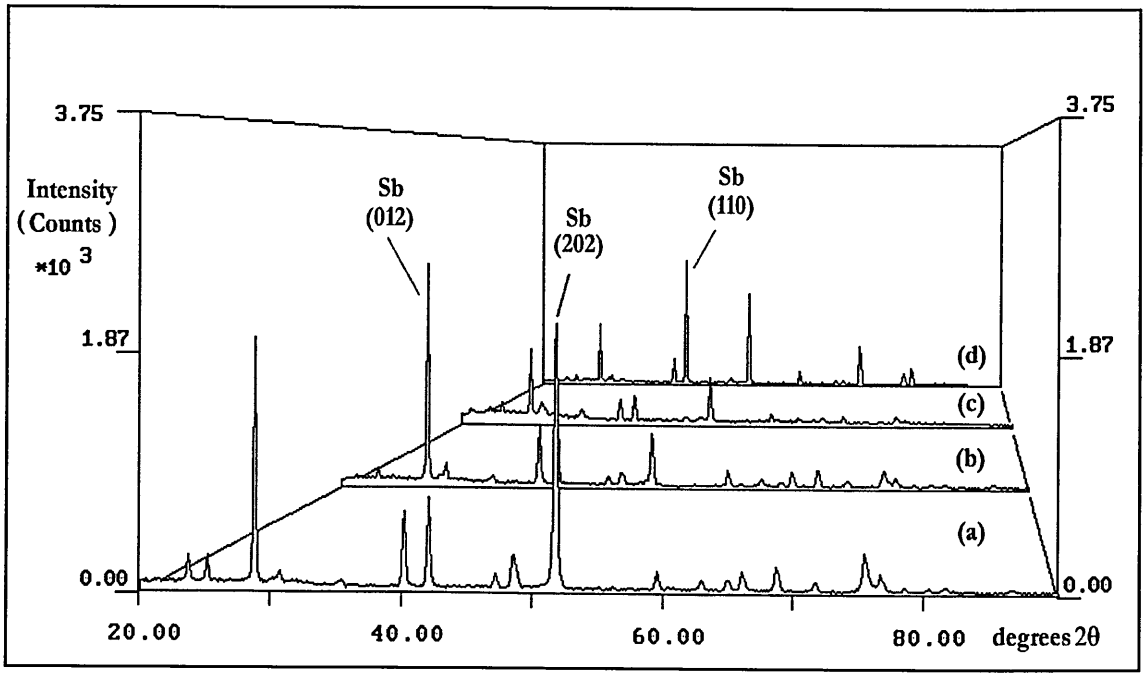

Figure 6.7 Diffraction patterns of films grown at (a) –0.50 V, (b) - 0.60 V, (c) - 0.70 V and - 1.50 V (vs. Pt ref.), from baths containing 0.3 mol dm^{-3} $InCl_3$, 0.01 mol dm^{-3} $SbCl_3$ & 0.2 mol dm^{-3} TEAC at 185 ^{o}C. For clarity, only the most intense reflections are labelled.

6.5 Electrodeposition of Elemental Sb and In from EG Electrolyte Solutions

Though not extensively studied, both In and Sb may readily be electrodeposited from aqueous solutions. Consequently, there exist several established methods in the literature, and a review of these elements' electroplating can be found in Lowenheim (1963). Typically, deposition involves galvanostatic plating from aqueous solutions, with indium being deposited from a metal/d-glucose complex in an alkaline cyanide bath[2], and Sb being plated from acid-citrate baths. On the other hand, deposition of these elements from organic solutions has not been particularly studied and, to the author's knowledge, no 'off the shelf' protocols can be found in the literature.

---

[2], Alkaline conditions are required whilst utilising cyanide baths to prevent the HCN formation. Complexation of the metal is necessary, as indium hydroxide is insoluble.

6.5.1 Electrodeposition of Elemental Sb from EG Electrolyte Solutions

Voltammograms were obtained from solutions of $SbCl_3$ (0.1 mol dm^{-3}) in EG at 185 ^{o}C, with and without (0.2 mol dm^{-3}) TEAC. Generally, the forms of the voltammograms were similar to that of figure 6.8. However, the potential at which the cell current began to rise to a significant level (- 0.30 V) was 400 mV more negative for the solution without TEAC. This can be explained in terms of a decrease in solution resistance caused by the presence of the TEAC, section 6.1. A series of films was deposited between –0.60 V and –3.00 V from TEAC containing plating solutions at 185 ^{o}C. Films grown at potentials below -1.00 V gave XRD patterns (figure 6.9) indicating the formation of amorphous deposits. SEM analysis (figure 6.10) showed that the morphology of the films was predominately powdery, with small clusters of 'whisker' features. At potentials more negative than -1.00 V, loosely adherent films of hcp Sb formed. These films' SEM micrograms revealed the formation of a compact base layer, on top of which <1 μm nodules were present.

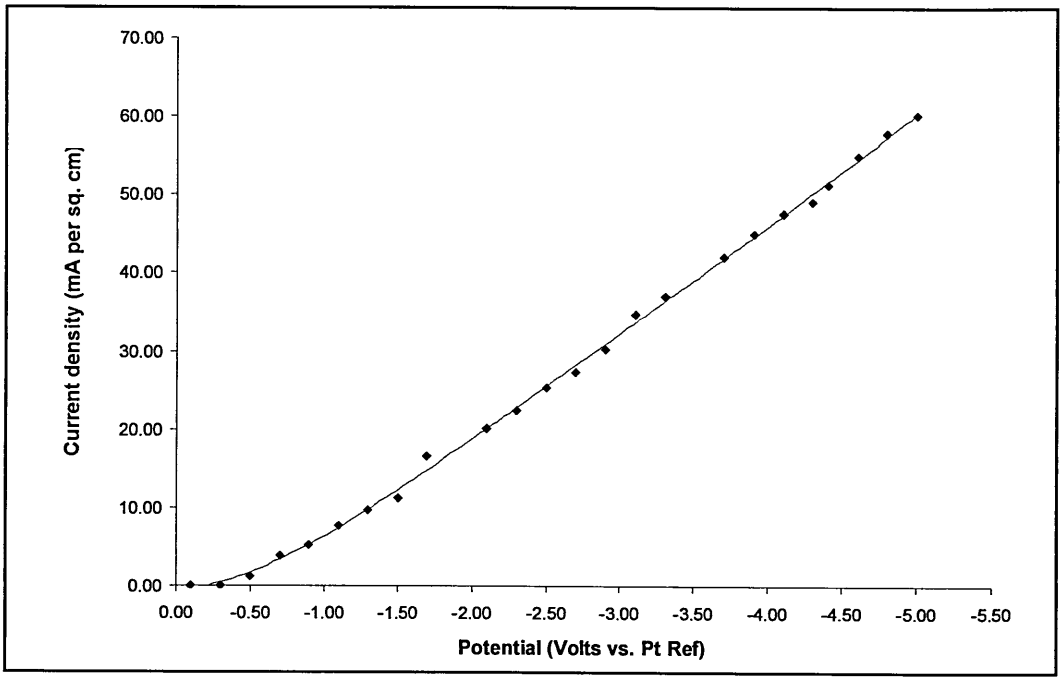

Figure 6.8 Voltammogram obtained at 185 ^{o}C with a stationary ITO electrode in an unstirred EG solution containing of 0.1 mol dm^{-3} $SbCl_3$ and 0.2 mol dm^{-3} TEAC.

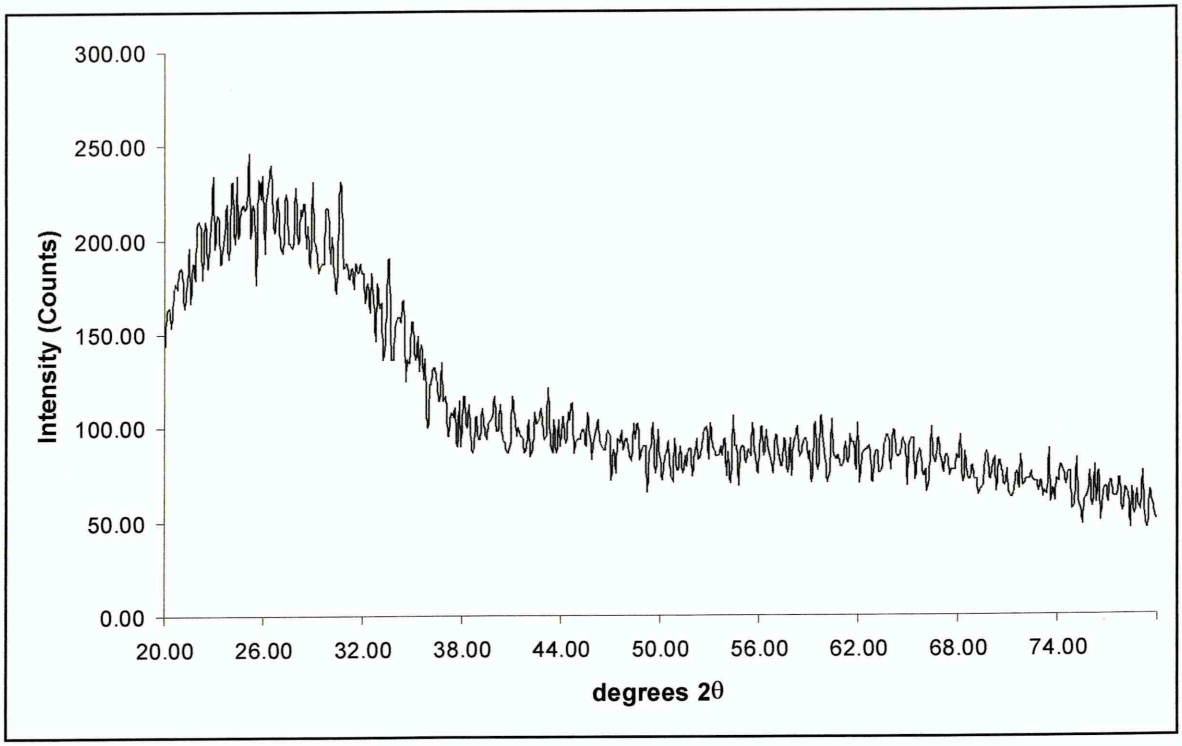

Figure 6.9 XRD pattern of a film deposited at –0.90 V (vs. Pt ref.).

Figure 6.10 SEM micrograph of a film deposited at –0.90 V (vs. Pt ref.).

6.5.2 Electrodeposition of Elemental In from EG Electrolyte Solutions

Voltammograms (figure 6.11) were collected from EG baths at 185 ^{o}C containing $InCl_3$ (0.1 mol dm^{-3}) with and without TEAC (0.2 mol dm^{-3}). As for those collected during the study of Sb deposition (section 6.5.1), the voltammograms indicated that the potential (-0.90 V) at which the current density rose from negligible levels was more positive (~500 mV) for solutions containing TEAC. Films were then grown from TEAC containing solutions at 185 ^{o}C, at deposition potentials between -1.00 V and -4.00 V. XRD patterns (figure 6.12) of the films grown at more positive potentials than -2.00 V showed the formation of amorphous deposits. In contrast, those deposits grown at potentials more negative than - 2.00 V yielded XRD patterns (figure 6.13) of tetragonal In. Only the most intensive reflection from In (In (101)) could be identified. This was because reflections from the other planes are relatively weak, for example the In (110) peak's intensity is 26 % that of the In (101) peak. In addition, the reflections from the In deposit were 'swamped' out by those from the substrate, because the electrodeposits were thin. Under the SEM (figure 6.14), the layers appeared to consist of a continuous compact bottom layer, on top of which an evenly distributed series of ~ 0.5 μm nodules had grown. Visually, the films were light grey and adhered well to the substrate.

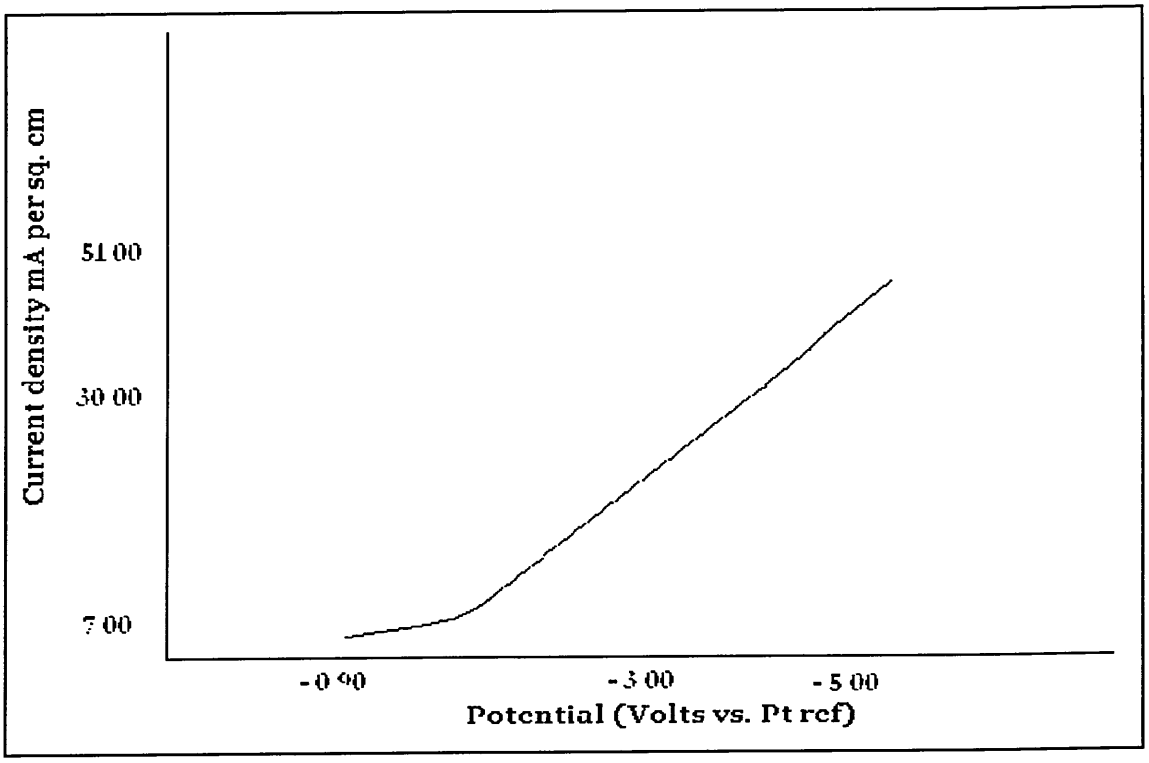

Figure 6.11 Voltammogram obtained at 185 ^{O}C from a stationary ITO electrode in an unstirred EG solution containing 0.1 mol dm^{-3} $InCl_3$ and 0.2 mol dm^{-3} TEAC.

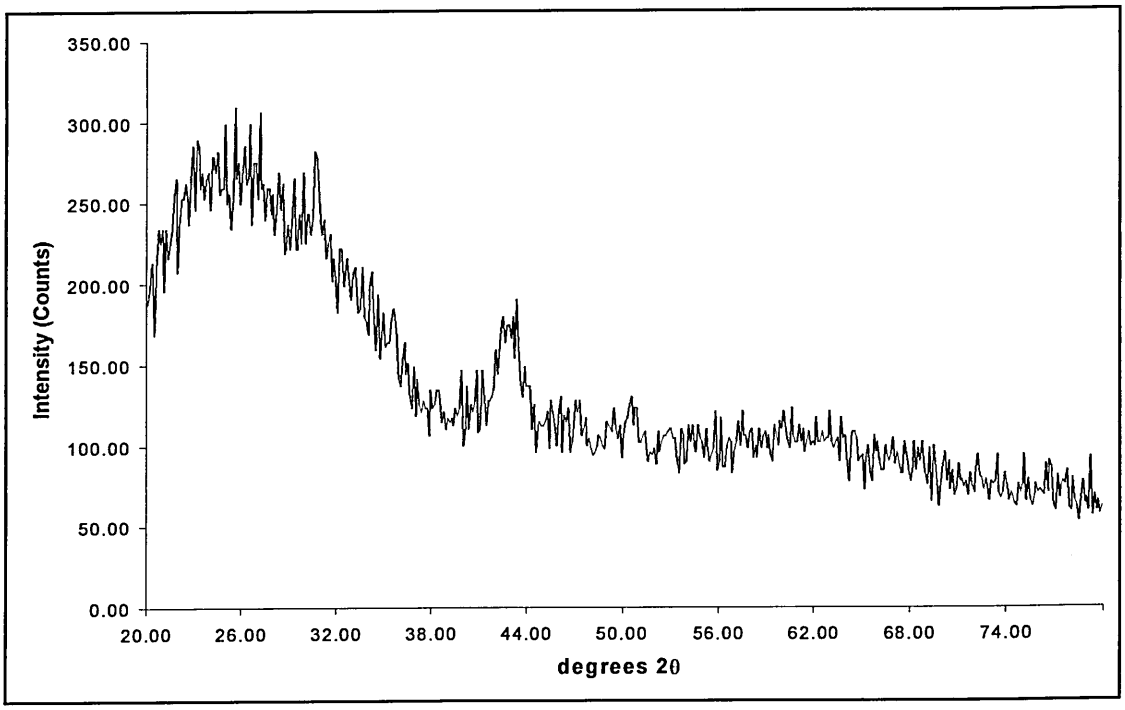

Figure 6.12 XRD pattern of a film deposited –1.50 V (vs. Pt ref.).

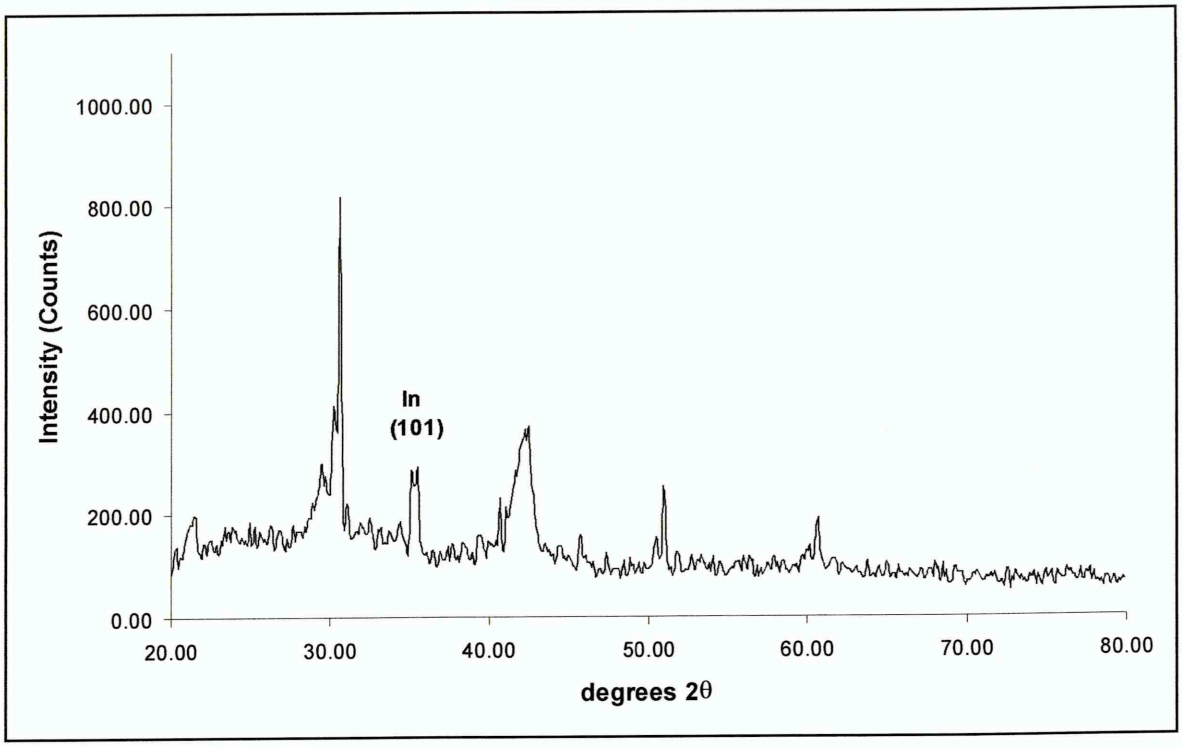

Figure 6.13 XRD pattern of a film deposited at –3.50 V (vs. Pt ref.). Peaks not labelled are due to the substrate.

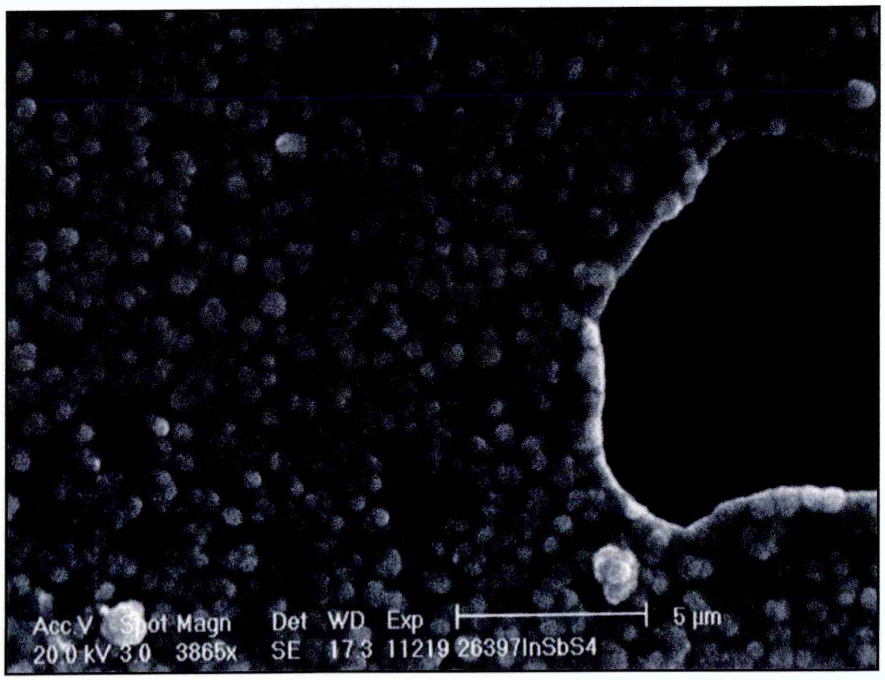

Figure 6.14 SEM micrograph of a film deposited at –3.50 V (vs. Pt ref.).

The above results indicate that the potentials at which both elements deposited from EG solutions were more negative than their aqueous counterparts, section 5.1. Further, as in the case for aqueous systems, the deposition potential of Sb from EG solutions occurs at much more positive reduction potentials than In, i.e. Sb is the noble species, section 2.2.3. The InSb growth experiments thus far described (sections 6.3 & 6.4) were performed at potentials that were only slightly more negative (up to and including - 1.50 V) than those applied during the aqueous InSb deposition studies, chapter five. Therefore, it was reasonable to assume that the results of the study of elemental Sb and In electrodeposition suggested that InSb deposition required the application of more negative potentials.

6.6 Study of InSb Electrodeposition from Chloride Solutions with TEAC- Part II

Voltammograms (figure 6.15) were collected at 185 ^{o}C from solutions whose compositions were the same as those used in section 6.4, i.e. $InCl_3$ (0.08 mol dm^{-3}), $SbCl_3$ (0.03 mol dm^{-3}) and 0.20 mol dm^{-3} TEAC. The voltammograms collected in this part of the study (figure 6.15) covered a greater range of potentials than before (section 6.4, figure 6.5), namely, -0.00 V to - 5.00 V, rather than 0.00 V to - 1.50 V. These voltammograms had two points (~ - 0.30 V & - 1.80 V) at which a sharp rise in current density was observed. Consequently, depositions were performed over a much broader range of potentials, spanning -1.00 V to - 4.50 V, table 6.4.

Films containing crystalline InSb material were generated for the first time during this study of non-aqueous InSb electrodeposition systems. These films, deposited at potentials more negative than - 2.00 V, gave XRD patterns indicating the formation of admixes of tetragonal In, hcp Sb and fcc InSb. The relative proportions of the In and Sb phases, as indicated by their XRD peak intensities, were seen to vary with deposition potential, figures 6.16 to 6.19. Specifically, the films' crystalline In contents were highest for films grown at the more negative potentials. One film deposited at - 3.00 V gave an XRD pattern suggesting the formation of a thin layer of fcc InSb without any co-phases, figure 6.20. Unfortunately, this result could not be repeated following numerous attempts.

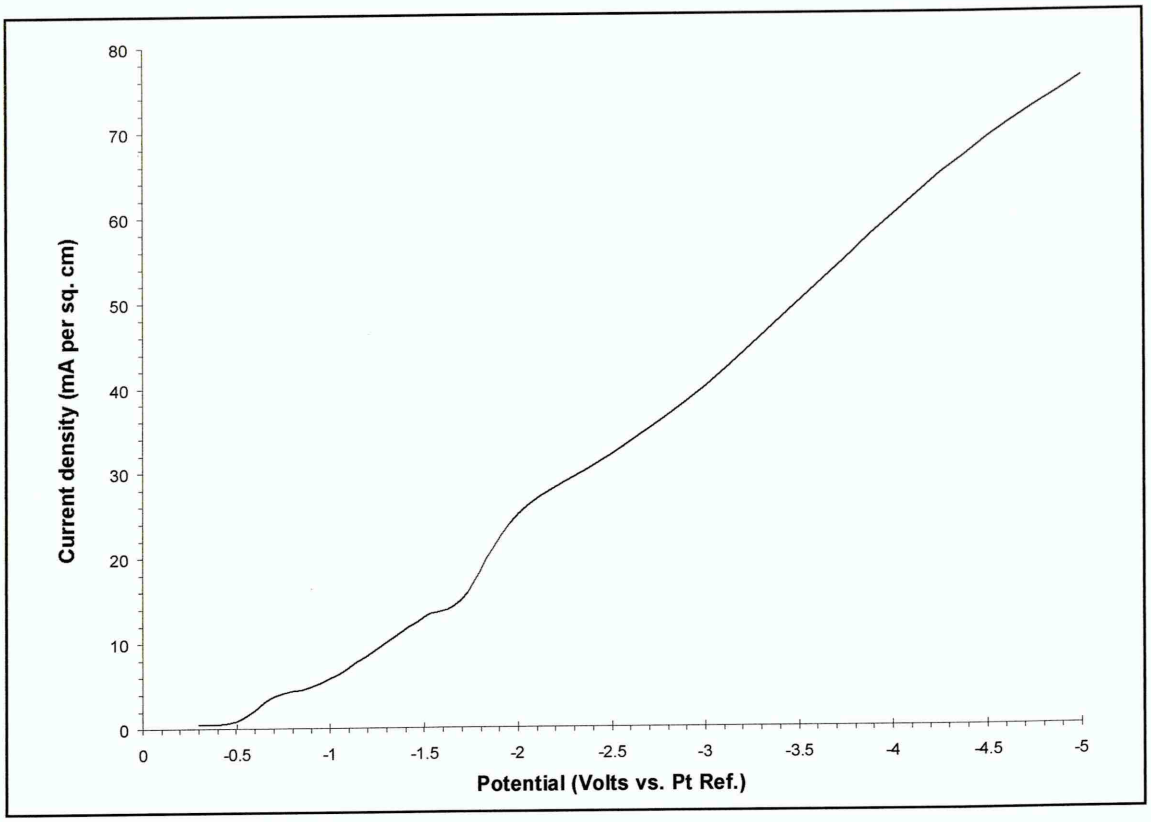

Figure 6.15 Voltammogram obtained at 185 ^{O}C from a stationary ITO electrode in an unstirred EG solution containing 0.08 mol dm^{-3} $InCl_3$, $SbCl_3$ 0.03 mol dm^{-3} and 0.2 mol dm^{-3} TEAC.

Deposition Potential Volts vs. Pt Ref.	Maximum Current Density mA cm^{-2}	Results Of XRD Analysis
-1.00	11.00	Sb
-1.50	14.48	Sb
-2.00	18.96	Sb
-2.25	20.80	(In), InSb, Sb
-2.50	21.49	(In), InSb, Sb
-2.75	22.35	(In), InSb, Sb
-3.00	23.45	In, InSb, (Sb)
-3.25	24.00	In, InSb, (Sb)
-3.50	31.59	In, InSb, (Sb)
-3.75	33.15	In, InSb, (Sb)
-4.00	32.29	In, InSb, (Sb)
-4.25	41.45	In, InSb, (Sb)
-4.50	56.55	In, InSb, (Sb)

Table 6.4 Summary of the XRD analysis of films under the conditions described in the text, the brackets indicate which phase has relatively the least intense peaks.

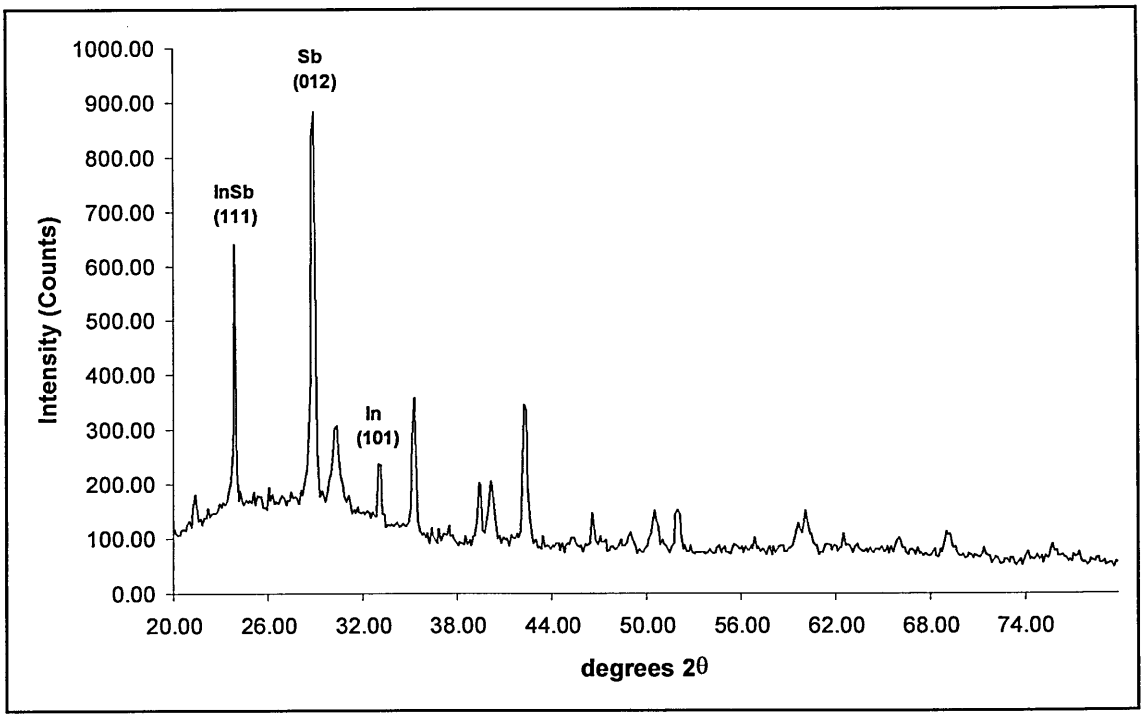

Figure 6.16 XRD pattern of a film deposited –2.75 V (vs. Pt ref.), illustrating the most intense peaks from the film's In, Sb and InSb phases.

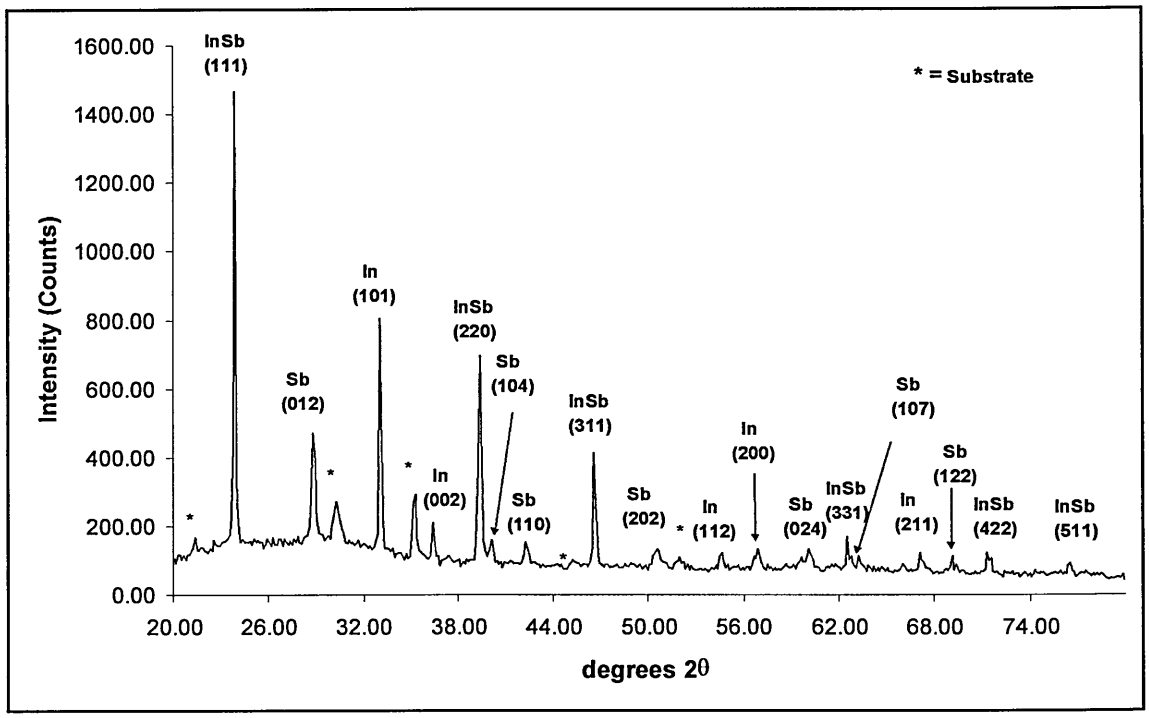

Figure 6.17 XRD pattern of a film deposited –3.00 V (vs. Pt ref.).

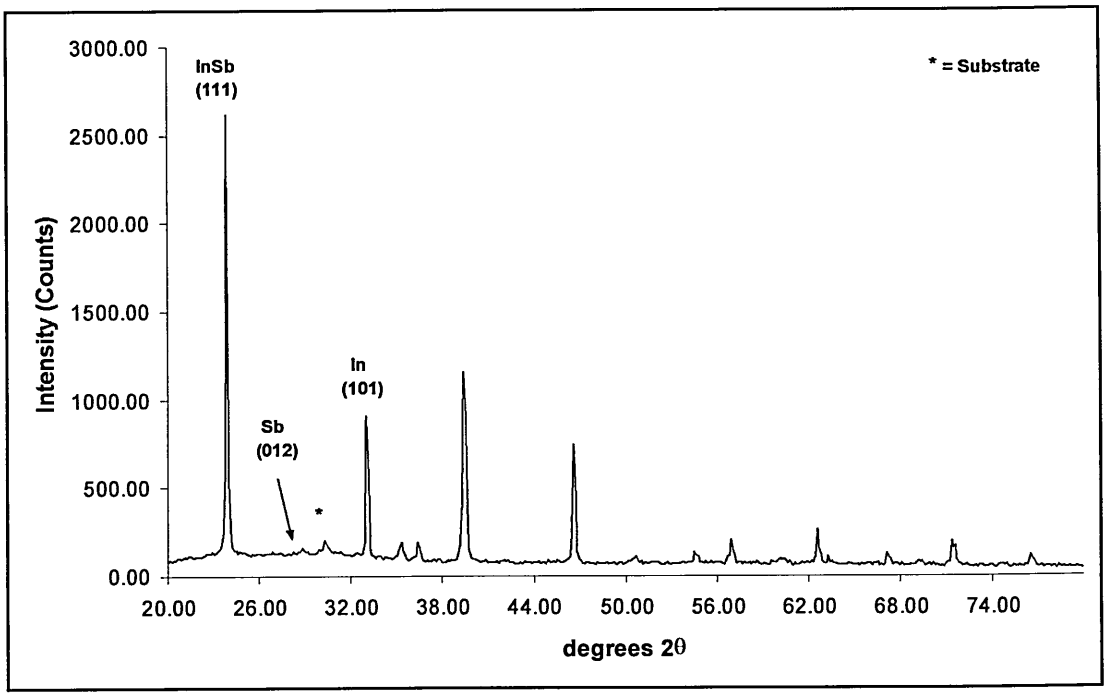

Figure 6.18 XRD pattern of a film deposited –3.75 V (vs. Pt ref.) illustrating the most intense peaks from the film's In, Sb, InSb phases and the substrate (*).

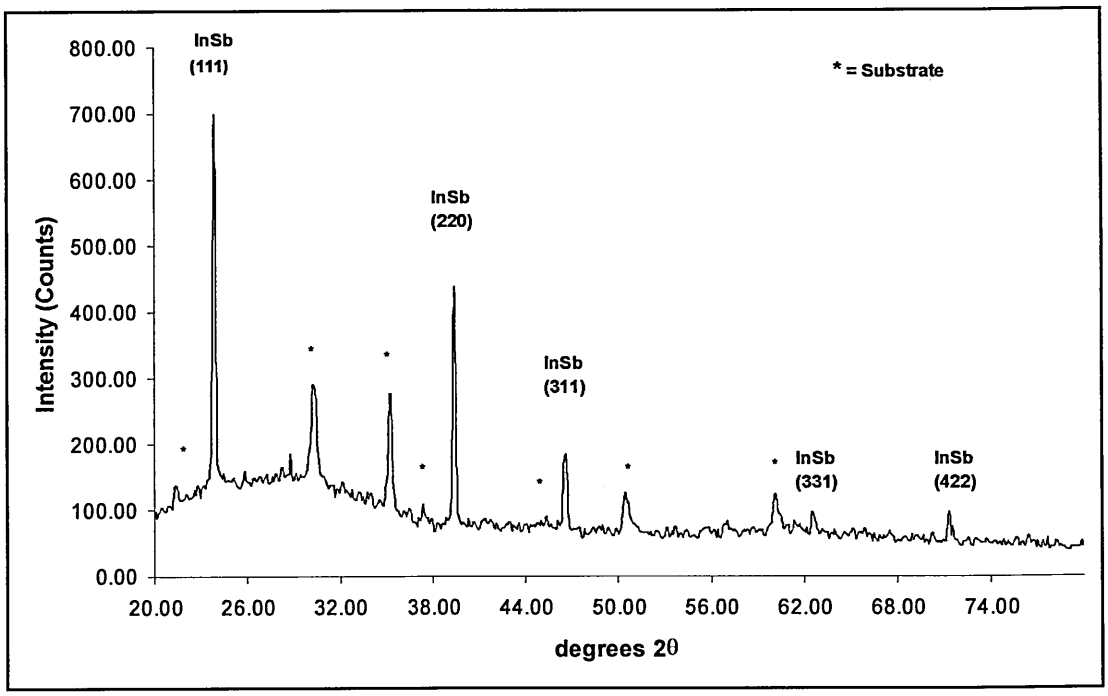

Figure 6.19 XRD pattern of a fcc InSb film deposited –3.00 V (vs. Pt ref.), see text.

Estimates of particle size were calculated for those films whose XRD patterns indicated an absence of any significant hcp Sb co-phase (chapter five, section 5.6). These were found to be on average approximately 75 nm, and films grown at potentials more negative than - 4.00 V had smaller (68-70 nm) particle sizes.

The visual appearance of the films generally changed with deposition potential. Those grown at potentials between - 1.75 V and - 2.50 V were silver to light grey in appearance, whilst those deposited at more negative potentials were nearly black in colour. It is reasonable to suggest that throughout this investigation, some of the films' variation in colour reflected differences in sample thickness. For example, all the films described in this section were grown for the same amount of time (1.5 minutes). Given that higher currents were achieved with the more negative potentials, it can be assumed that darker films were the thickest. Other factors should also be considered, for example, electrodeposited Sb films are typically black with a bluish tint, Mellor (1929). In addition, electrodeposited layers that are smooth (on a scale of 10 nm or so) reflect light specularly and appear 'bright', West (1971). All films adhered reasonably well to the substrate, though peeling was observed in the case of those samples deposited at the most negative potentials. Under the SEM, the films presented a multitude of features. Large areas of the films had an appearance that could best be described as akin to that of 'dry cracked mud'; figure 6.20, with large plateau regions dispersed on a layer of sub-micron sized nodules. As well as the aforementioned features, the films grown at potentials more negative than - 3.00 V had a homogeneous covering of 1-2 μm sized nodules, figure 6.21. 'Spot' EDX analysis (figure 6.22) was performed on selected films to see if the various aforementioned features had different compositions, though the process was complicated by the analysed material's thinness. This meant that the spectra included large Si, Sn, and it can be assumed, In signals from the ITO substrate. Another noticeable feature of the spectra was the large signal detected from a chloride.

These results above clearly demonstrate that InSb deposition from EG requires more negative deposition potentials than that used with aqueous solutions. XRD showed that the formation of crystalline admixtures of In, Sb and InSb predominated. Further, the deposition potential was seen to have an effect on the relative proportions of the crystalline phases. The next stage of the investigation studied the effect of the plating bath's composition on the relative proportions of these of crystalline phases.

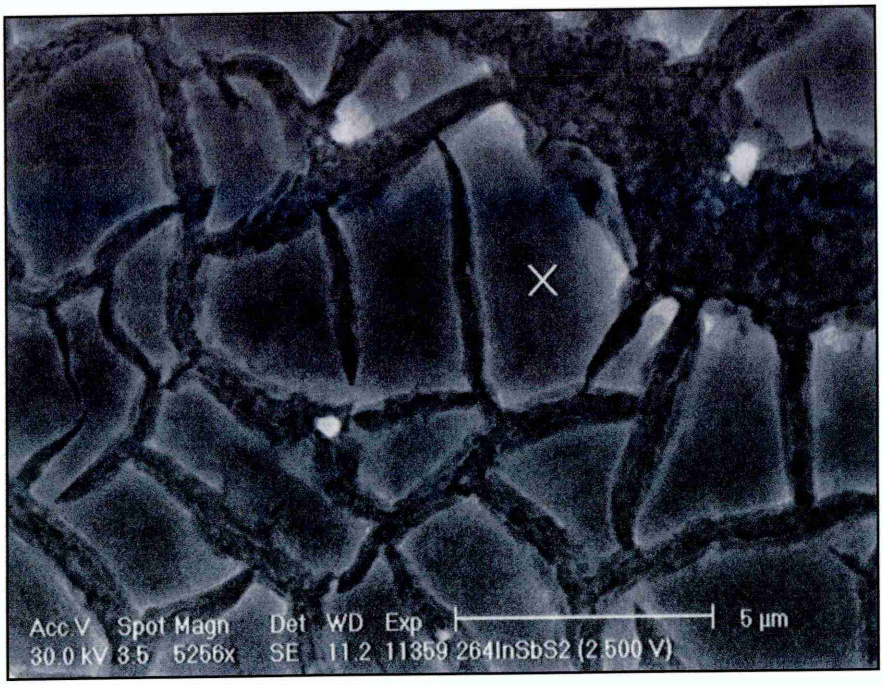

Figure 6.20 SEM micrograph of a film deposited at –2.75 V (vs. Pt ref.), the cross indicates a position where spot EDX analysis was performed.

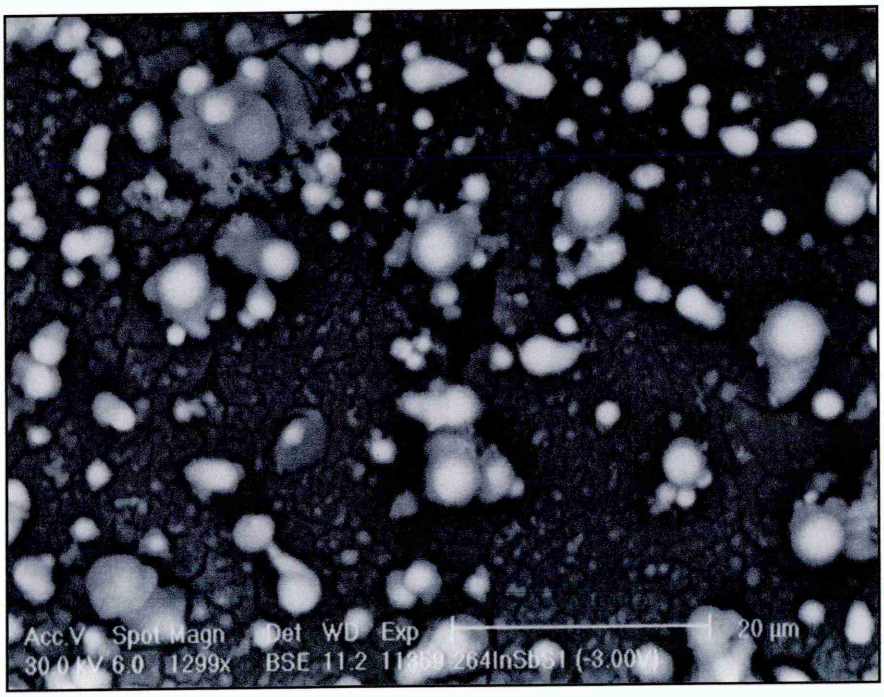

Figure 6.21 SEM micrograph of a film deposited at –3.25 V (vs. Pt ref.).

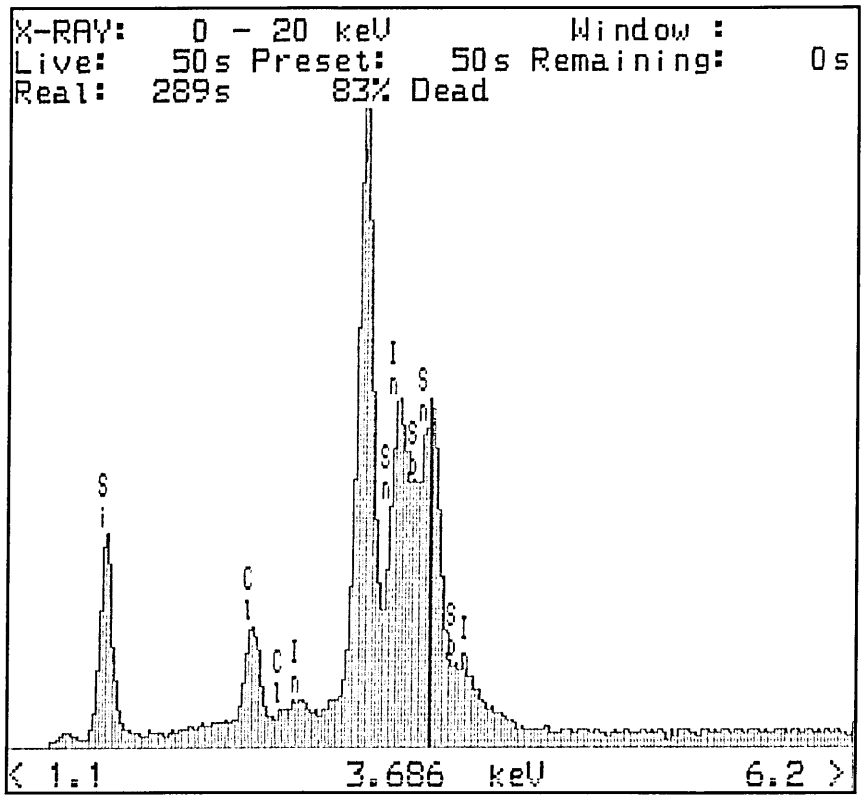

Figure 6.22 'Spot' analysis EDX spectra collected from an island plateau (as indicated by the cross in figure 6.20) on a film deposited at –2.75 V (vs. Pt ref.).

6.6.1 Study of the Relationship between Plating Bath and Film Composition

A series of electrolyte solutions of various $InCl_3$ and $SbCl_3$ 'metal percentages' (chapter five, section 5.4.3) were electrolysed to determine the relationship between plating bath composition and the relative proportions of the films' crystalline phases. The concentration of TEAC was the same (0.2 mol dm^{-3}) for every bath, whose compositions are given in table 6.5. All depositions were carried out at 185 ^{o}C on ITO substrates, at potentials between - 1.75 V and - 4.75 V, unless otherwise stated. An extensive review of the results obtained from Bath NA1 has already been given in the preceding sections 6.4 and 6.6.

As with Bath NA1, films grown from Bath NA2 demonstrated a dependence of film composition on deposition potential, and the results of the XRD analysis is given in table 6.6. Admixes of tetragonal In, hcp Sb and fcc InSb phases formed across a wide range (- 2.00 V) of potentials, figures 6.23 to 6.26. The intensity of the peaks attributable to the hcp Sb co-phase first decreased, and after levelling off, began to increase again. This suggests that the deposition of In begins to reach its maximum rate after - 4.25 V, figure

6.26. The XRD peak intensity for the In and Sb co-phases remained relatively equal whilst depositing at potentials between - 3.00 V and - 3.50 V, figure 6.24. Samples grown in this potential window were annealed under nitrogen at 250 ^{o}C for 45 minutes. This led to an increase in the intensity of the XRD peaks of In and Sb co-phases, rather than the formation of more InSb, figures 6.24 and 6.25. The average particle size (75 μm) was approximately the same for the annealed and as grown samples.

Plating Bath Reference	$SbCl_3$ (mol dm^{-3})	$InCl_3$ (mol dm^{-3})	$InCl_3$ 'metal percentage' (%)
Bath NA1	0.030	0.080	73
Bath NA2	0.040	0.070	64
Bath NA3	0.055	0.055	50
Bath NA4	0.070	0.040	36
Bath NA5	0.080	0.030	27

Table 6.5 Composition of the plating baths used.

Deposition Potential Volts vs. Pt Ref.	Maximum Current Density mA cm^{-2}	Results of XRD Analysis
-1.75	15.39	Sb
-2.00	14.09	Sb
-2.25	17.77	Sb, (InSb)
-2.50	18.98	(In), InSb, Sb
-2.75	20.05	(In), InSb, Sb
-3.00	20.52	In, InSb, Sb
-3.25	22.84	In, InSb, Sb
-3.50	26.32	In, InSb, Sb
-3.75	28.88	In, InSb, (Sb)
-4.00	30.56	In, InSb, (Sb)
-4.25	31.06	In, InSb, (Sb)
-4.50	36.44	(In), InSb, Sb
-4.75	47.00	(In), InSb, Sb

Table 6.6 Summary of the XRD analysis of films deposited on ITO substrates under the conditions described in the text, the brackets indicate which phase has relatively the least intense peaks.

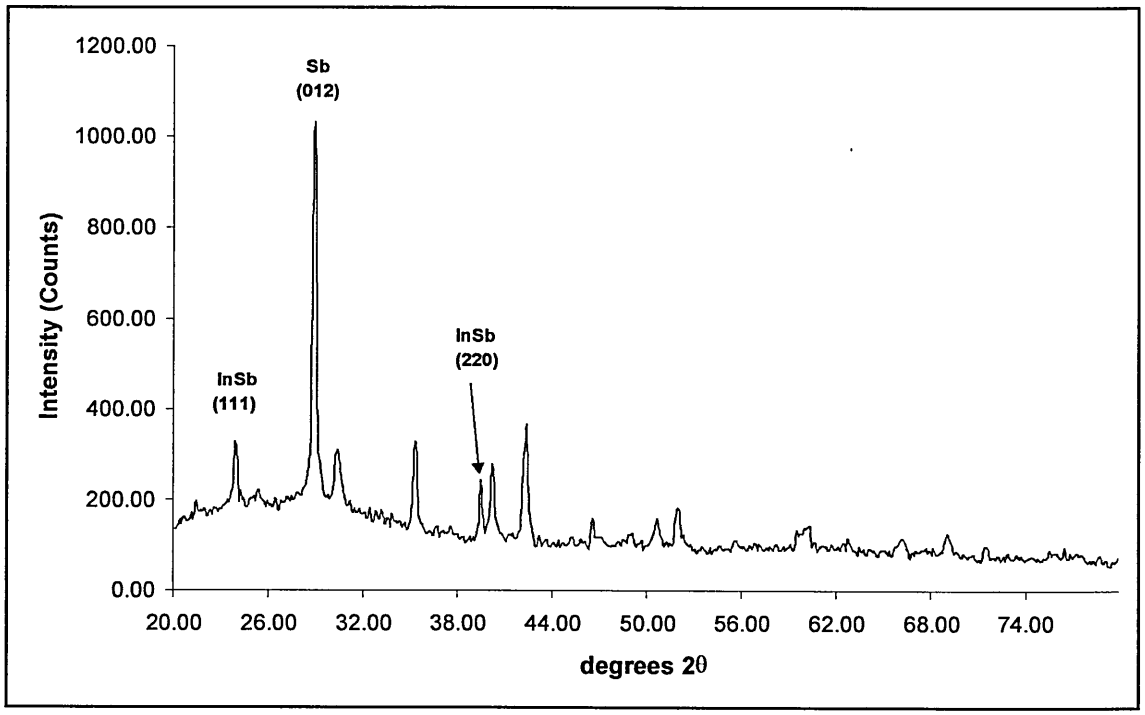

Figure 6.23 XRD pattern of a film deposited at –2.25 V (vs. Pt ref.).

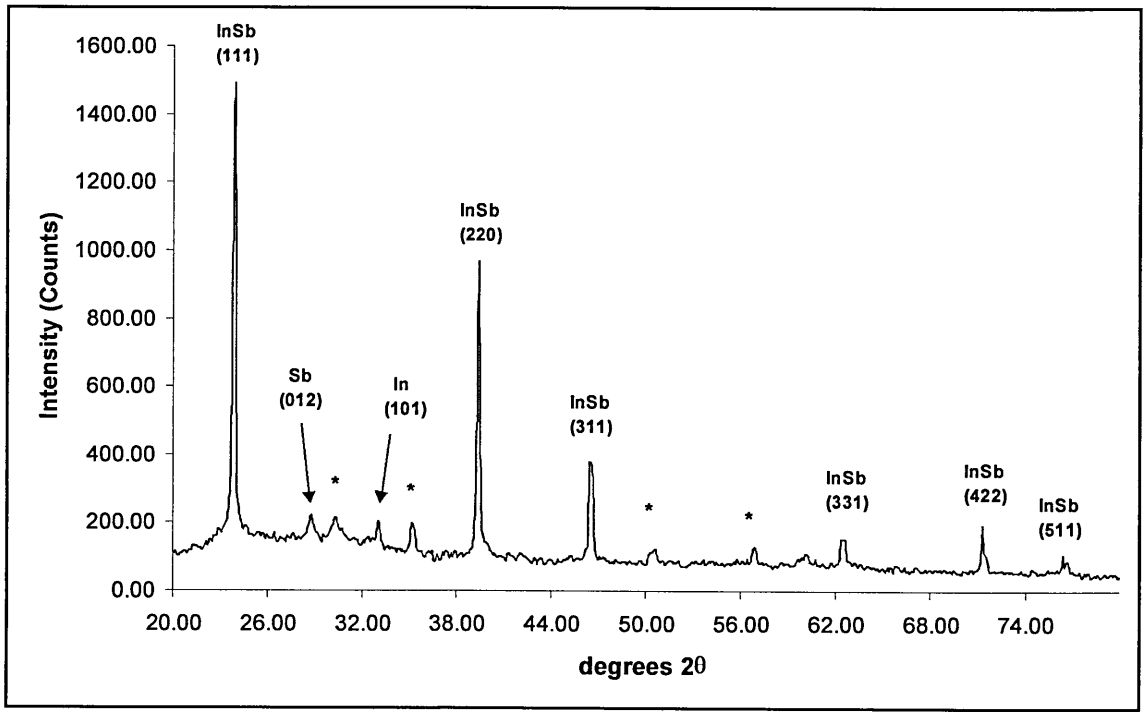

Figure 6.24 XRD pattern of a film deposited at –3.25 V (vs. Pt ref.).

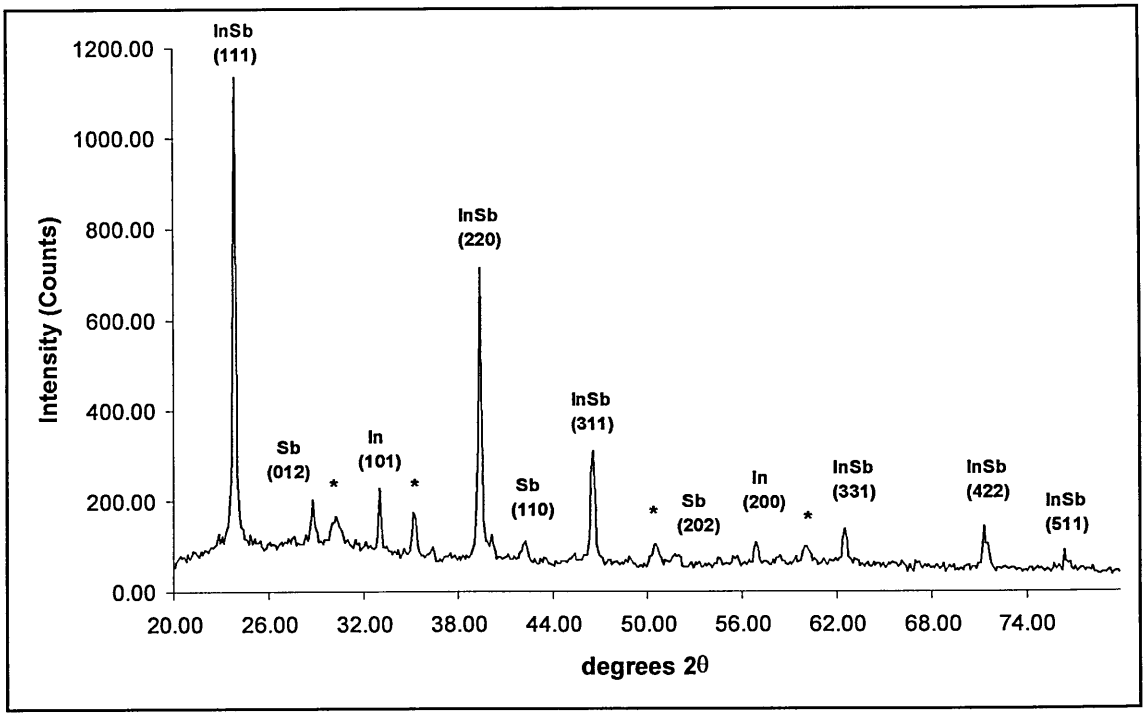

Figure 6.25 XRD pattern of a film deposited at –3.25 V (vs. Pt ref.), which had been annealed under nitrogen for 45 minutes at 250 ^{o}C.

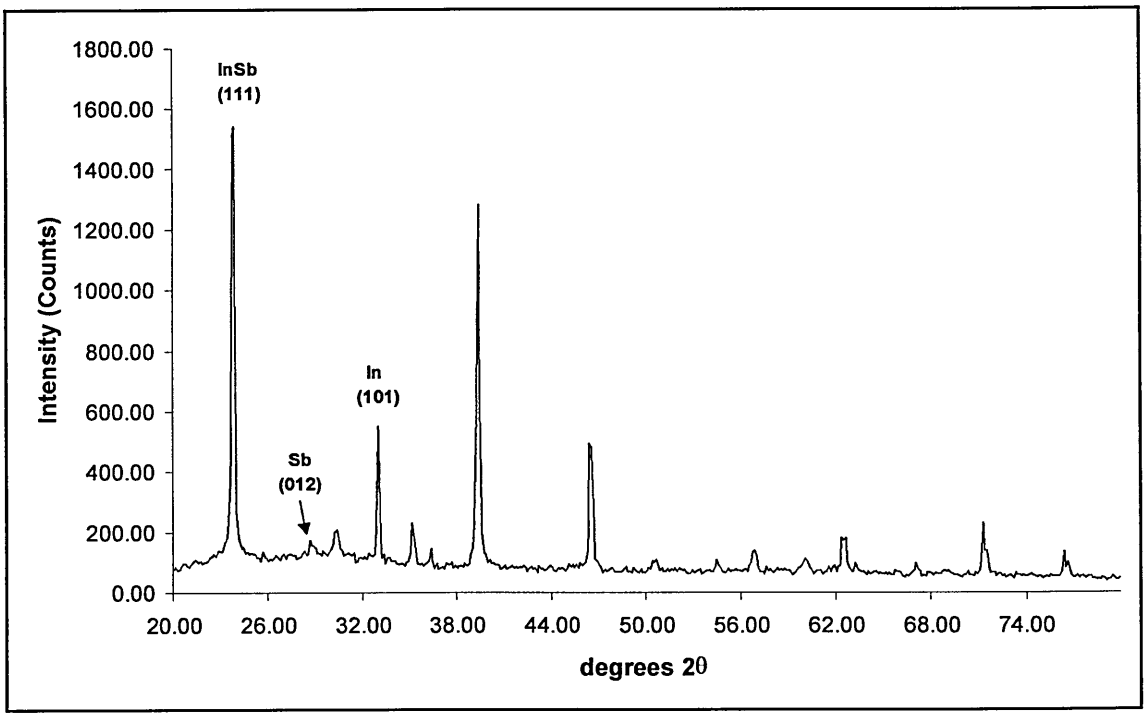

Figure 6.26 XRD pattern of a film deposited at –4.25 V (vs. Pt ref.).

The morphology of the films also changed with deposition potential. The films had a 'cracked mud' appearance under the SEM microscope, as shown in figure 6.20 (section 6.6). For deposits grown at potentials more negative than - 3.00 V, a high density of 1 μm sized nodules, coupled with fine needles, was seen to have developed from the island features that covered the substrate, figure 6.27. EDX spot analysis showed that the area between each of the islands was richer in Sb than the other various morphological features. Finally, the films were generally black in colour, exceptions being those grown at potentials more positive than - 2.50 V that appeared 'burnt' i.e. tarnished silver.

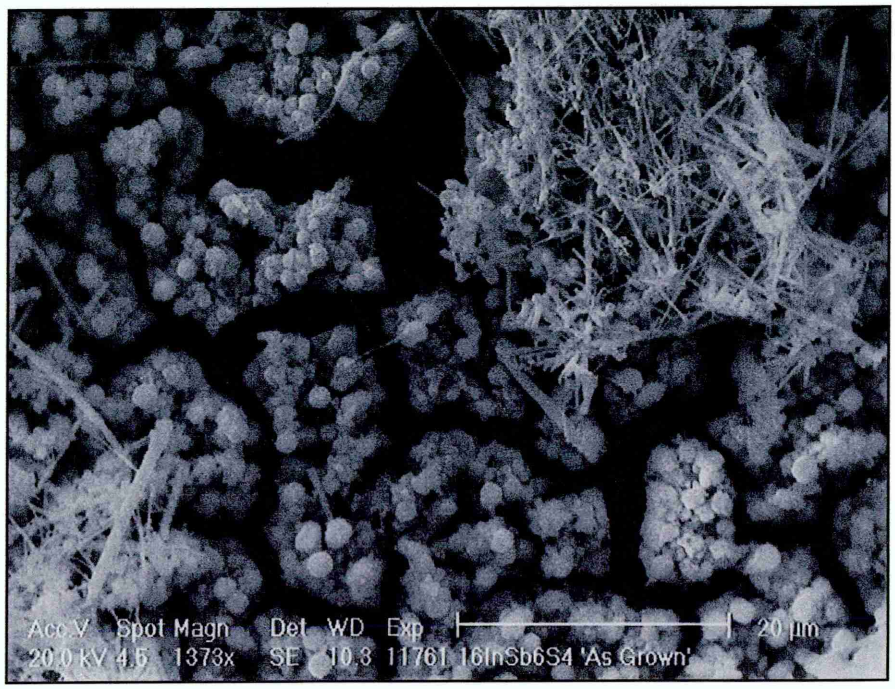

Figure 6.27 SEM micrograph of a film deposited at –3.25 V (vs. Pt ref.).

Under the potential range studied (- 1.75 V and - 4.75 V), Baths NA3 to NA5 all yielded thin grey or black films of hcp Sb only. Nodular growth predominated, and EDX analysis, again, proved limited in determining whether the films contained any In. Further, a chloride was seen to be included in all the films.

The above results suggest that films containing crystalline InSb form only when the concentration of the 'nobler' element (i.e. Sb) in the plating solution is less than that of the 'base' element (i.e. In). Furthermore, the relatively high current densities achieved produced predominately nodular growth, as well as resulting in the films adhering poorly to the substrate. Therefore, it was decided to investigate the electrolysis of solutions

containing much lower concentrations of $InCl_3$ and $SbCl_3$, though with the same metal percentages as used before. Moreover, given that current density is a function of the concentration of the precursor ions (chapter two), the effect of lowering the rate of deposition on the film's composition could be studied.

6.7 Electrodeposition of InSb from an EG Solutions Containing Low Concentrations of $InCl_3$ and $SbCl_3$

Voltammograms were obtained from EG solutions containing 0.007 mol dm^{-3} $InCl_3$, 0.004 mol dm^{-3} $SbCl_3$ and 0.02 mol dm^{-3} TEAC at 185 ^{o}C. They were characterised by an almost linear portion between - 1.75 V and – 2.75 V, following which the current density began to rise further, figure 6.28. At all potentials, the current density was smaller than that achieved when depositing from baths containing higher metal concentrations.

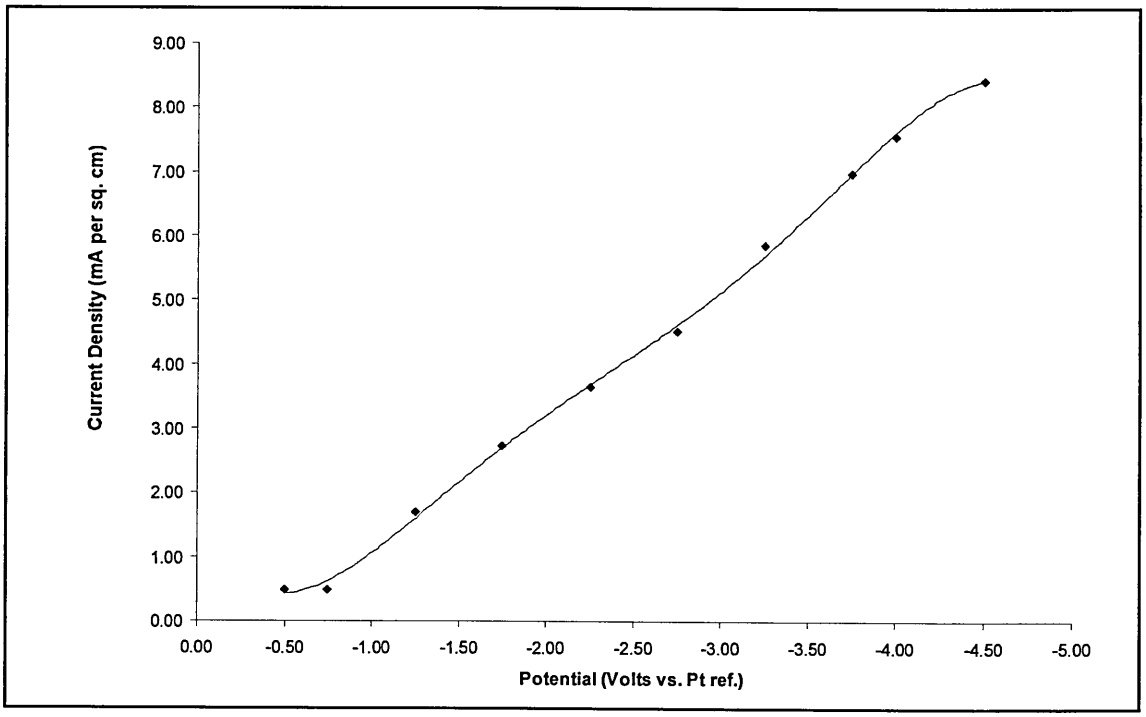

Figure 6.28 Voltammogram obtained at a stationary ITO electrode in an unstirred solution of 0.007 mol dm^{-3} $InCl_3$, $SbCl_3$ 0.004 mol dm^{-3} and 0.02 mol dm^{-3} TEAC at 185 ^{o}C.

A series of films were electrodeposited at potentials between - 1.00 V and – 3.75V. All suffered from poor adhesion, and peeled from the substrate if the growth time was allowed to exceed 90 seconds. In appearance, the deposits were either grey or tarnished (in electroplaters terms, 'burnt') silver. None of the films developed to an extent where all the substrate was covered.

All of the XRD patterns exhibited features corresponding to the presence of large amounts of amorphous material, e.g. 'hump like' features between 20^{O} to 40^{O} 2θ. Usually, this may be attributed to the films being thin, leading to patterns being dominated by features from the (glass)/ITO substrate, figure 5.3 (chapter five). However, this would mean that strong reflections from the ITO would be detected, as well as the amorphous background from the glass underneath. This was not the case for the majority of the patterns collected, as their ITO peaks had small intensities (figures 6.29 and 6.30). Thus, it can be concluded that the amorphous features principally derived from the deposited material. Nevertheless, it was still possible to ascertain that the crystalline composition of the films was dependent on the deposition potential applied, table 6.7.

Deposition Potential Volts vs. Pt Ref.	**Maximum Current Density MA cm^{-2}**	**Results Of XRD Analysis**
-1.00	1.26	Sb
-1.25	5.08	Sb
-1.50	5.88	Sb
-1.75	5.53	InSb, In, Sb
-2.00	5.90	InSb, In, Sb
-2.25	7.24	InSb
-2.50	8.06	InSb, In
-2.75	9.04	InSb, In
-3.00	10.25	InSb, In
-3.25	12.30	InSb, In
-3.50	14.48	InSb, In
-3.75	15.09	InSb, In

Table 6.7 Summary of the XRD analysis of films deposited on ITO substrates under the conditions described in the text.

One series of films whose XRD patterns did show strong reflections from the substrate material were those deposited at - 2.25 V. These patterns also suggested the formation of very thin films of fcc InSb, free of any other crystalline co-phase, figure 6.31. This is confirmed by table 6.8, which compares the d-spacing and relative intensity data from the films with those of the standard PDF data. With the exception of the InSb (400) peak, reflections from all the planes indicated on the PDF card were recorded, though some are not marked on the diffraction pattern (figure 6.31) because of their low intensity. This

result was difficult to reproduce, even with new plating baths and different batches of substrate. As mentioned above, all the films generated during this part of the investigation were limited in thickness, and had a tendency to fall from the substrate during deposition. Hence, in the most part, the films grown under these conditions had XRD patterns such as illustrated by figure 6.32. Whilst these patterns all had strong reflections from the InSb (111) peak, and none from In and Sb co-phases, they were dominated by features from the substrate.

The morphology of the films grown at - 2.25 V was found to be dominated by collections of very small nodules (<< 1 μm) measuring approximately 5 μm and upwards, grown on top of a bed of nodules of similar dimensions, figure 6.33. Finally, EDX analysis showed, in common with most of the materials deposited during this study, that a chloride was present in films generated, figure 6.34.

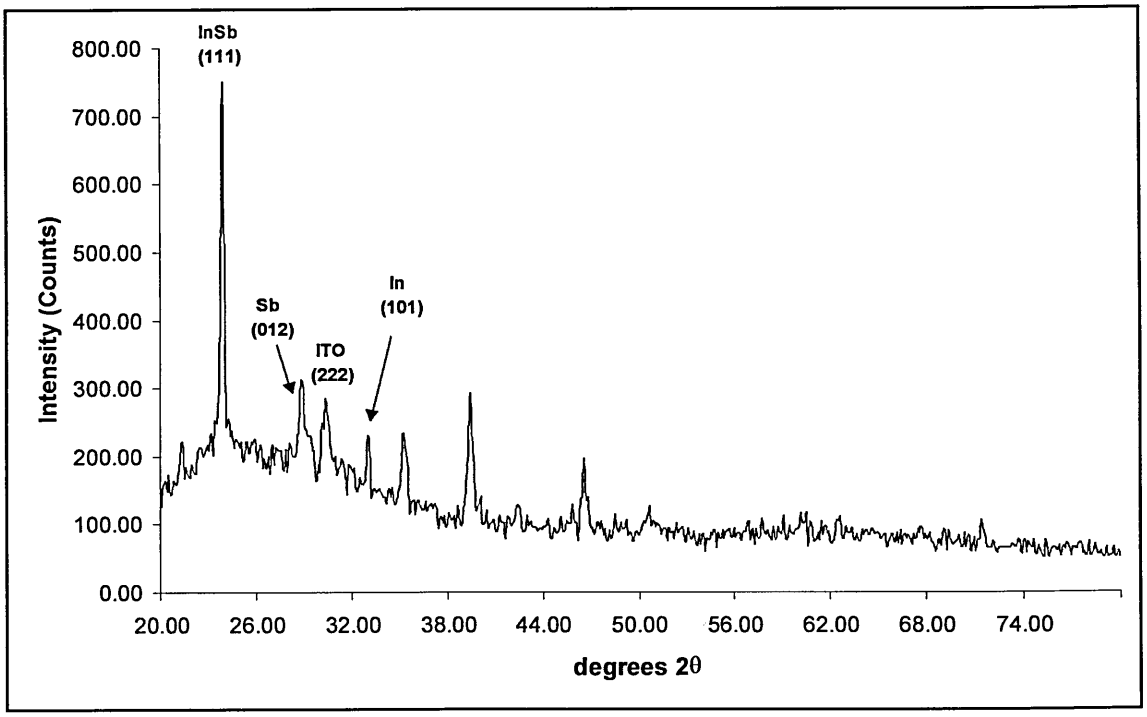

Figure 6.29 XRD pattern of a film deposited at –1.75 V vs. Pt ref.

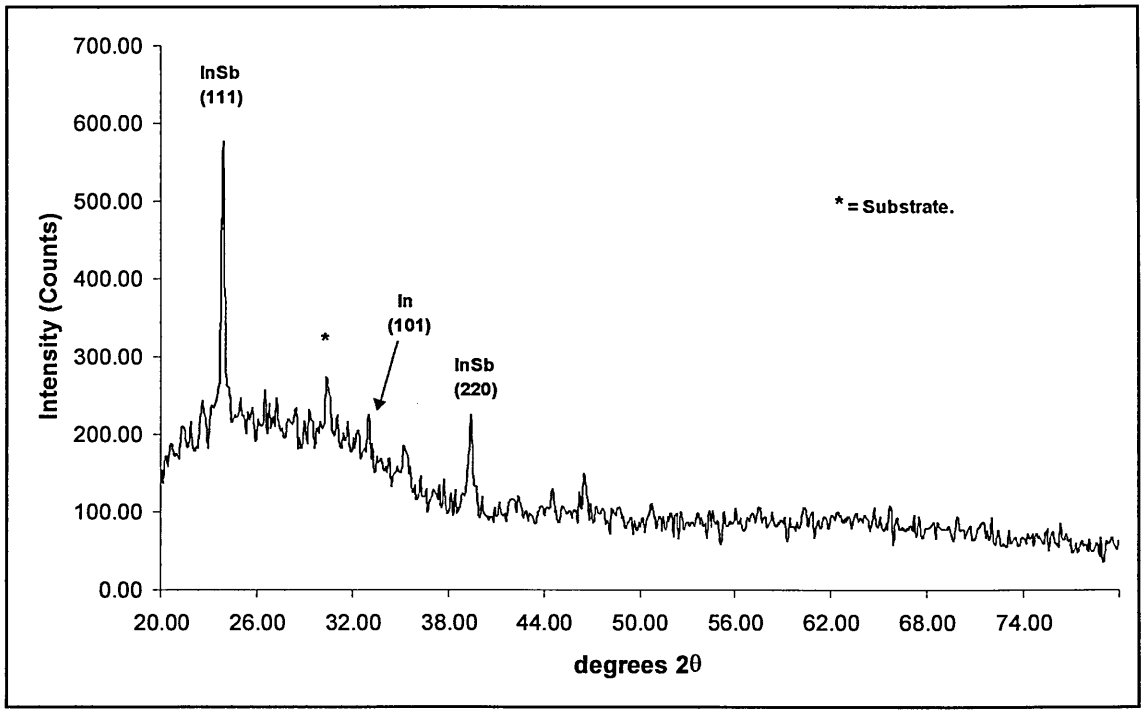

Figure 6.30 XRD pattern of a film deposited at –3.75 V vs. Pt ref.

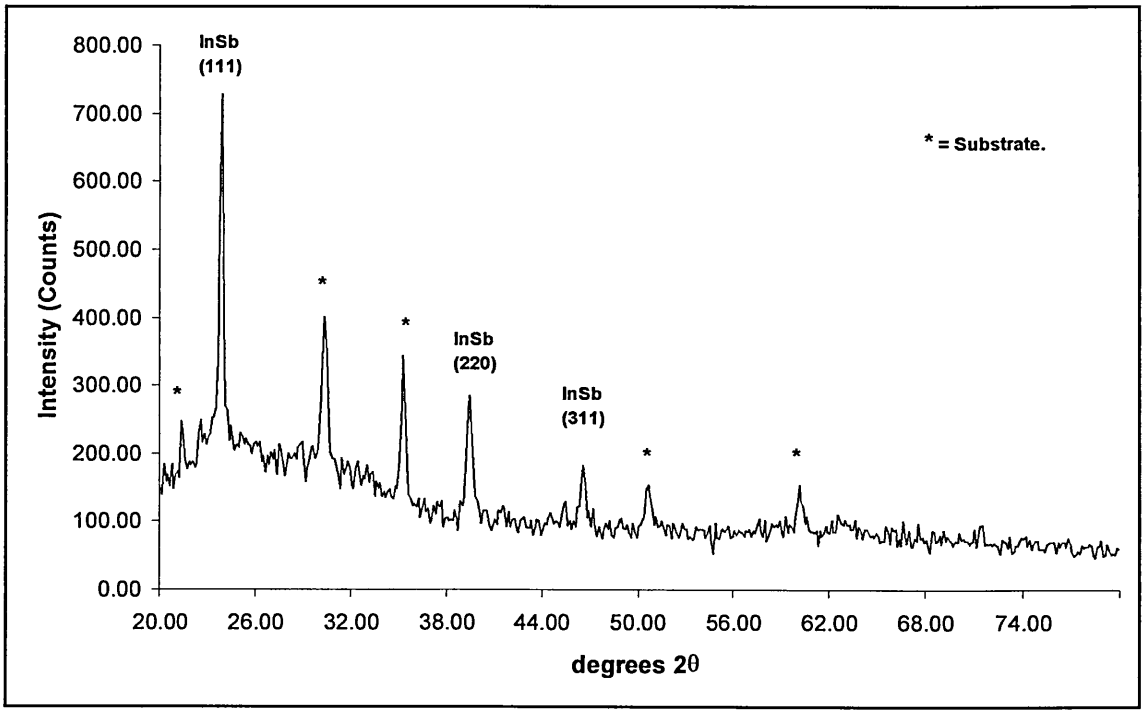

Figure 6.31 XRD pattern of a film deposited at - 2.25 V vs. Pt ref.

Sample			InSb			ITO		
Degree 2θ	dA Å	Int (%)	dA Å	h.k.l.	Int (%)	dA Å	h.k.l.	Int (%)
21.35	4.1584	11.8				4.1633	211	23.2
23.81	3.7341	100	3.74	111	100			
30.395	2.9384	44.8				2.9436	222	100
35.24	2.5447	41.4				2.5475	400	15.8
37.435	2.4004	3.6				2.4007	411	4.7
39.405	2.2848	34.3	2.29	220	80			
45.435	1.9946	4.5				1.9986	431	8
46.51	1.951	19	1.953	311	55			
50.62	1.8018	12.7				1.802	440	23.6
			1.62	400	16			
60.075	1.5389	9.5				1.537	622	13
62.535	1.4841	2.4	1.486	331	20			
71.455	1.3192	3.3	1.323	422	25			

Table 6.8 Comparison of diffraction data from film deposited at - 2.25 V (vs. Pt ref) with PDF card for InSb (No. 6-208) and experimentally obtained ITO diffraction data.

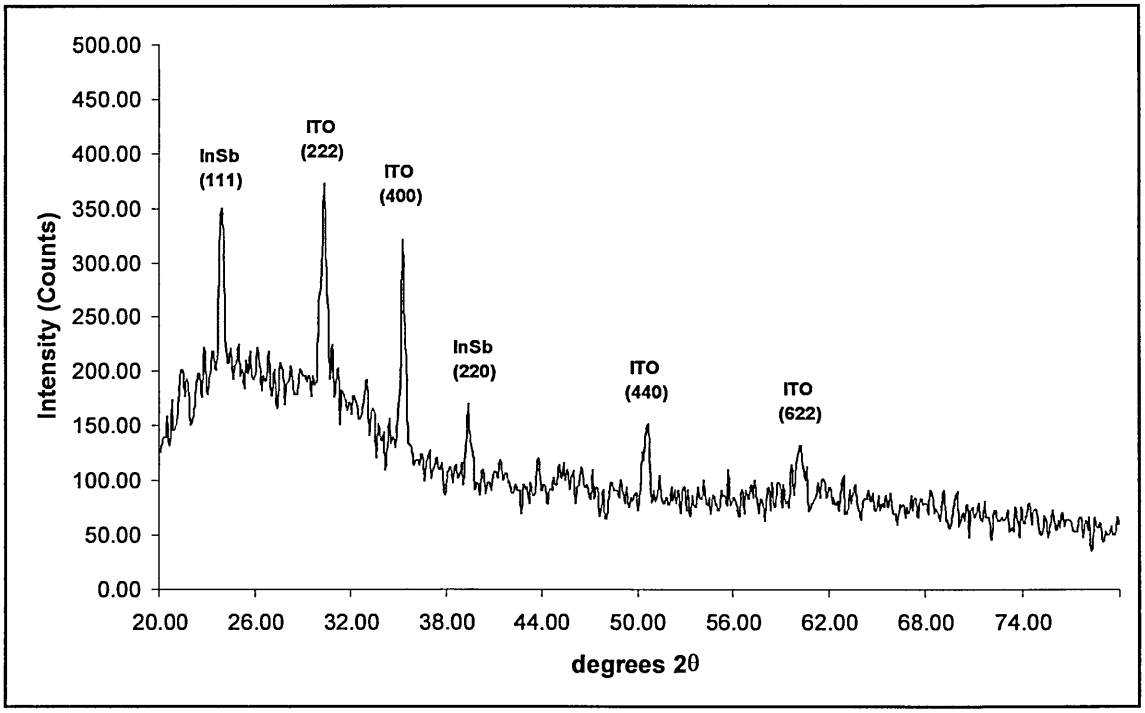

Figure 6.32 XRD pattern of a film deposited at - 2.25 V vs. Pt ref.

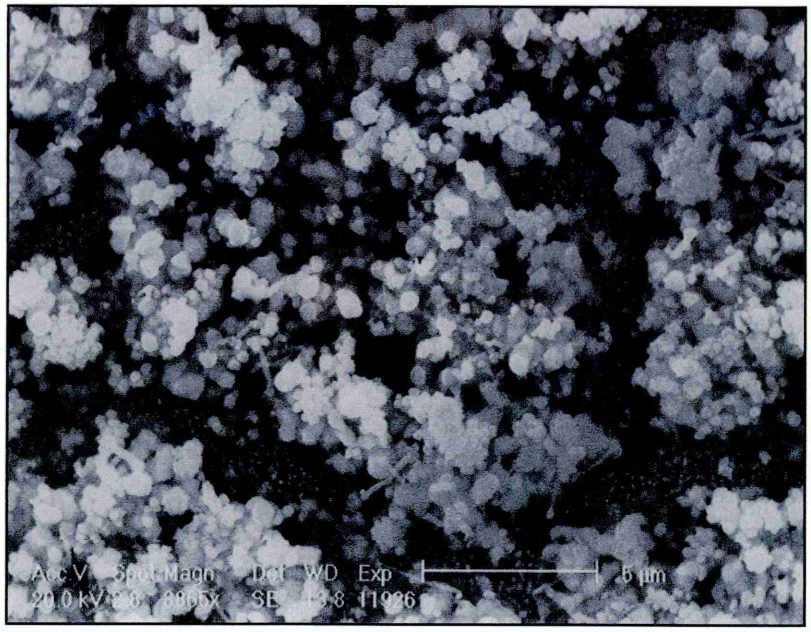

Figure 6.33 SEM micrograph of a film deposited at - 2.25 V vs. Pt ref.

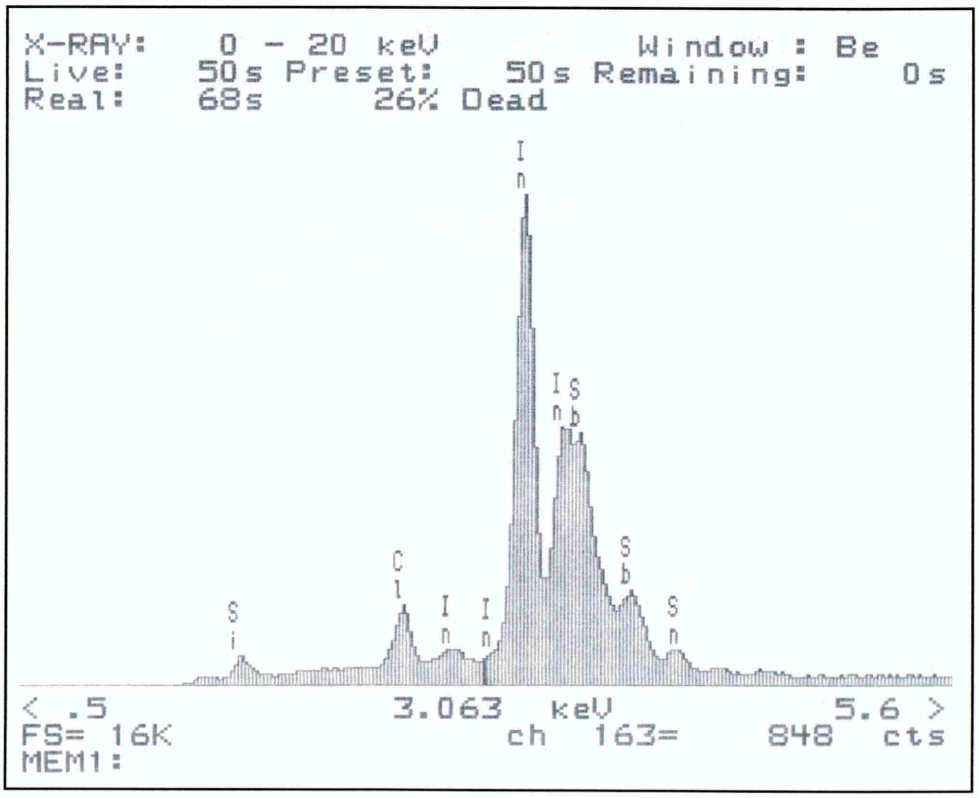

Figure 6.34 EDX spectra of a film deposited at - 2.25 V (vs. Pt ref.).

6.8 XRD Strain Analysis of Films Exhibiting Cracked Morphology

XRD strain analysis (chapter four, section 4.3.3) was performed in order to assess whether the island features described in section 6.6 were caused by the films fracturing through internal stresses. Figure 6.35 gives an example pattern of film that does not have a cracked appearance, but is exhibiting some strain. The film comprises hcp Sb only and was grown from Bath NA3 at - 2.25 V.

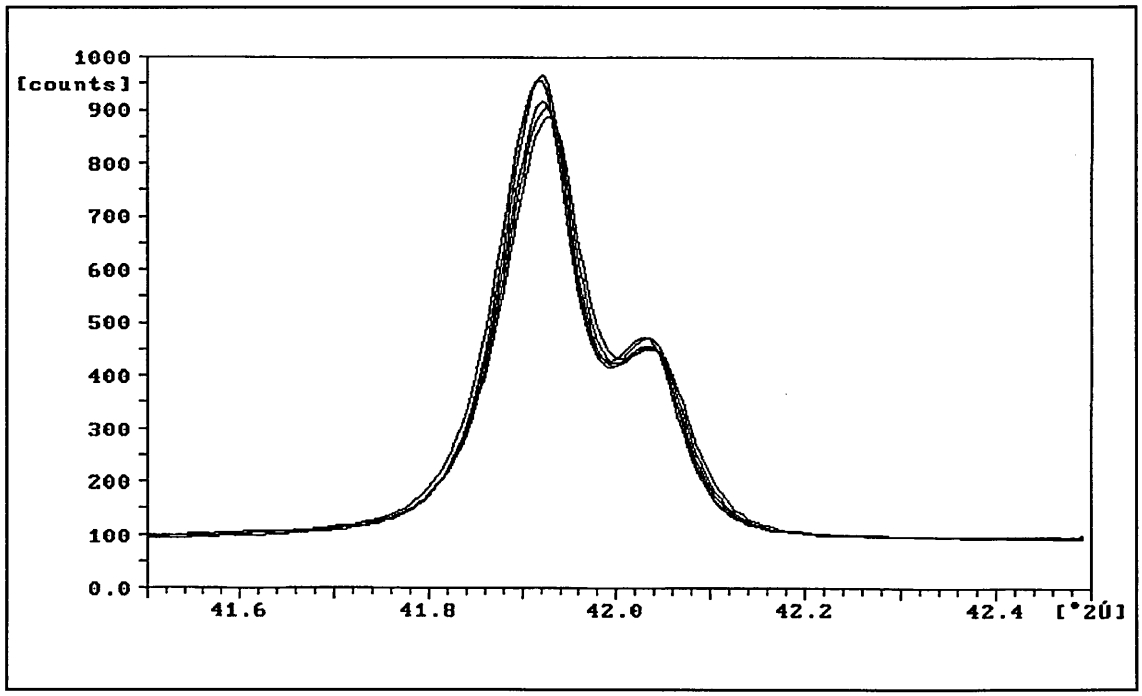

Figure 6.35 XRD strain analysis results for a hcp Sb film deposited from Bath NA3 (section 6.6) at - 2.25 V vs Pt reference. (0.25^{o} 2θ displacement between traces.)

Generally, electrodeposited films are grown in a state of internal stress, usually tensile (contractile) but small, West (1971). Indeed, previous reports of the production of 'cracked' deposits from non-aqueous solutions have been reported in the literature, Gore et al (1989) and Baranski et al (1981). The origins of such forces within the deposited film are numerous. For example, thermal expansion and solvent incorporation can produce strained materials that contract, and hence fracture, when removed from the plating solution. In addition, internal stresses may also develop from the interaction of microcrystallites growing from closely spaced nuclei. Here, contractive stress can be generated when microcrystallites coalesce. Further, if the impinging microcrystallites are slightly misorientated, 'misfit' boundaries result, which contribute to the final pattern of the film's stresses.

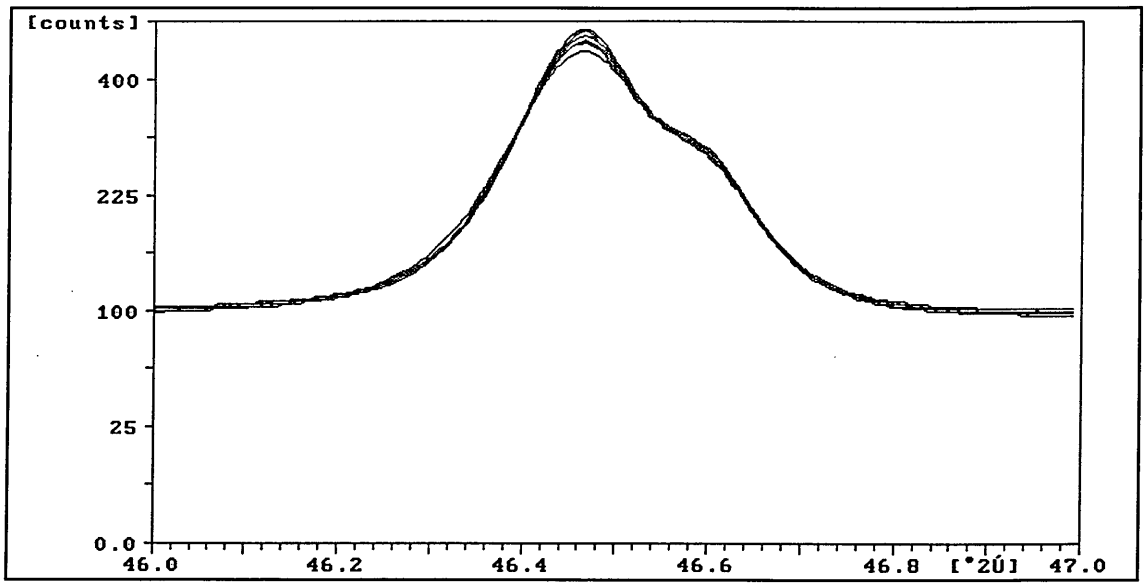

Figure 6.36 XRD strain analysis results for a film deposited from Bath NA2 at –3.25 V vs. Pt reference. (0.25° 2θ displacement between traces.)

In the case of the cracked films, the XRD strain analysis performed used the InSb (331) peak, because it does not overlap with those of the other components in the sample. Films were selected from those grown between - 2.75 V and - 3.25 V. The diffractometer was scanned through 46.00° to 47.00° 2θ several times, each time progressively offsetting the detector by 0.25° 2θ. The results imply an absence of any significant strain in the electrodeposits following removal from the electrolysis cell. As shown in figure 6.36, offsetting the detector causes the expected reduction in peak intensity, but no characteristic shift in peak position that would be associated with 'macro-strain'[3]. The presence of 'microstresses' in the deposit is more difficult to determine. Typically, microstress is indicated by peak broadening. However, this is also a characteristic for particle sizes of the same magnitude as produced in this study. Yet, it is reasonable to suggest that, given its extent, sample cracking is probably macrostress taking advantage of faults in the material on removal from the bath.

[3] Macrostress occurs if, following deformation, crystal grains within an appreciable volume of the material are similarly orientated in relation the applied stress, thus leading to a uniform change in the lattice d-spacing. Microstress lacks this homogeneity, and the change in lattice d-spacing varies throughout the crystal.

6.9 Analysis of Electrodeposited Films using GDOES Depth Profiling

Traditionally, GDOES depth profiling has been mostly used for the compositional analysis of metal finishings and bulk metal samples (Ives (1995)). However, recent reports have shown that the technique can be used for the analysis of complex semiconductor structures and electrodeposited films. Indeed, Dharmadasa et al (1995(b)) discussed depth profiling of AlInP/GaInP/AlInP quantum well structures, whilst Samantilleke et al (1998) made brief mention of the analysis of electrodeposited ZnSe. The strengths of GDOES have already been discussed (chapter four, section 4.3.4), though it is worth reiterating that the technique provides rapid depth profiling of μm coatings with minimum sample preparation. So far, for semiconductor materials, work has concentrated on qualitative rather than quantitative analysis. Even so, the GDOES depth profiling provides a wealth of information regarding semiconductor interfaces and dopant distribution. With this in mind, GDOES depth profiling of electrodeposited films was briefly studied. Particular emphasis was placed upon analysis of the chloride impurity, which featured in the majority of electrodeposited InSb layer's EDX spectra (chapter five and this chapter).

Familiarisation of the instrument was gained by depth profiling a variety of semiconductor materials. Initially, profiles were acquired from thin (~2 μm) CdS film samples electrodeposited by the author using an in-house developed protocol[4]. The determination of suitable instrumental operating conditions involved the use of an UBM™ laser profiler to ascertain the cross-sectional dimensions of the craters that were formed by the analysis. This allowed the determination of conditions under which uniform sputtering would be achieved; i.e. as characterised by the formation of craters with well defined vertical walls and flat bottoms. For CdS, the optimal operating conditions were found to be; voltage 450 V, current 12 mA, argon pressure of $\sim 10^{-3}$ hPa, giving an estimated sputter rate of 40 nm per second[5]. The CdS GDOES profiles (figure 6.37) clearly showed the CdS, ITO

---

[4] In short, 0.01 mol dm^{-3} $Na_2S_2O_3$ was added to an electropurified (12 hrs, - 0.620 V vs. SSC) solution of 0.2 mol dm^{-3} $CdCl_2.xH_2O$, and the pH adjusted to 3.5 with HCl. CdS was then deposited on to (glass)/ITO substrates from this bath at - 0.685 V for ~ 2 hrs at 85 ^{o}C (McGregor (1996)).

[5] Recalling that the ITO layer is ~110 nm thick (chapter four, section 4.2). In addition, the thickness of the CdS layer was estimated using Faraday's laws. Namely, film thickness = (QW/AρnF), where Q is the charge passed, W the material's R.M.M., A deposition area, ρ density, n the number of electrons and F Faraday constant.

and glass layers, together with advantageous carbon on the top of the CdS layer. Particular note should be made of the various photomultiplier sensitivities, as indicated by HS in the profiles.

More complex semiconductor structures were profiled (600 V, 10 mA, ~10^{-3} hPa), which included InP substrate/AlAsSb/InP cap heterostructures (figure 6.39) supplied by Dr T Dann at the BT laboratories, Martlesham Heath. These samples were mounted with silver dag paste onto aluminium stubs because of their low mechanical strength. However, in the most part the specimens shattered during analysis, as was the case for melt grown InSb and GaSb samples profiled. This tendency for sample shattering represents a limitation of the technique, which is being addressed in current work. Even so, some profiles were obtained from the specimens, showing all of the heterostructure's three layers and their interfaces.

Further difficulties were experienced when analysing the electrodeposited films generated for the study of InSb deposition. In general, the instrument failed to acquire profiles for the majority of the samples tested. Typically, the instrument was prevented from evacuating sufficiently, because of the roughness of the sample surfaces. Nevertheless, profiles were obtained from samples whose surfaces were smooth (600 V, 10 mA, ~10^{-3} hPa). Such samples (figures 6.40 & 6.41) include those grown from Bath NA5 (section 6.6.1), whose composition was 0.08 mol dm^{-3} $InCl_3$, $SbCl_3$ 0.03 mol dm^{-3} and 0.2 mol dm^{-3} TEAC. These showed the presence of indium in the deposits. This had been difficult to determine using EDX because of spectral overlap with the In of the ITO layer. Moreover, it can be assumed that this In was amorphous, given the absence of any of its peaks in the films' XRD patterns. In addition, the profiles indicate that the In concentration was greatest nearer the deposit's surface, as was the case for chloride. Therefore, it is reasonable to propose from these GDOES results that the film's In content was a result of some absorption mechanism.

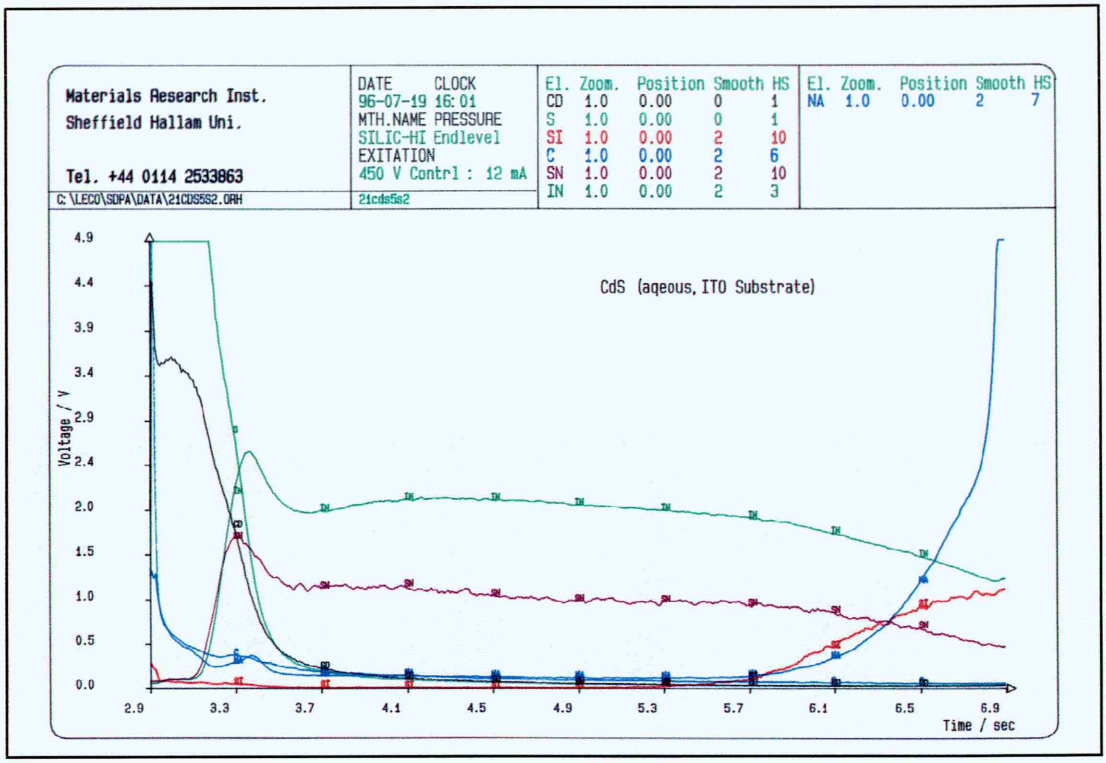

Figure 6.37 GDOES depth profile spectra of CdS electrodeposited on to an ITO substrate.

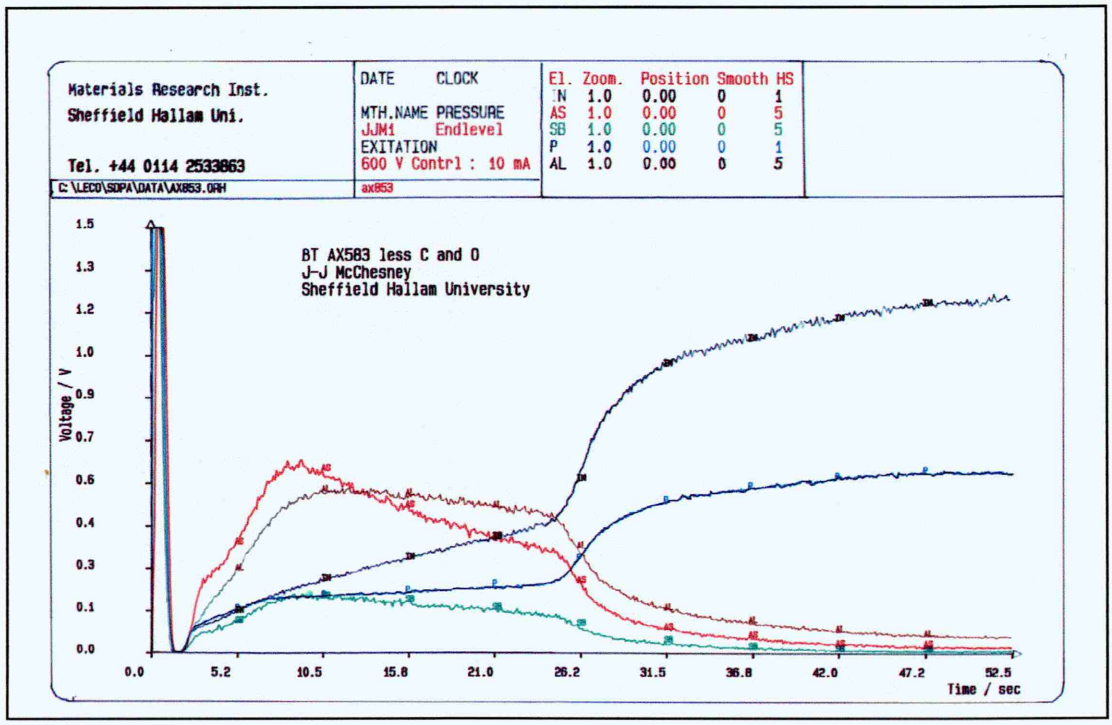

Figure 6.38 GDOES depth profile spectra of InP substrate/AlAsSb/InP cap heterostructure.

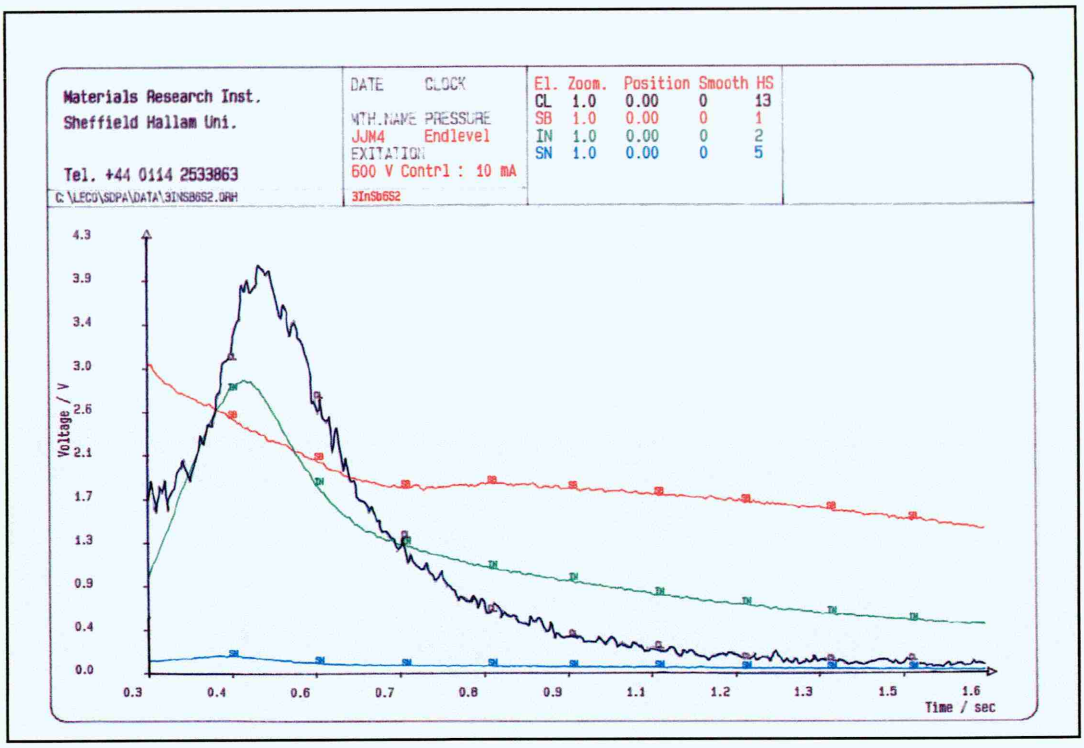

Figure 6.39 GDOES depth profile spectra of a film deposited at –2.25 V (vs. Pt Ref.) from 0.08 mol dm^{-3} $InCl_3$, $SbCl_3$ 0.03 mol dm^{-3} and 0.2 mol dm^{-3} TEAC.

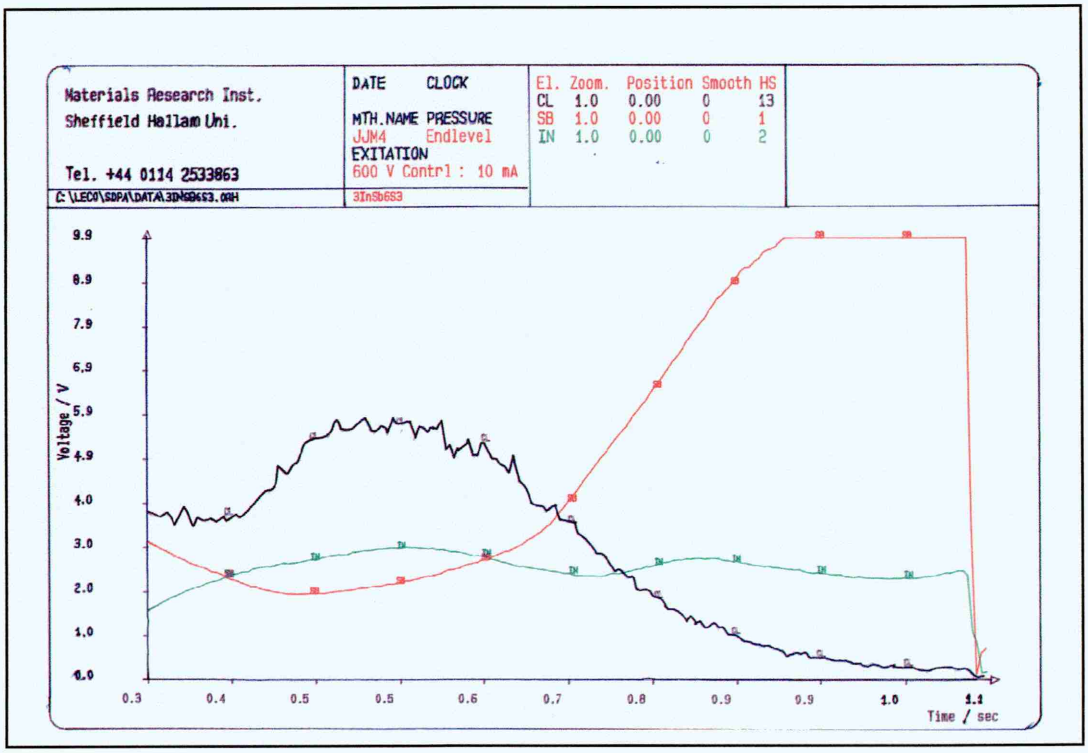

Figure 6.40 GDOES depth profile spectra of a film deposited at –3.75 V (vs. Pt Ref.) from 0.08 mol dm^{-3} $InCl_3$, $SbCl_3$ 0.03 mol dm^{-3} and 0.2 mol dm^{-3} TEAC.

6.10 Summary of the Study of the Electrodeposition of InSb from Non-Aqueous Electrolyte Solutions

- Potentiostatic deposition of InSb from non-aqueous electrolyte solutions was investigated for the first time.

- A first report was given of the deposition from non-aqueous plating baths of fcc InSb films that were free of any other crystalline co-phase. However, the formation of InSb was accompanied by the deposition of crystalline co-phases, under the majority of conditions used.

- The composition of the films, in terms of the crystalline phases present, was found dependent on the deposition potential applied, when the concentration of $InCl_3$ in TEAC containing EG solutions was larger than the $SbCl_3$. An investigation of the relationship between film and bath composition suggested that growth from EG is of a 'regular type' according to Brenner's (1963) classification system (chapter two, section 2.3.3).

- As in the case of the aqueous study, EDX analysis showed that a chloride was a major contaminant in films grown under all conditions. The sample's GDOES depth profiles indicated that a species containing chloride was entrapped near the films' surfaces[6], and that its cross-sectional distribution followed that of In.

- The first SEM analysis of InSb deposited from a non-aqueous solution showed a variety of morphological forms and, as for films deposited from aqueous solutions, nodular growth predominated.

- Particle size estimates of InSb grown from non-aqueous solutions were made for the first time, showing that they were on average larger than those grown from aqueous

---

[6] X-Ray Photoelectron Spectroscopy (XPS) was actually performed on samples grown from EG baths, but the analysis results were lost through instrumental failure. However, it was seen that peaks whose energies were associated with the chloride species was reduced after etching the film's surface for a short time. Further, sample charging made it difficult to determine what form the halogen was in. For example, the energies of the $3d_{5/2}$ peaks of In from $InCl_3$ and In from InCl were too close to be resolved (445.1 & 445.9 eV). However, a pair of widely spaced doublets could be resolved from the In 3d peaks, and a cursory study suggests these derive from $InCl_3$/InCl and In/InSb. Obviously, further analysis is necessary.

solutions. A short investigation of samples that had a cracked appearance was performed. In the absence of any significant macro-stress, a mechanism for the aforementioned cracking was proposed.

Chapter 7

Study of the Electrodeposition of GaSb

7.1 Introduction

Of the semiconductor electrodeposition methods reviewed in chapter 3, the direct co-deposition of GaSb from aqueous electrolyte solutions has been studied the least extensively. Indeed, only Paolucci et al (1990) have made brief mention (one paragraph) of an unsuccessful attempt to utilise such a preparative route in a paper concerning electroplating GaSb via sequential elemental deposition (section 3.4.5). However, the electrochemically analogous GaAs has been studied to a certain extent, and reasonable material has been generated by annealing material deposited galvanostatically (or with controlled voltage electrolysis) from acidic electrolyte solutions (chapter 3, section 3.4.3).

A general 'rule of thumb' for the deposition of alloys (or compounds) is that the components' equilibrium potentials should be within 200 mV of each other (chapter 2, section 2.3.1). For deposition of InSb from aqueous solutions (chapter 5, section 5.1), the large difference (0.550 V) between the components' equilibrium potentials necessitated the use of a chelating agent. In the case of GaSb deposition, under acidic conditions, the precursor ions' equilibrium potentials are even further apart (0.772 V), reactions 7.1 & 7.2. Further, as shown by the Pourbaix (1961) diagram for the gallium-water system (Appendix I), the equilibrium potentials of those species that are stable under alkaline conditions become progressively more negative with increasing alkalinity.

Reaction 7.1 $Ga^{3+}_{(aq)} + 3e^- \leftrightarrows Ga_{(S)}$ $E^O = -0.560V$

Reaction 7.2 $SbO^+_{(aq)} + 2H^+ + 3e^- \leftrightarrows Sb_{(s)} + H_2O$ $E^O = +0.212\ V$

From the system's Pourbaix diagram, it can also be seen that the stability region for Ga metal lies well below the line representing the onset of hydrogen evolution. Hence, Ga metal is most commonly deposited from alkaline electrolyte solutions. Therefore, the electroplater is faced with a dilemma when depositing Ga alloys (or compounds). To

minimise hydrogen evolution, and thereby maximise the current efficiency of the process, alkaline baths should be employed. However, whilst using alkaline conditions, the probability of alloy (compound) formation is low. This is because of the large difference in the equilibrium potentials of the precursor ions stable in such solutions. This difference, to a certain degree, may be reduced by the use of a chelating agent, especially in terms of making the reduction potential of the Sb species more negative.

With the above in mind, the conditions used by Paolucci et al (1990) can be further explained. The authors selected an alkaline bath, to negate hydrogen evolution concerns. In addition, they addressed the issue of the difference in equilibrium potentials by using a bath whose concentration of the gallate species was greater than that of the more noble antimony bearing species (0.15 M Ga^{3+}, 0.05 M Sb^{3+}). Moreover, they employed a chelating agent, whose concentration (citrate 0.1 M) was such that it was most likely that the majority of species not chelated would contain gallium. Nevertheless, the films deposited consisted of Sb alone.

For the electrochemically analogous GaAs, the use of either galvanostatic (or constant voltage) electrolysis is a general feature of the deposition methodologies developed thus far. In view of this, it is worth continuing the discussion of section 6.1 (chapter 6), with the aid of equation 7.1, to justify the use of these 'unselective' growth modes. Equation 7.1 represents a breakdown of the various potentials associated with the cell.

Equation 7.1 $$E_{applied} = E_{Cathode} - E_{Anode} - IR - \eta$$

(Where E is potential, I current, R resistance and η overpotential.)

In the case of constant voltage electrolysis, concentration polarisation leads to a reduction in the current passing through the cell, as well as a decrease in η. To maintain the algebraic equality of equation 7.1, and recalling that E_{Anode} is constant because it derives from the oxidation of the plentiful water, the value of $E_{Cathode}$ increasingly shifts to values that are more negative. Consequently, it becomes possible to reduce species whose discharge voltages are more negative than the cathode's original potential. (Consequently, the electrolysis mode is said to lack selectivity.)

In the case of GaAs, the following scenario was proposed Yang et al (1992). The initial stages of growth establish a current deriving mostly from As deposition. This current falls as concentration polarisation sets in. At a certain point, the cathode's potential attains a level that is negative enough for Ga to also deposit. If the elements Ga and As are deposited, the mixture is expected to be thermodynamically unstable due to the negative free-energy of formation for $GaAs_{(S)}$. Further, as Yang et al (1992)[1] state 'according to the phase diagram of GaAs, a mixture of Ga and As is not thermodynamically stable and should convert to GaAs with either excess Ga and As'.

Reaction 7.3 $Ga_{(S)} + As_{(S)} \rightarrow GaAs_{(S)}$ ΔG^{O}_{298} =-83.67 kJ/mol

Similarly, the free energy of formation of GaSb from its elements is negative (ΔG^{O}_{298} =-38.9 kJ/mol, Berger & Pamplin (1994)), although in comparison this loss is more than half that of GaAs. Therefore, following the same argument proposed for GaAs by Yang et al (1992), it was decided that this study of GaSb electrodeposition would begin with the application of methodologies utilising the controlled voltage electrolysis mode.

7.2 Constant Voltage Deposition

The method for constant voltage deposition was based upon that used by Dharmadasa and Blomfield (unpublished) during their investigation of GaAs deposition. An electrolyte solution was made up containing 0.05 mol dm^{-3} $Ga_2(SO_4)_3$, and 0.005 mol dm^{-3} $SbCl_3$. A white precipitate formed immediately, and this was assumed to be due to the formation of antimonyl oxychlorides, given that the pH measured was 0.9. The solution was heated to 70 ^{O}C, and voltammograms were obtained by manually scanning the applied potential across the cell whilst recording the current density achieved, figure 7.1. The voltammograms were characterised by an increase in current density at approximately -2.45 V that was accompanied by the (visible) onset of gas evolution at both the anode and

[1] It should be noted that the authors still found it necessary for the generation of 'reasonable quality 'GaAs, to anneal the deposited samples under nitrogen for several hours (>8 hrs) at 300 ^{o}C

cathode. A series of depositions were then carried out between -2.19 V and -3.20 V on ITO substrates, table 7.1.

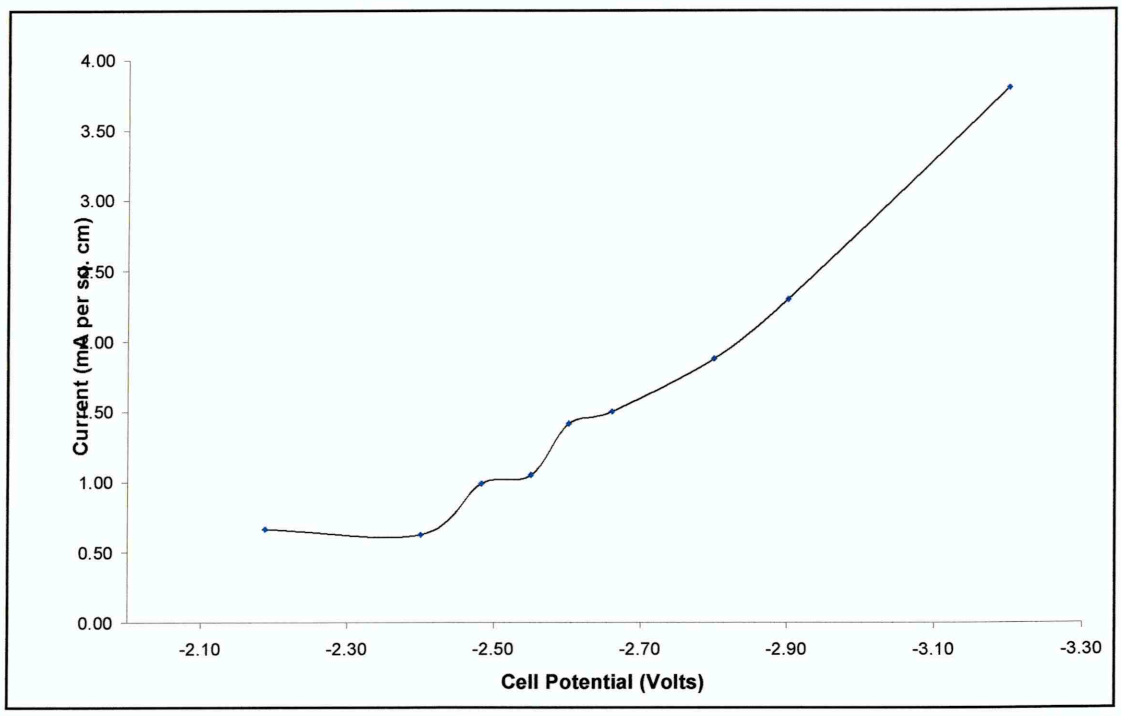

Figure 7.1 Voltammogram obtained at a stationary ITO electrode at 70 ^{O}C in an unstirred solution of 0.05 mol dm^{-3} $Ga_2(SO_4)_3$, and 0.005 mol dm^{-3} $SbCl_3$.

Deposition Potential Volts	Maximum Current Density mA cm^{-2}	Results of XRD Analysis
-2.19	1.33	Sb
-2.40	1.61	Sb
-2.48	2.30	Sb
-2.55	2.35	Sb
-2.60	2.83	Sb
-2.66	2.56	Sb
-2.80	4.28	Sb
-2.90	4.60	Sb
-3.20	7.60	Sb

Table 7.1 Summary of the XRD analysis of films deposited under the conditions described in the text.

The films deposited were grey to black in colour, and generally adhered poorly to the substrate. Those films grown at potentials more negative than -2.55 V had a tendency to begin to peel from the substrate surface within the first few minutes of growth.

Moreover, gas could be seen evolving from both electrodes at these potentials, and was seen to contribute to the films' peeling. Consequently, most of the films did not completely cover the substrate, resulting in the samples' surface having a patchy appearance, as shown by figure 7.2. The films' XRD patterns were recorded, and all were found to consist solely of hcp Sb. The lack of complete surface coverage, together with the films' thinness, was apparent from the samples' XRD patterns, as they were dominated by features from the ITO substrate, figure 7.3. Following the initial characterisation, the films were annealed at 250 ^{O}C under nitrogen for 4 hrs, and their XRD patterns recorded to determine whether any gallium (m.p. 29.75 ^{O}C, b.p. 2227 ^{O}C) would be crystallised if present. However, the XRD patterns of the films before (figure 7.4) and after (figure 7.5) the annealing process gave no indication of the presence of Ga in the films, as later confirmed by EDX (Figure 7.6). Indeed, the only noticeable difference between the XRD patterns was a slight increase in the heights of the peaks attributable to hcp Sb in the annealed samples. This indicated an increase in the crystalline content of the films.

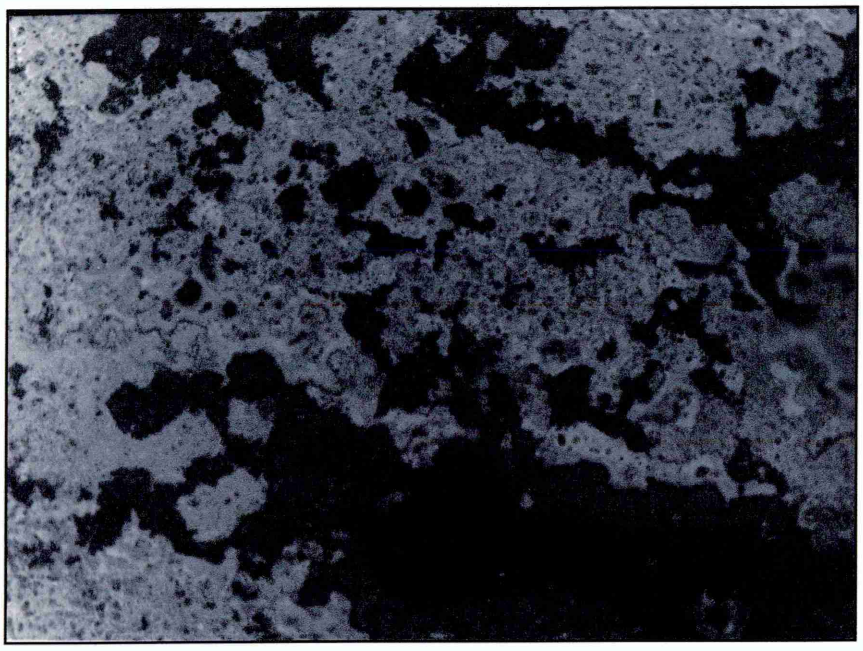

Figure 7.2 Photograph taken with an optical microscope at ×500, showing the surface of a film deposited at -2.7 V.

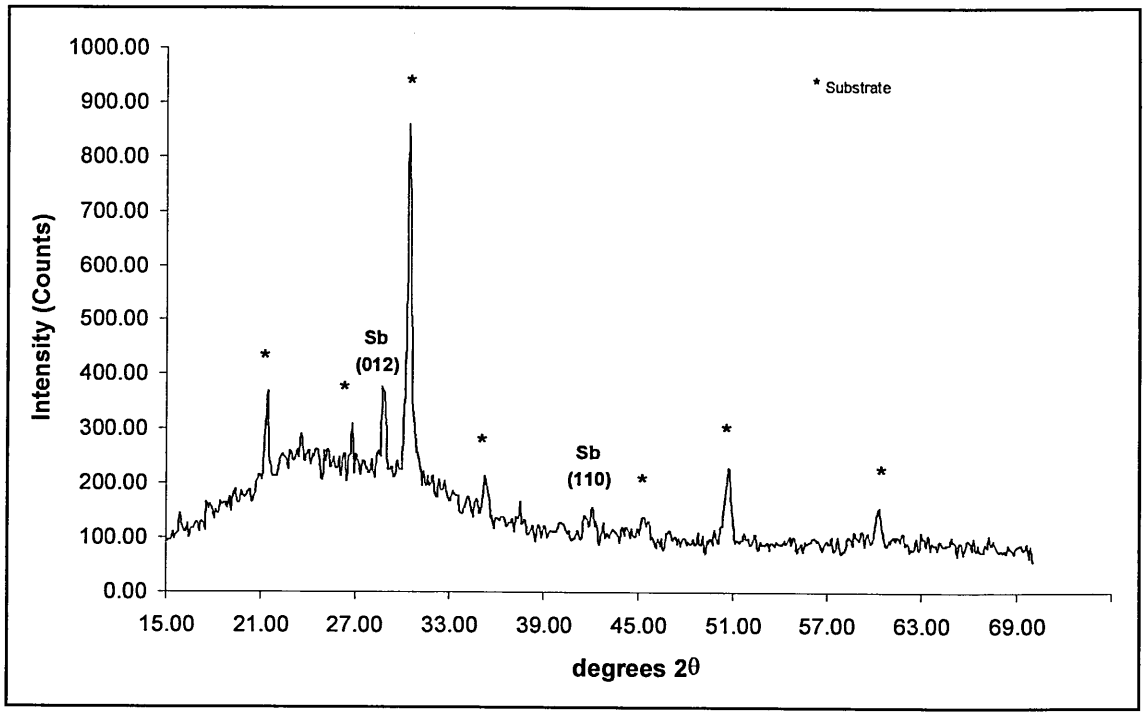

Figure 7.3 XRD pattern of a film deposited at -2.55 V.

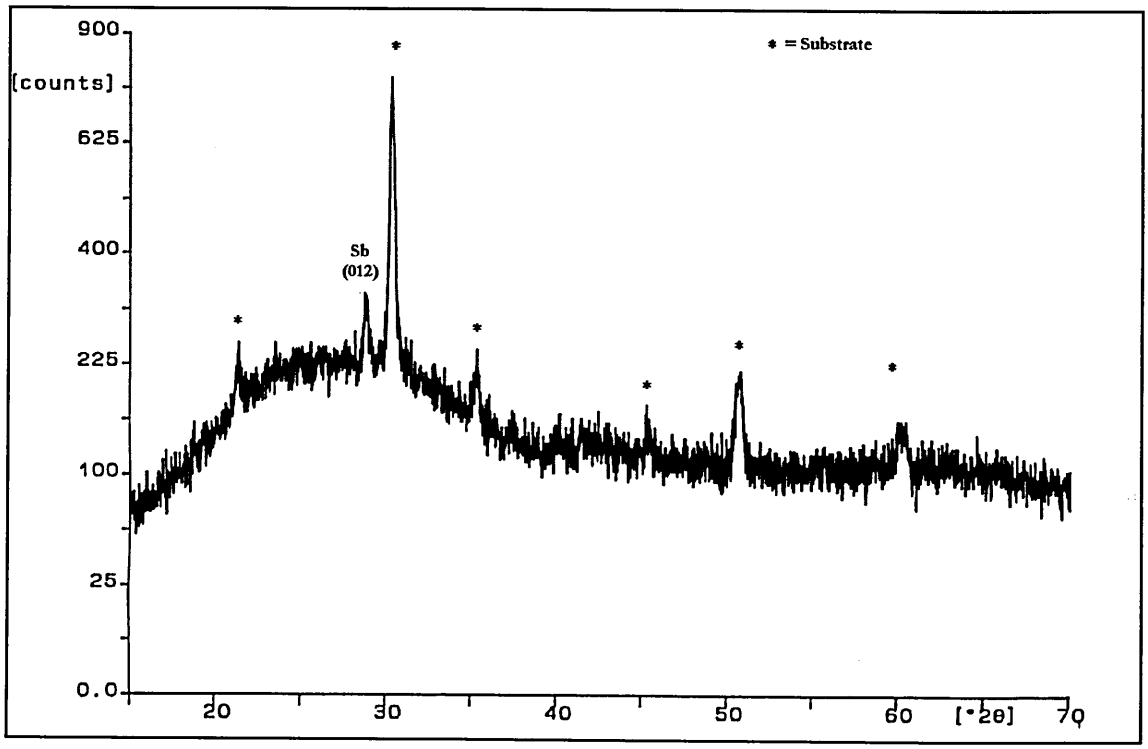

Figure 7.4 XRD pattern of film deposited at -2.66 V.

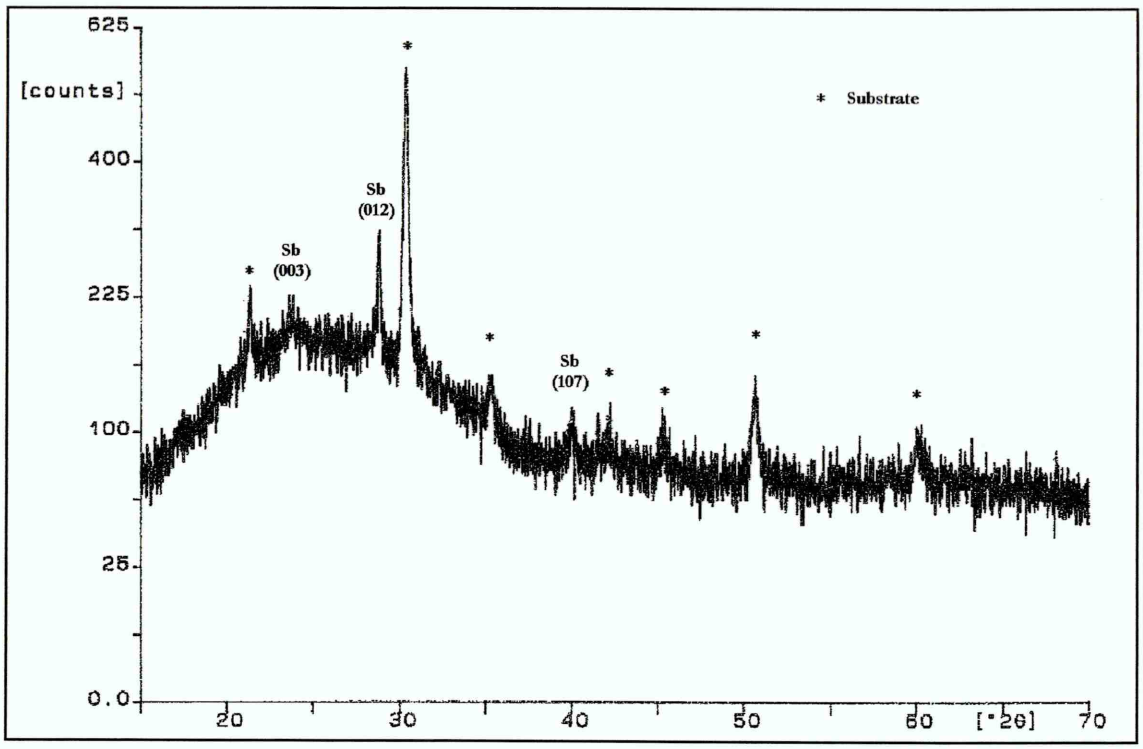

Figure 7.5 XRD pattern of film deposited at -2.66 V following annealing under N_2 at 250 ^{O}C for4 hrs.

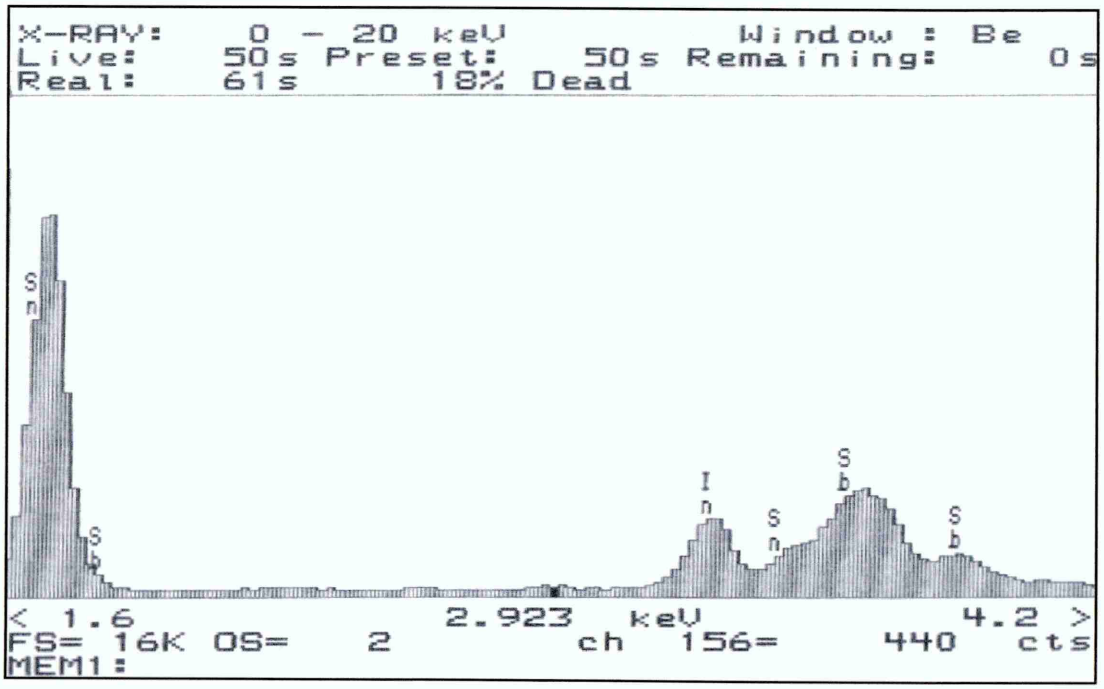

Figure 7.6 EDX spectra of a film deposited at -3.20 V, the signals from In and Sn are due to the ITO substrate material.

A decrease in current density with time was observed during the deposition experiments, as discussed in section 7.1. In order to further investigate this feature of the deposition system, a series of depositions was carried out whilst measuring the cathode's potential against an Ag/AgCl reference electrode. The cathode's potential (against the reference electrode) was seen to become progressively more negative with time, and the current density was seen to decrease. A consequence of the polarisation of the cathode (by approximately 200 to 250 mV) was gas evolution. It is likely that 'poisoning' of the electrode by gas bubbles contributes to the decrease in current density caused by concentration polarisation.

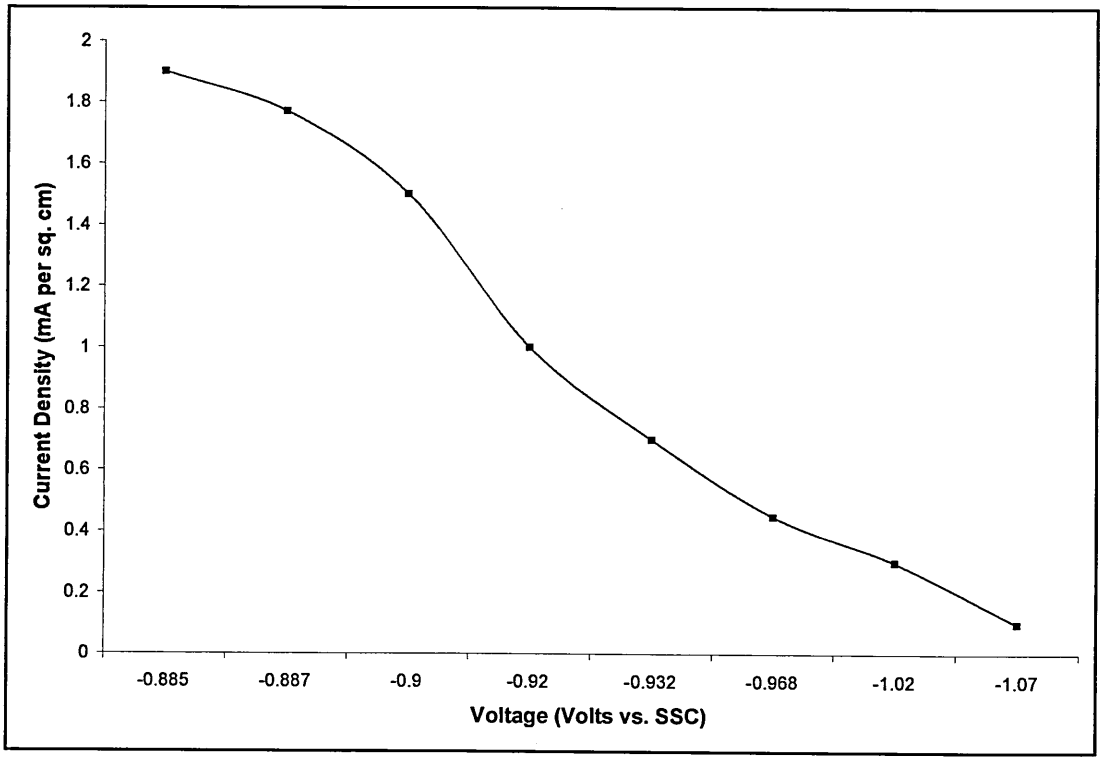

Figure 7.7 Graph showing the decrease in current density with cathode potential (as measured against a Silver-Silver Chloride (SSC) reference electrode) during a constant voltage deposition experiment (applied potential -2.40 V).

Given the absence of Ga in any of the films deposited, solutions were prepared containing 0.1 mol dm^{-3} $Ga_2(SO_4)_3$, and 0.005 mol dm^{-3} $SbCl_3$. The formation of a white precipitate was also observed for these plating baths. Depositions were carried out within the same range of applied cell potentials as before (-2.20 V to -3.20 V), which yielded thin films of hcp Sb and no phases containing Ga species.

7.3 Potentiostatic Deposition from Aqueous Solutions

The results above indicate that the difference in the reduction potentials of the gallium and antimony species could not be resolved by the polarisation of the cathode during constant voltage electrolysis. Instead, the observed cathodic polarisation led to the generation of gas, rather than the deposition of Ga, as well as a decrease in the current density during the electrolysis. Therefore, as it affords greater control of the growth potential, section 7.1, potentiostatic deposition was investigated. This was achieved by electrolysing a series of solutions containing $GaCl_3$, table 7.2, with ITO (and copper) substrates at 80 ^{O}C.

Ga/Sb Molar Ratio	Concentration of $Ga_2(SO_4)_3$ (mol dm^{-3})	Concentration of $SbCl_3$ (mol dm^{-3})
1000/1	0.50	0.0005
100/1	0.50	0.005
40/1	0.04	0.001
10/1	0.05	0.005
5/1	0.05	0.01
1/1	0.05	0.05

Table 7.2 The concentrations of the electrolyte solutions used during the investigation of GaSb potentiostatic deposition.

Under most conditions, black spongy deposits were formed, which exhibited poor adhesion to the substrate material. The XRD patterns and EDX spectra collected showed that these films consisted of finely divided hcp Sb. The presence of a small amount of a chloride was indicated only by the EDX spectra taken from films that visually appeared to be the thickest.

Mixtures of cubic GaSb and hcp Sb (figure 7.8) were however deposited. This is, to the authors knowledge, the first report of the direct electrochemical co-deposition of GaSb from aqueous electrolyte solutions. EDX analysis (figure 7.9) of the deposits demonstrated the presence of Ga in material deposited. The films formed under the following set of conditions: 0.04 mol dm^{-3} $GaCl_3$, 0.001 mol dm^{-3} $SbCl_3$, 80 ^{O}C, ITO substrate, applied potentials more negative than - 0.80 V (Ag/AgCl reference). Deposits consisting solely of hcp Sb were grown at potentials more positive than - 0.80 V. The GaSb/Sb films were dark grey in colour and had good adherence to the substrate. Films

grown at potentials more negative than - 1.00 V, at which the evolution of gas from the electrodes could be seen, had a tendency to peel from the substrate.

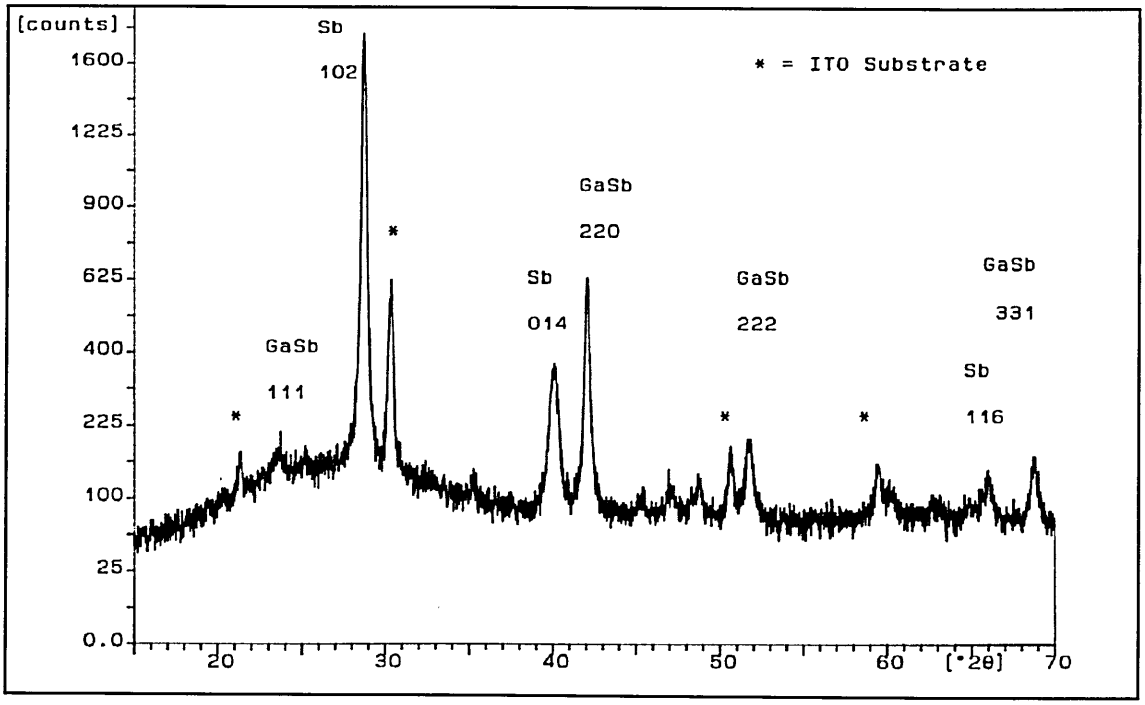

Figure 7.8 XRD pattern of a film deposited at - 0.80 V (vs. Ag/AgCl).

Voltammograms were obtained (figure 7.10) from the aforementioned solutions, and it was found that the onset of gas evolution coincided with an increase in current at approximately - 1.00 V. It is worth noting that according to the Pourbaix diagram for the Sb-water system (Pitman et al (1957)) the generation of stibine (SbH_3) is favourable at very negative potentials. Therefore, it is reasonable to suggest that some of the gas generated was not hydrogen. Indeed, Paolucci et al (1990) measured the loss of Sb due to SbH_3 generation by polarising 500 nm thick Sb films at various potentials for 100 seconds in a 5 mol dm^{-3} KOH solution. The authors found that Sb loss through such a degradative pathway was as high as 75% at - 2.10 V (vs. SCE).

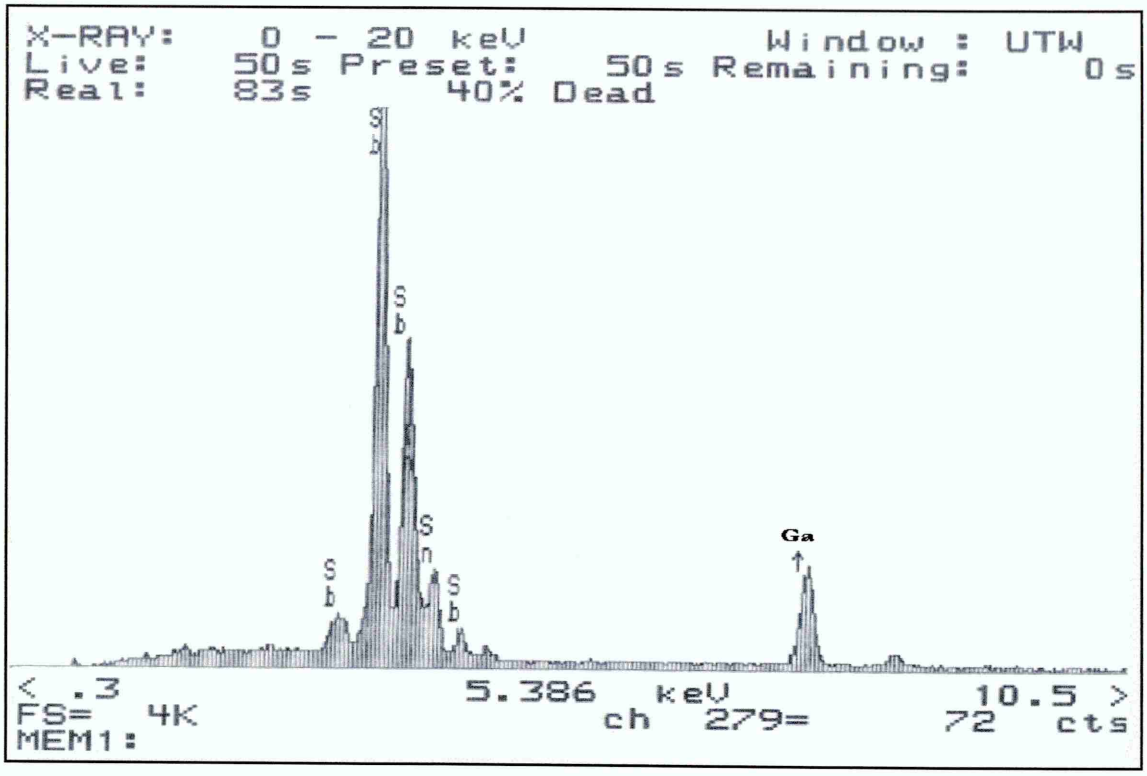

Figure 7.9 EDX spectra of a film deposited at - 0.80 V (vs. Ag/AgCl).

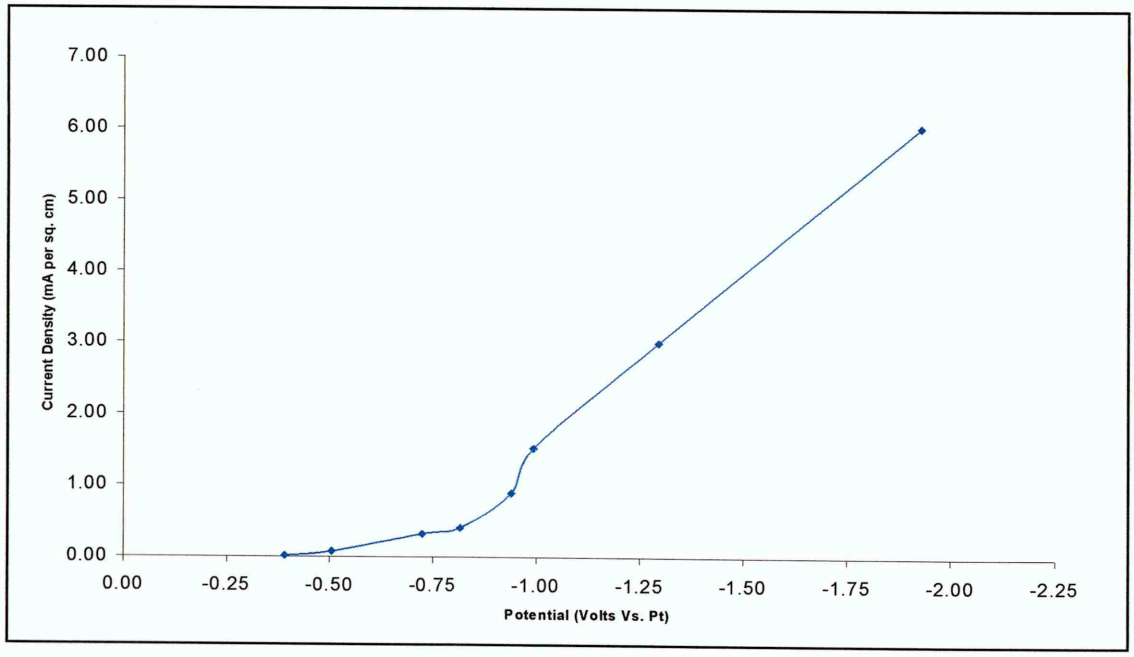

Figure 7.10 Voltammogram obtained at 80 ^{O}C at a stationary ITO electrode in an unstirred solution containing 0.04 mol dm^{-3} and $GaCl_3$, 0.001 mol dm^{-3} $SbCl_3$.

SEM micrograms show the films containing gallium to be dominated by loose collections of fibrous needles, figure 7.11. These needles were on average below 1 μm in length.

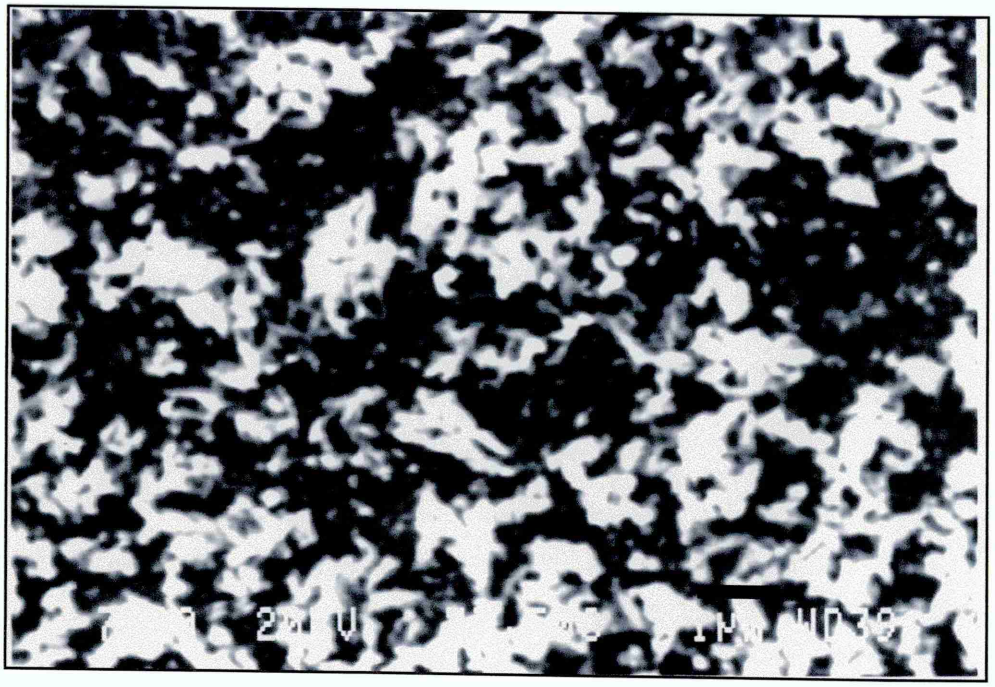

Figure 7.11 SEM micrograph (with 1 cm ~ 1 μm) of a film deposited at - 0.80 V (vs. Ag/AgCl).

The final part of the investigation of GaSb deposition from aqueous electrolyte solutions involved the electrolysis of electrolyte solutions containing a citric acid complexant. The composition of the solutions was 0.3 mol dm^{-3}, 0.10 mol dm^{-3} $GaCl_3$ and 0.001 mol dm^{-3} $SbCl_3$. Clear solutions were made up by dissolving first the citric acid, then the $SbCl_3$, and finally $GaCl_3$. Films were then potentiostatically deposited from these baths at potentials between - 0.50 V and - 1.25 V, at a temperature of 80 ^{o}C. Under all conditions very thin films of hcp Sb were grown that poorly adhered to the substrate.

7.4 Potentiostatic Deposition from Non-Aqueous Solutions

The results of the previous section lead to the conclusion that the co-deposition of Ga and Sb is limited by the onset of H_2 and, most likely, stibine evolution. It was therefore decided to limit the availability of hydronium ions by employing ethylene glycol (EG) and anhydrous precursors. Solutions were made up containing 0.08 mol dm^{-3} $Ga_2(SO_4)_3$ and

0.02 mol dm^{-3} $SbCl_3$. Whilst $SbCl_3$ was found to dissolve readily, the $Ga_2(SO_4)_3$ was found to be poorly soluble in EG, even when left for 4 hrs at 140 ^{O}C, and was visible as a light brown precipitate. Nevertheless, the temperature of the solutions was raised to 180 ^{O}C and depositions carried out at voltages between - 0.75 V and - 2.00 V (vs. Pt ref.). Surface coverage and adherence was poor for all the layers grown. Indeed, most deposits consisted of a patchy light grey material, with a uniform covering of large particles across the entire area of the substrate. Though the EDX spectra of the films showed them to contain Ga, figure 7.12, XRD analysis of the films revealed them to be a mixture of hcp Sb and rhombohedral $Ga_2(SO_4)_3$, figure 7.13. The SEM micrograms taken of the films strongly suggest that, in light of the XRD results, the $Ga_2(SO_4)_3$ present in the films was in fact from the precipitated material mentioned above. (Anhydrous $GaCl_3$ was also investigated for use as a source of Ga. However, its tendency to hydrate on contact with air presented handling difficulties that would require modification of the current experimental apparatus.)

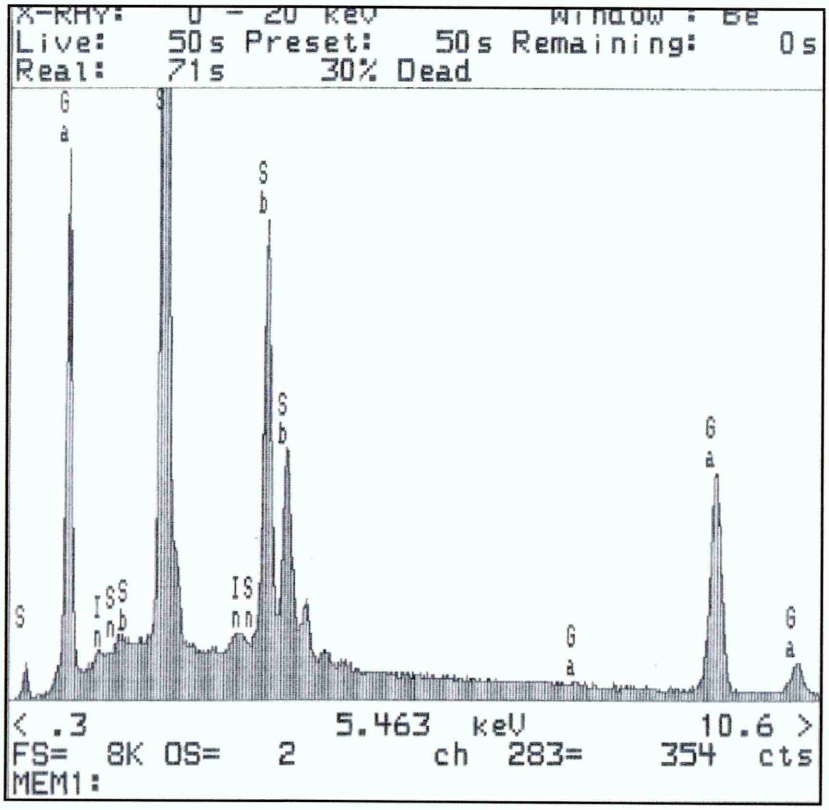

Figure 7.12 EDX spectrum of a film deposited at –1.75 V (vs. Pt ref.).

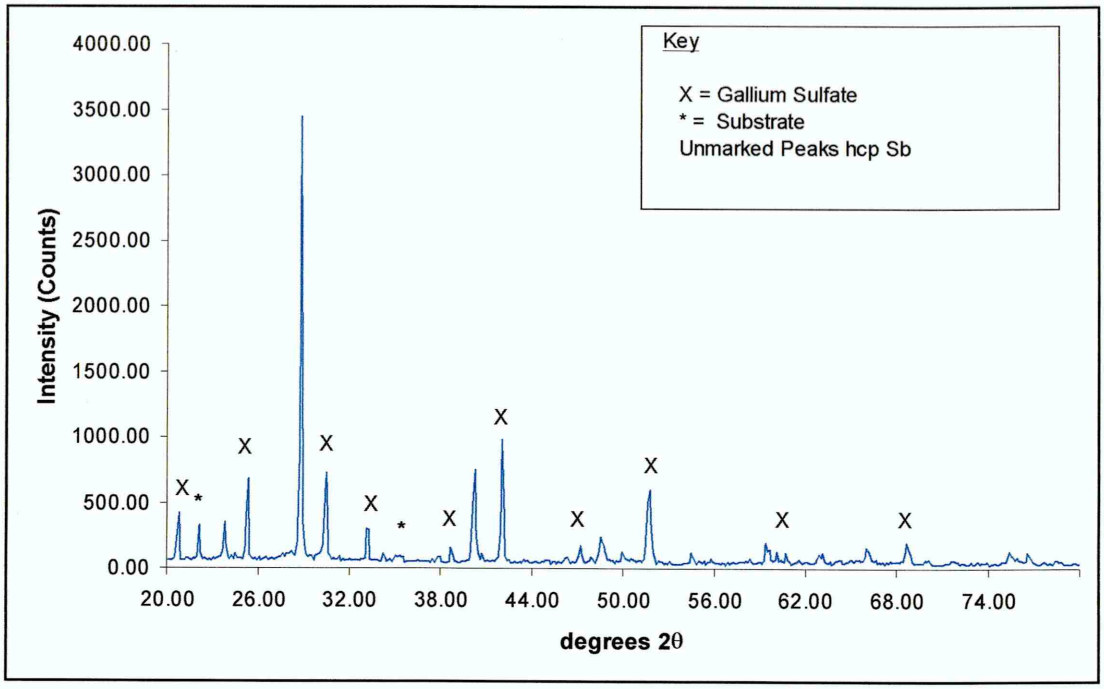

Figure 7.13 XRD pattern of a film deposited at –1.75 V (vs. Pt ref.).

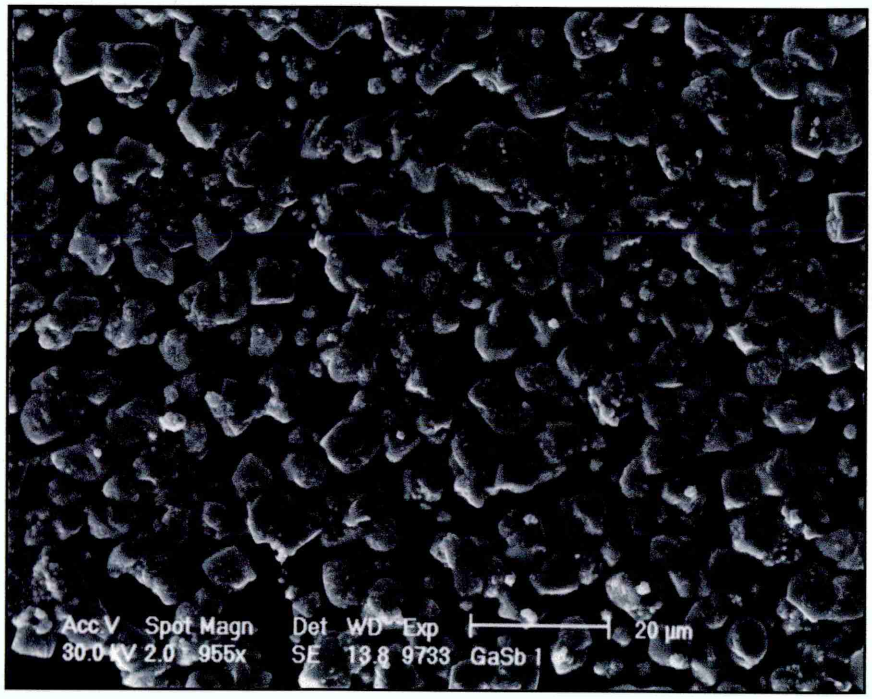

Figuer 7.14 SEM microgram of a film deposited at –1.705 V (vs. Pt ref.).

7.5 Summary of the Study of the Electrodeposition of GaSb

- The direct co-deposition of GaSb from an aqueous electrolyte solution was studied in detail for the first time. Conditions were reported for the direct growth of GaSb via potentiostatic electrolysis. The XRD patterns of the GaSb containing films indicated the presence of an hcp Sb co-phase.

- First reports from a SEM study of admixtures of GaSb and Sb deposited from aqueous solutions showed that the films' morphology was dominated by small fibrous needle like features.

- EDX studies suggested that no significant amount of any chloride was included in any of the materials grown.

- Under the conditions employed, deposition using a constant voltage mode of electrolysis did not produce films containing Ga. Though polarisation of the cathode was evident, it was found that the evolution of H_2 and SbH_3 inhibited the reduction of Ga containing films.

- New work on the deposition of GaSb demonstrated practical difficulties in using non-aqueous solvents, in that $Ga_2(SO_4)_3$ was insoluble in EG and that anhydrous $GaCl_3$ hydrated on contact with air.

Chapter 8

Discussion

8.1 Introduction

Since its discovery, electroplating has been mainly used to generate coatings on metal surfaces, in order to confer products with certain decorative, mechanical and anti-corrosion properties. In response to this, over the years a multitude of methodologies has been developed to electroplate various metals and alloys for such purposes. Generally, these plating systems are based on the galvanostatic electrolysis of aqueous solutions at (or near) room temperatures.

Similarly, research in semiconductor electrodeposition has also been motivated by the materials' applications, and this has led to the field essentially concentrating on a small group of II-VI materials that are used in photovoltaic devices. Consequently, the devices formed from these materials have reached efficiencies comparable to those based on materials grown by other preparative routes, which is a reflection of the technique's capability for producing materials of well-defined composition and morphology. To this aim, authors have published many well-documented methods for electrodepositing these materials, which generally involve the potentiostatic electrolysis of aqueous solutions at temperatures below 100 ^{o}C, section 3.3.

In comparison with the above, only a relatively small number of articles have been published in the literature concerning III-V electrodeposition. Whilst these are critically reviewed in chapter three of this thesis, it worth reiterating that there is a bias towards interpreting results from III-V electrodeposition experiments from a thermodynamic, rather than kinetic, viewpoint. This is despite the Gibbs free energies for the formation of III-V compounds being less favourable than, for example, those of II-VI compounds[1], i.e. perhaps indicating that for III-V compounds growth kinetics could play a crucial role.

---

[1] For example, the standard molar Gibbs energy of formation (KJ mol at 298.15 K) of CdTe and CdS are –92.5 & -156.5 respectively, whilst those of InSb and GaSb are –25.5 & -38.9 respectively.

Methods do exist for the generation of In and Ga alloys of Sb, based on 'traditional' galvanostatic plating. However, very little has been published regarding the direct electrodeposition and kinetics of InSb and, even more so, GaSb. This chapter discusses the results obtained during this new study of InSb and GaSb electrodeposition, with an emphasis on a kinetic viewpoint.

8.2 Electrodeposition of InSb

It is common for authors to quote a thermodynamic condition for electrochemical co-deposition for two or more elements. This condition states that the respective equilibrium potentials of the elements' precursor ions plus their overpotentials (i.e. their respective deposition potentials) should be within 200 mV of each other. Explicitly, where $E_{(A)}$ and $E_{(B)}$ are the components' equilibrium potentials in an alloy $A_xB_{(1-x)}$ (or compound), and η_A & η_B their respective overpotentials:

Equation 8.1

$$E_{(A)} + \eta_A \approx E_{(B)} + \eta_B$$

Yet electrochemical systems are dynamic, even at equilibrium. This can be readily shown by deriving the familiar Nernst equation using kinetic principles. Consider reaction 8.1, as stated in chapter two, at equilibrium the rates of the anodic process (v_a) and cathodic process (v_c) are equal and opposite.

Reaction 8.1

$$M^{n+} + ne^- \leftrightarrows M$$

Following the argument of Crow (1994), there will be an activation barrier to both anodic and cathodic processes ($\Delta G_a^{\ddagger}$ & $\Delta G_c^{\ddagger}$ respectively), whose rates may be expressed in terms of Arrhenius equations (8.2 & 8.3), with k_a and k_c the corresponding rate constants and M^{n+} the metal ion concentration at the electrodes surface.

Equation 8.2

$$v_a = k_a \exp^{-(\Delta G_a^{\ddagger}/RT)}$$

Equation 8.3

$$v_c = k_c \left[M^{n+}\right] \exp^{-(\Delta G_c^{\ddagger}/RT)}$$

At equilibrium $v_a = v_c$, so that,

Equation 8.4

$$k_a \exp\left[-\frac{\Delta G_a^{\ddagger}}{RT}\right] = k_c\left[M^{n+}\right]\exp\left[-\frac{\Delta G_c^{\ddagger}}{RT}\right]$$

Therefore,

Equation 8.5

$$\frac{\exp\left[-\Delta G_a^{\ddagger}/RT\right]}{\exp\left[-\Delta G_c^{\ddagger}/RT\right]} = \frac{k_c}{k_a}\left[M^{n+}\right]$$

Recalling that $\Delta G = \Delta G_c^{\ddagger} - \Delta G_a^{\ddagger} = nF\Delta\phi$, with F the Faraday constant and $\Delta\phi$ the difference in Galvani potentials of a species in a metal lattice and in solution:

Equation 8.6

$$\exp\left[-\frac{\Delta G}{RT}\right] = \frac{k_c}{k_a}\left[M^{n+}\right] = \exp\left[nF\Delta\phi/RT\right]$$

Equation 8.7

$$\frac{nF\Delta\phi}{RT} = \ln\left[\frac{k_c}{k_a}\right] + \ln\left[M^{n+}\right]$$

Equation 8.8

$$\Delta\phi = \frac{RT}{nF}\ln\left(\frac{k_c}{k_a}\right) + \frac{RT}{nF}\ln\left[M^{n+}\right]$$

Or,

Equation 8.9

$$\Delta\phi = \Delta\phi^{\circ} + \frac{RT}{nF}\ln\left[M^{n+}\right]$$

Despić & Jović (1995), stated that the condition given by equation 8.1 serves as only a 'rough assessment' of whether co-deposition can occur, in that deposition potentials are an undefined quantity unless the current is specified. The authors then went on to propose that a better definition of co-deposition would be that the partial current densities, i.e. those fractions of the overall current density due to each reducing species, should be within a similar range.

Consider, the formation of $A_XB_{(1-X)}$,

Equation 8.10

$$xA + (1-x)B \leftrightarrows A_xB_{(1-x)}$$

The composition of the deposit formed with respect to the components' partial currents (i_A and i_B), will be:

Equation 8.11

$$x = \frac{n_A}{n_A + n_B} = \frac{\frac{i_A}{p}}{\frac{i_A}{p} + \frac{i_B}{q}}$$

Equation 8.12

$$(1-x) = \frac{n_B}{n_A + n_B} = \frac{\frac{i_B}{q}}{\frac{i_A}{p} + \frac{i_B}{q}}$$

Equation 8.13

$$\frac{i_A}{i_B} = \frac{p}{q}\frac{x}{(1-x)}$$

(n_A & n_B are equal to the number of moles of each component deposited, and p & q the number of electrons needed for the reduction of each of the two components.)

Equations 8.2 & 8.3, expressed the rates of the cathodic (subscript c) anodic (subscript a) processes associated with a particular species in terms of Arrhenius equations. These can be stated in terms of cathodic and anodic currents. Following the imposition of an overpotential (section 2.2.7):

Equation 8.14

$$i_c = nFk_c[M^{n+}]\exp\left[-\frac{(\Delta G_c^\circ)^\ddagger}{RT}\right]\exp\left[-\frac{\alpha nF\eta}{RT}\right]$$

Equation 8.15

$$i_a = nFk_a[M^{n+}]\exp\left[-\frac{(\Delta G_a^\circ)^\ddagger}{RT}\right]\exp\left[\frac{(1-\alpha)nF\eta}{RT}\right]$$

(The partial current for each species, for example i_A, in solution will be equal to i_c- i_a.)

Once an overpotential is applied to the system to bring about deposition, the anodic part of the current falls to a negligible level (i_a tends to zero), and the high field approximation of the Butler-Volmer equation is applicable. Thus, the cathodic processes are activation controlled, and the partial currents of the species reducing (A and B) can be given by the following two equations:

Equation 8.16

$$i_A = i_{O,(A)} \exp[-(\alpha_A F/RT)(E_{DEP} - E_A^O)]$$

Equation 8.17

$$i_B = i_{O,(B)} \exp[-(\alpha_B F/RT)(E_{DEP} - E_B^O)]$$

Recalling that $(E_{DEP}) - (E^O) = \eta$, it is now evident that the partial current (say i_A) associated with the deposition of a species (A) will be related to its exchange current ($i_{O,(A)}$) and the applied overpotential.

Equation 8.12 showed that the composition of the deposit formed was determined by the ratio of the partial currents, substituting equations 8.15 and 8.16 into equation 8.12.

Equation 8.18

$$\frac{i_A}{i_B} = \frac{p}{q}\frac{x}{(1-x)} = \left[\frac{i_{O,A}}{i_{O,B}} \exp\left((F/RT)(\alpha_A E_A^O - \alpha_B E_B^O)\right)\right] \exp[(F/RT)(\alpha_A - \alpha_B)E_{DEP}]$$

Hence, the values of the current ratio depend not only upon the exchange currents ($i_{O,A}$ & $i_{O,B}$), the transfer coefficients[2] (α_A & α_B), and the equilibrium potentials, but also, in an exponential way, upon the potential across the electrode-electrolyte interface. Thus, a species will be deposited in excess of another if its exchange current is higher and its equilibrium potential more positive ('noble'), figure 8.1.

---

[2] Transfer coefficients are described in section 2.2.5.

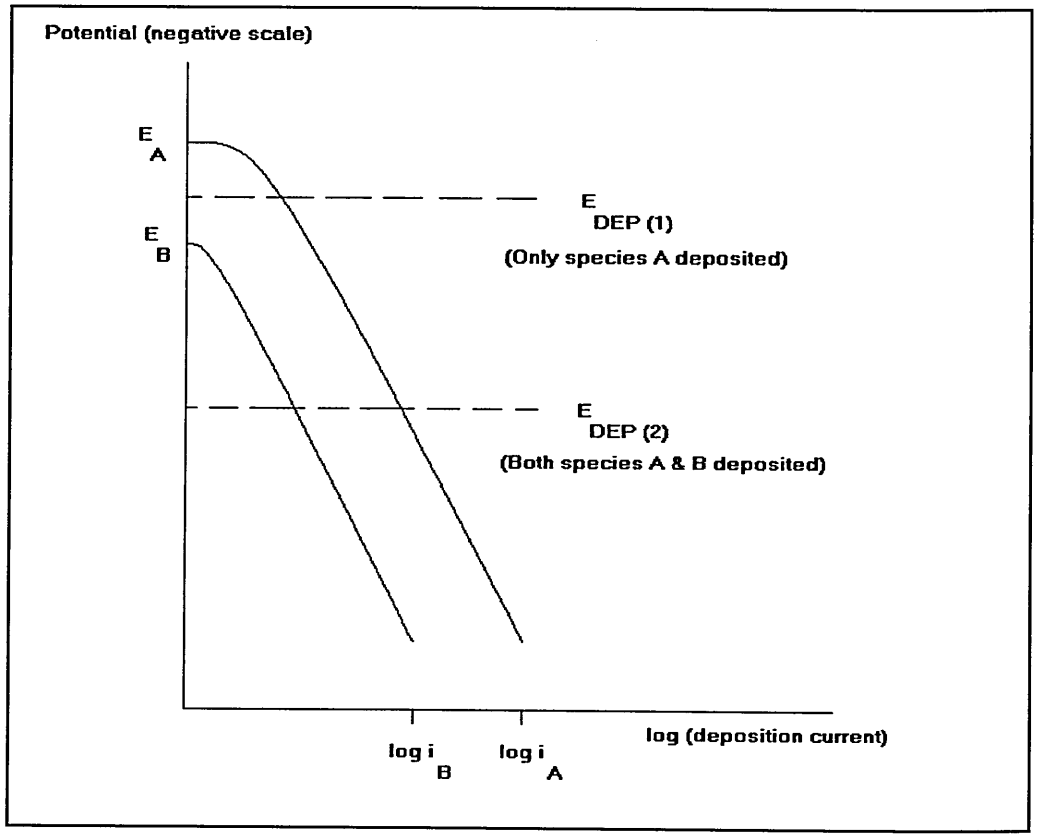

Figure 8.1 The alloy deposition of two species A & B in which the equilibrium potential E_A is more positive than E_B and the exchange current $i_{O,A} > i_{O,B}$ – and with the transfer coefficients $\alpha_A = \alpha_B$ (after O'M Bockris & Reddy 1970). The deposition potential E_{DEP} (1) is more positive than E_{DEP} (2).

8.2.1 Deposition from Aqueous Solutions Part I – The Role of Deposition Potential

The results recorded during this investigation provide a suitable vehicle for advancing the application of a kinetic approach to interpreting the processes involved in the deposition of InSb. As illustrated in figure 8.2, this variation in film composition was found to follow a general pattern. Specifically, films consisting of a single hcp Sb phase formed at the most positive potentials, whilst those deposited at the most negative potentials were found to contain a mixture of co-deposited tetragonal In and fcc InSb phases. Further, depending upon the conditions employed, growth at potentials intermediate of these extremes generated mixtures of InSb with Sb and/or In. With the exception of those grown on Ti substrates (section 5.3.2), there was a tendency for films deposited from aqueous solutions

to consist of mixtures of In and InSb[3], figure 5.19. In contrast, films comprising mixtures of InSb, Sb and In could be grown quite readily on to Ti substrates from aqueous solutions (e.g. figure 5.12), or on to ITO substrates from non-aqueous solutions (e.g. figure 6.24).

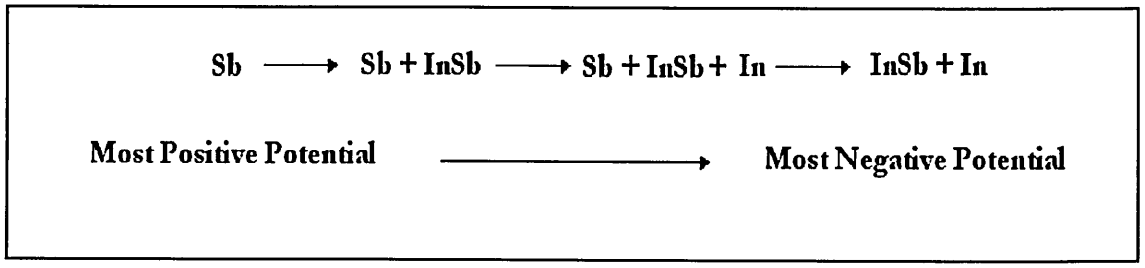

Figure 8.2 Variation of deposit composition with deposition potential.

The change in film composition with deposition potential can be illustrated through a comparison of XRD patterns obtained from films deposited on ITO substrates at - 0.50 V and - 1.00 V. As shown in figures 5.17 & 5.19 (section 5.4.1), under the conditions employed, a single hcp Sb phase formed on the cathode at - 0.50 V, whilst both In and InSb co-phases were generated at - 1.00 V. Further, based upon a qualitative examination of the relative XRD peak heights of the phases, it was shown that a change in composition with deposition potential could occur within a small potential 'window'. An example of this is depicted in the XRD patterns given in figures 5.11 & 5.12 (section 5.3.2). These figures show that within 100 mV, the intensity of most intense XRD peak attributed to the Sb phase decreased substantially, whilst those due to the co-deposited In and InSb phases increased noticeably.

At first, the above relationship between film composition and applied potential, for growth on Ti substrates, appears to be the same as that reported by Ortega & Herrero (1989). However, the results reported in this thesis are distinguished from that of these authors, in that the formation of films containing In, Sb and InSb co-phases was observed. Moreover, after an extensive study (section 5.3.1) no potential was found at which stoichiometric InSb formed. Indeed, amorphous films (containing In & Sb) formed in the potential window between the deposition of Sb 'rich' and In 'rich' InSb. Figure 8.3, illustrates the change in

---

[3] For brevity, prefixes indicating the crystal structures of the materials electrodeposited are in general omitted. These were, in all cases, fcc InSb, tetragonal In and hcp Sb.

film composition with deposition potential when using a Ti substrate, by overlaying the results of the deposits' XRD analysis and a typical voltammogram.

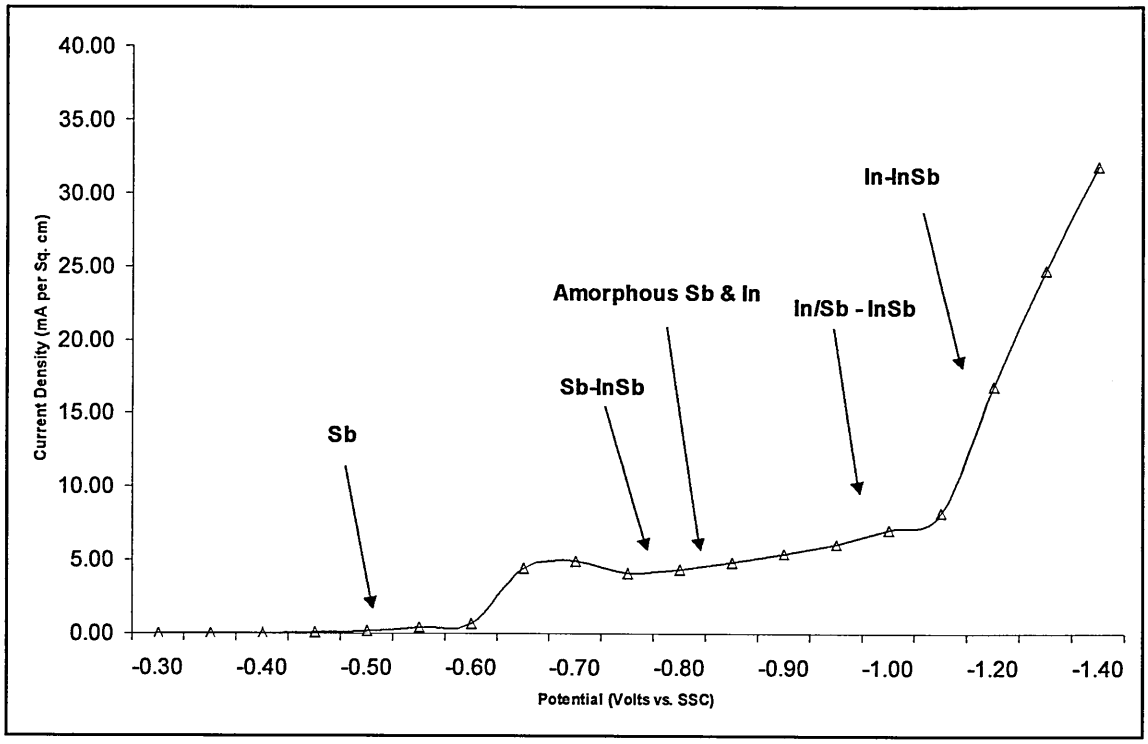

Figure 8.3 Graph illustrating the change in film stoichiometry, as indicated by XRD, with deposition potential for the room temperature electrolysis on a titanium substrate of a solution containing: 0.033 mol dm^{-3} $InCl_3$, 0.047 mol dm^{-3} $SbCl_3$ and 0.3 mol dm^{-3} citric acid, (section 5.3).

The portion of the above curve in which only Sb deposited (~–0.40 V to - 0.65 V) may be explained in terms of the figure 8.1. The equilibrium potential for the Sb species in solution is nobler (more positive) than that of the In species (for example, reactions 8.3 & 8.4). Despite the use of a citric acid complexant, it can be assumed that the difference in the two species' equilibrium potentials remains large[4]. In addition, the applied overpotential is insufficient to overcome the kinetic barriers to In deposition (equation 8.15), i.e. the exchange current density for In deposition is negligible. This is equivalent to the line on figure 8.1 showing the deposition of a single species only.

[4] This can be seen in the voltammograms obtained by Sadana & Singh (1985).

Reaction 8.2 $SbO^+ + 2H^+ + 3e^- \rightarrow Sb + H_2O \qquad E^O = +0.212\ V$

Reaction 8.3 $In^{3+} + 3e^- \rightarrow In \qquad E^O = -0.338\ V$

As the deposition potential is made more negative, the observed current does not increase exponentially, rather it begins to almost level out (~-0.70 V to -0.80 V) because of 'concentration polarisation'. Under such conditions, the rate of mass transport of the Sb species to the electrode's double layer is such that it can not keep up with that of their reduction, i.e. the electron transfer process. Under such conditions, the deposition of Sb is no longer activation limited, and Fick's law of diffusion can used to give the following expression for the partial current for Sb, now referred to as the 'limiting current' $i_{limiting}$, equation 8.19.

Equation 8.19
$$i_A = i_{limiting} = -\frac{DnFc_A^O}{\delta}$$

D is the diffusion coefficient, $c_A{}^O$ the concentration of the ions in solution, and δ the thickness of the double layer.

The partial current for the In can still expressed as:

Equation 8.20
$$i_B = i_{O,(B)} \exp\left(-(\alpha_B F/RT)(E_{DEP} - E_B^O)\right)$$

Again, expressing the partial currents as a ratio:

Equation 8.21
$$\frac{i_A}{i_B} = \frac{i_L}{i_{O,B}} \exp\left((\alpha_B F/RT)(E_{DEP} - E_B)\right)$$

Equation 8.22
$$= \frac{DnFc_A^O}{\delta \times i_{O,B}} \exp\left((\alpha_B F/RT)(E_{DEP} - E_B)\right)$$

Modifying figure 8.1, it can now be readily seen that the more negative the deposition potential is, the greater the proportion of the less noble species in the deposit (i.e. In). This is demonstrated in figure 8.4.

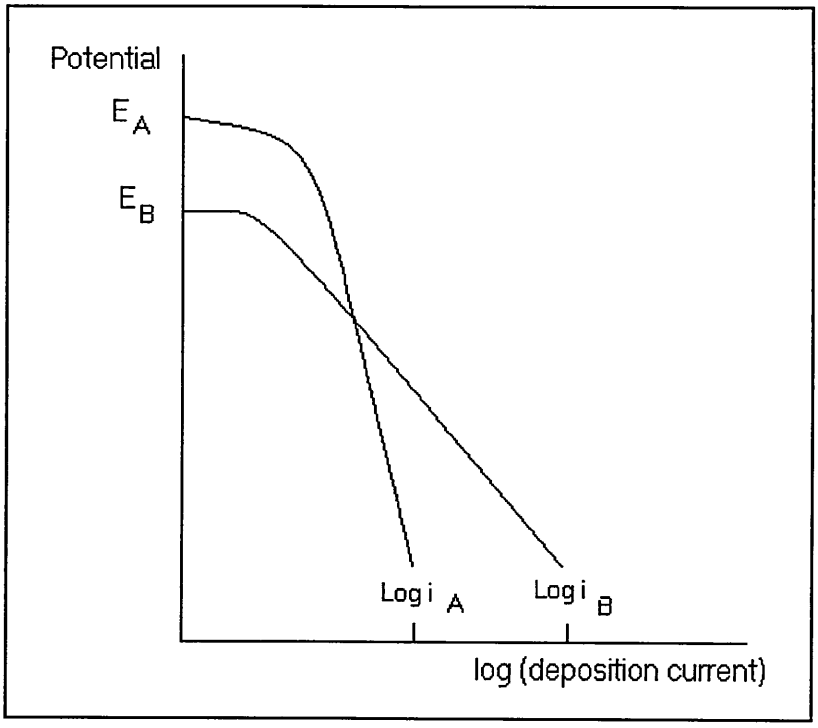

Figure 8.4 The alloy deposition of two species A & B ($E_A > E_B$) in which the deposition of A is transport limited (after O' M Bockris & Reddy 1970).

As Sb-In plating is (Sb) diffusion limited, it can be classed as a 'regular solution' according to the classification system devised by Brenner (1963), section 2.2.3. However, this categorisation should be approached with caution. Brenner's (1963) classification system is based on the relation between the composition of the deposit and the 'metal ratio'; that is the ratio of the total concentrations of the two (reducible) species in solution. For the composition of the deposit to mirror that of the solution, the reduction of *both* species has to be diffusion limited and this is not the case for the systems under study. Consider equation 8.19 that shows the rate of deposition of In to be proportional to the overpotential applied, which is equal to the deposition potential minus the *equilibrium potential.* Now, according to the Nernst equation, the concentration of the ions in solution should be greatly increased or decreased[5] if the value of the equilibrium potential, and hence deposition rate at a specified overpotential, is to be altered. This means that the composition of the solution (proportion of In ions) can be changed extensively without changing the composition of the deposit, i.e. a deposit of a certain composition can be

[5] This is the basis of using complexants in electrochemical systems, section 5.1.

grown from baths having different metal ratios. Such behaviour was illustrated in section 5.4.3, which showed that the effect on film composition of reducing the concentration of In species in solution was minor, when depositing on to ITO substrates from aqueous solutions. This could be taken to imply that in order to achieve the required composition one should change the concentration of Sb ions in solution. However, this strategy would fail because by increasing the Sb content (to counter the formation of In 'rich' InSb), diffusion control would be reduced. Hence, given that the Sb species in solution is nobler, Sb rich InSb would form because at the deposition potential required to deposit the less noble In, the rate at which Sb forms would be higher, explicitly, $(E_{DEP}-E_{Sb}) >> (E_{DEP}-E_{In})$.

8.2.2 Deposition from Aqueous Solutions Part II – The Origins of Nodular Growth Morphology

Another interesting consequence of the mass transport limitation of the deposition of Sb, was seen in the film's morphology, which tended to exhibit nodular growth patterns. This phenomenon can be explained by using the concepts introduced in section 2.5.2. In the aforementioned section it was shown that electrocrystallisation (i.e. electrochemical crystal growth) is fundamentally composed of two processes, these being electrodeposition and electrogrowth. Further, it was seen that crystallographic growth occurs when the *electrodeposition process*, which generates adatoms from the ions in solution, is occurring under activation control. This means that the *electrogrowth* processes that follow the generation of the adatoms is under diffusion control. In other words, at low overpotentials the rate of the formation of adatoms is relatively low. Following electronation, these adatoms sweep out across the substrate's surface along concentration gradients, to be quickly incorporated into growing crystal planes where the surface free energy is highest[6].

The large overpotential associated with limiting current conditions means that great numbers of adatoms are generated over the entire substrate surface, because the kinetic barriers to growth on all of the different sites (kink, step, plane etc.) can be overcome.

---

[6] In this study, deposition at high temperature increased the average 'particle' (or grain size) of the materials generated. At high temperature, the kinetic energy of the adatoms is high, however, this is balanced by a reduction of the kinetic barriers to the adatoms being incorporated into the growing crystal grains.

Moreover, it also leads to the rate at which the adatoms form being fast in comparison to the rate at which they can diffuse across the surface of the substrate, i.e. the electrode's surface becomes 'swamped' with adatoms. Practically, the adatoms, now unable to sweep along concentration gradients, 'pool together' in regions where charge transfer (adatom formation) is occurring at the highest rate, which will be where the diffusion layer's thickness is the smallest. (Recalling equation 8.19, under limiting current conditions, the partial current associated with the reduction of a species is inversely proportional to diffusion layer thickness δ.)

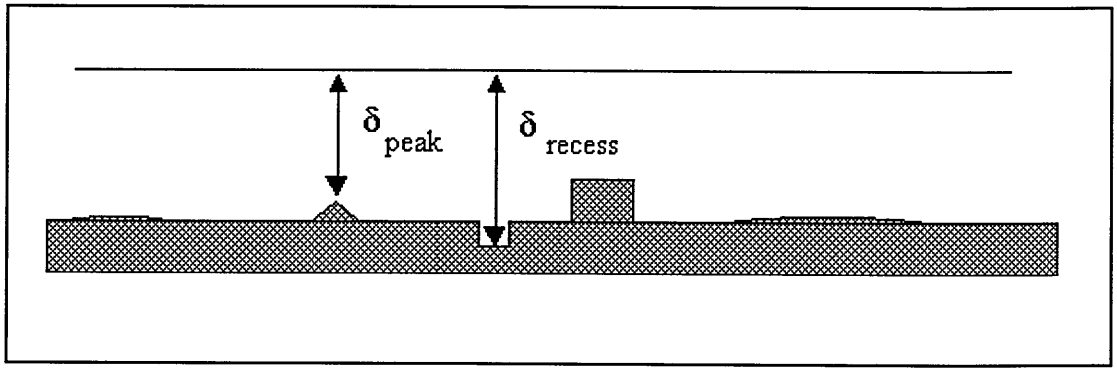

Figure 8.5 A representation of a 'rough' surface on which, when diffusion-controlled, the growth rate is higher at a peak than a recess.

Now, as illustrated in figure 8.5, the presence of crystal imperfections and freshly grown nuclei make the substrate's surface atomically 'rough', and therefore the diffusion layer thickness non-uniform. Growth occurs therefore at points that protrude from the substrate's surface. This effect is exaggerated during growth, the peaks becoming 'higher' and the recesses getting 'lower'. The nodular shapes in the deposits derive from complex diffusion profiles to the tips of the aforementioned peaks, which become hemispherical in shape. If the overpotential is increased, a point will be reached where it becomes so large that the diffusion layer thickness is very large in comparison to $\delta_{recess} - \delta_{peak}$. Under these conditions, crystallographic growth fails, as the adatoms begin to 'stick' to the substrate's surface in a random way, with the result of amorphous deposits being formed.

When the overpotential becomes sufficiently negative, the activation barriers to the deposition of In are overcome. At first, the rate of In deposition is low in comparison to that of Sb. Consequently, the deposit morphology is dominated by the Sb deposition, and therefore the deposits are amorphous. Thereafter, with increasing overpotential, the

diffusional limitations on crystal growth decrease, as the activation barriers to In deposition (and InSb formation) begin to swamp out the effects of Sb concentration polarisation and the films then become crystalline again.

8.2.3 Deposition from Aqueous Solutions Part III – The Conditions for Compound Formation

Returning to the results gained on the Ti substrate material, so far, the deposition system has been described in terms of the relative partial currents of In and Sb. This in itself does not say anything about whether or not InSb will form as a consequence of these species being reduced. In the literature, this is usually dealt with, again, in terms of thermodynamics. An alloy (or compound) will assume an equilibrium potential when placed in a solution of its own ions, and this potential can be described in terms of a Nernst equation. Thus, for the formation of an ideal alloy $A_{(x)}B_{(1-x)}$, from a solution of ions A^{p+} and B^{q+}, with all the other terms taking their usual meanings.

Equation 8.23

$$E_{(AxB(1-x))} = E^{O}{}_{AxB(1-x)} + \frac{RT}{(xp+(1-x)q)F} \ln \frac{(A^{p+})^{x} a(B^{q+})^{(1-x)}}{A^{x}B^{(1-x)}}$$

The position of this equilibrium with respect to those attained by the respective single metals in their pure form will depend on the activities of the ions in solution, and the standard equilibrium potential $E^{O}{}_{AxB(1-x)}$. This latter term will itself be strongly influenced by the change in Gibbs free energy associated with the formation of the species[7]. Hence, where the standard equilibrium potential of the pure metal A is more positive than that for the B, ($E^{O}{}_{A} > E^{O}{}_{B}$), the alloy's standard equilibrium potential will be more positive than $E^{O}{}_{B}$, i.e. $E^{O}{}_{AxB(1-x)} > E^{O}{}_{B}$.

Take for example the deposition of CdTe, which in principle can be thought of as a two-stage mechanism (Meulenkamp & Peter (1996)), where the equilibrium potential associated with reaction (8.4) being nobler than of reaction (8.5):

---

[7] A detailed derivation proving this is given in Despić & Jović (1995).

Reaction 8.4 $HTeO_2^+ + 3H^+ + 4e^- \rightarrow Te^0 + 2H_2O$

Reaction 8.5 $Cd^{2+} + Te^0 + 2e^- \rightarrow CdTe$

In kinetic terms, the rates of reactions 8.4 & 8.5 must be equal for the formation of stoichiometric CdTe to occur, and the formation of an elemental Te co-phase to be avoided. In order to bring about this, a deposition potential is selected that is slightly more positive than the equilibrium potential of the Cd^{2+}/Cd. This is because at this point no free Cd can form, and the rate of the compound's formation (reaction 8.3) is at its highest.

From the results presented herein, we can clearly see a difference in the electrodeposition of CdTe and InSb. In the case of the InSb, stoichiometric material is not formed, despite essentially the rates of In and Sb deposition being equal under the conditions employed. Instead, mixtures containing In, InSb and Sb were generated. Now, for the generation of InSb electrochemically, with all things being equal, the rate-determining step is the *chemical reaction* that results in the formation of InSb from the deposited Sb and In species, which is the analogue of 8.5 above. The distinction therefore derives from the magnitude of the kinetic barriers to compound formation, CdTe being lower than InSb, section 8.1.

Now according to classical chemical kinetics the rate (R) for the chemical reaction given in reaction 8.6, may be written as equation 8.24.

Reaction 8.6 $In^{3+} + Sb^O + 3e^- \rightarrow InSb$

Equation 8.24 $R = k\left[In^{3+}\right]^m\left[Sb^O\right]^n$

(The indices m & n relate to the order of a reaction, whilst the proportionality constant k is the rate constant for the chemical reaction.)

In the first instance, it may be proposed that the rate of the formation of InSb may be increased by increasing the rate of deposition of In and Sb, which are essentially controlled electrochemically. However, it was seen that this is not as straightforward as might appear. As shown above, if the concentration of the precursor ions in solution is raised, diffusion control is lost for Sb deposition. Given that the equilibrium potential of Sb/SbO^+ is nobler than In/In^{3+}, at a specified overpotential more Sb than In will deposit, section 8.1.1.

This does lead to the formation of more InSb, though this is coupled with the formation of an antimony co-phase. Making the deposition potential more negative does increase the rate of InSb formation. Unfortunately, given that the rate of Sb deposition is diffusion controlled, and therefore has a maximum growth rate, the second strategy would lead to the formation of an In co-phase with the InSb. Certainly, this has can be seen in the results of this investigation, figure 8.3.

The key, therefore, to stoichiometric InSb deposition is the rate constant (k) associated with the compound's formation, equation 8.24. This rate constant is related to the activation energy of the chemical reaction $E_A^{\ddagger}$ (the symbol of which should not be confused with deposition potential), as follows.

Equation 8.25 $$k = \text{constant} \times \exp(-E_A^{\ddagger}/(RT))$$

From the above equation (8.25), it is now clear that the electrochemical system's temperature should be raised from room temperature, to increase the probability of InSb formation. However, this also means that water becomes no longer a suitable solvent, as its boiling point is 100 ^{O}C. Hence, non-aqueous solvent systems with boiling points above 100 ^{O}C require consideration.

8.2.4 Deposition from Aqueous Solutions Part IV –The Effect of the Substrate

Before leaving the discussion of the aqueous systems, it is well worth mentioning an interesting phenomenon regarding the substrates. During the study, it was observed that the number of phases co-depositing was not only dependent upon the deposition potential, but also on the type of the substrate used, table 8.1.

Substrate	Sb	Sb & InSb	Sb, InSb &In	InSb & In
Ti	√	√	√	√
ITO	√	√		√
Cu	√			√

Table 8.1 The phases observed, following deposition under various conditions, according to type of substrate used.

The substrate was also seen to have an effect upon the deposition potential of Sb, and it can be assumed, that of In. Consider figure 5.33, in which the voltammograms obtained at different electrode materials were overlaid for comparison. It can be seen that the potential at which the current density first rises, and therefore where the reduction of the Sb species becomes evident, is different for each substrate. Specifically, this potential becomes more positive as the conductivity of the substrate increases, Ti < ITO < Cu.

Such a trend is not surprising, given that the three different substrate materials belong to two groups of 'conducting' materials, i.e. a metal (Cu) and two metal oxides. Essentially, untreated Ti is a non-conductor because it readily forms a thick oxide layer upon its surface. If the film thickness is sufficiently small, < 3 nm, quasimetallic behaviour can appear, as the electrons are able to tunnel through the oxide layer. In contrast, thicker oxide layers become quasimetallic if, as in this study, they are given a surface treatment that generates partly reduced metal cations within the material. This effectively makes the treated oxide layers a degenerate semiconductor through n type doping of the material. ITO is also a degenerate semiconductor, in that In_2O_3 is purposely doped by the manufacturer with Sn, making it an n-type semiconductor and, again, 'quasimetallic' in character.

At this point, it is worth digressing somewhat. Consider a p-n junction that is formed when n- and p- type semiconductors are brought into intimate contact. As soon as the junction is formed, electrons diffuse from the n-type material into the p-type material, whilst holes diffuse in the opposite direction. Consequently, a narrow depletion layer (~ 1 μm) is formed with the newly created negatively charged ions on the p-type material's side opposing their positive charged counterparts in the n-type material. The driving force for this transfer is the system's desire to equilibrate the two materials' Fermi levels[8]. Therefore, how much charge is moved whilst creating the depletion layer will be related to the difference in Fermi levels. Now, in order to generate a current (carried by the majority carriers) through the junction an electromotive force (EMF) has to be supplied by a battery that is large enough to overcome the excess charge residing within the depletion layer. Namely, the battery's EMF has to be larger than the junction's contact potential.

---

[8] Here, the reference point for the Fermi levels is the energy of a free electron at rest in a vacuum.

The above processes are analogous to that taking place when an interface is formed by the immersion of a metal into a solution of its own ions. This especially becomes clear by defining the electrochemical potential (μ^E_e) of a number of moles of electrons (N_e) in terms of their Fermi energy[9] (ε_F), thus:

Equation 8.26

$$\mu_e^E = \varepsilon_F N_e$$

In section 2.2.3, which is derived the Nernst equation, a reaction of the following type was considered:

Reaction 8.7

$$M^{n+} + ne^- \leftrightarrows M$$

At equilibrium, the electrochemical potentials of the left and right hand sides of the reaction are equal, and applying equation 8.26:

Equation 8.27

$$\mu^E_{M^{n+}} + n(\varepsilon_F N_e) = \mu^E_M$$

Substituting the above equation, into the form of the Nernst equation given in section 2.2.3;

Equation 8.28

$$\Delta\phi = \frac{\mu^E_{M^{n+}} + n(\varepsilon_F N_e) - \mu^E_M}{nF} + \frac{RT}{nF}\ln\frac{a_{M^{n+}}}{a_M}$$

Hence, it can be seen that the Fermi energy of the electrode's electrons affects the nobility of the reducing species. The higher the Fermi energy of the electrons, the more noble the deposition potential. This corresponds to what is intuitive from reaction 8.7, the more available electrons are, the more to the right that the equilibrium will lie.

---

[9] The occupation of the energy levels of the conduction band in metals described by the Fermi function, $f(\varepsilon) = \left(1 + \exp\frac{\varepsilon - \varepsilon_F}{kT}\right)^{-1}$, where ε is the energy of the given level. The Fermi level corresponds to that energy level which is half filled.

Given the above argument, the relationship between the number of phases deposited and the substrate is caused by the nobility of the Sb and In species being different at each substrate. The substrate whose electrons have the highest Fermi energy will have the most positive equilibrium potential for Sb and In reduction. Accordingly, the kinetics of the system (section 8.1.1) are 'moved' up to potentials that are more positive, in comparison to those on the Ti substrates. Namely, the deposition of Sb becomes diffusion limited at lower overpotentials than on Ti, and the deposition of In occurs at more positive potentials, making the formation of In rich InSb favourable at less negative potentials.

Some authors[10] discuss the above effects in terms of the electron work function Φ, which is characteristic of a material. This is done by introducing the concept of the 'real' potential (α) that is equal to - Φ ((Koryta et al (1993)). This real potential is essentially derived from the work done by a charged (z) species, whose chemical potential is μ, escaping from the surface of a phase, and is defined, with the surface potential χ as:

Equation 8.29 $$\alpha = \mu + zF\chi$$

The electrochemical potential μ^E_e is related to the surface potential and Volta potential ψ (section 2.2.2);

Equation 8.30 $$\mu_e^E = \mu + zF(\chi + \psi)$$

Equation 8.31 $$\mu_e^E = \alpha - zF\chi + zF\chi + zF\psi$$

---

[10] The term 'real potential', and its use by authors can be explained thus. Absolute values for inner Galvani potentials of the solid (ϕ_M) and solution (ϕ_S) phases can not be measured. This is because the surface potential term (χ) in the equation $\phi = \chi + \psi$ can not be measured. We therefore determine $\Delta\phi$, by measuring it against a reference electrode (i.e. reference $\Delta\phi$). Though, as $\Delta\phi = \phi_M - \phi_S = (\chi_M + \psi_M) - (\chi_S + \psi_S)$, values for ϕ_M and ϕ_S can still not be judged. In contrast, difference in the Volta potential (ψ) can be determined, because the electron work function of a material can be measured through the photoelectric effect. The Volta potential is that due to the excess charge at the interface, and is therefore analogous to the contact potential described above.

Hence, the electrochemical potential of a phase is related to the material's electron work function. The greater the work function, the higher the electron's electrochemical potential, and the above argument given for the 'extra' nobility of Sb and In applies.

The story does not end here. Wikstrom et al (1973) investigated the kinetics of Sb in acidic chloride solutions. The authors proposed a mechanism for Sb electrodeposition in which the rate-determining step (at low overpotential) was the adsorption of the antimonyl species onto the electrode. Obviously, the heats of adsorption on the surfaces of the substrates used in this investigation will be different. This leads to the conclusion that the heats of adsorption of Sb, and hence rate of Sb deposition, increase in the order Ti<ITO<Cu. Again, the potential at which Sb deposition becomes diffusion limited is the most positive for the Cu substrate.

8.2.5 Deposition from Non-Aqueous Solutions – The Role of Temperature

As with the aqueous systems, a dependence of film composition on deposition potential was observed when electrolysing non-aqueous solutions. General speaking, films 'rich' in the noble species (Sb) predominated at the more positive potentials, whilst the less noble species (In) were found in excess for the most negative deposition potentials. Nevertheless, this relationship was distinct from the aqueous systems, as the 'potential windows' in which the various species formed were considerably wider, especially that in which a mixture of In, Sb and InSb formed. This so much so, that it indicated that different processes were occurring at the electrode.

In the first instance, it can be expected that the deposition potentials of the various species will be more negative for the non-aqueous systems, because an extra overpotential has to be applied to overcome the resistance of the electrolyte solution. This can be demonstrated by examining the results of section 6.3, which showed that essentially negligible current densities were generated from solutions containing no supporting electrolyte. Consequently, a supporting electrolyte (tetraethylammonium chloride, TEAC) was used to decrease the solution's resistance, and an increase in the current density recorded was observed, section 6.4. Another interesting consequence of the addition of TEAC to the solvent was that at low overpotentials, a dependence of crystal orientation on deposition potential was seen in the XRD patterns of the Sb films deposited, namely, that

the XRD patterns showed that the crystal plane from which the most intense reflections (figure 6.7) originated changed with deposition potential.

Despite the addition of the supporting electrolyte, it was necessary to apply a large overpotential for In bearing species to be deposited. This was investigated further by conducting a study of the deposition of elemental In and Sb (section 6.5), and this led to the conclusion that the difference in Sb and In deposition potentials was considerable. Indeed, loosely adherent hcp Sb was generated at potentials–1.00 V (vs. Pt ref.), whilst crystalline (tetragonal) In only formed at potentials more negative than –2.00 V (vs. Pt ref.). It was also seen that it was possible to deposit amorphous In bearing films, despite the system's temperature being above that of the metal's melting point (156 ^{o}C).

Returning to the deposition of InSb, the voltammograms (e.g. figure 6.15) collected from the solutions prepared from $InCl_3$, $SbCl_3$ and TEAC were distinguished from their aqueous counterparts. However, as in the case of the aqueous systems, a general increase in current density with potential was observed and no large plateau region was seen in which the current density was, in essence, insensitive to potential.

The above results may be explained by considering the solution chemistry of the non-aqueous systems. When dissolved in non-aqueous solutions, it can be assumed that In exists in a variety of forms, which include $InCl^{2+}$, $InCl_2^{+}$, $InCl_4^{-}$, $InCl_5^{2-}$ and $InCl_6^{3-}$ (Mackay & Mackay (1989)). In the presence of such a large excess of TEAC, the majority of In species will not take part in the reduction process as they were negatively charged, e.g. $InCl_4^{-}$. By analogy to the aqueous system, the equilibrium potentials[11] of $InCl^{2+}$ and $InCl_2^{+}$ will be more negative than that of InSb, but more positive than In^{3+}. However, because these species are present in very low concentrations, the solution being mostly comprised of anions, the species equilibrium potentials are very negative (Nernst equation). This was seen when attempting the deposition of the metal from a solution of its salt. The amorphous layers that are formed at the more positive potentials likely contained Cl

[11] For aqueous solutions, for $InCl + e^- = In + Cl^-$ and $In^{3+} + 3e^- = In$, the standard electrode potentials are -0.34 V and -0.338 V respectively (Mackay & Mackay (1989)).

species, which did not crystallise because their melting point was above that of the pure metal[12]. Only when the deposition potential was made very negative did the In metal form.

The fact that the concentration of reducible ionic In species in solution was low was demonstrated in section 6.6.1. Here it was seen that InSb deposition occurred only when the ratio of $InCl_3$ to $SbCl_3$ dissolved in solution was greater than one. Whereas for the aqueous solutions InSb could be deposited from solutions containing less $InCl_3$ than $SbCl_3$, the non-aqueous solutions would only yield Sb films if the metal ratio approached 50% In and Sb.

It can be also suggested that the presence of a large excess of Cl^- ions in solution would affect the deposition of the Sb. Namely, it will be inhibited to some extent by the adsorption of the ion at the electrode. Hence, it is likely that an indicator of such effects was seen in the observed change (at low overpotentials) of the most intense Sb XRD peak with deposition potential when depositing InSb (section 6.3). As the 'strength' of Cl^- adsorption is different for the various crystal planes, the inhibition of the particular growing crystal faces will also be different, resulting in the growth of only those faces on which Cl^- adsorption is weakest.

The above considerations can be summarised in thermodynamic terms thus. The equilibrium potential of InSb is considerably more positive than that for the In species in solution. This is because the formation of InSb is more favourable at the temperatures used[13], as well as equilibrium potential for the $In/InCl_n^{(n-3)}$ couple being more negative because the reducing species' are in low concentrations. The difference between the equilibrium potential of InSb and Sb remained large, because the equilibrium potential of the latter is still very noble. Hence, for the non-aqueous systems, the formation of mixtures of In and InSb alone is not favoured, as was the case for the majority of the work conducted in aqueous solutions. This is shown schematically in figure 8.6.

---

[12] Inclusion of chlorine in the films is further discussed in section 8.2.6.

[13] Recall $\Delta G = \Delta G^{O} + RT \ln K$, where K is the equilibrium constant, and $\Delta G = -nFE$.

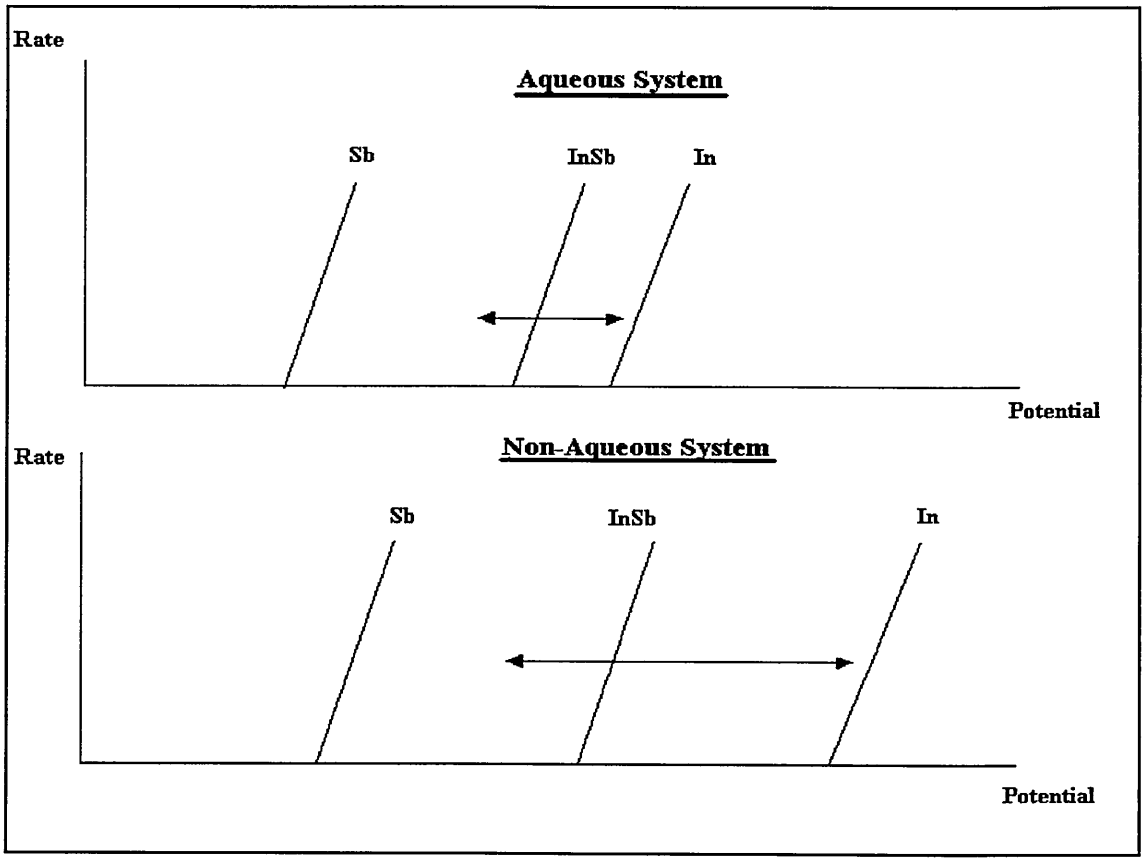

Figure 8.6 'Idealised' schematic showing the relative positions of the equilibrium potentials for the formation of In, Sb and InSb. The arrows indicate the 'potential window' in which the formation of mixtures of all three phases occurs. In this diagram, the difference in the deposition potentials of the various species should be compared, rather than their absolute values, because the scale of the potential axis will be different for the two systems.

Having established the above, the kinetics of the system can now be approached. For the aqueous systems, the following equations were used to correlate the experimental factors with the rate of Sb and In deposition, respectively:

Equation 8.18

$$\frac{i_A}{i_B} = \frac{p}{q}\frac{x}{(1-x)} = \left[\frac{i_{O,A}}{i_{O,B}}\exp\left((F/RT)(\alpha_A E_A^O - \alpha_B E_B^O)\right)\right]\exp[(F/RT)(\alpha_A - \alpha_B)E_{DEP}]$$

Equation 8.22

$$= \frac{DnFc_A^O}{\delta \times i_{O,B}}\exp\left((\alpha_B F/RT)(E_{DEP} - E_B)\right)$$

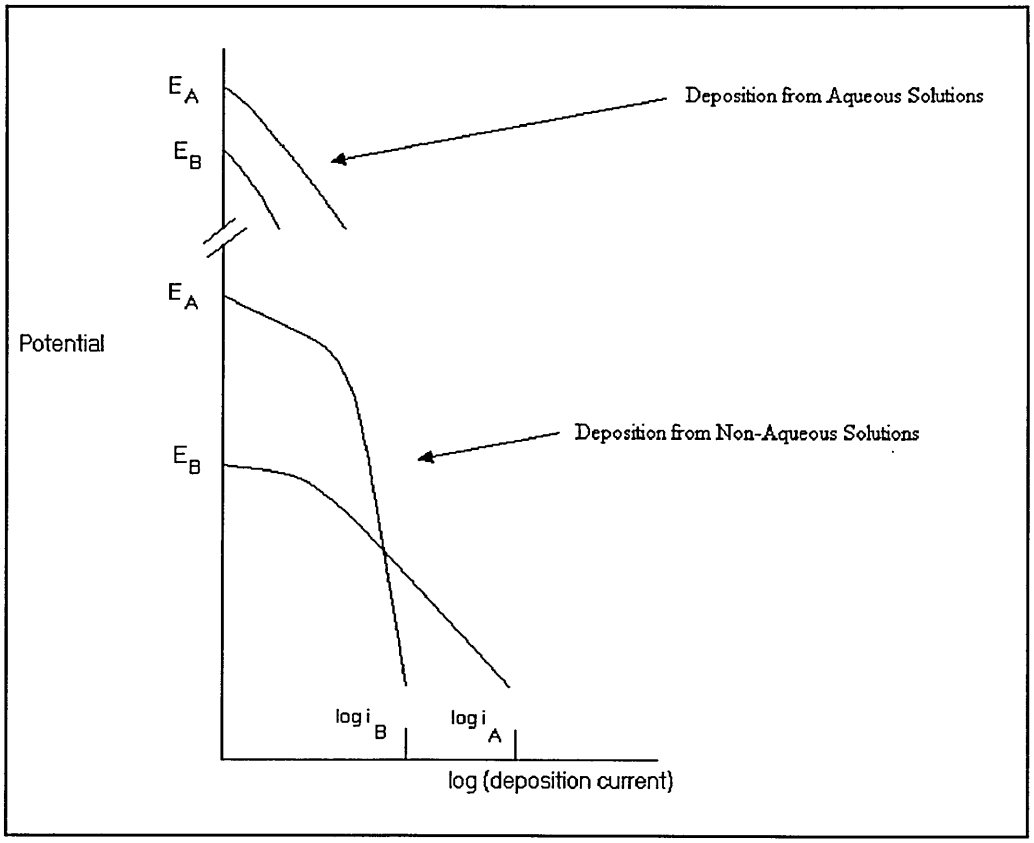

Figure 8.7 The alloy deposition of two species A & B ($E_A > E_B$) from a non-aqueous solution.

Whilst films consisting of three phases were formed over a wide range of potentials, the relative proportions of the phases with respect to each other changed with deposition potential. This can be seen when comparing the XRD patterns given in figures 6.16 to 6.18. These show that the relative intensities of the reflections from the In phase's crystal planes grew larger with respect to their Sb counterparts, as the deposition potential was made more negative. Eventually a point was reached where the reflections from the Sb planes were to all extent indistinguishable from the background. This indicates that Sb deposition did become diffusion limited. However, in comparison to the aqueous systems, this occurred at potentials that were sufficiently negative for the rate of In deposition to be also high. In effect this was a result of the interplay between the solution's high temperature improving the diffusion of the cations to the electrode, the solution's resistivity, Cl^- adsorption and the temperature of solution lowering the activation barriers to Sb deposition. Therefore, equation 8.18 was appropriate to the system over a wider range of potentials. Further, as the difference in equilibrium potentials was large for the pure Sb and In, and the E_{DEP} for InSb deposition highly negative, 3 phase deposits containing large

amounts of pure Sb occurred over a wide range of potentials. This is shown schematically in figure 8.7.

The presence of reflections from the In and Sb co-phases in the InSb films' XRD patterns, however minor their intensities, indicated that there were still kinetic barriers to the formation of the compound even at the high temperatures employed. In other words, the rate of the electrochemical reduction of In and Sb was such that the chemical reaction forming InSb was still too slow to keep pace.

To complete this discussion of the effects of the various parameters on InSb deposition the results given in section 6.7 will be discussed. Here, XRD patterns (figures 6.32 & 6.35) were presented that showed the formation of thin (large ITO peaks were evident) films of InSb, but without any reflections that could be attributed to the presence of In and Sb co-phases. These films were grown from electrolyte solutions whose precursor concentrations were, in comparison to those before, very low, specifically, 0.007 mol dm^{-3} $InCl_3$, 0.004 mol dm^{-3} $SbCl_3$ & 0.02 mol dm^{-3} TEAC.

The formation of the admixtures can be described in terms of three rate equations, i.e. those describing the deposition of In, Sb deposition, and InSb formation. As shown in figure 6.24, conditions were found where the rate of the formation of Sb and In co-phases was low in comparison to that of InSb. By reducing the concentration of the all precursors in solution, the rates of *all* aforementioned processes were lowered. However, because the rate of the formation of InSb was very much higher than that of the co-phases, its emergence from the substrate could be observed. It should be noted that this strategy was only appropriate to the non-aqueous system. For the aqueous (low temperature) system, the rates of Sb and In co-phase formation greatly outweighed that of InSb formation, because the kinetic barrier to the latter process was high. Therefore, the converse would be true whilst applying a similar strategy.

Before closing this discussion of InSb electrodeposition, with a proposed mechanism for chloride incorporation in the deposits, it is worth contrasting the results presented herein with those obtained by Styrkas et al (1964), and Kochegarov & Belitskaya (1971). The conditions used by these authors are summarised in section 6.1, though it should be mentioned that their deposition experiments involved not only galvanostatic deposition of the alloy, but also the use, at lower temperatures, of different electrolyte solutions. Given these conditions, the films formed tended to contain mostly amorphous material, which

required prolonged heating for the compound to be formed. This is in contrast to the predominately crystalline material generated during the investigation described here, which under certain conditions was in the most part crystalline InSb. Common to both reports was a dependence of film composition on current density. Unsurprisingly, they found that the In content of the films increased with current density. It can be concluded that the results of these authors were in agreement with those of this study, having shown the 'link' (section 8.2) between current density and deposition potential. Kochegarov & Belitskaya (1971) did provide some brief results regarding the relationship between bath and film composition, with respect to the applied current density. These show that the alloy would only form from glycerol solutions that contained $InCl_3$ in excess of the concentration of the tartrate of Sb, though the behaviour of the chloride in solution was not discussed. Most importantly, Styrkas et al (1964) suggested that the deposition of InSb was limited kinetically. This was despite the galvanostatic method employed by the authors being, in nature, less appropriate to the deposition of crystalline InSb, i.e. in comparison to the potentiostatic method used for this investigation, with its greater control over film composition. However, the results presented here provide further proof of this proposition. Therefore, it can be concluded that, overall, the results and conclusions of this study both extend and complement those of the aforementioned authors. For example, the voltammograms obtained during this study enable further investigation of the deposition of Sb under limiting current conditions when using non-aqueous solutions.

8.2.6 Inclusion of Chlorides in the Films

Early on, Gore (1855) established that the electrodeposition of Sb from HCl solutions produces films containing the halogen. Further, it is well known that electrodeposited Sb films containing significant amounts of entrapped $SbCl_3$ are amorphous and, upon gentle heating, have a tendency to crystallise with the loss of the entrapped halogen. Indeed, this form of Sb is often referred to as 'explosive' Sb. With regards to Sb-In alloy and compound InSb deposition, the incorporation of impurities in the deposits, such as chlorides, has not been studied to any extent. Hence, this section discusses the presence of the halogen in the films electrodeposited during this study.

Usually electrodeposited thin films contain impurities. These impurities do not necessarily originate from cations, but also can be a consequence of the inclusion of anions, uncharged species and particularly organic and inorganic colloids. The inclusion of such foreign

material within electrodeposits can have both a positive and negative effect upon the properties of the film formed. For example, deposition of metals from aqueous solutions at highly negative potentials results in the evolution of hydrogen, and a large increase in the concentration of hydroxyl ions near to the cathode's surface. Consequently, precipitation of metal hydroxides and basic salts occurs. These products are then included in the deposit, which may become fine grained, burnt in appearance and spongy. The inclusion of foreign material can also interfere in the deposition kinetics by reducing the film's conductivity, e.g. if hydroxides are included. In addition, inclusion most often takes place at high-energy sites in the lattice. This effectively reduces the number of sites (chapter two) that would be otherwise available for the growth of the desired crystal. However, this does not imply that the inclusion of any foreign material is necessarily detrimental to an electrodeposited thin film's final properties. Indeed, as discussed in chapter three, Dennison (1994) demonstrated the benefits, e.g. lower bulk resistance, of in situ doping of CdS and CdTe with Cl^- during electrodeposition.

Foreign substances mostly arrive at the cathode via diffusion and convection, with the transport of positive charges obviously only involving electrostatic migration. Rapid agitation of the electrolyte solution can also 'throw' foreign particles against the cathode. Impurities can be mechanically entrapped into a lattice, or physically bound to the cathode surface by adsorption and chemisorption.

EDX results given in chapters five and six show that the deposition of films from both aqueous and non-aqueous electrolyte solutions was accompanied by chloride inclusion. Based on the intensity of the EDX peaks, these results suggest that the films grown from non-aqueous solutions had a greater amount of the incorporated halogen (figures 5.6, 5.32, 6.3. 6.22 & 6.34). In the case of films deposited from aqueous solutions, the amount of halogen incorporated into the films appeared relatively insensitive to deposition potential (hence, current density), and was small for all the deposits formed. The converse was true for those samples grown from non-aqueous solutions. It was found that the EDX peaks from the chloride were larger for the films electrodeposited at the most negative potentials (i.e. higher current densities). The effect of the concentration of the precursors in the plating bath could not be easily distinguished. EDX analysis of films grown from non-aqueous solutions containing low concentrations of $InCl_3$ and $SbCl_3$ (0.007 mol dm^{-3} & 0.004 mol dm^{-3} respectively) still yielded large EDX peaks for chlorides if the deposits were formed at the most negative deposition potentials. Finally, the GDOES depth profiling

(and XPS) results given at the end of chapter six indicate that the halogen was distributed mostly towards the surface of the films.

From the results summarised above, a model for the presence of chlorides in the films can be proposed for deposition at the most negative overpotentials. (The reduction of $InCl^+$ etc. is dealt with in section 8.2.5.) At the more negative potentials, indium containing films are deposited under limiting current conditions, where the rates of In and Sb discharge are high. Consequently, the concentration of chloride ions in the double layer becomes large compared to that in the bulk of the solution. In the case of the aqueous solutions, the chloride ions remain in solution because they are readily solvated by water molecules. In contrast, there is a tendency for the chloride ions to precipitate out of the non-aqueous solutions as indium chloride. This precipitated indium chloride is then mechanically incorporated on the surface of deposit. The precipitation of the ionic indium chloride is a consequence of the low heat of solvation offered by EG, as well as its low dielectric constant. Another factor for the lower solubility of the chloride in these solutions would be the presence of Cl^- from TEAC, i.e. the common ion effect. It is likely that the precipitation of antimony chloride also occurs. However, this will be to a lesser extent, as the concentration of Sb species in the double layer is smaller than indium species, and the compound's degree of covalence is higher. An alternate proposition for chloride inclusion in the films would be that it is a result of adsorption or chemisorption. However, this is unlikely because the negative charge on both cathode and ion would prevent such a large amount of the halogen being incorporated into the films. Adsorption of Cl_2 produced at the anode and dissolved in solution is again unlikely as, especially given the non-aqueous solution's temperature, its concentration at the cathode is probably very small.

8.3 The Electrodeposition of GaSb

A short investigation of the deposition of GaSb from aqueous and non-aqueous solutions was performed during this study. In the absence of a significant amount of background literature, the investigation relied on the few published reports of studies that have been performed concerning the deposition of the analogous compound GaAs, section 3.4.3.

It was realised early on that the primary difficulty in depositing GaSb was the great difference in equilibrium potentials (E^o) of the two species. Although this is also true for the case of the InSb, which could only be deposited under limiting current conditions, the

difference in E^O for the Ga^{3+}/Ga couple (reaction 8.8) and SbO^+/Sb couple (reaction 8.2) was larger.

Reaction 8.8 $Ga^{3+}_{(aq)} + 3e^- \leftrightarrows Ga_{(S)}$ $E^O = -0.560V$

Two strategies were employed during this investigation to deposit GaSb from aqueous solutions, the first of which utilised a controlled-voltage electrolysis methodology. This method purposely allowed the cathode to become polarised to very negative potentials, as was used in GaAs deposition (Yang et al (1992)). The background to this technique is dealt with in sections 6.1 & 7.1, though it is worth mentioning here that the polarisation of the cathode is attained by concentration polarisation. The second strategy involved potentiostatic electrolysis of solutions whose concentrations of Ga ions were in excess of that of Sb.

8.3.1 Controlled-Voltage Electrolysis

Deposition experiments were conducted at 70 ^oC from solutions containing the $Ga_2(SO_4)_3$ very much in excess of the $SbCl_3$, specifically 0.05 mol dm^{-3} & 0.005 mol dm^{-3} respectively. Using XRD and EDX analysis, it was determined that films containing either the Ga metal or GaSb compound could not be generated at any of the deposition potentials applied. Instead, across the entire range of cell potentials applied (-2.19 to –3.20 V), ITO substrates were coated with thin films of hcp Sb.

Voltammograms were obtained, and these showed the two notable increases in current density with applied potential, which were separated by a relatively small plateau region. The plateau region was marked by an improvement in film adhesion and, according to XRD analysis, the Sb phase's crystallinity. Given the low concentration of Sb, the plateau region can be assumed to represent the applied potential region where Sb deposition becomes diffusion limited. However, as was the case for the entire applied potential region, the current density was low. Indeed, the levels achieved were, in comparison, an order of magnitude lower than those produced during the deposition of InSb from non-aqueous systems. Accordingly, the 'improvement' in crystallinity can be attributed more to the generation of thicker films. Further, the Sb deposition rate was low enough not to generate the conditions found when depositing In, where the rate of the formation adatoms exceeded their incorporation into the growing crystal planes, which would of have

resulted in the films being amorphous. At the higher applied potentials, the current density rose sharply, with the evolution of gas being easily observed at the cathode. It was demonstrated that the current density was prone to rapidly decrease (in minutes) under these conditions. The cathode's potential was measured against a reference electrode, and it was shown that the decrease in current density was accompanied by a relatively large negative polarisation of the cathode (see figure 7.7). These factors indicate that the electrode's surface became 'poisoned' with hydrogen bubbles, which accumulated quickly during the experiments.

Increasing the concentration of the gallium salt did not produce Ga bearing films. At the higher concentrations of Ga salt, the formation of a white precipitate was observed when the applied cell potential was particularly negative. Yang et al (1992) reported a similar effect, and proposed that this was a consequence of the formation of the insoluble gallium hydroxide at the cathode. Such an effect is produced when, at the more negative potentials, hydrogen is being produced at a high rate on the electrode. This depletes the double layer of hydrogen ions, making the pH in the local area next to the electrode more basic, thereby facilitating the formation of gallium hydroxide.

The absence of Ga in the films can be explained in thermodynamic terms. As shown in its Pourbaix diagram (appendix I), the stability region for Ga lies well below that of the line representing hydrogen evolution (section 2.2.8). Further, it can be assumed that the equilibrium potential of GaSb is close to that of Ga, as its Gibbs free energy of formation is small (-38.9 KJ mol). Hence, even if Under Potential Deposition occurs, as is the case for say CdTe formation, (section 3.3.2.) of Ga^{3+} on Sb^0, the formation of GaSb does not occur at a potential that is more positive than that of hydrogen evolution.

The results discussed above implied the need for greater control over the electrode's potential, given the close proximity of the deposition potentials for Ga and hydronium reduction. Therefore, it was decided to continue the study with a potentiostatic deposition methodology.

8.3.2 Potentiostatic Deposition

In general, the XRD patterns recorded from the films deposited potentiostatically showed that they consisted of Sb only. Indeed, as confirmed by EDX analysis, these films did not contain any significant amounts of Ga. However, the direct potentiostatic co-deposition of

GaSb from an aqueous solution was achieved by the electrolysis of a solution containing 0.4 mol dm^{-3} $Ga_2(SO_4)_3$ and 0.001 mol dm^{-3} $SbCl_3$. The formation of GaSb was confirmed by the film's XRD patterns (figure 7.8) and their EDX spectra (figure 7.9), which showed that the films were Sb 'rich' GaSb. To the author's knowledge, this is the first report of the direct co-deposition of GaSb from an aqueous solution.

An investigation was conducted of the relationship between film and electrolyte bath composition. The molar ratios of Ga to Sb in the plating baths ranged from 1:1 to 1000:1. GaSb was not deposited from any of the baths, other than that discussed above. It could be proposed that the absence of Ga in the films deposited from those baths containing a high concentration of its salt indicates that the element's deposition involves Sb, namely, under potential deposition of Ga on Sb^0 is not possible when the concentration of the antimonyl ions is low.

The use of a citric acid complexant was investigated. As expected, this did not result in the formation of GaSb. In the first instance, the presence of the complexant makes the solution's pH even more acidic, hence increasing the rate of hydrogen evolution. Secondly, it should be recalled that the purpose of the complexant is to shift the deposition potential of Sb to more negative potentials. This does nothing about 'lowering' the deposition potential of Ga below that of hydrogen.

The results of the controlled voltage and potentiostatic deposition can be discussed in kinetic terms. Indeed, equations 8.16 and 8.19 still apply, the latter defining the current density under 'limiting current' conditions, which is valid for Sb deposition.

Equation 8.16 $$i_A = i_{O,(A)} \exp[-(\alpha_A F/RT)(E_{DEP} - E^O_A)]$$

Equation 8.19 $$i_A = i_{limiting} = -\frac{DnFc^O_A}{\delta}$$

Here, the evolution of hydrogen and the deposition of Ga are both described by equation 8.16. However, under the condition employed, the exchange current density $i_{(O,A)}$ for hydrogen was higher than that of Ga, implying that the kinetic activation barriers to Ga reduction are greater than that of hydrogen evolution (equation 8.14). Moreover, the overpotential ($E_{DEP} - E^O_A$) associated with the H^+/H_2 is larger than that of the Ga^{3+}/Ga couple. The kinetics of the deposition system are illustrated in figure 8.8.

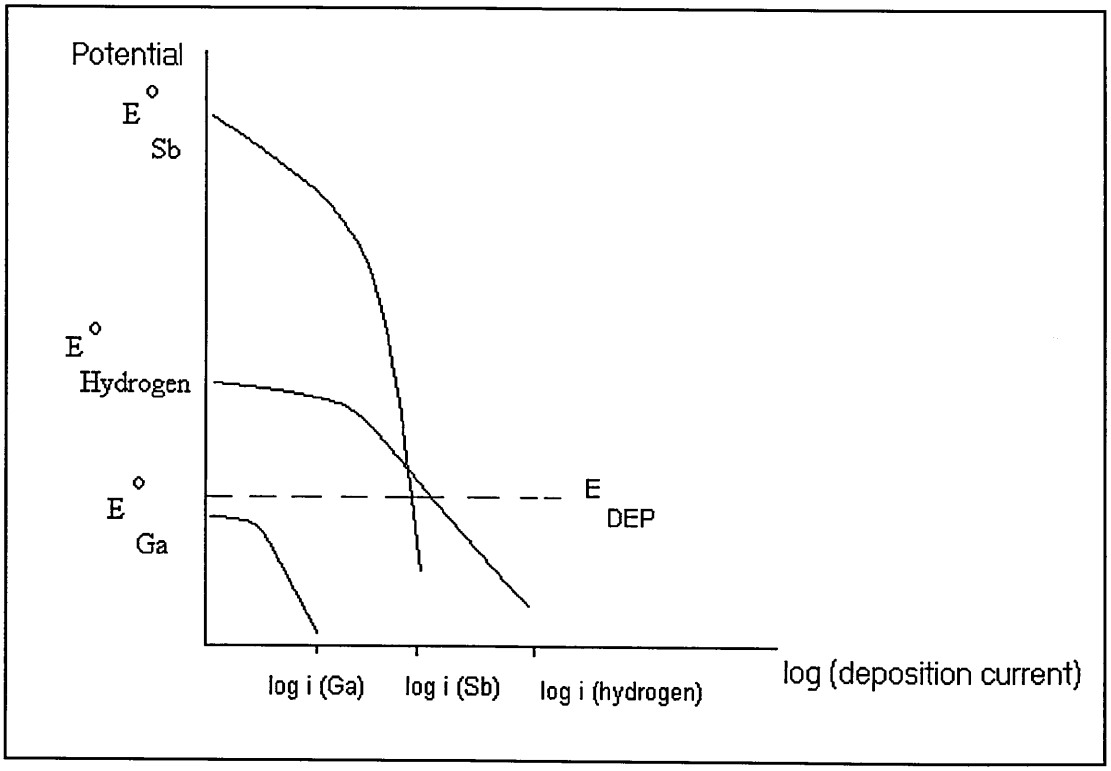

Figure 8.8 The co-deposition of Ga and Sb, in the presence of hydrogen evolution.

Deposition of GaSb, as in the case of GaAs (Yang et al (1992)), from acidic aqueous solutions was therefore shown to be prevented by the co-evolution of hydrogen. It can also be assumed that GaSb would be similar to InSb, in that its deposition at low temperatures would be limited by kinetic limitations. This led to the conclusion that the use of non-aqueous solutions should be also considered for GaSb deposition. However, as proven by the results of section 7.4, the use of such solvents for GaSb demonstrated practical difficulties in the first instance, because $Ga_2(SO_4)_3$ was found to be insoluble in EG, and the alternative precursor used, anhydrous $GaCl_3$, deliquesced on contact with air.

Chapter 9

Conclusions & Suggested Future Work

9.1 Introduction

Electrochemical deposition of semiconductors is a particularly rich field of research. As shown in chapter three, the demands placed on the materials, in terms of their applications, have shaped the way in which investigators have approached the development of methods for their electrochemical growth. Semiconductor materials are primarily required to have definite compositional, morphological and crystallographic properties, so that they may demonstrate certain electrical and photoelectric properties when used in device structures. Therefore, the approach used in this study concentrated on investigating the effect of the system's electrochemical parameters on the aforementioned material properties.

9.2 The Electrodeposition of InSb

The direct electrochemical co-deposition of InSb was achieved via the potentiostatic electrolysis of both aqueous, and for the first time, non-aqueous electrolyte solutions. Both systems utilised a three electrode cell, the cathode's potential being measured, according to the solvent, against a silver-silver chloride electrode and Pt reference electrode respectively. Ti, Sn doped In_2O_3 (ITO) and Cu substrate materials were used during the aqueous deposition studies, whilst that of the non-aqueous systems used ITO substrates exclusively. The deposition experiments were carried out from electrolyte solutions made up from $InCl_3$ and $SbCl_3$ in purified water, with a citric acid complexant, or in ethylene glycol (EG), with a tetraethylammonium chloride (TEAC) supporting electrolyte. Electrolysis was performed with aqueous solutions at room temperature, or near the boiling point of EG (185 ^{o}C). The following sections summarise the conclusions that may be drawn from the results gained during the investigation of InSb electrodeposition.

9.2.1 Experimental Parameters and Composition

The composition of the films grown from both aqueous and non-aqueous electrolyte solutions was greatly influenced by the deposition potential used. Growth at the most

positive potentials generated hcp Sb films, whilst growth at the most negative potentials produced fcc InSb films 'rich' in tetragonal In. The formation of InSb free from In and/or Sb co-phases could not be achieved whilst depositing from low temperature aqueous electrolyte solutions. Indeed, the electrodeposition onto Ti substrates of InSb, free of In and Sb co-phases (Ortega & Herrero (1989) could not be duplicated. Rather the formation on Ti of admixtures consisting of fcc InSb, tetragonal In and hcp Sb was reported for the first time. Moreover, the formation of films containing mixtures of these three phases was common when electrolysing the non-aqueous solutions.

In reviewing the literature, it was seen that investigators typically discuss the effects on film composition of the various electrochemical parameters in terms of the system's thermodynamics. Hence, for the Sb-In system, the equilibrium potentials of the Sb ionic species are more noble (i.e. have a more positive deposition potential) than that of In, and consequently Sb deposition is more favourable than In. However, this view, whilst correct, was seen to provide only a limited picture of the system under study, and therefore the system's kinetics were considered.

The direct co-deposition of In and Sb from aqueous solutions is possible because the deposition of Sb is limited by its diffusion to the electrode. First proposed by Sadana & Singh (1985), this study provides direct proof of this proposition. Linear sweep voltammograms obtained during this study, when compared with, for example, the film's XRD patterns, clearly indicate that In deposition only occurs at potentials where Sb deposition is diffusion limited.

A kinetic model for the system was developed using the concept of partial currents, the sum of these being the current recorded during the experiments. The thermodynamic condition for the co-deposition of Sb and In is that the equilibrium potentials of the depositing species plus their respective overpotentials are within 200 mV. Similarly, a kinetic condition for Sb and In co-deposition can be stated, based the general one proposed by Despić & Jović (1995), namely, that the partial currents, i.e. those fractions of the overall current density due to each reducing species, should be within a similar range.

Expressions were derived that provided a relationship between the partial currents of the depositing species and the various experimental parameters. (For the deposition of Sb, this involved using an equation that was modified to take in to account the fact that its deposition with In only occurred when it was diffusion limited.) These expressions

allowed the change in film composition with deposition to be described in kinetic terms. Essentially, at the more positive growth potentials, the rate of Sb deposition is higher than that of In, because its exchange current density is larger, and its equilibrium potential more positive. When the growth potential is made more negative In rich InSb is formed because the rate of In deposition exceeds that of Sb, the latter becoming diffusion limited.

Changing the concentration of the precursors in the electrolyte solution was seen to have only a limited effect upon the deposit composition, certainly in relation to that of the deposition potential. Such a conclusion was derived from the analysis of the XRD patterns of films grown from baths having different concentrations of $InCl_3$ dissolved in them. These results can be explained by remembering that the 'effective' antimonyl species in solution (i.e. not chelated with citric acid) is deliberately low in comparison to that of In^{3+}. (This was necessary in order to bring their equilibrium potentials closer together and facilitate co-deposition.) Hence, the effective concentration of In^{3+} being in such excess, means that its concentration can be significantly varied without radically changing the composition of the film. Therefore it can be concluded that it is with caution that, as proposed by Sadana & Singh (1985), this particular system should be described as of a 'regular' type according to Brenner's classification system.

Growth was performed from the aqueous solutions on three different substrate materials, Ti, ITO and Cu. The results show that the number of possible phases that formed under the various deposition conditions was different for each substrate. Films could be deposited on Ti that consisted of either Sb, Sb rich InSb, In rich InSb or admixtures of the two elements and InSb. In contrast only Sb or In rich InSb formed on Cu. To explain such observations, it was necessary to consider the electronic properties of the materials, either in terms of their electrons' Fermi energies or work functions, as well as the role of adsorption on the kinetics of antimonyl reduction. It was proposed that the substrate whose electrons have the highest Fermi energy (Cu) (or electron work function) would have the most positive equilibrium potential for In and Sb reduction. In other words, the exchange current densities of the two species are high, consequently making the formation of In rich InSb more favourable. These results highlight the importance of the substrate in the development of an electrochemical synthesis route. If a particular electronic device requires a certain substrate, e.g. ITO for a photo detector, then it may be so that an electrochemical synthesis route developed using a different substrate might well require modification.

The above considerations lead to the conclusion that the deposition of InSb, free from Sb or In co-phases, was kinetically limited when depositing from low temperature aqueous electrolyte solutions. Therefore, an investigation of the deposition of InSb from high temperature non-aqueous electrolyte solutions was made. This led to the first report of the potentiostatic co-deposition of InSb from such a system.

In general, the relationship between deposition potential and film composition was seen to be the same as described above for the aqueous systems. However, the relative proportion of the InSb in the films was much larger than that of any In or Sb co-phase. Moreover, it was demonstrated that the formation of admixtures of Sb, In and InSb occurred within a larger potential window than for the aqueous systems. This was so much so that crystallisation of amorphous In (m.p. 156 ^{o}C) during deposition can not wholly explain such a phenomenon. In order to explain such an effect both the system's kinetics and thermodynamics were considered. It can be concluded that the formation of 3 phase admixtures at high temperature is favoured by three factors. Firstly, because the growth temperature is high, the kinetic barriers to the formation of the compound are overcome more, than was the case for the low temperature aqueous systems. Secondly, Sb deposition becomes diffusion limited at potentials that are more negative than the aqueous systems, even allowing for the solution's inherent resistance. Thirdly, the concentration of reducible In species is low, most of it being in the form of anions, and therefore its deposition also occurs at more negative potentials.

In contrast to the aqueous solutions, the composition of the electrolyte was seen to have a greater effect on the films' stoichiometry. This can be attributed to the low concentrations of reducible In species in solution. Hence, In deposition only occurred when the amount of $InCl_3$ dissolved in solution was greater than that of the $SbCl_3$. Reducing the concentrations of both In and Sb precursors in solution generated films whose XRD patterns indicated the formation of thin films of InSb alone. This is unsurprising, given that the formation of the compound's phase proceeds at a greater rate than that of the elements. Hence, although all the respective rates of the formation of all three phases were effectively lowered, that of InSb deposition was large enough for its deposition to be observed in the XRD patterns acquired. However, these results were difficult to reproduce. This is probably because once the films exceeded a certain thickness, the quantity of the In and Sb co-phases in the deposits was large enough to yield identifiable XRD peaks.

Having summarised the most essential results from this investigation, the most important conclusion from this work can be stated. This is that, although InSb deposition was achieved, to the authors knowledge, at the highest temperature reported for such systems, the formation of the compound is still kinetically limited.

It is also worth returning to the condition described by Despić & Jović (1995) for alloy deposition, so that it may be rewritten in terms of compound formation. Specifically, for the electrodeposition of a compound of stoichiometric composition, the partial currents should be in the same proportion as in the compound, and the conditions should be such that the kinetic barriers to the compound's formation are overcome.

9.2.2 Particle Size & Morphology

The first SEM study of electrodeposited films containing InSb showed that their morphology was predominately nodular in form, whether deposited from aqueous or non-aqueous systems. Usually, the films were seen to consist of a homogeneous compact underlayer, presumably (through GDOES analysis) rich in Sb, on top of which grew ~1 to 5 μm sized nodules. This morphology was a consequence of the deposition being performed under limiting current conditions, and a detailed explanation is given in section 8.8.2.

Mengoli et al (1991) reported an average estimated crystallite size of 35 nm for InSb formed after the post growth annealing of electrodeposited In on Sb. However, in the absence of reported data, the authors were unable to make any comparisons with crystalline films grown by other electrochemical methods. Therefore, crystallite sizes were estimated for a representative sample of the films grown during this investigation. The particle sizes calculated for the films grown during this study compared well with those of the aforementioned authors. Indeed, samples grown at room temperature had an average particle size of 50 nm, whilst those grown from the high temperature solutions were on average 75 nm large.

Finally, XRD strain analysis was performed in order to assess whether or not the observed 'cracked' appearance of some of the deposits was a consequence of the films fracturing through internal stresses. Based on the resulted obtained, it was suggested that, given its extent, sample cracking in the deposits was likely a result of macrostress taking advantage of faults in the material upon removal from the bath.

9.2.3 Inclusion of Chlorides in the Deposits

The presence of impurities in electrodeposited InSb has not been studied before. EDX analysis of the films deposited during this investigation showed them to be significantly contaminated with chlorides. Further, GDOES depth profiles acquired from the films indicated that the halogen was entrapped near the films' surface, and that its cross-sectional distribution followed that of In. The inclusion of chlorides was seen in most of the samples, but this was particularly evident for those containing In, and this was especially true for those grown from non-aqueous solutions. This was explained in terms of the tendency for the chloride ions to precipitate out of the non-aqueous solutions as indium chloride, the precipitate then being mechanically incorporated on the surface of deposit.

9.3 The Electrochemical Deposition of GaSb

The direct co-deposition of GaSb from an aqueous electrolyte solution was studied in detail for the first time. Conditions were reported for the direct growth of GaSb via potentiostatic electrolysis. The XRD patterns of GaSb containing films indicated the presence of an hcp Sb co-phase. First reports from a SEM study of admixtures of GaSb and Sb deposited from aqueous solutions showed that the films' morphology were dominated by small fibrous needle like features. EDX studies did not suggest that any significant amount of chlorides were included in any of the materials grown.

Under the conditions employed, deposition using a constant voltage mode of electrolysis did not produce films containing Ga. Though polarisation of the cathode was evident, it was found that the evolution of H_2 (and presumably) SbH_3 inhibited the reduction of Ga containing films.

The deposition systems were again considered from both a thermodynamic and kinetic viewpoint, and it was proposed that many of the conclusions drawn from the InSb system investigation were equally applicable. The greatest difference in the systems was that Sb-Ga electrodeposition was kinetically limited by the concurrent evolution of hydrogen. The growth of Ga containing films is complicated by the fact that the reduction potentials for the compound's and the elements' deposition are more negative than that for the gas evolution reaction. Thus, in the aqueous solution, with its plentiful supply of hydronium ions, the portion of the deposition current due to the reduction of Ga^{3+} is small in comparison to H^+ reduction. Given the results of the InSb investigation, these results

suggest that the deposition of GaSb of the desired quality can only be achieved from non-aqueous solutions. Yet, whilst new work was carried out on these systems, it was seen that certain practical difficulties are associated with using non-aqueous solvents, in that $Ga_2(SO_4)_3$ was insoluble in EG and that anhydrous $GaCl_3$ hydrated on contact with air.

9.4 Suggested Future Work

Even before the materials are used for the fabrication of semiconductor devices, the electrochemical deposition of InSb and GaSb still offers many interesting opportunities for further research.

The formation of InSb, and presumably GaSb, is still kinetically limited at 185 °C. Therefore, it is obvious to suggest that it would be of interest to investigate the electrodeposition of these compounds at higher temperatures. Such work would not necessarily require growth temperatures within the same region as those used by other techniques, which are typically above the melting points of the compounds. This is particularly so, given that the temperatures of the systems described herein are quite low in comparison to, for example, melt growth techniques.

Growth at higher temperatures would first entail the selection of a suitable solvent and solute, and many of the considerations outlined in this thesis (sections 5.1, 6.1 & 7.1) would equally apply to any solvent-solute system. A cursory examination of standard tables[1] of the physical properties of common non-aqueous solvents shows that their boiling points typically lie between 100 °C to 200 °C, making them unsuitable. However, one solvent whose boiling point is outside this range is glycerol (Propane-1,2,3-triol), which boils at ~ 300 °C. Indeed, as summarised in section 6.1, it was from this solvent that Kochegarov & Belitskaya (1971) attempted the galvanostatic deposition of InSb at the relatively low temperature of 125 °C, the solutes being $InCl_3$, and $K(SbO)C_4H_4O_6.1/2H_2O$ (potassium antimony tartrate), with a KOH supporting electrolyte. (A similar precedent exists for the growth of Sb-Ga alloys. Again, the method used involved the alloy's galvanostatic deposition at low temperatures, Khamudkhanova et al (1973)). Mindful of the conclusions drawn from this work, the potentiostatic deposition of InSb from the aforementioned

[1] Suitable examples are given in Sawyer et al (1995).

electrolyte solution could be investigated, but at temperatures near to the boiling point of glycerol. Moreover, so that the chloride contamination of the sample is avoided, the indium chloride could be replaced with its sulphate.

An alternate to the electrolysis of non-aqueous solvents would that involving the use of molten salt systems. These systems have allowed various semiconductors to be electrodeposited over an extremely wide temperature range (300 to 1000 ^{o}C), chapter three. An example solvent system is the LiCl-KCl melt (liquidus temperature 355 ^{o}C), into which the metal oxides and antimony oxide could be dissolved. In developing a protocol using molten salts, care would have to be taken in selecting conditions that avoid problems with the volatility of the materials in solution as well as the solvent, especially with respect to that of the antimony. Such study would also involve a methodical study of the relative proportions of the components making up the melt, so that a suitable liquidus range could be achieved, whilst enabling the deposition of the compounds. Another reason for fine control over the melt composition is that metals can exhibit several stable oxidation states in chloride melts, therefore making the reduction of several different species possible.

Another intriguing possibility for molten salt growth is the use of 'organic' melts. An example of a low temperature system was reported by Carpenter & Verbrugge (1994), section 3.4.4. These authors studied the deposition of InSb at (50-60 ^{o}C) from chloroindate melts, derived from $InCl_3$ and 1-methyl-3-ethylimidazolium chloride, with $SbCl_3$. These solutions were shown to exhibit good chemical and thermal stability, and high intrinsic electrical conductivities. Unsurprisingly, the temperature being so low, non-stoichiometric films were produced. However, quaternary ammonium chloride salts with higher melting points are available, for example those derived from benzimidazole.

Turning to the analysis of the films, the GDOES depth profiles obtained during this study point to a variation in film composition with sample depth. This phenomenon, and the inclusion of chlorides in the films, could be analysed using XPS (X-Ray Photoelectron Spectroscopy), given the technique's ability to provide information regarding the chemical state of the elements within films. In addition, an estimation of the percentage of, for example, indium in the form of InSb could be made. Further composition depth profiling using SIMS (Secondary Ion Mass Spectroscopy) could be performed with a view to determining what impurities are present in the deposits. Finally, there exists a multitude of techniques available for determining the material's photo-electronic properties, an example

of which would be the measurement of the electrodeposited InSb's band gap using FTIR reflectance spectrometry.

The aim of all the above measures would be to optimise the materials' growth, and to extend the semiconductor electrochemical deposition field as a whole. Ultimately, it is hoped that this would lead to the fabrication of some of the devices discussed in chapter one. This achieved, there would be a multitude of opportunities for new work in characterising and developing the devices themselves.

Abbot S. A., 1993, Chem. Soc. Rev., pp 435-440

Allonge P., Souteyrand E., 1993, J. Electroanal Chem., No. 362, pp 79-87

Andre J.P., Hallais J., Schiller C., 1975, J. Crystal Growth, Vol. 31, pp 147-150

Baranski A. S., Fawcett W. R., McDonald A. C., de Nobriga R. M., MacDonald J. R., 1981, J. Electrochem. Soc., Vol. 128, No. 5, pp 963-968

Baranski A. S., Fawcett W. R., 1984, J. Electrochem. Soc., Vol. 131, No. 11, pp 2509-2514

Barrow B. M., 1988. Physical Chemistry, 5th Ed., McGraw-Hill International Editions, N.Y., pp. 771-774

Basol B. M., 1988, Solar Cells, Vol. 23, pp 69-88

Basol B. M., 1992, Doga. Turk., J. Phys., Vol. 16, p 107

Berger L. I., Pamplin B. R., 1994, "Handbook of Chemistry and Physics", (Ed. D. R. Lide), CRC Press, USA, 12-78

Bespalko O. M., Vdovenko I.D., 1972, "Korroziya i Zashchita Metallov", (Ed. Delimarskii Y. K.), Naukova Dumka, Kiev, pp 10-14 [Chemical Abstracts, 78, (1963) 78890V]

Bhattacharya R. N., Rajeshwar K., J. Electrochem. Soc., 1985, Vol. 132, No. 3., pp 732-724

Bhattacharya R. N., Wiesner H., Berens T. A., Matson R. J., Keane J., Ramanathan K., Swartzlander A., Mason A., Noufi R. N., 1997, J. Electrochem. Soc., Vol. 144, No. 4, pp 1376-1379

Biefield R. M., 1986, J. Cryst. Growth, Vol., 75, p 255

Bindell J., 1992, "Encyclopedia of Materials Characterization. Surfaces Images, Thin Films.", (Eds. C. R. Brundle, C. A. Evans, S. Wilson, L. E. Fitzpatrick), Butterworth-Heinemann, M.A., Chapter 2, pp 70-84

Blomfield C. J., 1995, PhD Thesis, Sheffield Hallam University

Brenner A., 1963, "Electrodeposition of Alloys: Principles and Practice", Academic Press, N. Y.

Busch G., Kern R., Steigmeirer E., 1957, Proc. Int. Commission on Electrochemistry Thermodynamics and Kinetics 9th Meet, [Chemical Abstracts, 54, (1960) 11752e]

Cabrera N., Vermilyea D. A., 1958, "The Growth and Perfection of Crystals", (Eds. R. H. Doremus, R. W. Roberts, D. Turnbull), John Wiley & Sons, Inc. N.Y., p 393

Campbell T. A., Koster J. N., 1999, Crystal Research & Technology, Vol. 43, No. 3, p 275

Carpenter M. K., Verbrugge M. W., 1990, J. Electrochem. Soc., Vol. 137, No. 1, pp 123-129

Carpenter M. K., Verbrugge M. W., 1994, J. Mater. Res., Vol. 9, No. 10, pp 2584-2591

Cattarin S., Furlanetto F., Musiani M. M., Guerriero P, 1994, J. Appl. Electrochem., Vol. 24, pp 439-448

Cattarin S., Musiani M., Casellato U., Rossetto G., Razzini G., Decker F., Scrosati B., 1995, J. Electrochem. Soc., Vol. 142, No. 4, pp 1267-1272

Chandra S., Khare N., 1987, Semicond. Sci. Technol. Vol. 2, pp 214-219

Chandra S., Khare N., 1987, Semicond. Sci. Technol. Vol. 2, pp 220-225

Chapman D. L., Phil. Mag., 1913, Chpt. 7

Chu T. L., Chu S. S., Solid State Electronics, 1995, Vol. 38, No. 3, pp 533-549

Colletti L. P., Flowers B. H., Stickney J. L., 1998, J. Electrochem. Soc., Vol. 145, No. 5, pp 1442-1449

Colyer C. L., Cocivera M., 1992, J. Electrochem. Soc., Vol. 139, No. 2, pp 406-409

Crow D. R., 1994, "Principles and Applications of Electrochemistry", 4th Ed., Blackie Academic & Professional, London, pp. 88-108

Cullity B. D., 1978, "Elements of X-Ray Diffraction", Addison-Wesley Publishing Company Inc., London

Cuomo J. J., Gambino R. J., 1968, J. Electrochem. Soc., Vol. 115, No. 7, pp 755-759

Damjanovic A., 1964, "Modern Aspects of Electrochemistry", (Eds. J. O'M Bockris, B. E. Conway), Butterworths Publications Ltd., London, Vol. III, p 224

Darkowski A., Cocivera M., 1987, J. Electrochem. Soc., Vol. 132, No. 11, pp 2768-2771

Davis L, 1993, Thin Solid Films, Vol. 236, pp 1-5

De Mattei R. C., Elwell D., Feigelson R. S., 1978, J. Crystal Growth, Vol. 43, pp 643-644

De Mattei R. C., Elwell D., Feigelson R. S., 1981, J. Electrochem. Soc., Vol. 128, No. 8, pp 1712-1714

De Mattei R. C., Feigelson R. S., 1992, "Electrochemistry of Semiconductors and Electronics", (Eds. J. McHardy, F. Ludwig), Noyes Publications, N.Y.

Dennison S., 1993, Electrochimica Acta, Vol. 38, No. 16, pp 2395-2402

Dennison S., 1994, J. Mater. Chem., Vol. 4, No. 1, pp 41, pp 41-46

Dennison S., 1995, J. Mater. Chem., Vol. 5, No. 11, pp 1885-1892

De Ruolz C. R. M., Acad. Sci., 1842, Vol. 15, p 1140

Despić A. R., Jović V. D. 1995, "Modern Aspects of Electrochemistry", (Ed. R. E. White), Plenum Press, N.Y., Vol. 24, pp 143-232

Dharmadasa I. M., Blomfield C. J., Gregory G. E., Haigh, J., 1995(a), Semicond. Sci. Technol., Vol. 9, pp 185-187

Dharmadasa I. M., Ives M., Brooks J. S., France G. H., Brown S. J., 1995(b), Semicond. Sci. Technol., Vol. 10, pp 369-372

Dioum I., Vedel J., Tremillon B., 1982, J. Crystal Growth, Vol. 139, p 329-333

Dukovic J. O., 1990, IBM J. Res. Develop., Vol. 34, No. 5, pp 693-705

Edamura T., Muto J., 1993, Thin Solid Films, Vol. 235, pp 198-201

Elwell D., 1981, J. Crystal Growth, Vol. 52, pp 741-752

Elwell D., Feigelson R. S., Simkins M. M., 1981, J. Crystal Growth, Vol. 52, pp 171-175

Elwell D., Feigelson R. S., Rao G. M., 1983, J. Electrochem. Soc., Vol. 130, No. 5, p 1021

Elwell D., Rao G. M., 1988, J. App. Electrochem., Vol. 18, pp 15-22

Engelken R. D., Van Doren T. P., 1985, J. Electrochem. Soc., Vol. 132, No. 12, pp 2904-2909

Faust C. L., 1963, "Modern Electroplating", (Ed. F. A. Lowenheim), John Wiley & Sons, N.Y.

Fedot'ev N. P., Bibikov N. N., Vyacheslavov, Grilikhes S. Y., 1962, "Electrolytic Alloys", Mashgiz, USSR

Fleishman M., Thirsk H. R., 1962, "Advances in Electrochemistry and Electrochemical Engineering", (Ed. P. Delahay, C. Tobias), Vol. 3, pp 145-210

Frank F. C., 1947, Discussions Faraday Soc., Vol. 5, p 48

Fulop G. F., Taylor R. M., 1985, Annu. Rev. Mater. Sci., Vol. 15, pp 197-210

Gao Y., Han A., Lin Y., Zhao Y., Zhang J., 1994, J. Appl. Phys., Vol. 75, No. 1, pp 549-552

Gatos H. C., 1982, "Materials Processing in the Reduced Gravity Environment of Space", (Ed. G. Rhindone), North-Holland, Amsterdam

Geiss R. H., 1992, "Encyclopedia of Materials Characterization. Surfaces Images, Thin Films", (Eds. C. R. Brundle, C. A. Evans, S. Wilson, L. E. Fitzpatrick), Butterworth-Heinemann, M.A., Chapter 3, pp 120-134

Golan Y., Hodes G., Rubinstein I., 1996, J. Phys. Chem., Vol. 100, pp 2220-2228

Goodman C. H. L., (Ed.), 1974, "Crystal Growth, Theory and Techniques", Plenum Press, London

Gorbunova K. M., Ploukarov Y. M., 1967, "Advances in Electrochemistry and Electrochemical Engineering", (Ed. C. W. Tobias), Interscience, New York, Vol. 5, pp 249-294

Gore G., 1855, Phil. Mag., Vol. 7, p 73

Gore R. B., Pandey R. K., Kulkarni S. K., 1989, J. Appl. Phys., Vol. 65, No. 7, pp 2693-2698

Goto F., Shirai K., Ichimura M., 1998, Sol. Eng. Mater. & Sol. Cells, Vol. 50, pp 147-153

Gouy G., 1910, Compt. Rend., Vol. 149, p 654

Grahame D., 1947, Chem. Rev., Vol. 41, p 441

Green T. A., Russell A. E., Roy S., 1998, J. Electrochem. Soc., Vol. 145, No. 3, pp 875-881

Gruszecki T., Holmström B., 1993, Sol. Eng. Mater. & Sol. Cells, Vol. 31, pp 227-234

Guillemoles J. F., Cowache P., Lusson A., Fezzaa K., Boisvion F., Vedel J., Lincot D., 1996, J. Appl. Phys., Vol. 79, No. 9, pp 7293-7302

Guillen C., Herrero J., 1995, J. Electrochem. Soc., Vol. 142, No. 6, pp 1834-1838

Harris D.C., 1987, "Quantitative Chemical Analysis", 2nd Ed., W. H. Freeman and Company, N.Y.

Haywood S. K., Zheng L., Sweileh G. M., Lakrimi M., Mason N. J., Walker P. J., 1998, IEE Proc.-Opto, pp 287-291

Helmholtz H. L. F. Von, 1879, Ann. Physik, Vol. 7, p 337

Ives M., 1995, PhD Thesis, Sheffield Hallam University

Jayachandran M., Chokalingam J., Venkatesan V. K., 1989, J. Mater. Sci. Lett., Vol. 8, pp 563-565

Kampmann A., Cowache P., Vedel J., Lincot D., 1995, J. Electroanal. Chem., Vol. 387, pp 53-64

Kashyout A. B., Aricò A. S., Monforte G., Crea F., Antoncucci V., Giordano N., 1995, Sol. Eng. Mater. & Sol. Cells, Vol. 37, pp 43-53

Khamudkhanova S. Z., Rubinchik G. F., Murtazaev A.M., 1973, Dokl. Akad. Nauk. Uzb., Vol. 30, No. 6, pp 47-48

Kochegarov V. M., Belitskaya T. B., 1971, Zh. Prikl. Khimi., Vol. 44, No. 2, pp 455-457

Königstein C., Neumann-Spallart M., 1998, J. Electrochem. Soc., Vol. 145, No. 1, pp 337-343

Koryta J., Dvořák J., Kavan L., 1993, "Principles of Electrochemistry", 2nd Ed., John Wiley & Sons, N.Y., p 153

Kozlov V. M., Agrigento V., Bontempi D., Canegallo S., Moraitou C., Toussimi A., Bicelli L. P., Serravalle G., 1997, J. Alloys & Compounds, Vol. 259, pp 234-240

Kröger F. A., 1978, J. Electrochem. Soc., Vol. 125, No. 12, pp 2028-3034

Lagally M. G., 1993, Physics Today, November, pp 24-31

Lee C. H., Kröger F. A., 1982, J. Electrochem. Soc., Vol. 129, No. 5, pp 936-942

Li D. Y., Szpunar J. A., 1993, J. Electron. Mater., Vol. 22, No. 6, pp 653-657

Lockhande C. D., 1987, Solar Cells, Vol. 22, p 133

Lockhande C. D., Pawar S. H., 1989, Phys. stat. sol. (a), Vol. 111, pp 17-40

Löizos Z., Spyrellis N., 1991, Thin Solid Films, Vol. 204, pp 139-149

Lowenheim F. A., (Ed.), 1963, "Modern Electroplating", 2nd Ed., John-Wiley & Sons Inc., N.Y.

Lyons L. E., Morris G. C., Tandon R. K., 1989, Sol. Eng. Mater., Vol. 18, pp 315-331

Mackay K. M, Mackay R. A., 1989, "Introduction to Modern inorganic Chemistry", 4th Ed., Blackie, London

Markov I., Valova I., Illieva M., Kristev I., 1983, J. Crystal Growth, Vol. 65, p 611

McCann J. F., Skyllas-Kazacos M., 1981, J. Electroanal. Chem., Vol. 119, pp 409-412

McGregor S. M., Dharmadasa I. M., Wadsworth I., Care C. M., 1996, Optical Materials Vol. 6, pp 75-81

Mellor J. W., 1929, "A Comprehensive Treatise on Inorganic and Theoretical Chemistry" Longmans, Green & Co., Vol. IX, p 124

Mengoli G., Musiani M. M., Paolucci F., 1991, J. of Appl. Electrochem., Vol. 21, pp 863-868

Mengoli G., Musiani M. M., Paolucci F., 1992, J. Electroanal. Chem., Vol. 332, pp 199-211

Meulenkamp E. A., Peter L. M., 1996, J. Chem. Soc. Faraday Trans., Vol. 92, No. 20, pp 4077-4082

Milnes A. G., Polyakov A. Y., 1993, Sol. Stat. Electron., Vol. 36, No. 6, pp 803-818

Mishra K. K., Rajeshwar K., 1989, J. Electroanal. Chem., Vol. 273, pp 169-182

Mogilov V. M., Falicheva A. I., 1974, Zahshcita Metallov, Vol. 10, pp 192-196

Molin A. N., Dikusar A. I., Kiosse G. A., Petrenko P. A., Sokolovsky A. I., Saltanovsky Y. G., 1994, Thin Solid Films, Vol. 237, pp 66-71

Molin A. N., Dikusar A. I., 1994, Thin Solid Films, Vol. 237, pp 72-77

Mondal A., McCandless B. E., Birkmire R. W., 1992, Sol. Eng. Mater. & Sol. Cells, Vol. 26, pp 181-187

Monnier R., 1983, Chimia, Vol. 37, p 109

Mori E., Mishra K. K., Rajeshwar K., 1990, J. Electrochem. Soc., Vol. 137, No. 4, pp 1100-1106

Morris G. C., Tanner P. G., Tottszer A., 1991, Materials Forum, Vol. 15, pp 21-29

Moutinho H. R., Al-Jassim M. M., Levi D. H., Dippo P. C. & Kazmerski L. L., 1998, J. Vac. Sci. Technol. A, Vol. 16, No. 3, pp 1251-1257

Murali K. R., Jayachandran M., Rangarajan N., 1987, Bull. Electrochem., Vol. 3, p 261

Natarajan C. Sharon M, Lévy-Clément C., Neumann-Spallart M., 1994, Thin Solid Films, Vol. 237, pp 118-123

Okimura H., Koizumi Y., Kaida S., 1995, Thin Solid Films, Vol. 254, pp 169-174

Okubo T, 1988, J. Electrochem. Soc.: Reviews and News, Vol. 135, No. 8, 369C, p 376

O'M Bockris J., 1963, Proc. R. Soc., A274, p 55

O'M Bockris J, 1967, "Fundamental Aspects of Electrocrystallization", Plenum Press, London

O'M Bockris J., Reddy A. K. N., 1970, "Modern Electrochemistry", MacDonald, London

Ortega J., 1991, Anales De Quimica, Vol. 87, pp 641-644

Ortega J., Herrero J., 1989, J. Electrochem. Soc., Vol. 136, No. 11, pp 3388-3391

Ostroumov V. V. & Styrkas A.D., 1963, Vestn. Leningr. Univ. Ser. Fiz. Khem., Vol. 18, No. 10, pp 101-107

Pangarov N. A., 1962, Electrochim. Acta, Vol. 7, p 139

Panicker M. P. R., Knaster M., Kröger F. A., 1978, J. Electrochem. Soc., Vol. 125, No. 4, pp 566-572

Paolucci F., Mengoli G., Musiani M., 1990, J. App. Echem., Vol. 20, pp 868-873

Pearsall N. M., Chemistry & Industry, 1993, January, pp 51-55

Perrault G. G., 1989, J. Electrochem. Soc., Vol. 136, No. 10, pp 2845-2849

Pitman A. L., Pourbaix M., de Zoubov N., 1957, J. Electrochem. Soc., Vol. 104, No. 10, pp 594-600

Pletcher D., 1991, "A First Course in Electrode Processes", The Electrochemical Consultancy, UK

Pottier D., Maurin G., 1989, J. Applied Electrochem., Vol. 19, pp 361-367

Pourbaix M., 1961, "Atlas of Electrochemical Equilibria in Aqueous Solutions", Pergamon Press, UK

Power G. P., Peggs D. R., Parker A. J., 1981, Electrochimica. Acta, Vol. 26, No. 5, pp 681-682

Qi B., Kim D., Williamson D. L., Trefny J. U, 1996, J. Electrochem. Soc., Vol. 143, No. 2, pp 517-523

Rai J. P., 1993, Sol. Eng. Mat. & Sol. Cells, Vol. 30, pp 119-126

Rajeshwar K., 1992, Adv. Mater., Vol. 1, pp 23-29

Rastogi A. C., Balakrishnan K. S., 1989, J. Electrochem. Soc., Vol. 136, No. 5, pp 1502-1506

Rogalski A., 1989, Prog. Quantum Electron. , Vol. 13, pp 191

Routkevitch D., Bigiaoni T., Moskovitis M., Xu J. M., 1996, J. Phys. Chem., Vol. 100, pp 14037-14047

Russ J. C., 1984, "Fundamentals of Energy Dispersive X-Ray Analysis", Butterworths & Co. (Publishers) Ltd, UK

Sadana Y. N., Singh J. P., 1985, Plating and Surface Finishing, pp 64-70

Sadana Y. N., Singh J. P., Kumar R., 1985, Surface Technology, Vol. 24, pp 319-353

Sahu S. N., 1989, J. Materials Sci. Letts., Vol. 8, pp 533-534

Sahu S. N., 1992, J. Mater. Sci.: Mater. Electron., Vol. 3, pp 102-106

Samantilleke A. P., Boyle M. H., Young J., Dharmadasa I. M., 1998, J. Mater. Sci.: Mater. Electron., Vol. 8, pp 231-235

Sangwal K., Rodriguez-Clemente R., 1991, "Surface Morphology of Crystalline Solids", Trans Tech Publishers, USA

Saraby-Reintjes A., Peter L. M., Ozsan M. E., Dennison S., Webster S., 1993, J. Electrochem. Soc., Vol. 140, No. 10, pp 2880-2888

Sawyer D. T. Sobkowiak A. J., Roberts J. L., 1995, "Experimental Electrochemistry for Chemists", John Wiley and Sons, N.Y.

Searson P. C., 1992, Solar Energy Mater. Solar Cells, Vol. 27, pp 377-388

Sharma R. C., Chang Y. A., 1989, J. Electrochem. Soc., Vol. 136, No. 5, pp 1356-1502

Skoog D. A., 1979, "Principles of Instrumental Analysis", 3rd International Ed., Saunders College Publishing, USA

Smart C.F., 1956, US Patent 2,755,537

St. Claire De Ville H., 1854, Compt. Rend. Acad. Sci. Paris, Vol. 39, p 323

Stern O., 1924, Z. Elekrochem., Vol. 30, p 508

Styrkas A. D., Ostroumov V. V., Anan'eva G. V., 1964, Zh. Prikl. Khim. (Leningrad), Vol. 37, No. 11, pp 2398-2403

Szekely G., 1951, J. Electrochem. Soc., Vol. 98, p 936

Takahashi M., Ousaki K., Kita H., Suzuki Y., 1985, J. Appl. Phys., Vol. 58, No. 10, p 3809

Tomkeiwicz M., Ling I., Parson W. S., 1982, J. Electrochem. Soc., Vol. 129, No. 1, pp 2016-22

Villegas I., Stickney J. L., 1992, J. Electrochem. Soc., Vol. 139, No. 3, pp 686-694

Wei C., Rajeshwar K., 1992, J. Electrochem. Soc., Vol. 139, No. 4, pp L40-L41

West J. M., 1971, "Electrodeposition and Corrosion Processes", 2nd Ed., Van Nostrand Reinhold Company, London

Wicelinski S. P., Gale R. J., 1987, The Electrochemical Society Extended Abstracts, Honolulu, HI, Oct 18-23, Vol. 87-2, Abstract 1495, p 2040

Wicelinski S. P., Gale R. J., Wilkes J. S., 1987, J. Electrochem. Soc., Vol. 134, pp 262-263

Wikstrom L. L., Thomas N. T., Nobe K., 1973, J. Electrochem. Soc., Vol. 122, No. 9, pp 1201-1206

Willardson R. K., Beer A. C., (Eds.), 1975, "Semiconductors and Semimetals, Vol. 10, Academic Press, J D Wiley, N.Y.

Yang M. C., Landau U., Angus J. C., 1992, J. Electrochem. Soc., Vol. 139, No. 12, pp 3480-3488

Zaburdaeva F. I., Kochegarov V. M., 1965, Izv. Vyssh. Uchebn. Zaved. Tsvetn. Metall., Vol. 8, No. 2, pp 89-95 [Chemical Abstracts, 63, (1965) 9530e]

Zanio K, 1978, (Ed. R. K. Williamson & A. C. Beer), "Cadmium Telluride - Semiconductors and Semimetals", Academic Press, N.Y.

Zytkiewicz Z. R., Dobosz D., 1995, Acta Physica Polonica A, Vol. 88, No. 5, pp 965-968

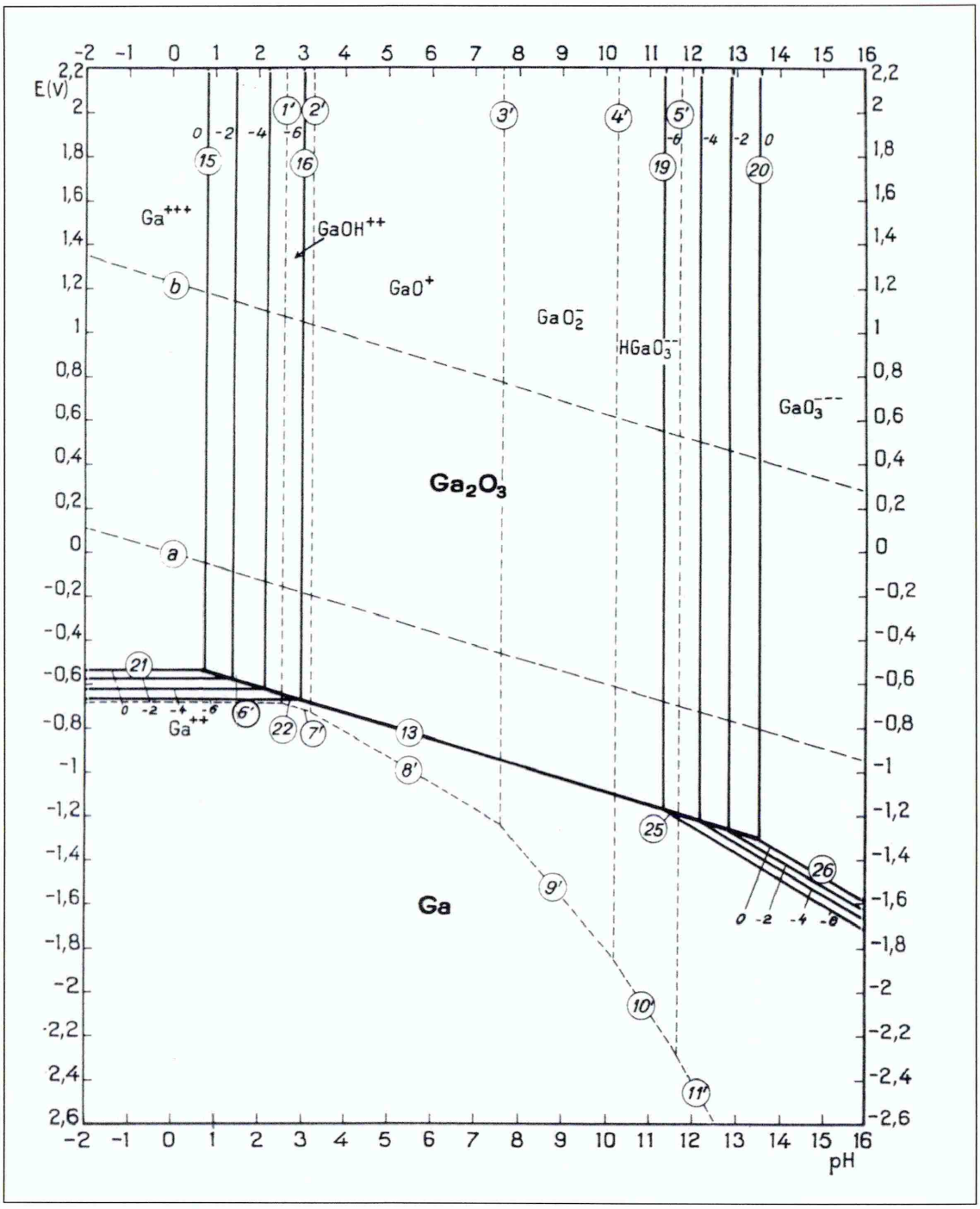

Potential – pH equilibrium diagram for the system gallium-water at 25 ^{O}C, Pourbaix (1966). The numbers relate to specific equilibria given in the aforementioned reference. The line marked (a) represents H_2 evolution, whilst that marked (b) represents the evolution of O_2, (See section 2.2.8.).

Appendix II

Refereed Publications

[1] "Electrochemical Growth of GaSb & InSb for Applications in Infra-Red Detectors and Optical Communication Systems"

McChesney J-J, Haigh J, Dharmadasa IM, Mowthorpe DJ, *Optical Materials* **6**, 63, (1996)

[2] "Photoemission study of the formation of Intimate In-InGaAs (100) Contacts at Room and Cryogenic Temperatures"

Cammack DS, McGregor, McChesney J-J, Dharmadasa IM, Clark SA, Dunstan PR, Burgess SR, Wilks SP, Elliot M, *J. Appl. Phys.*, **81**(12), 7876, (1997)

[3] "An investigation of the Properties of Intimate In-$In_xGa_{1-x}As$ (100) Interfaces Formed at Room and Cryogenic Temperatures"

Cammack DS, McGregor, McChesney J-J, Clark SA, Dunstan PR, Burgess SR, Wilks SP, Peiró F, Ferrer J-C, Cornet A, Morante JR, Kestle A, Westwood DI, Elliot M, *App. Surf. Sci.*, **132/124**, 510, (1998)

Conferences Attended

Condensed Matter and Materials Physics
Leeds University, December 1993

1st International Conference, Electroactive Materials
Sheffield Hallam University, May 1996

Oral "Electrochemical Growth of GaSb & InSb for Applications in Infra-Red Detectors and Optical Communication Systems"

Mid-Infra-Red Optoelectronics Materials & Devices

Oral "Growth of Thin Film Infra-Red Materials using Electrochemical Deposition"